Spectroelectrochemical analysis of bianthrone monolayers

Abstract

The redox chemistry of quinones and their analogues can be seen in virtually all living organisms and without them, important biological functions would not be possible. They are an essential component in bioenergetics and occur naturally as components in many biochemical molecules. The redox properties of quinone and its analogues, particularly species that display an observable change between their oxidised and reduced species, has also shown potential in the field of molecular electronics and sensors and also provide accessible models for the study of electron transfer. Much work has been done to develop an understanding of such molecules and further study is vital to expand this understanding and encourage the exploitation of these molecules.

In work prior to this thesis, focus has been placed on the electrochemical and photochemical analysis of bianthrone in solution. In brief, bianthrone undergoes a conformational change from a puckered form to a twisted form when undergoing a two-electron transfer in solution. This was described as an ECE mechanism.

However, no electrochemical studies had been carried out on bianthrone self-assembled monolayers immobilised on electrode surfaces and no evidence existed to suggest that the conformational behaviour of bianthrone in monolayer form would be comparable to its behaviour in solution.

Studies into the formation of self-assembled monolayers of bianthrone on mercury electrodes were carried out. General electrochemical properties suggest that bianthrone undergoes a two-electron, two-proton transfer. Bianthrone voltammetry showed evidence of current spikes that appeared in the voltammetry as the surface coverage approached full surface coverage. These spikes were indicative of intermolecular interactions between molecules on the surface. Studies into the dynamics of bianthrone monolayer formation were carried out by comparing a theoretical model, obtained from a paper by Hubbard et al. that described the influence of diffusion of molecules to the surface and the reorganization of molecules on the electrode surface, with surface coverage/time data obtained by cyclic voltammetry. . The diffusion rate constants ranged from 6.0×10^{-11} for 0.09 µM to 1.5×10^{-12} for 0.3 µM. The surface reorganization rate constants, K, ranged from 9.31×10^{-7} for 0.09 µM to 9.8×10^{-8} for 0.3 µM.

A spectroelectrochemical cell in which electrochemistry could be carried out while being incorporated into a Raman microscope was fabricated to examine bianthrone monolayers adsorbed on mercury electrodes. The potential of the cell was held at different points between where the monolayer was fully oxidised and fully reduced according to the cyclic voltammetry obtained and Raman spectra were recorded at these points. The spectra taken at these potentials were compared and contrasted to elucidate any structural differences that occurred in the reduction of the monolayer. This analysis revealed some subtle changes in intensity in the lower wavenumber region of the spectra. However, there were no changes indicative of a large structural change to the monolayer. As a result of this analysis, it is not believed that bianthrone undergoes conformational changes that would induce major structural changes to the monolayer upon reduction.

Studies into the formation of bianthrone monolayers on glassy carbon electrodes were carried out. The voltammetry is consistent with a surface adsorbed molecule undergoing a two-electron, two-proton transfer. Unlike adsorption on mercury, current spikes are not observed. Studies into the dynamics of monolayer formation on GC were also carried out using the same theoretical model as published by Hubbard et al. Values for the surface reorganization rate constant were obtained. This value ranged from $1.26 \times 10^7 \pm 0.05$ cms^1 for 1 μM to $4.36 \pm 0.02 \times 10^8$ cms^1 for 20 μM. A spectroelectrochemical cell similar to the mercury electrochemical cell in which electrochemistry could be carried out but that could still be incorporated into a Raman microscope was fabricated for use with a GC electrode. Raman spectra of bianthrone monolayers recorded in the absence of an applied potential compared favourably with the spectra of solid bianthrone and spectra obtained in the literature. The potential of the cell was held constant at different points between where the monolayer was oxidised and reduced according to the voltammetry obtained. The spectra recorded at each potential were compared and contrasted to elucidate any structural differences that may have occurred at these potentials as the monolayer is reduced. Some changes in intensity at certain bands were observed, however, there were no large changes in the spectra associated with large structural changes arising from conformational changes in the molecule. From this, it was concluded that conformational change in the molecule did not occur when it was immobilised on the glassy carbon surface.

Electrochemistry was carried out on bianthrone in the solid state, on a glassy carbon electrode. Evidence of "breaking in" phenomenon was observed from voltammetric studies of the solid layer.

Spectroelectrochemical Analysis of Bianthrone Monolayers

Darragh Lucey, BSc (Hons)

A Thesis presented at Dublin City University for the degree of
Doctor of Philosophy

Supervisor: Prof. Robert J. Forster
School of Chemical Sciences,
Dublin City University

November 2006

Declaration

I hereby certify that the material, which I now submit for assessment on the programme of study leading to the award of Doctor of Philosophy is entirely of my own work and has not been taken from the work of others save and to the extent that such works has been cited and acknowledged within the text of my work

Signed _Dornah Lheey_

Date _1/11/06_

ID No: _97556688_

This thesis is dedicated to all my family, without whom its completion would not have been possible

1.0 Introduction And Literature Review

What you know'd fill a book   What you don't know'd fill a library
Bill Cussen

1 1 Molecular switching

The demand for high data storage densities, high switching rates, all optical switching devices and miniaturization has stimulated the search for organic molecules suited for applications in switching devices [1] [2] The synthesis of molecular switches and molecular storage elements can give answers to fundamental questions on the level of molecular and nanoscale dimensions, and leads to further development of model concepts with respect to possible modes of operation of molecular memories

The basic requirement for a switch is bistability, in other words, the occurrence of two different forms of a molecule, which can be converted by means of an external source Any material or device that has two stable states which can be reversibly switched from one state to another and whose states can be readily identified at any instant can in principle be used as a memory element using binary logic Below is a simple schematic of the process

$$S_1$$
$$A \longleftrightarrow B$$
$$S_2$$
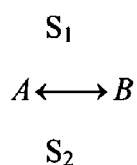
The bistability may be based on various properties of molecules like electron transfer, isomerizations, differences in complexation behaviour and photocyclization, whereas light, heat, pressure, magnetic or electric fields, chemical reactions etc can be used to achieve the change in the bistable state Photoreversible compounds, where the reversible switching process is based on photochemically induced interconversion, play an important role in this field [3] Photochromism, which is defined as the reversible change, induced by light irradiation, between two states of a molecule having different absorption spectra, can be the basis for a molecular switch However, the molecules must cope with many other necessary demands to be suitable for a practical device The most important requirements for the use of photochromic compounds as molecular switches are [4]

- Photochemical switching between the two forms should be possible

- No thermal interconversion of the isomers should occur in a large temperature range, allowing storage of information infinitely

- The isomers should be fatigue resistant, with the possibility to perform the write/erase cycle many times, and no thermal or photochemical degradation to any side product should occur

- Both forms should be readily detectable

- A non–destructive read-out procedure should be achieved, allowing an efficient switching process and avoiding the necessity of long irradiation times

- Fast response times should be reached, leading to fast switching cycles

- Retention of all the properties is necessary when the switchable compound becomes part of a macromolecular structure

The development of a molecular switching or optical data storage device initially involves the design and synthesis of molecules which possess the above properties, followed by the incorporation of these compounds into supramolecular assemblies in order to obtain ordered molecular systems

Typical examples of reversible photochromic processes are *cis/trans* isomerizations or photocyclization reactions A natural example of *cis-trans* isomerism is the isomerization of olefinic compounds that form the basic process of vision [5] This involves the 180^0 rotation around a carbon-carbon double bond The absorption of photons results in the conversion of 11-cis retinal bound as a Schiff base via the amino acid lysine to the protein opsin together forming rhodopsin, to 11-trans retinal The λ_{max} of the cis form is 498 nm while the λ_{max} of the trans form is 380 nm The structural disturbance of the retinal moiety of rhodopsin leads to a conformational change of the whole protein molecule and, via a cascade of reactions, eventually creates a nerve pulse responsible for vision The principle of this process has been exploited in other photochromic systems

Bacteriorhodopsin, a pigment related to rhodopsin, with retinal as the photoresponsive element in the all-trans form was examined as a potential switching device [6] This protein is similar to rhodopsin, is stable under extreme conditions of pH and salt concentration and exhibits excellent photochemical activity when dissolved in polymer films The protonated all-trans Schiff base of retinal (B form, λ_{max} = 570 nm)

can be converted to the deprotonated cis isomer (M form, λ_{max} = 412 nm) by irradiation at 568 nm, with a switching time in the μ-second range. The B and M forms represent the 0 and 1 codings for digital information. Problems with the short lifetime of the M form were overcome by the use of mutated bacteriorhodopsin. By using holographic techniques it was possible to store patterns of digital information. This provides a good example of a molecular switch that is operable by a simple conformational change. Other examples include azobenzenes. Here there are two conformations that can be detected by their differences in UV absorption spectra. In principle, the azobenzenes could function as molecular switches by applying light of different wavelengths to obtain varying amounts of cis and trans isomers, where the excess of either can be detected by the change in uv spectra. However, some drawbacks exist. One is the thermal reisomerization of the Z isomer to the more stable E isomer, with the lifetimes of the Z isomer varying from minutes to several days at room temperature. Another drawback is that the detection method used to assess the isomer ratio can influence the isomerization process. Thus, it is a destructive read-out procedure.

Other examples of molecular switching techniques include reversible host-guest chemistry,[7] changes in conductivity,[8] selective reduction,[9] photocyclizations,[10] chiroptical molecular switching,[11] and molecular electronics (involving reversible electron transfer)[12].

A good example of surfaces that exhibit dynamic changes in interfacial properties in response to an electrical potential can be found in a paper by Choi et al[13]. Here it was found that changes in wetting behaviour were caused by surface-confined, single layered molecules undergoing conformational transitions between a hydrophilic and a moderately hydrophobic state. (16-Mercapto)hexadecanoic acid (MHA) was chosen as a model due to its ability to self assemble on gold surfaces and due to a hydrophobic chain capped by a hydrophilic carboxylate group. This could facilitate changes in the overall surface. To create a monolayer with sufficient spacing between the individual MHA molecules, a strategy that exploits synthesis and self-assembly of a MHA derivative with a globular end group was employed. This resulted in a self-assembled monolayer that was densely packed with respect to the space-filling end groups but showed low-density packing with respect to the hydrophobic chains.

11

Subsequent cleavage of the space-filling end groups established a low density SAM of MHA   The equilibrium low-energy conformational state of each of the sparsely packed MHA molecules was an all trans state   Upon applying an electric potential, the negatively charged carboxylate groups experienced an attractive force to the gold surface, causing the hydrophobic chains to undergo conformational changes   This chain bending disrupted the all trans conformational state and caused the aliphatic MHA chains to adopt a mixture of trans and gauche conformations

These examples provide concrete evidence of the feasibility of molecular switches and give a practical insight into the operation of such switches   The study of molecular switches is a topic of great relevance in modern science   Much of the work carried out involves the analysis of various molecules that meet the requirements outlined earlier   With this in mind, and with the benefit of previous work on the subject, it is believed that bianthrone has the potential to be employed as a molecular switch   The next section provides information on bianthrone   Briefly, bianthrone has been seen to exhibit two distinct conformations and bistability   It is the purpose of this work to determine whether bianthrone is a suitable candidate for use as a molecular switch when immobilised on a surface

1 2 Bianthrone

Bianthrone, 10(-10-oxo-9 (10H)-anthracenylidene)-9(10H)-anthracenone, is a heterocyclic molecule, which at room temperature exists as a yellow compound Its basic structure is that of two planar ring systems connected by a central double bond with a single oxygen molecule doubly bound to each ring system

It can exist in two main conformations depending on certain conditions, which are shown in Figure 1 2 1 The first is that of a puckered system whereby the two ring systems are folded away from each other to minimise strong steric interactions between hydrogens located at the 1 and 8' (and 1'and 8) positions This conformation is most prevalent at room temperature Its other conformation is where the molecule is twisted about the central, 9,9' double bond at an angle of approximately 57^0 [14] These two forms exist in thermal equilibrium with one another, in other words at room temperature the puckered form dominates while as the temperature rises the twisted form, which appears as a green colour, becomes more prevalent

A   **B**
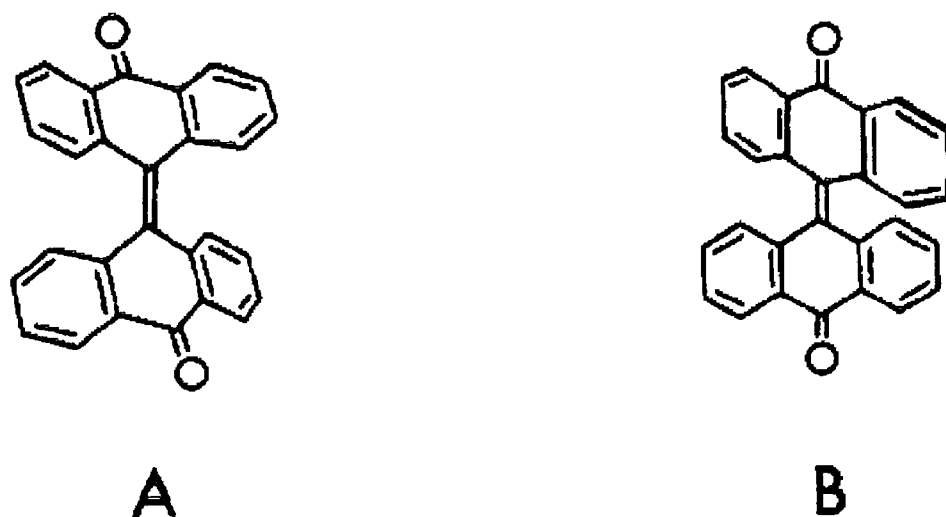
Figure 1 2 1 The two conformations of bianthrone

The conversion from the puckered form to the twisted form can also be induced by electrochemical reduction,[15 16] pressure and by photochemical means [17]

The existence of these two metastable states and the ability to detect these distinctive states gives rise to a binary response and therefore makes bianthrone a potential molecule for molecular based switching or data storage or processing.

Evans et al carried out analysis of the pathways involved in the reduction of bianthrone.[18] In this analysis, the electrochemical reduction of the low temperature, puckered form of bianthrone was carried out at a platinum cathode in DMF. A scheme describing the reduction pathway of bianthrone was proposed which is shown in Figure 1.2.2.
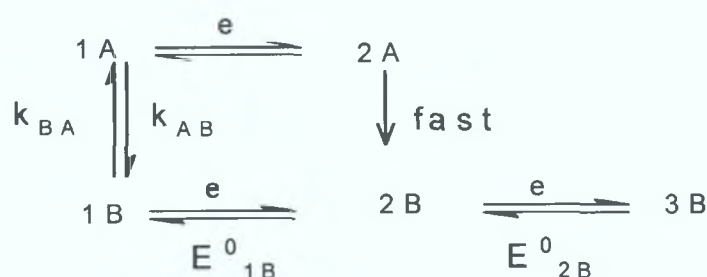
Figure 1.2.2: Redox pathway of bianthrone. Here 1A refers to the A conformation detailed in Figure 1.2.1, 1B refers to the B conformation. This pathway is reproduced from reference 12 by Evans et al.

From their analysis, Evans and Olsen proposed that bianthrone reduction occurs via an ECE mechanism, i.e., electron transfer (E), followed by conformational change (C), followed by a second electron transfer (E). The results obtained by cyclic voltammetry, shown in Figure 1.2.3, showed a single reduction peak on the first half cycle 1A to 3B followed by two oxidation peaks observed on the second half cycle, which corresponds to the conversion of 3B to 2B and 2B to 1B. 1B is the high temperature thermochromic form of bianthrone. The 1B to 2B and 2B to 3B processes were observable at high scan rates. It was shown that 1B disappears at slower scan rates by the disappearance of the 1B to 2B reduction peak. It was also found that the 1B/2B and 2B/3B redox couples were adequately represented by rapid electron transfer reactions, since these reactions involve only minor changes in

configuration   Conversion of 1A to 3B involved an irreversible two-electron reduction
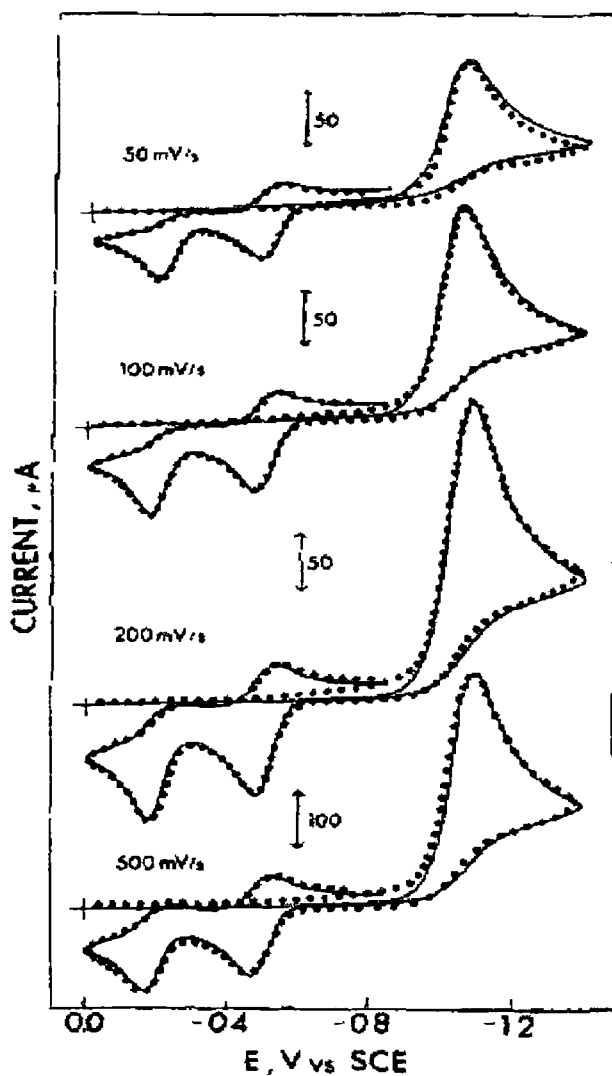
Figure 1 2 3   Cyclic voltammograms of bianthrone reproduced from reference 12 by Olsen and Evans   Electrochemical cell used was the disk portion of a platinum ring disk electrode as working electrode with an aqueous SCE as reference   Solution contained 1 12 mM bianthrone in 0 10 TEAP in DMF   The large reduction peak at approximately −1 2 V represents the reduction of the A form of bianthrone to the radical dianion (1A→3B)   The two oxidation peaks on the reverse scan represent the oxidation steps of the dianion 3B to 1B (3B→2B→1B)

From the absorbance spectra of the stable species involved in the proposed scheme, which were obtained from thin layer spectroelectrochemistry, it was shown that by adjusting the potential it was possible to obtain spectra corresponding to each of the constituents in the scheme (Figure 1 2 4) Firstly, a spectrum for the puckered form of the molecule was obtained The potential of the cell was adjusted to $-1\ 4$ V which resulted in a spectrum being obtained for the 3B form of the molecule showing absorbance at 520 nm Further adjustment of the potential to $-0\ 4$ V resulted in the oxidation of 3B to 2B The final adjustment of the potential to $0\ 4$ V resulted in the original spectrum being obtained This corresponds to the pathway 2B to 1B to 1A
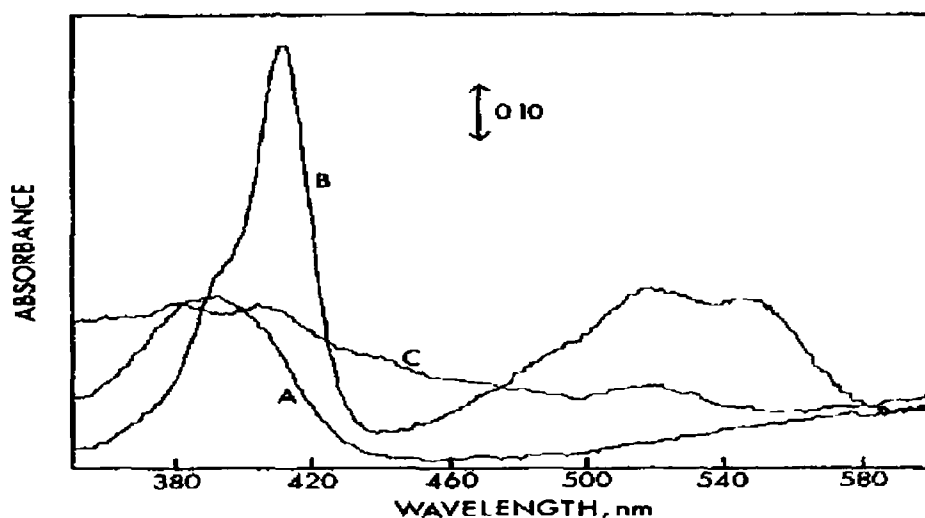
Figure 1 2 4 Spectra of bianthrone obtained at various stages in the redox process Spectrum A is of bianthrone in its initial state, B is a spectrum of the dianion, denoted 3B in the reaction scheme, C is the spectrum of the anion radical 2B Solution was 1 29 mM bianthrone in 0 10 M TEAP in DMF Figure was taken from reference 12 by Olsen and Evans

The molar absorptivity was found to be $1\,5 \times 10^4$ M^{-1}cm^{-1} for the 3B form of the molecule at 520 nm From their analysis of the data they found that the conversion of 1A to 3B is diffusion controlled This was confirmed by the use of Equation (1 1)

$$A = \frac{2\varepsilon C * D^{\frac{1}{2}} t^{\frac{1}{2}}}{\pi^{\frac{1}{2}}} \quad (1\ 1)$$

where ε is the molar absorptivity of the product, C* is the reactant concentration D is the diffusion coefficient and t is time This equation is applicable for a diffusion controlled electrode reaction that produces an absorbing product For a diffusion controlled reaction, plots of A vs $t^{1/2}$ should be linear 1B is formed from the oxidation of 3B The 1B form of the molecule gave a distinct absorbance at 665 nm The formation of 1B is a more acceptable interpretation of the pathway (rather than the conversion of 1A by the oxidation of 3B) as electron transfer between structurally similar B forms of the molecule is rapid 1B is not at conformational equilibrium and will convert to 1A as it diffuses away from the electrode

In a subsequent paper by Evans et al, the rates of conformational change in the anion radicals of bianthrone, as well as 3,3'-dimethyl, 3,3'-dimethoxy, and 1,1'-dimethyl derivatives of bianthrone were calculated [19] Pulse radiolysis was employed to study these molecules The rate of conformational change between the A$^-$ and the B for bianthrone was found to be $7\,4 \times 10^4$ s$^-$ for bianthrone The radiolysis experiments were carried out in isopropanol-water solutions The action of radiation on the solvent mixtures produces the $(CH_3)_2C^\bullet OH$ radical Radiolysis of i-PrOH produces solvated electrons $(CH_3)_2C^\bullet OH$ and $(CH_3)_2CHO$ The alkoxyl radicals react with I-PrOH to form $(CH_3)_2C^\bullet OH$ Radiolysis of water produces H, OH, and aqueous electrons The hydrogens and hydroxides react with I-PrOH to produce $(CH_3)_2C^\bullet OH$ In short, most of the primary radicals of radiolysis are converted in fractions of microseconds to $(CH_3)_2C^\bullet OH$ These radicals will react with bianthrone in its A form to produce anion radicals, in the following reaction

$$(CH_3)_2C^\bullet OH + A \rightarrow (CH_3)_2CO + H^+ + A^{-\bullet}$$
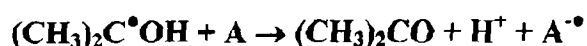
The radical will then undergo conformational change,

$$A^{-\bullet} \rightarrow B^{-\bullet}$$
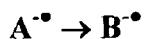
or it will decay into final products by second order reactions
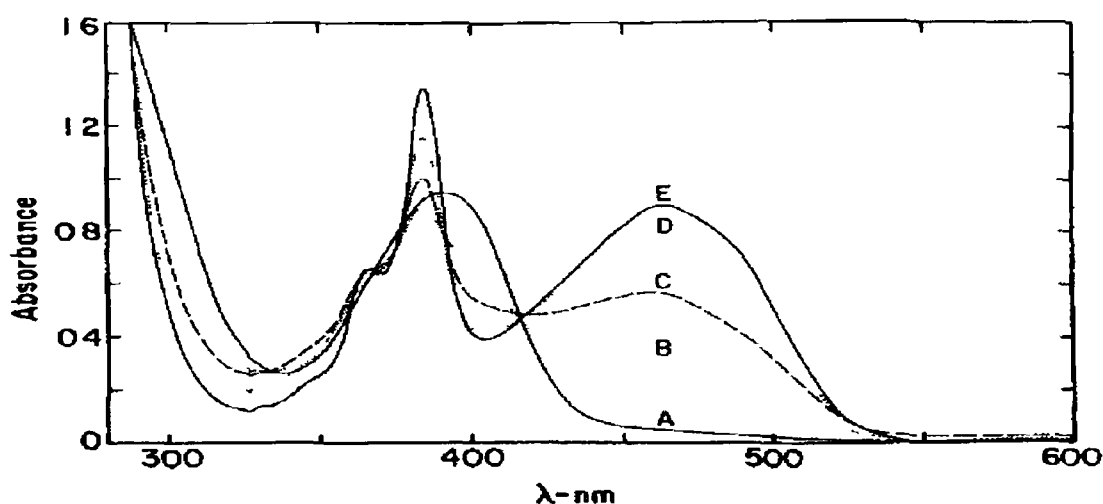
Figure 1 2 5   Absorption spectra of bianthrone and its radiolytic product taken from reference 13 by Neta and Evans Spectrum A is one taken before irradiation Spectrum B to E were taken after 5, 10, 15, and 20 minutes of irradiation

Steady-state radiolysis of bianthrone showed bleaching of the 390 nm absorption band accompanied by build-up of absorption at 384nm and 463nm These absorptions showed reasonable conversion of bianthrone into products Figure 1 2 5 shows this Spectrum A is that of bianthrone while spectra B through E represent absorption spectra following 5, 10, 15, and 20 minutes irradiation The bleaching of the bianthrone absorption band at 390 nm manifests itself as a narrowing of the band, while the evolution of the bands at 463 nm and 386 nm can be seen

18

Consequently, the product of radiolysis is the two-electron product, present as an anion BH   Evidence for these processes were obtained from pulse radiolysis experiments   At short timescales, the formation of $A^{-\bullet}$ and the conversion of $A^{\bullet}$ to $B^{\bullet}$ could be followed, evidenced by kinetic traces at 460 and 550 nm   Using decay traces it was possible to calculate the rate constant assigned to the conformational change, which, as already stated was 7×10^4 s^{-1} This rate constant corresponds to a $\Delta G^{\ddagger}$ of 10 8 kcal/mol at room temperature, which is approximately half that of the same reaction for the neutral species 20 2 kcal/mol   This was considered to be due to reduced resistance to twisting about the central double bond in the anion radical   It was also observed that there is a difference in equilibrium constant between the neutral and anion radical forms of bianthrone   In the neutral form $K_{AB} = [B]/[A] = 2 \times 10^{-3}$ at room temperature when dissolved in DMF, while in the anion radical form $K_{AB^-} = [B^{-\bullet}]/[A^{-\bullet}]$ was estimated to be quite large, at 2×10^{13} as, in their analysis, $B^{\bullet}$ was strongly favoured

Evans carried out further analysis in collaboration with Matsue on the effect of disproportionation on the reduction of bianthrone at elevated temperatures [20]   In his previous work, Evans showed that the reduction of bianthrone occurred via an ECE mechanism, a cyclic voltammogram is shown depicting the reduction (Figure 1 2 6) [15][18,19]

19

1000

500

0

Current, microamps

A→ B^{2-}

B^{-}→ B^{2}

B → B^{-}

B^{-}→ B

B^{2} → B^{-}

-05 -10 -15

Potential, V vs AgRE
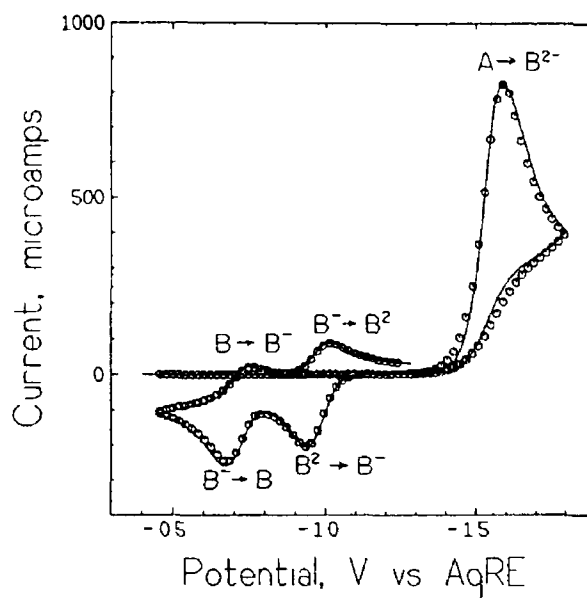
Figure 1 2 6 Cyclic voltammogram showing the potentials at which the conversions occur, taken from reference 14 by Matsue and Evans Solution was 1 9 mM bianthrone in 0 1 M TEAP in benzonitrile Working electrode was a platinum disk electrode Reference was a silver wire in contact with 0 1 M silver nitrate

The analysis published in this paper was based on the possibility of another mechanism It was expected that, at higher temperatures, K_{AB} would be sufficiently large to allow the conversion of the A to the B form and then the reduction of B to B^{-} and then to B^{2-} would occur In other words, the reduction would occur via a CEE mechanism Cyclic voltammograms were taken at 0 2 V/s scan rate and at three different temperatures, 60, 70 and $80^{0}C$ It was found that at temperatures above 60 ^{0} C considerable reduction current is obtained on the first negative sweep but the current rose sharply near E^{0}_{2B} (the potential at which $B^{-\bullet}$ is converted to B^{2-}) as opposed to E^{0}_{1B} (B to $B^{-\bullet}$) This suggests that there is a large proportion of $B^{-\bullet}$ being produced near E^{0}_{2B} while very little B is available for reduction near E^{0}_{1B} This behaviour was explained by including reproportionation in the CEE scheme The $B^{-\bullet}$ is formed from the reaction

$$B + e^{-} \Leftrightarrow B^{-}$$

20

which is reduced near E^0_{2B} giving an equivalent amount of B^{2-} As this diffuses away from the electrode, it comes into contact with B, which is present at a small but significant equilibrium concentration The following reaction takes place

$$B^{2-} + B \Leftrightarrow 2B^-$$
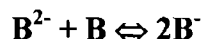
B diffuses to the electrode giving more current and producing more B^{2-} As a result the concentration of B in the diffusion layer is depleted requiring replenishment from the reaction

$$A \Leftrightarrow B$$

Consequently reproportionation gives a larger current by the production of B in a thicker reaction zone than would be present if reproportionation were absent

Comparison of the high temperature voltammograms with digital simulations of cyclic voltammograms was deemed necessary to ascertain whether the CEE scheme with reproportionation would account for the experimental data The simulations constructed were finite difference simulations that were fit to the experimental data by varying k_{BA} For this a value for the equilibrium constant K_{AB} at various temperatures was calculated by spectroscopic measurement of the absorbance due to B A plot of log K_{AB} vs $1/T$ yielded a value for $\Delta H^0 = 3\ 7$ kcal/mol and a value for $\Delta S^0 = -1\ 3$ kcal/mol Calculations of K_{BA} at various temperatures were also carried out From this data it was found that a linear relationship exists between log (K_{BA}/T) and $1/T$ The activation enthalpy, from this plot was found to be $15\ 7$ kcal/mol and the activation entropy was found to be $-1\ 3$ cal/molK

In a further investigation,[21] Evans and Matsue set out to examine the applicability of the reduction scheme of bianthrone to the reduction scheme of other substituted bianthrones, namely 2,3,2', 3'-dibenzo-7,7'-dimethybianthrone, and 5,6,5', 6',-dibenzo-2, 2'-dimethylbianthrone It was found that these derivatives behaved in a manner completely analogous to bianthrone To be more specific, they produced cyclic voltammograms that were similar in form to those of bianthrone Thus, indicating an ECE reduction mechanism It was found that the substitution

methyl groups and benzannelation in 5,6,5', 6',-dibenzo-2, 2'-dimethylbianthrone did not affect the rate constant for the conversion from the B to the A form of the molecule, k_{BA} as both bianthrone and 5,6,5', 6',-dibenzo-2, 2'-dimethylbianthrone have values of 3-4 s^{-1} The substitution in 2,3,2', 3'-dibenzo-7,7'-dimethybianthrone however produced a k_{BA} value ten times that of both bianthrone and 5,6,5', 6',-dibenzo-2, 2'-dimethylbianthrone This effect was due to the linear benzannelation of 2,3,2', 3'-dibenzo-7,7'-dimethybianthrone as opposed to the angular benzannelation of 5,6,5', 6',-dibenzo-2, 2'-dimethylbianthrone In comparison with bianthrone however, both substituted compounds behaved in similar fashion to bianthrone

Mattar and Sutherland[22] investigated the oxidation and reduction of bianthrone in a basic dimethyl sulfoxide solution Their investigation was carried out using simultaneous electrolysis-electron paramagnetic resonance spectroscopy and cyclic voltammetry It was found that the cyclic voltammograms closely resembled those of bianthrone in DMF and benzonitrile as carried out by Evans During the initial scan between 0 5V and −1 5V a single two-electron peak is found at −0 975V This is due to the reduction of the A form into B^{2-}

$$A + 2e^{-} \Leftrightarrow B^{2-}$$
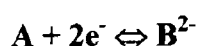
The return sweep gives peaks corresponding to

$$B^{2-} \rightarrow B^{-} + e^{-}$$

and

$$B^{-} \rightarrow B + e^{-}$$
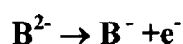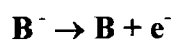
These peaks occur at −0 3V and −0 09V respectively The data concurs with Evans' interpretation that the reduction of A to B^{2-} is an ECE reaction irreversible due to the conformational change B^{2} can be easily oxidised to B^{-} and then B in rapid reversible reactions Again this concurs with Evans' findings

Simultaneous electrolysis electro paramagnetic resonance (SE-EPR) spectroscopy was employed to detect any radical anions in solution at specific values of potential It was proven that bianthrone was in the A form by applying a potential less than that required to reduce A to B^2 but greater than those required to reduce B to B^- and B^- to B^2 It was found that when the applied potential exceeded $-0\,975V$ a spectrum almost identical to a simulated spectrum formed by the splitting of four sets of four equivalent hydrogens To confirm that the EPR spectrum was due to B^{*-} the neutral A form was reduced chemically A bianthrone solution in DMSO was made up and its UV-vis was recorded This was repeated after the addition of increasing amounts of NaOH
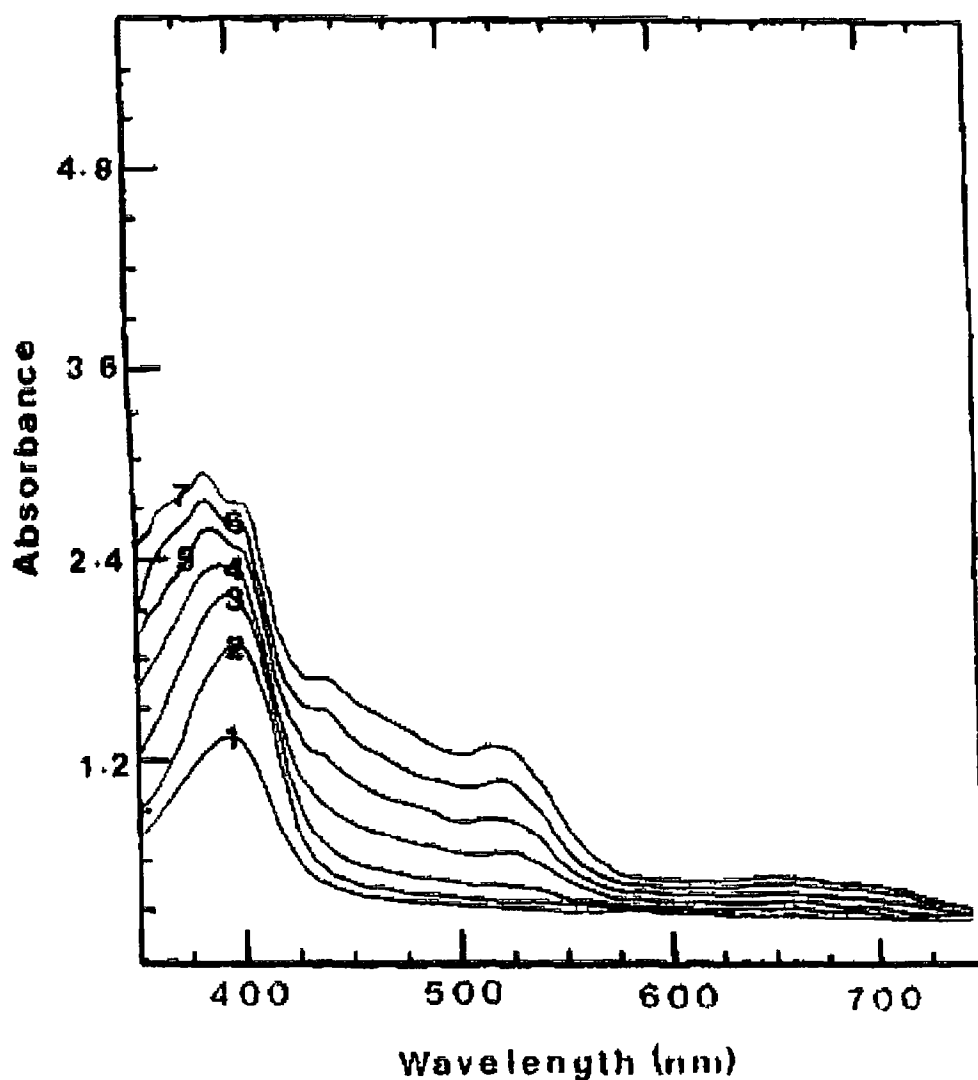
Figure 1 2 7 uv-vis spectra of titration of bianthrone with increasing volumes of NaOH solution, taken from reference 16 by Mattar and Sutherland Solution was 1 01 mM bianthrone

The spectra recorded after addition of NaOH differed from the initial spectrum in that one or more new species maxima at 410 nm and 515 nm were recorded (Figure 1 2 7) These spectra are similar to spectra generated by Olsen and Evans for B⁻ EPR studies of these solutions yielded spectra identical to the spectrum that was originally recorded using EPR

1 2 1 Photo induced processes.

In a study carried out by Nicodem et al[23] the photocyclization of bianthrone was investigated This was carried out to examine the behaviour of bianthrone in its excited state, whether the photocyclization of bianthrone to helioanthrone occurs via its singlet state or its triplet state It was found that using toluene as a solvent, cyclization was generated through the singlet state, while in a heavy atom solvent such as bromoform the triplet excited state is formed The bromoform is expected to induce intersystem crossing from the singlet to the triplet state and to shorten the lifetime of the triplet state by inducing intersystem crossing to the ground state With this in mind it was expected the triplet state would have just as long a lifetime in toluene This was not observed however and it was concluded that, with toluene as a solvent, photocyclization occurs from the singlet state

In a study carried out by Anders et al,[24] picosecond time resolved excited state absorption spectroscopy was employed to determine the evolution and lifetime of the photochromic states in anthracene based molecular systems, including bianthrone and bianthrone substituted with a trimethyl fulvene group Following the excitation of a bianthrone solution dissolved in cyclohexane, a broad band was observed at 520 nm, which was present for up to 4 psec Following this the spectrum was shifted to a longer wavelength 610 nm The excited state consists of two peaks, a strong peak ca 610 nm and weaker one at ca 550 nm It was noted that the spectrum was quite different to that of the B form of the molecule Therefore, while strong photoinduced absorption occurs, twisting is largely absent It was also noted that the time resolved spectra of anthracene are remarkably similar to those of bianthrone, including the red shift and the two peaks ca 610 nm and 550 nm This suggests that the photoinduced absorption originates from a state localised on the ring system The temporal evolution of the respective spectra being so alike suggests that, in the case of bianthrone, the evolution may not be due to unpuckering of the molecule (a phenomenon that does not affect anthracene) but due to the relaxation of the solvent cage about the excited state

Bianthrone
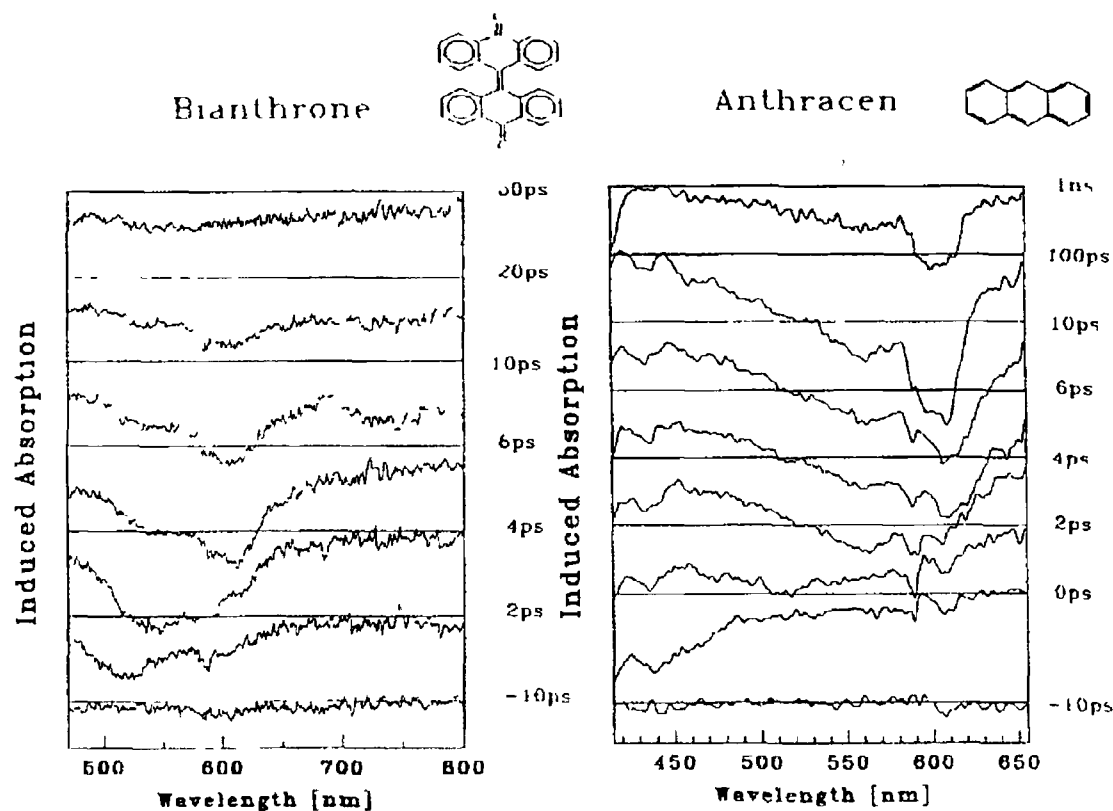
Anthracen

Figure 1 2 1 1   Temporal evolution of the transient absorption spectra of

bianthrone and anthracene

When bianthrone was substituted with trimethyl fulvene, photoexcitation led to a broad feature ca 550nm within 4 psec, thus following the same trend as observed in the unsubstituted form   After 6 psec a broad absorption band ca 650 nm was observed   This continued to evolve, shifting to 700nm after 10 psec   This is similar to bianthrone behaviour in a polar environment and was concluded to be due to the twisted transfer state

26

BATMΓ
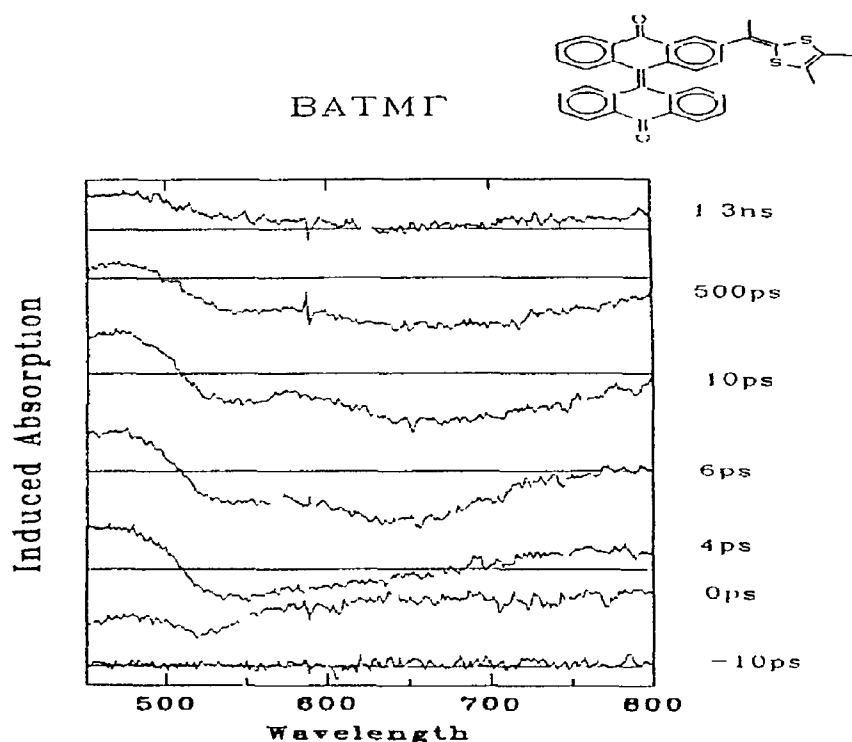
Figure 1 2 1 2   Temporal evolution of transient absorption spectra of fulvene substituted bianthrone

In comparisons between the spectra of the substituted and unsubstituted forms after 10 psec it was determined that the unsubstituted molecule's behaviour was characteristic of a localised anthracene ring system while the further red shift of the fulvene substituted form was assigned to the twisted induced charge transfer state driven by the fulvene group   The decay of the substituted bianthrone spectra was observed to be substantially longer than the unsubstituted form

Sommer-Larsen et al carried out a study on bianthrone covalently linked to 2,3-dimethyl-6-alkyl-1, 4-dithiafulvene[25]   In this study it is proposed that such a molecule has potential applications in molecular switches   It was shown in their study that a charge transfer state was involved in the initial stages of the switch process   An explanation for the fact that there is no evidence of a transfer state of the B molecule was proposed   The lowest unoccupied molecular orbital (LUMO) is similar in both the A and B forms of the molecule while the highest occupied molecular orbital (HOMO) and the second highest (HOMO-1) are interchanged in the A and B forms Consequently, there is an interchange of the charge transfer state and an excited state

27

from A to B occurs. The result is in the crossing over of the system from the potential curve of the charge transfer state to the potential curve of the localised bianthrone state before the minimum of the charge transfer potential curve of the B form is reached. Thus, the substitution of a donor molecule should influence the initial stage of the switch process but not the final stage. The mixing of the donor HOMO and the bianthrone HOMO in the B form results in a raising of the bianthrone HOMO in the B form and a lowering of the HOMO-1 level of the B form. From their analysis, a means of optimising the molecule so that the switch process involves an initial ground state with the molecule in the A form over the charge transfer state reached by direct excitation in the charge transfer band (bianthrone still in its A form) to the charge transfer state with the molecule in the B form was proposed. Avoidance of crossing between potential curves so that the charge transferred state continues to be the lowest excited state in the B form was proposed to be most efficiently achieved by lowering the HOMO of the bianthrone molecule. This can be done by substituting electron withdrawing groups in the 1,1 3,3 6,6 and 8,8 position. In order to avoid affecting the switching process only the 3,3 and 6,6 positions are feasible.

Jorgensen et al carried out the synthesis of a 1,4-dithiafulvenyl substituted bianthrone molecule[26] and examined their electrochemical properties. Again, this work was carried out to investigate substituted bianthrone molecules for their potential applications as molecular switches. Described in this paper are schemes by which the donor substituted bianthrone molecule can be synthesized

The uv-vis spectrum of the final product was similar to bianthrone except for an extra absorption peak at 480 nm. It was concluded, with supporting evidence from quantum mechanical calculations and solvatochromic investigations, that this was due to charge transfer from the donor to the acceptor parts of the molecule. The redox behaviour of the substituted switch molecules proved more complicated than unsubstituted bianthrone. Cyclic voltammetry was employed to investigate redox behaviour. When scanned positively, a single redox couple was observed at 0.22V, which corresponds to the oxidation of the 1,4-dithiafulvenyl part, i.e. the donor group, to the cation radical. On reduction an irreversible peak was observed at −1.27V corresponding to an irreversible two electron reduction of the bianthrone part to the dianion in the B form. Analogous to bianthrone, as the potential becomes more positive, two reversible one-electron couples were observed, corresponding to

oxidation to the monoanion and then to the neutral B form When oxidation was carried further an extra reversible couple was generated at 0 44V, which was ascribed to the donor part with the bianthrone still in the B form

1.2.2 Bianthrone Monolayers:

The main focus of the studies presented in this thesis is the formation of bianthrone monolayers on electrodes. It is intended that the rate of monolayer formation along with the monolayer structure, intermolecular distance, and its behaviour when immobilised on an electrode surface will be reported. These aspects are important to the ultimate objective of achieving a molecular reorientation of the bianthrone molecule on the surface of an electrode. Therefore, it is necessary to look at previous studies on bianthrone monolayers in order to gain knowledge on this subject.

A scanning tunnelling microscopy (STM) investigation of 4,4'-dimethylbianthrone adsorbed on Cu (111) was carried out by Cuberes et al.[27] Bianthrone monolayers were formed by sublimation in ultra high vacuum (UHV) onto the copper substrate. The images and data obtained from this study revealed the formation of well-ordered domains that coexist with moving molecules in a 2-dimensional molecular gas phase for coverages just below a complete monolayer. It was shown that the molecules adopt their A conformation in the ordered layers. In the image below (Figure 1.2.1.1) it can be seen that well ordered molecular islands exhibit periodic corrugation. The amplitude of this corrugation is approximately 1.2Å and is observed in the form of protrusions that appear as parallel zigzag rows along well-defined directions. It can also be seen from spikes and noisy protrusions in the topographic image that diffusing molecules are also present outside the islands. It was found that ordered molecular arrangements appear in three different domains distinguished from the directions followed by the zigzag rows, and that only one domain grows upon a terrace. For a densely packed monolayer it was found that the Cu steps often coincided with rotational domain boundaries.

From the STM image below in Figure 1.2.1.2 it was concluded that the chemical structure of 4,4'-dimethylbianthrone is consistent with two protrusions per molecule, each of which corresponds to an anthrone component. Consequently, single molecules in ordered domains appeared as pairs of consecutive protrusions in the zigzag rows with maximum separation of ca. 7Å. It was apparent that the molecular

orientation repeats itself within a row and along every two rows The symmetrical appearance of two lobes within a molecule strongly suggested that in ordered domains on Cu(111) the molecules are in their A conformation
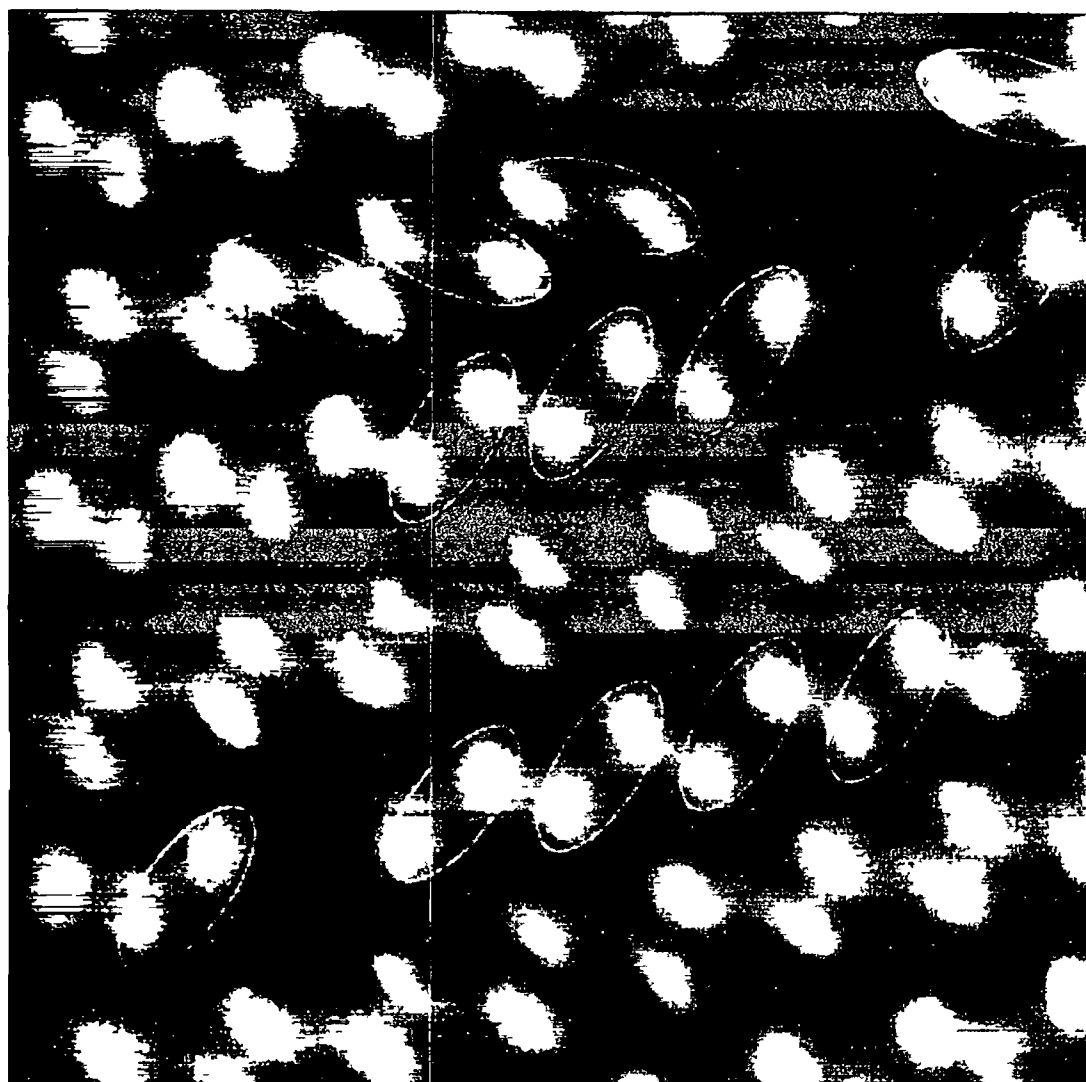
Figure 1 2 2 1 The ellipses outline individual molecules Figure is taken from reference 21 by Cuberes et al The STM image was taken over a 65 Å x 65 Å topographic area The tunnelling current was 80 pA and the tunnelling voltage was 1587 mV

Both anthrone components were thought to lie parallel, though puckered, to the surface with one anthrone component in direct contact and one slightly above A proposed arrangement suggests that the molecular axis (oxygen to oxygen) orients parallel to a Cu (110) direction for molecules in a zigzag row and parallel row to a (112) direction for those in the next parallel row
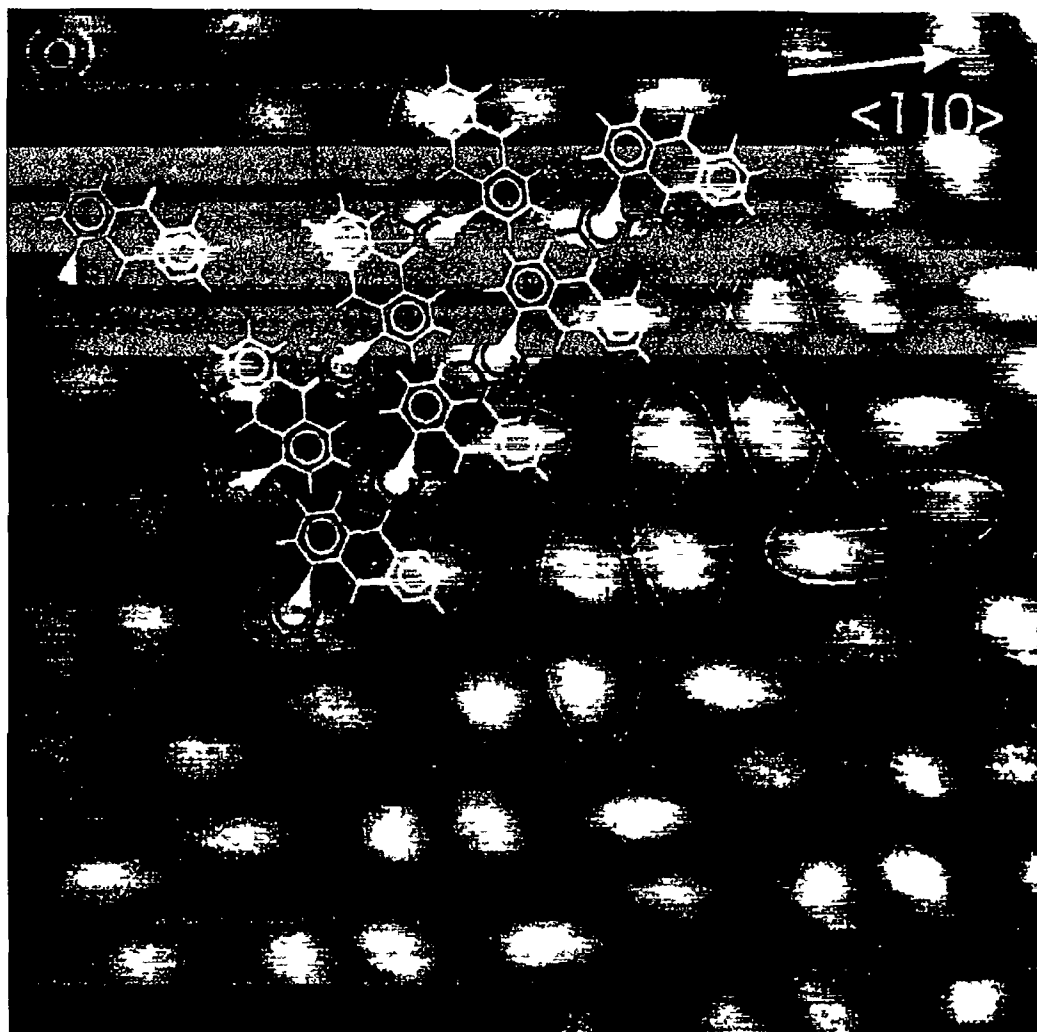
Figure 1 2 2 2 Figure is taken from reference 21 by Cuberes et al From this image it can be concluded that the molecules are in the A conformation, the anthrone components lying parallel (though puckered) with the substrate The STM image was taken over a 55 Å x 55 Å surface area with a 90 pA tunnelling current and a 1178 mV tunnelling voltage

From the data obtained, they argue that molecular interactions between the substituted methyl groups of one molecule and the ring system of another are crucial for the formation of well ordered molecular domains, and that these interactions depend on the relative orientation of the molecules It was shown that when the molecules meet in the proper orientations, two-dimensional crystals can form with a high packing density However, chemisorption alone is not strong enough to immobilise the molecules on the substrate and it was observed some molecules could diffuse along the surface providing there were sufficient empty sites From this behaviour, it was concluded that the molecules could be present in a two dimensional gas phase trapped at the surface due to chemisorption but with molecules free to diffuse, and the two dimensional molecular crystal stabilised at fixed surface sites due to interactions between molecules

The results from this paper do not allow conclusions to be made regarding conformational changes Most experimental studies including many referenced here were carried out in solution and it is not possible to conclude that such properties also occur when molecules are adsorbed on a surface However, the fact that chemisorption could not be proved to be sufficient to hinder conformational change gives rise to the hope that photochromism can be induced in adsorbed monolayer films, possibly on other substrates

The research carried out thus far proves that bianthrone is stable in both conformations and that its conformational changes are controllable by changing external conditions However, this research has concentrated on bianthrone behaviour in solution, and little research has concentrated on its behaviour when on a surface It is hoped that this and subsequent work will elucidate whether molecular reorientation on a surface is possible

1.3 Theory of electron transfer

In order to fully examine redox switching in a monolayer it is necessary to consider the theories on which electron transfer is based. Electron transfer, both within supramolecular assemblies and across the electrode/film interface, is one of the most important events that occur in interfacial supramolecular assemblies. The following section describes the theories behind electron transfer reactions.

Electron transfer can be divided into two categories, homogeneous and heterogeneous. The two differ in terms of driving force. Homogenous electron transfer is generally dictated by the electronic nature of the reactant molecules while the rate of heterogeneous electron transfer can be controlled externally by an applied potential.[28] The most relevant theories describing electron transfer processes are the Marcus theory and Butler-Volmer formalism describing electrode kinetics.

The most convenient electron transfer model for homogeneous reactions is:

$$A\text{-}L\text{-}B \rightarrow A^{-}\text{-}L\text{-}B^{-}$$

A and B representing redox active units linked through L. L may be a physical bridge or through space. There are two factors that influence the rate at which an electron moves from the reactant to the product. Firstly, the Franck-Condon principle dictates that the electron transfer is instantaneous; therefore there should be no change in nuclear configuration during the transfer of the electron. Secondly, the first law of thermodynamics states that energy must be conserved; consequently the transfer of the electron must be isoenergetic. The rate of electron transfer is given as

$$k_{ET} = \upsilon exp(-\Delta G^{\ddagger}/RT) \quad (1.2)$$

$\Delta G^{\ddagger}$ is the Marcus free energy of activation; υ is the frequency factor, which describes the rate of reactive crossing of the transition state. $\Delta G^{\ddagger}$ exhibits a quadratic dependence on ΔG^{0}, the standard Gibbs free energy as follows:

$$\Delta G^{\ddagger} = (\Delta G^{0} + \lambda)/ 4\lambda \quad (1.3)$$

λ is the total reorganization energy and is defined as the energy required to distort the reactant geometry in order to attain the equilibrium configuration of the product state The reorganization energy, λ, comprises two contributions λ_{in} and λ_{out} λ_{in} involves changes in the molecular geometry of the reactant as it reaches the product state, λ_{out} involves the reorganization of the solvent and the surrounding media Equation (1 3) predicts a parabolic relationship between the free energy of activation and the free energy of electron transfer Over the range of ΔG^0 the electron transfer rate should increase as ΔG^0 increases Under the following conditions

$$\lambda = \Delta G^0 \quad (1\ 4)$$

and

$$\Delta G^{\ddagger} = 0 \quad (1\ 5)$$

Electron transfer becomes free of activation and reaches its maximum Any further increase in driving force leads to ΔG^0 becoming less than $\Delta G^{\ddagger}$ causing a decrease in electron transfer rate This is referred to as the Marcus inverted region These states are illustrated in Figure 1 3 1

(a) Normal   (b) Activationless   (c) Inverted
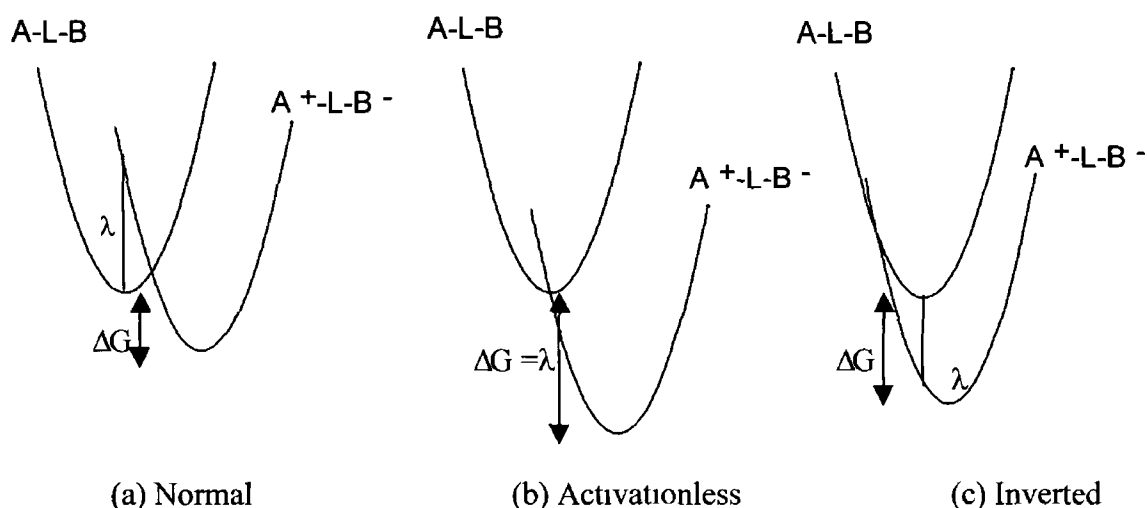
Figure 1 3 1   Reaction coordinate parabolas for electron transfer

36

1.3.1 Heterogeneous electron transfer:

The model for homogeneous electron transfer, i.e.,

A-L-B

is also applicable to heterogeneous electron transfer. However, in this case A represents an electrode characterised by a continuous or semi continuous density of states instead of molecular orbitals. There are three elementary steps involved in the electron transfer process of a reactant adsorbed on an electrode surface. They are thermal coupling, electronic coupling and elementary electron transfer. For thermal coupling it is necessary to consider the highest occupied molecular orbital (HOMO) and the lowest occupied molecular orbital (LUMO). In many circumstances, the HOMO donor state and the LUMO acceptor state can be considered to be well defined and static. However, they vary continuously about a mean value due to random thermal fluctuation and the ingress and egress of solvent dipoles from the solvent shell. These fluctuations have the potential to facilitate or impede the oxidation or reduction of the reactant at any given time. Electron transfer can only occur when the energy of the electrode and molecule are identical. Given that the free energy required to create activated states is many times higher than the thermal energy, the proportion of oxidised adsorbate with enough activation energy is low.

Other factors aside from resonance are necessary for heterogeneous electron transfer. Once isoenergetic reactants have been created the donor/acceptor orbitals and the electrode states must couple electronically. The extent to which the redox centres and the electrode are coupled increases exponentially with decreasing distance from the electrode. What follows is elementary electron transfer. According to the Franck-Condon principle at the instant of electron transfer, the redox centre switches from the oxidised to the reduced form, while maintaining its internal structure and solvation shell. The transfer is instantaneous, so energy cannot be transferred into or out of the surrounding medium. Consequently the internal energy of the reactants and products must be identical. The transfer of an electron between the donor/ acceptor

moieties and the electrode can happen via electron hopping or a superexchange mechanism.

An investigation into the role of distance on the dynamics of electron transfer has been carried out by Finklea et al.[29] Thiols with pendant redox centres ($HS(CH_2)_nCONHCH_2pyRu(NH_3)_5$, n=10,11,15) were adsorbed onto gold electrodes to form mixed, electroactive monolayers with diluent thiols. The diluent thiols were alkanethiols and ω-mercaptoalkanecarboxylic acids. Cyclic voltammetry and chronoamperometry were used to examine the kinetics of electron transfer. In their study, a plot of $\ln k^0_{app}$ vs. n, the number of methylene groups in the redox centre terminated adsorbed thiol molecule showed clearly that distance played a significant role in the rate of electron transfer. It was found that the electron transfer rate constant decreased with increasing distance between the electrode and the redox centres. It was shown that the insertion of even one methylene group had a marked effect on the standard rate constant. Symmetrical slopes in Tafel plots eliminated the possibility that the electron tunnelling mechanism involved through space tunnelling and it was hypothesized that the electron tunnelling occurred through the alkyl chain.
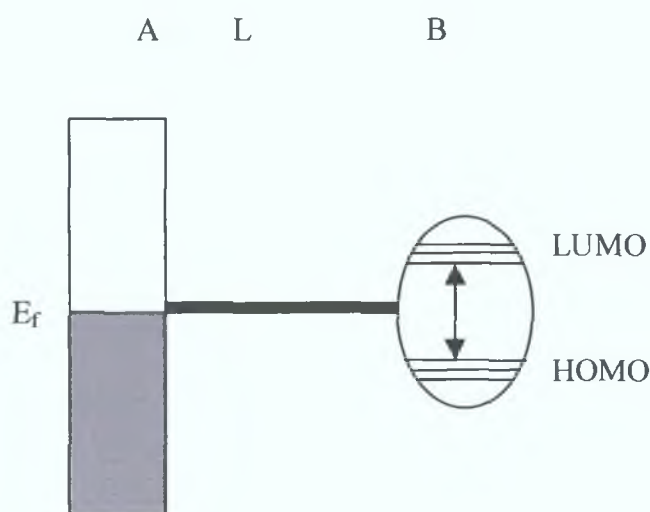
Figure 1.3.1.1: Schematic of a typical interfacial supramolecular assembly, A-L-B, when A is a metal electrode showing the relative molecular band structures of A and B. E_f is the Fermi level

1 3 1 1 The Butler-Volmer model

For this model the following simplified reaction is considered

$$Ox + e^- \overset{k_f}{\underset{k_b}{\longleftrightarrow}} Red$$
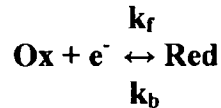
Simplified activated complex theory suggests Arrhenius dependence of k_f, the forward rate constant, on $\Delta G^\ddagger$, the chemical free energy of activation, as follows

$$k_f = \frac{k_B T}{h} \exp\left(\frac{-\Delta G^{\neq}}{RT}\right) \quad (1\ 6)$$

here h equals Planck's constant, k_B is Boltzmann's constant, R is the universal gas constant and T is temperature. In an electrochemical experiment, the driving force can be controlled externally via the instrument and the free energy of reaction depends on the electrochemical driving force, in other words the applied potential relative to the formal potential $E^{0'}$. The chemical free energy of activation, $\Delta G^\ddagger$ is here replaced by the electrochemical free energy of activation, $\overline{\Delta G^{\neq}}$. The electrochemical rate constant for reduction is given by

$$k_f = \frac{k_B T}{h} \exp\left(\frac{-\overline{\Delta G^{\neq}}}{RT}\right) \quad (1\ 7)$$

Both chemical and electrical components contribute to the electrical free energy of activation. A shift in the potential to a value, E changes the energy of electrons in the electrode by $-nFE$. The barrier for the oxidative process $\overline{\Delta G_b^{\neq}}$ is consequently less than $\Delta G_b^\ddagger$ by a fraction of the total energy change, $(1-\alpha)$. α is the transmission coefficient with values in the range of 0 and 1. The free energy of activation can be separated as follows

39

$$\overline{\Delta G_f^{\neq}} = \Delta G_f^{\neq} + \alpha n FE \quad (1\ 8)$$

$$\overline{\Delta G_b^{\neq}} = \Delta G_b^{\neq} - (1-\alpha)nFE \quad (1\ 9)$$

substitution into

$$k = \frac{k_B T}{h} \exp\left(\frac{-\Delta G^{\neq}}{RT}\right) \quad (1\ 10)$$

gives

$$k_f = \frac{k_B T}{h} \exp\left(\frac{-\Delta G_f^{\neq}}{RT}\right) \exp\left(\frac{-\alpha n FE}{RT}\right) \quad (1\ 11)$$

for reduction, and

$$k_f = \frac{k_B T}{h} \exp\left(\frac{-\Delta G_b^{\neq}}{RT}\right) \exp\left(\frac{(1-\alpha)nFE}{RT}\right) \quad (1\ 12)$$

for oxidation $\Delta G^{\ddagger}/RT$ is independent of the applied potential in both equations and is designated k_f^0 and k_b^0 in the forward and backward reactions These are rate constants for the reaction at equilibrium However, if the system is at equilibrium at the formal potential and the product of the rate constant and bulk concentration are equal for the forward and backward reactions, then the rate constant for the forward reaction and backward reaction are equal This is the standard heterogeneous rate constant, k^0 By substituting, the following are obtained

$$k_f = k^0 \exp\left(\frac{-\alpha n F(E - E^{0\prime})}{RT}\right) \quad (1\ 13)$$

$$k_b = k^0 \exp\left(\frac{(1-\alpha)nF(E-E^{0\prime})}{RT}\right) \quad (1\ 14)$$

The dynamics of the system are described by the standard heterogeneous rate constant The larger the value of k^0 the shorter the timescale required to establish equilibrium concentrations described by Nernst

There are some drawbacks to using the Butler Volmer theory As predicted by Butler Volmer, the rate constants for simple outer sphere electron transfer reactions will increase with increasing electrical driving force However, experimentally, this is only found to be true within a limited range of overpotentials For sufficiently large overpotential values the rate constant is independent of driving force The theory also fails to take into account the dependence of heterogeneous rate constants on distance, and it cannot predict how internal structural changes will affect the heterogeneous rate constants

1 3 1 2 Marcus Theory of heterogeneous electron transfer

The issues neglected by Butler-Volmer theory are directly addressed by the Marcus theory It is necessary to consider a system where the electrochemical driving force is zero Transition state theory examines the intersection of the free energy curves for the oxidised and the reduced form The rate of reaction depends on the product of the number of molecules with sufficient energy to reach the transition state at a particular time and the probability that they cross over the transition state The number of molecules at the transition state depends on the free energy of activation, ΔG^0 The electron transfer rate constant is given by

$$k^0 = \upsilon\sigma \exp\left(\frac{-\Delta G^0}{RT}\right) \quad (1\ 15)$$

This equation is equivalent to the equation describing homogeneous electron transfer. The difference here is σ, which is the reaction layer thickness. Marcus theory assumes that a simple parabola can describe the dependence of the free energy of activation on the reaction coordinate. Thus, the free energies of the outer sphere solvent reorganization and the inner sphere vibrations contribute to the total free energy as:

$$\Delta G_{TOTAL} = \Delta G_{OS} + \Delta G_{IS} \quad (1.16)$$

Here, the heterogeneous electron transfer rate constant is sensitive to the structure of the redox centre and the solvent.

The sensitivity of the standard heterogeneous rate constant to the overpotential, η depends on the extent of electronic coupling between the reactant and the electrode. For strongly coupled reactants electron transfer occurs predominantly through states near the Fermi level of the electrode and the adiabatic potential dependent rate constant is given by the product of the frequency factor v_n and the density of the acceptor states in the molecule, D_{ox} as follows:

$$k_f(E) = v_n D_{OX} \left(4\pi\lambda_{OX} kT\right)^{-\frac{1}{2}} \exp-\left[\frac{(\lambda_{OX} - E)^2}{4\lambda_{OX} ET}\right] \quad (1.17)$$

For diabatic systems, electrons below the Fermi level may be transferred and it is necessary to sum over all the electron energies rather than just at the Fermi level. The Fermi function, E_f, describes the distribution of occupied states within the metal

$$n(E) = \left(\frac{1}{1 - \exp\left[(E - E_f)/kT\right]}\right) \quad (1.18)$$

The dependence of the diabatic electron transfer rate constant is given by:

$$k(E) = v_n N_{OX} \left(4\pi\lambda_{OX} kT\right)^{-\frac{1}{2}} \int_{-\infty}^{\infty} \frac{\exp-\left[(\lambda_{OX} - E)^2/4\lambda_{OX} kT\right]}{\exp(E - E_f)kT + 1} \quad (1.19)$$

The effects of the strength of the electronic coupling on $k(E)$ is only apparent at high driving forces when the overpotential is more than half the reorganization energy The most notable consequence of the k_f and k_b reactions is that they both predict curvature in plots of lnk versus η At high driving forces k no longer depends on overpotential but reaches a maximum when the overpotential is approximately equal to the rate constant This region is comparable to the Marcus inverted region described for homogeneous electron transfer reactions

1.4 Models for Double Layer structure

A major factor of the work presented in this thesis involves the immobilisation of bianthrone on an electrode surface Adsorption of this kind can significantly change the double layer structure It is the intention of the work presented here and studies intended in the future to achieve a level of understanding of the double layer structure of the bianthrone monolayer In order to understand the behaviour of species immobilised on electrodes it is necessary to understand the structure of, and factors that influence the electric double layer Two main models have been proposed for the double layer structure at an electrode, the Helmholtz and the Gouy-Chapman models[30]

The solution side of the double layer consists of several layers The closest to the electrode, the inner layer, consists of solvent molecules and species that are specifically adsorbed species This layer is referred to as the Helmholtz layer The electrical centres of the specifically adsorbed molecules are known as the Inner Helmholtz Plane (IHP) and are at a distance x_1 The total charge density from the specifically adsorbed species is σ^i Solvated ions can approach the metal distance to a distance of x_2 The locus of the centres of these ions is called the Outer Helmholtz Plane (OHP) The interaction of these ions involves only long-range electrostatic forces Their interactions are independent of the chemical properties of the ions and are non-specifically adsorbed The non-specifically adsorbed ions are distributed in the diffuse layer, which extends from the OHP into the bulk solution The excess charge density in the diffuse layer is denoted σ^d The total excess charge density on the solution side of the double layer is described by

$$\sigma^s = \sigma^i + \sigma^d = -\sigma^m \quad (1\ 20)$$

1.4.1 The Helmholtz model for Double Layer structure

Metallic electrodes are good conductors and do not support electric fields across their thickness This would mean that any excess charge in the metallic phase resides on the surface Helmholtz proposed that the counter charge also resides on the surface producing two sheets of opposite charge This is analogous to a parallel plate capacitor The relationship between stored charge density, σ, and voltage drop, V is

$$\sigma = V\left(\frac{\varepsilon\varepsilon_o}{d}\right) \quad (1\ 21)$$

The differential capacitance is given by

$$\frac{\partial\sigma}{\partial\sigma} = C_d = \frac{\varepsilon\varepsilon_0}{d} \quad (1\ 22)$$

This is a flaw in the model as it predicts C_d as being constant, which is not observed in real systems

1.4 2 The Gouy-Chapman model for Double Layer structure

The fact that the charge on the electrode is confined to the surface does not mean that the same is true for the solution For instance, at low concentration of electrolyte, the solution phase will have a low density of charge carriers and it may take a significant thickness of solution to have a sufficient charge to counterbalance σ^M A finite thickness would arise would arise due to an interplay between the tendency of charge on the metallic phase to attract or repel charge carriers and the tendency of thermal processes to randomise them

The Gouy-Chapman model incorporates a diffuse layer of charge in the solution The area adjacent to the electrode would contain the highest concentration of excess charge In this area the electrostatic forces are strong enough to overcome

thermal processes, with greater distance, these forces become progressively weaker and the concentration progressively lower. It is best to visualise the solution as divided into laminae parallel to the electrode and with a thickness, d_x. The laminae are in thermal equilibrium with each other but the ions in the laminae are of different energy due to the differing electrostatic potential. The number concentration of species in two laminae have a ratio determined by a Boltzmann factor. Examining a lamina far from the electrode where every ion is at its bulk concentration n_i, the population of any other lamina is given by

$$n_i = n_i^0 \exp\left(\frac{-z_i e\phi}{kT}\right) \quad (1\ 23)$$

n_i^0 refers to the population at bulk concentration, z_i is the signed charge on the ion, e is the charge on the electron, ϕ is the electrostatic potential, k is the Boltzmann constant and T the absolute temperature. The total charge per unit volume in any lamina is

$$\rho(x) = \sum_i n_i z_i e = \sum_i n_i z_i e \exp\frac{(-z_i e\phi)}{kT} \quad (1\ 24)$$

$\rho(x)$ is related to the potential at distance x by

$$\rho(x) = -\varepsilon\varepsilon_0 \frac{d^2\phi}{dx^2} \quad (1\ 25)$$

The previous two equations can be combined to form the Poisson-Boltzmann equation

$$\frac{d^2\phi}{dx^2} = \frac{-e}{\varepsilon\varepsilon_0} \sum_i n_i^0 z_i \exp\left(\frac{-z_i e\phi}{kT}\right) \quad (1\ 26)$$

if

46

$$\frac{d^2\phi}{dx^2} = \frac{1}{2}\frac{d}{d\phi}\left(\frac{d\phi}{dx}\right)^2 \quad (1.27)$$

then

$$d\left(\frac{d\phi}{dx}\right)^2 = \frac{2kT}{\varepsilon\varepsilon_0}\sum_i n_i^0 \exp\left(\frac{-z_i e\phi}{kT}\right) + Cons\tan t \quad (1.28)$$

at distances far from the electrode, $\phi = 0$ and $d\phi/dx = 0$. Hence

$$\left(\frac{d\phi}{dx}\right)^2 = \frac{2kT}{\varepsilon\varepsilon_0}\sum_i n_i^0\left[\exp\left(\frac{-z_i e\phi}{kT}\right) - 1\right] \quad (1.29)$$

When considered in a system containing a symmetrical electrolyte:

$$\left(\frac{d\phi}{dx}\right) = -\left(\frac{8kTn^0}{\varepsilon\varepsilon_0}\right)^{1/2}\sinh\left(\frac{ze\phi}{2kT}\right) \quad (1.30)$$

Equation (1.30) can be rearranged and integrated as follows:

$$\int_{\phi_0}^{\phi}\frac{d\phi}{\sinh(ze\phi/2kT)} = -\left(\frac{8kTn^0}{\varepsilon\varepsilon_0}\right)^{1/2}\int_0^x dx \quad (1.31)$$

ϕ_0 is the potential drop across the diffuse layer. The result of the integration is

$$\frac{2kT}{ze}\ln\left(\frac{\tanh(ze\phi/4kT)}{\tanh(ze\phi_0/4kT)}\right) = -\left(\frac{8kTn^0}{\varepsilon\varepsilon_0}\right)^{1/2}x \quad (1.32)$$

The potential across the diffuse layer always decays away from the surface. At large values of potential drop (i.e., at a highly charged electrode) the drop is precipitous due to the compact nature of the layer. As the potential drop goes towards zero the drop becomes more gradual.

1 4 3 The relationship between the charge density of the electrode and the potential drop of the diffuse layer

To elucidate this relationship it is useful to imagine a Gaussian surface in the shape of a box placed in the system with one end at the interface, and the perpendicular sides extending into the solution until $d\phi/dx$ is approximately zero This box contains all the charge in the diffuse layer opposite the portion of the electrode surface adjacent to the end According to Gauss' law the charge is

$$q = \varepsilon\varepsilon_0 \oint_{surface} \xi \bullet dS \quad (1\ 33)$$

ξ in Equation (1 33) represents field strength Since field strength is zero at all points, except at the end, at the interface we get

$$q = \varepsilon\varepsilon_0 \left(\frac{d\phi}{dx}\right)_{x=0} \int_{\substack{end \\ surface}} dS \quad (1\ 34)$$

or

$$q = \varepsilon\varepsilon_0 A \left(\frac{d\phi}{dx}\right)_{x=0} \quad (1\ 35)$$

Substituting

$$\frac{d\phi}{dx} = -\left(\frac{8kTn^0}{\varepsilon\varepsilon_0}\right)^{1/2} \sinh\left(\frac{ze\phi_0}{2kT}\right)$$

and given that $q/A = \sigma^s$, we get

$$\sigma^m = -\sigma^s = \left(8kT\varepsilon\varepsilon_0 n^0\right)^{1/2} \sinh\left(\frac{ze\phi_0}{2kT}\right) \quad (1\ 36)$$

1 5 Self-Assembled Monolayers

There is an intense interest in the formation, characterisation and properties of spontaneously adsorbed monomolecular films. This interest stems from the many applications in chemical sensing[31], control of wettability and friction,[32] corrosion protection[33], molecular switching, and biomimetic processes

An organized self-assembled monolayer (SAM) is a single layer of molecules on a substrate in which the molecules exhibit a high degree of orientation, molecular order and packing[34] In self-assembly the monolayer spontaneously forms on exposure of the substrate to a solution or vapour containing the molecules of that will make up the monolayer. The main reason for this is that the substrate environment is energetically more favourable than that in solution. A good example of this phenomenon is the spontaneous adsorption of sulphur containing species, particularly thiols that adsorb onto metal surfaces such as gold, platinum, and mercury[35 36 37 38 39 40 41] Also, quinone species such as anthraquinones have been immobilised in monolayers on electrode surfaces[42] When a mercury electrode is immersed in such a solution, a monolayer forms on the surface. Electrochemical oxidation and reduction of the surface species can be observed. Strong adsorptions from aqueous solutions of some ions and many organic compounds (species containing aromatic rings, double bonds, and long hydrocarbon chains in particular) on metal and carbon surfaces can occur

Adsorption involves the formation of some type of bond between the adsorbate and the electrode surface. The interaction may be electrostatic, charge dipole in nature or it may be due to a covalent bond. Specific adsorption of an electroactive species can alter the electrochemical response, e g by forming a blocking layer on the surface of the electrode

Molecules attach themselves to the surface in one of two ways, by chemisorption or by physisorption. Physisorption involves long range, weak interaction between the electrode surface and the adsorbed molecule. Chemisorption involves the immobilisation of the adsorbate via a chemical bond

Alkane-thiols, with the general formula $HS(CH_2)_nX$ are one of the most extensively examined self-assembled monolayer formations[43] Self-assembly refers to

the formation of ordered monolayers by spontaneous adsorption from solution with strong interactions between the adsorbates and the surface and with itself.

Bain et al[35] studied the formation of monolayer films by spontaneous assembly of organic thiols from solution onto gold. They studied the wettability and composition of the monolayers using x-ray photoelectron spectroscopy; contact angle measurements and optical ellipsometry were also employed to study the kinetics of formation of the monolayer films on gold electrodes. They found that long chain alkanethiols adsorb from solution to form ordered, oriented monolayers. The properties of the films were found not to be dependent on chain length. It was also found through XPS that the monolayers oriented with the tail group, denoted X in the general formula, exposed at the monolayer-liquid interface. The adsorption of the simple n-alkanethiols generated the formation of hydrophobic monolayers, while alkane-thiols terminated by alcohol or carboxylic acids formed hydrophilic surfaces that were wet by water. In terms of stability, thiol monolayers were found to be stable indefinitely at room temperature. When heated to 80^0 C in hexadecane, the monolayers were found to desorb from the surface. The ellipsometric data found a mean thickness of 1.5 Å per methylene group. This value was seen as consistent with previous results. The contact angle measurements provided sensitive examination of the outermost few angstroms of the surface. The high contact angle data obtained for water on the methyl terminated thiols and the low contact angles obtained for alcohol and carboxylic acid terminated monolayers indicated that the surface of the monolayers comprised a densely packed array of the tail groups of the thiols. The high contact angles of hexadecane methyl ester or methyl ether terminated thiols provided support for a model in which the thiols are highly oriented so that only the methyl groups are directly exposed to the contact solution. XPS further supported the model of the tail groups being located at the surface and also that the thiols were bound to the gold through sulphur.

In their paper, Finklea and Hanshew[36], found that thiols with attached pentaamine(pyridine)ruthenium redox centres, $(HS(CH_2)_nCONHCH_2pyRu(NH_3)_5^{2+}$, adsorbed from acetonitrile solutions onto gold electrodes to form electroactive monolayers. Their study employed cyclic voltammetry and chronoamperometry. Mixed monolayers were formed when the thiols were co adsorbed with alkanethiols and with ω mercaptoalkanecarboxylic acids; the diluent thiol was, in each case

slightly shorter than the electroactive thiol. The redox centres were found to be stable for pH 4.0 aqueous Na_2SO_4 electrolyte and their formal potential was found near 0 V vs. SCE. The voltammetry was found to be close to ideal, with zero peak splitting and a peak half width of 90-100mV, at sufficiently slow scan rates, for each combination of electroactive and diluent thiol. Their findings gave evidence for the existence of populations of fast redox centres, which are capable of mediating charge transfer to the monolayer. Rates of direct electron transfer were obtained also. It was interesting to note that in their measurement of Tafel plots, the values for standard rate constant for the thiols were larger in the anodic branch than the cathodic branch. This implies that there are slight differences in monolayer conformations for the two oxidation states of the redox centres. The mechanism of electron transfer proposed was through bond tunnelling.

Pan et al examined the kinetics of adsorption for two alkanethiols (dodecanethiol and mercaptoundecanol) on gold electrodes, paying attention to the effect of preadsorbed contaminants.[38] Quartz crystal microbalance measurements were employed. The conditions that they chose resembled those used by Bain et al in their investigation, using in situ methods and carefully cleaning the gold surfaces prior to adsorption. These alkanethiols adsorbed on gold to form monolayers, which were stable under prolonged exposure to the alkanethiol solutions. The adsorption process was approximately described by the Langmuir isotherm, except in the fact that there were systematic deviations in exponential fits to ir frequency shifts versus adsorption data. This was indicative of an initial fast adsorption process followed by a slower one, in agreement with Bain and co workers' findings. Adsorption times were also comparable to those found by Bain et al.

Bretz and Abruna performed a rather extensive investigation of the adsorption-desorption processes of redox active osmium thiol monolayers.[37] The general formula of these molecules was $[Os(bpy)_2Cl(Py-(CH_2)_n-SH)](PF)_6$, where n = 4,6 or 9. They carried out their investigation on gold and platinum electrodes using cyclic voltammetry. It was found that the adsorption of these complexes was most adequately described using the Freundlich isotherm. This is an isotherm that does not require saturation coverage and is expressed as

$$\Gamma = k(C)^{1/n} \quad (1\ 37)$$

where k is related to the sorption capacity and n characterizes the energy distribution of the adsorption sites This isotherm is predicated on a distribution of adsorption energies resulting from surface heterogeneities Excellent linearity was observed, lending support to the case that this describes the adsorption behaviour More than one equivalent layer of the osmium complex was deposited, but it was found that this multilayer was porous and permeable to solution species Cyclic voltammograms were taken for the multilayer on a gold electrode, at a potential range where no redox waves were observed In the presence of $1\ 2$ mM $Ru(NH_3)_6Cl_2$, a redox wave associated with the Ruthenium complex was observed This indicates that the adsorbed material is quite permeable to the ruthenium complex in solution The amount of complex adsorbed was seen to be insensitive to pH, between pH 1 and pH 5, and ionic strength of the supporting electrolyte However, the formal potential of the osmium redox couple did vary with changes in the ionic strength of the supporting electrolyte At low ionic concentration, where the Debye length is larger than the distance between the electrode and the osmium metal centre, the electroactive centre experiences incomplete charge screening This was believed to be partly responsible for variations in formal potential Interesting aspects of the adsorbed complex were uncovered during investigation into the annealing time The term refers to a period of time required by the adsorbed complex to reorganize to a lower energy, more stable, configuration In a series of experiments, during which the multilayer/electrode assembly was held at a constant potential, in clean supporting electrolyte, to allow the multilayer to reorganize, the length of annealing time was studied as a function of the length of time required to desorb 95% of the multilayer The rate of desorption decreased significantly with increasing annealing time up to 24 hours after which the length of annealing time only marginally affected the rate of desorption The rate of desorption decreased as a result of reorganization into a more stable, lower energy configuration A further series of experiments to determine the activation energy for desorption for the annealed multilayer, were carried out The apparent result of these experiments was that the osmium thiol multilayer required a period of 24 to 48 hours to reorganize from a higher energy state to a lower one

Faulkner et al carried out studies on 2,6-anthraquinonedisulfonate (2,6-AQDS), 1,5-anthraquinonedisulfonate (1,5-AQDS) and 2-anthraquinonemonosulfonate (2-AQMS) with extensive studies carried out on 2,6-AQDS.[44] It was found that 2,6 AQDS undergoes reversible charge exchange with the electrode in an adsorbed state. The peaks observed were symmetric with a ΔE_p close to zero and their peak heights varied linearly with scan rate, thus confirming the fact that 2,6-AQDS was adsorbed at the mercury electrode surface. The adsorbed redox couple showed a standard potential more positive than that for the dissolved species, indicating that the reduced form was more easily adsorbed. Over the concentration range 2.5×10^{-8} to 5×10^{-5} M it was found that adsorption obeyed the Langmuir isotherm with a saturation limit of 0.94×10^{-10} molcm^{-2}. At concentrations greater than 2.5×10^{-5} M a pair of reversible current spikes were observed which the authors proposed were due to hydrogen bonding. From pH studies carried out on 2,6-AQDS, it was found that the formal potentials of both the adsorbed and dissolved species shifted negatively by approximately 60 mV/pH unit for pH <8. This indicated that the charge transfer reactions involved a coupled two-proton two-electron transfer.

Zhang and Anson carried out voltammetric and ir studies on 1,5-AQDS, and 2,6-AQDS adsorbed on graphite electrodes.[45] They found that when adsorbed on pyrolytic graphite, both anthraquinones exhibited multiple voltammetric peaks with magnitudes that changed as the adsorption proceeded. Experiments involving ir revealed that both anthraquinones initially adsorbed in a flat configuration on the electrode surface, which was not ir active. With time, and increasing surface concentrations, adsorbed molecules appeared which were ir active. This development of ir activity was considered to be due to reconfiguration on the surface in which the molecules reoriented more perpendicular to the electrode surface. This phenomenon was reflected voltammetically in the development of new voltammetric peaks.

Studies of anthraquinone monolayers have been carried out by Forster.[42] A mercury microelectrode was immersed in a solution of 2-hydroxyanthraquinone (2OH-AQ), reversibly adsorbing a monolayer, for study by cyclic voltammetry. Initial scan rate dependence studies in a 10μM solution of 2OH-AQ revealed that the peak shapes were independent of scan rate and the peak currents varied linearly with scan rate. These are characteristic of a surface confined electroactive film. It was found that reduction followed a two-electron, two-proton transfer mechanism. The dependence of surface coverage, Γ, on bulk concentration of the 2OH-AQ solution

was accurately described by the Langmuir isotherm. Cyclic voltammograms were taken in 10 mM anthraquinone solutions. This ensured that the currents observed for the solution phase species was significantly larger than those of the surface confined species. When compared to the cyclic voltammograms taken at lower concentrations a shift in the formal potential of approximately 0.15 V was observed. This indicated that the reduced form of the molecule, trihydroxyanthracene was more strongly adsorbed than the oxidised form. Microsecond time scale chronoamperometry was employed to time-resolve double layer charging and electron transfer of the confined anthraquinone moieties. This technique allowed for the double layer capacitance to be measured even at potentials where the monolayer was redox active. It was observed that the magnitude of the free energy of adsorption, ΔG_{ads}, varied for fully oxidised and fully reduced monolayers. These differences were believed to correspond to different extents of intermolecular hydrogen bonding in the oxidised and reduced films.

A study involving the electrochemistry of a surface confined species that undergoes an ECE mechanism (electrochemical change, chemical change, electrochemical change) was carried out by Hayes and Shannon.[46] Here they report the electrochemistry of surface confined 4-aminothiophenol (4-ATP) monolayers on gold electrodes using cyclic voltammetry and grazing angle FTIR spectroscopy. Cyclic voltammetry and FTIR spectroscopy demonstrated that the electrooxidation of 4-ATP proceeded via an ECE mechanism yielding a desorbed species and an adsorbed quinone containing species that displayed reversible surface confined electrochemistry. The electrochemistry revealed a single irreversible peak at approximately 0.73 V and a redox couple at 0.5 V. The peak at 0.73 V was seen to dramatically reduce in size after the first complete cycle leaving the redox couple at 0.5 V. Scan rate dependence revealed that the redox couple was due to a surface confined species. The peak at 0.73 V was assigned to the oxidation of the adsorbed 4-ATP in its protonated form to the radical cation. The molecule appeared to be adsorbed intact before the desorption potential was reached. Grazing angle FTIR of a freshly prepared 4-ATP monolayer on a gold substrate showed bands typical of the molecule oriented along the surface normal. Following cycling until the peak at 0.73 V decreased and the appearance of the surface bound redox couple at 0.5 was observed, a sharp band was observed at 1690 cm^{-1} which was assigned to the carbonyl stretch of an adsorbed quinone species. From this data and based on previous studies

of 4-ATP on silver, a mechanism was proposed The mechanism involves the initial oxidation of the adsorbed 4-ATP to its cation radical, which reacts with a neighbouring 4-ATP molecule forming a dimer The strained dimeric species partially desorbs from the surface and is hydrolysed by water to yield the final product that contains a quinone group that gives rise to the redox couple at 0 5 V

It should be noted that the collection of articles presented here is not intended to be exhaustive but merely to provide a general background to some of the techniques and phenomena discussed in this thesis All articles presented are of some relevance to the work presented

1.5.1 Adsorption Isotherms

The term adsorption isotherm refers to the relationship between the amount of substance i adsorbed on the electrode per unit area, Γ_i, the activity in the bulk solution, a_i and the electrical state of the system, E or q^m at a given temperature[12]. It is obtained from the condition of equality of electrochemical potential for bulk and adsorbed species, i, at equilibrium

$$\overline{\mu^A} = \overline{\mu_i^b} \quad (1.38)$$

where $\overline{\mu^A}$ is the electrochemical potential of the adsorbed species, and $\overline{\mu_i^b}$ is the electrochemical potential of the species in the bulk solution. Thus

$$\overline{\mu_i^{0,A}} + RT \ln a_i^A = \overline{\mu_i^{0,b}} + RT \ln a_i^b \quad (1.39)$$

Each $\overline{\mu_i^0}$ term is the standard electrochemical potentials and a_i^A and a_i^b are the activities of species i adsorbed and in the bulk solution respectively. The standard free energy of adsorption, $\overline{\Delta G_i^0}$, which is a function of electrode potential, is defined as:

$$\overline{\Delta G_i^0} = \overline{\mu_i^{0,A}} - \overline{\mu_i^{0,b}} \quad (1.40)$$

thus

$$a_i^A = a_i^b \exp\left(\frac{-\overline{\Delta G_i^0}}{RT}\right) = \beta_i a_i^b \quad (1.41)$$

This is the general form of an adsorption isotherm with a_i^A being a function of a_i^b and β_i. Different isotherms result from different assumptions of the relationship between a_i^A and Γ_i. One of the most widely applicable isotherms is the Langmuir isotherm. It takes the form

56

$$\frac{\Gamma_i}{\Gamma_s - \Gamma_i} = \beta_i a_i^b \quad (1.42)$$

Examples of the applicability of the Langmuir isotherm are widespread in the literature. One example of its use is by Forster in the analysis of 2-hydroxyanthraquinone (2OH-AQ).[42] It was found that the Langmuir isotherm best described the adsorption of the anthraquinone in that a plot of the bulk concentration of anthraquinone divided by the surface coverage versus the bulk concentration was linear, which the Langmuir isotherm predicts. From the data collected, two key pieces of information were extracted. The surface coverage of a dense monolayer was found to be 1 x 10^{-10} molcm^{-2}. The calculation of the free energy of adsorption $\Delta G^{\ddagger}$, which is the difference in free energy between a surface active molecule in solution and in the adsorbed state, was possible from the adsorption coefficient according to Equation (1.43).

$$\beta_i = \exp\left(\frac{-\Delta G^{\ddagger}}{RT}\right) \quad (1.43)$$

The value for the adsorption coefficient was calculated to be 6.3 x 10^6 M^{-1} which corresponded to a free energy of adsorption of 38.7kJmol^{-1}.

It is useful to consider the conditions under which it was derived and its limitations.[47] The isotherm is only applicable to monolayer adsorption. It is assumed that the standard free energy of adsorption is independent of coverage. For this to apply the surface must be completely homogenous and no lateral interactions between the adsorbed species may occur. True homogeneity is rare. Mercury electrodes come close to having homogenous surfaces. Surfaces have active sites on which the standard free energy of adsorption is high and other less active sites. As the fractional surface coverage increases the most active sites are occupied first followed by the less active. Lateral interactions depend on the nature of the adsorbed species and their average distance apart. Ion-ion interactions are long-range interactions given that they decay with the first power of distance. Dipole-dipole interactions decay with r^{-3} while chemical interactions decay with r^{-6} and are only influential at high values of

surface coverage The surface is assumed to have well defined sites with each molecule of adsorbate occupying one site Equilibrium is assumed between bulk and surface confined species

The Langmuir isotherm is often written in terms of the fractional surface coverage, θ

$$\frac{\theta}{1-\theta} = \beta_i a_i^b \quad (1\ 44)$$

It can also be written in terms of the concentration of a species in solution by including activity coefficients in the β term giving

$$\Gamma_i = \frac{\Gamma_s \beta_i C_i}{1 + \beta_i C_i} \quad (1\ 45)$$

As already stated, the Langmuir isotherm is relevant when there are no interactions between adsorbed species There are isotherms that relate to systems involving interactions between surface confined species Namely, the Frumkin and the Temkin isotherms The mathematical representation of the Temkin isotherm is

$$\Gamma_i = \frac{RT}{2g} \ln\left(\beta_i a_i^b\right) \quad (1\ 46)$$

In the case of the Frumkin isotherm, the assumption that the standard free energy of adsorption is independent of coverage does not hold true when interactions are taken into account In this case a linear dependence if the energy of adsorption on coverage is observed

$$\overline{\Delta G_i^0}\left(Frumkin\right) = \overline{\Delta G_i^0}\left(Langmuir\right) - 2g\Gamma_i \quad (1\ 47)$$

The Frumkin isotherm takes the form

$$\beta_i a_i^b = \frac{\Gamma_i}{\Gamma_s - \Gamma_i} \exp\left(\frac{-2g\Gamma_i}{RT}\right) \quad (1\ 48)$$

g expresses the rate of change of adsorption energy with increasing coverage and is given units of J/mol per mol/cm^2 A positive g value indicates attractive interactions between molecules and a negative indicates repulsive ones The Langmuir isotherm is a special case of the Frumkin and is achieved by setting g at zero

1.5.1.1 The rate of adsorption

The growth rate of a monolayer, usually represented by time dependent fractional surface coverage, can be represented by mathematical models. Many of these models incorporate, or are modifications of, the Langmuir adsorption model.[48] This is characterised by the growth rate being proportional to the number of available sites on the substrate:

$$\frac{d\Theta}{dt} = R(1 - \Theta) \quad (1.49)$$

This gives rise to a simple growth law

$$\Theta = 1 - e^{-Rt} \quad (1.50)$$

If growth nucleates after a certain time, t_c, this can be taken into account in the following

$$\Theta = 1 - e^{-R(t-t_c)} \quad (1.51)$$

Examples of growth curves following this model are available in the literature.[49] While fits that describe reasonable fits to experimental data have been reported, so too have systematic deviations from the data model. A frequent deviation involved the existence of multiple time scales and phases in monolayer growth. Examples have been reported where the first adsorption step resulted in 80-90% at fast time scales followed by a slower time scale for the remainder.[50]

The Langmuir growth law is only valid, however, if the adsorbate molecules do not interact with each other. In a more realistic picture, other factors must be taken into account. For instance, one would expect that the energy gain for adsorption at a domain boundary would be larger than for an isolated molecule. This would have an impact on the growth rate. Also if the supply of the adsorbate to the surface is limited by diffusion effects from the bulk solution then there will also be an impact on the growth rate.

The adsorption models used in this thesis have been reported previously to correlate polymer adsorption data [51] [52] and an extensive discussion was provided by Hubbard et al [53] The models take into account the effect of diffusion of molecules to the surface

$$\Gamma(t) = \Gamma_m \left[1 - \exp\left(-\frac{2C_0}{\Gamma_m} \left(\frac{Dt}{\pi} \right)^{1/2} \right) \right] \quad (1\ 52)$$

where $\Gamma(t)$ is the surface coverage at a given time, Γ_m is the saturation surface coverage, C_0 is the bulk concentration of the adsorbing molecule in solution, D is the bulk diffusion coefficient, t is time and π has its usual meaning The second model describes a regime dominated by thermodynamic or surface kinetic effects

$$\Gamma(t) = \Gamma_m \left[1 - \exp\left(\frac{KC_0 t}{\Gamma_m} \right) \right] \quad (1\ 53)$$

$\Gamma(t)$, Γ_m, C_0 and t have the same meanings as in Equation (1 52) and K is the surface reorganization rate constant It is important to note that K designates an entire set of surface kinetic processes A more in depth discussion is seen in chapter 3 of this thesis

1.6 Methods of Analysis

1 6 1 Cyclic Voltammetry

As can be seen in chapters 3 through 5 of this thesis, cyclic voltammetry plays a vital part in the work presented It has been used to probe the redox properties of bianthrone monolayers, in the calculation of heterogeneous electron transfer rate constants, and also in the investigation of monolayer formation dynamics Therefore, it is important to detail the theories that underpin the technique

Cyclic voltammetry consists of cycling the potential of a stationary electrode immersed in a solution and measuring the resultant current[54] The excitation signal is a linear potential scan with a triangular waveform Symmetrical triangular scan rates range from a few millivolts per second to hundreds of volts per second The triangular potential excitation signal sweeps the potential of the working electrode back and forth between two designated values called switching potentials The triangle returns at the same speed and allows the display of a complete voltammogram with cathodic and anodic waveforms one above the other The current at the working electrode is measured under diffusion controlled, mass transfer conditions

The important parameters of a cyclic voltammogram are the magnitudes of the anodic and cathodic peak currents, i_{pa} and i_{pc} respectively, the anodic and cathodic peak potential, E_{pa} and E_{pc}, and the half peak potential $E_{p/2}$ The peak current is given by

$$i_p = n^{3/2} F^{3/2} (\pi \upsilon D_{ox} / RT)^{1/2} C_{ox} \chi(\sigma t) \quad (1\ 54)$$

$\chi(\sigma t)$ is a tabulated function whose value is 0 446 for a simple diffusion controlled electron transfer reaction, R is in $JK^{-1}mol^{-1}$, and T is in Kelvin At 25^0C this reduces to

$$i_p = (2\ 69 \times 10^5) n^{3/2} A D_{ox}^{1/2} \upsilon^{1/2} C_{ox} \quad (1\ 55)$$

More detailed descriptions of the characteristics of cyclic voltammograms can be found in chapter 3, 4 and 5
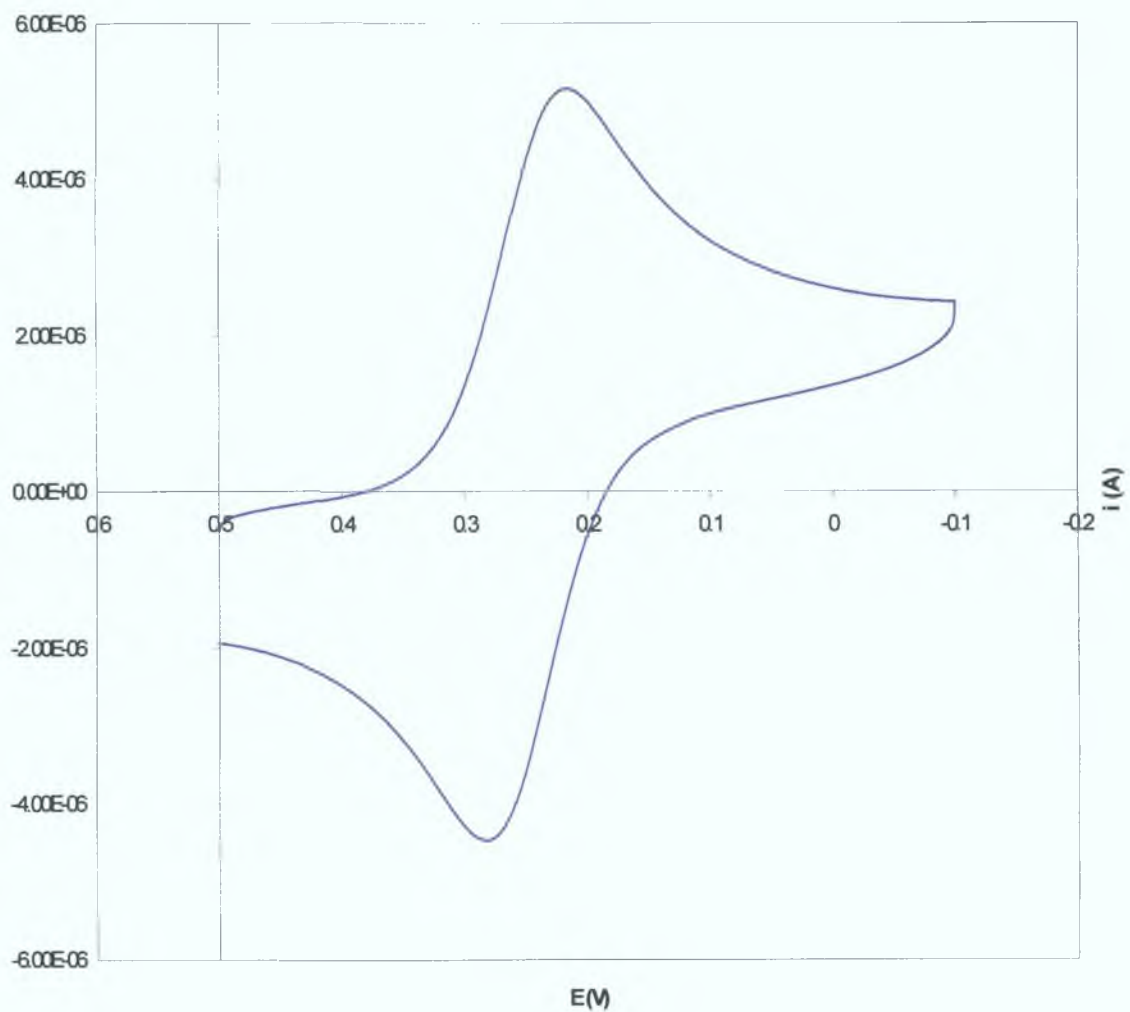
Figure 1.6.1.1: An example of a cyclic voltammogram, taken from the CHI 440 software, of 0.5 mM $K_3Fe(CN)_6$ dissolved in 0.4 M KNO_3

1 6 2 Raman Spectroscopy

Raman spectroscopy has played a vital part in the work presented in this thesis in the analysis of bianthrone monolayers and bianthrone in the solid state Therefore, it is important that the theory that underpins the technique is considered

The Raman effect occurs when monochromatic radiation is scattered by molecules and a small fraction of the scattered radiation has a different frequency to that of the incident radiation It is named after V C Raman who discovered the effect in 1928 This effect has proved valuable in the elucidation of molecular structure, for locating specific functional groups or chemical bonds in molecules and lately in the elucidation of surface orientation on the surfaces of electrodes and colloids

The Raman effect arises when a beam of intense monochromatic radiation passes through a sample containing molecules that undergo a change in molecular polarizability as they vibrate Polarizability is defined as the value of the induced dipole moment divided by the strength of the field that caused the induced dipole moment

Classic electromagnetic theory predicts the Raman effect, although a quantum mechanical treatment is necessary to give a detailed explanation According to the classical theory, polarization, P, the dipole moment per unit volume is given by

$$P = \alpha E \quad (1\ 56)$$

Where E is the magnitude of the electric vector of the electromagnetic field that acts on the molecule and α, the polarizability, is the proportionality constant Since the magnitude of the electric vector of the electromagnetic field varies with time, t, in a sinusoidal manner

$$E = E_0 \cos 2\pi \nu t \quad (1\ 57)$$

The polarization becomes

$$P = \alpha E_0 \cos 2\pi v t \quad (1.58)$$

The polarizability, α, consists of two parts, α_0, the polarizability when the atoms of a molecule are in their equilibrium positions, and a second term, the sum of the polarizabilities of the molecule due to the various rotational and vibrational motions. Each term of the second part varies with the frequency associated with the particular rotation or vibration.

$$\alpha = \alpha_0 + \Sigma \left(\frac{\delta \alpha_0}{\delta r} \right) r_n \cos 2\pi v_n t \quad (1.59)$$

where α_n is the polarizability associated with the nth rotational or vibrational mode and r_n is the maximum displacement of the involved atoms. Combining Equations (1.58) and (1.59) gives

$$P = E_0 \alpha_0 \cos 2\pi v t + E_0 \Sigma \left(\frac{\delta \alpha_n}{\delta r} \right) r_n \cos 2\pi v_n t \cos 2\pi v t \quad (1.60)$$

and

$$P = E_0 \alpha_0 \cos 2\pi v t + 1/2 E_0 \Sigma \left(\frac{\delta \alpha}{\delta r} \right) r_n \{ \cos 2\pi (v - v_n) t + \cos 2\pi (v + v_n) t \} \quad (1.61)$$

The first term has the frequency of the incident radiation and is the Rayleigh scattering. The second term represents the Stokes (v-v_n) and the anti-Stokes (v+v_n) Raman bands. It is important that $\delta \alpha_n / \delta r$ cannot be zero.

Most collisions of the incident photons with the sample molecules are elastic i.e. Rayleigh scattering. An illustration of this can be seen in Figure 1.6.2.1 as the green arrow coming from the molecule. According to the first term of Equation (1.61), the electric field produced by the polarized molecule oscillates at the same frequency as the passing electromagnetic wave so that the molecule acts as a source, sending out radiation of that frequency in all directions. The incident radiation does

not raise the molecule to any particular quantized level, rather the molecule is considered to be in a virtual excited state. As the electromagnetic wave passes, the polarized molecule ceases to oscillate and returns to its original ground level in a very short time (approximately 10^{12} seconds)

A small proportion of the excited molecules may undergo changes in polarizability during one or more of the normal vibrational modes. According to the second term of Equation (1 61), this is the basis of the Raman effect. This is seen in Figure 1 6 2 1 as the red arrow. Usually incident radiation is absorbed by a molecule in the lowest vibrational state. If the molecule reemits by returning to an excited vibrational level, v_v of the ground electronic state rather than the original vibrational state, the emitted radiation is of lower energy i e lower frequency than the incident radiation (v_0 - v_v). The difference in frequency is equal to a natural vibration frequency of the molecules ground electronic state. Several such shifted lines are normally observed in the Raman spectrum corresponding to different vibrations in the molecule. Some molecules initially absorb radiation while they are in an excited vibrational state and decay to a lower energy level so that the Raman frequency is higher than the incident radiation. These are known as anti-Stokes lines. The resultant spectrum, therefore consists of a relatively strong component with frequency unshifted (Rayleigh scattering) corresponding to photons scattered without energy exchange and the two components of the Raman spectrum, Stokes and anti-Stokes lines. Normally, only the Stokes lines are considered in chemical analysis. These are more intense because, under usual circumstances, most molecules are initially in the lowest vibrational level
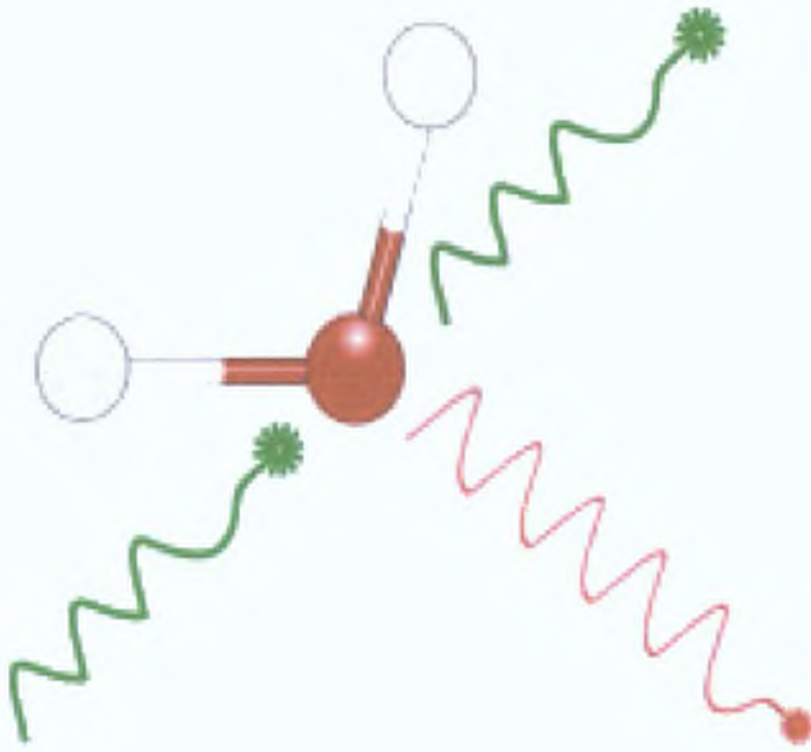
Figure 1.6.2.1: Diagram of the Raman effect, the green arrow indicates incident excitation from an excitation source and Rayleigh scattering which has the same wavelength as the excitation. The red arrow indicates Raman scattering, which has a different wavelength to the excitation wavelength, and the Rayleigh scattering
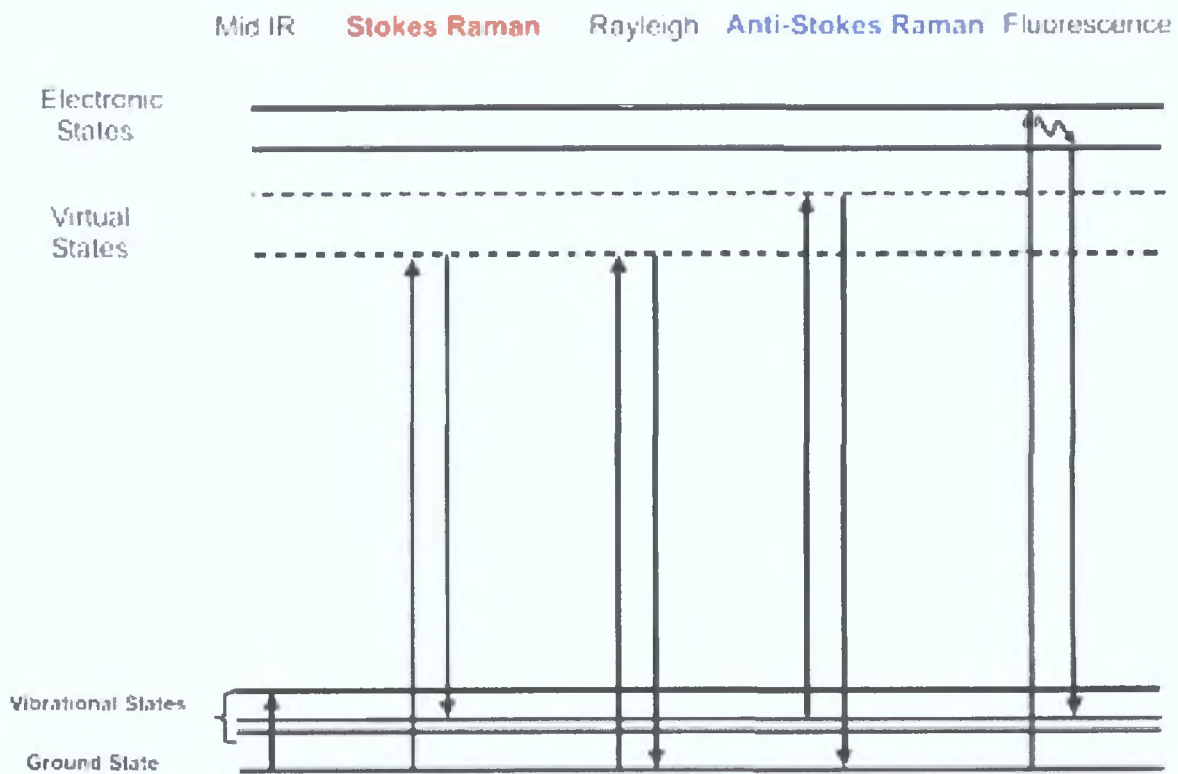
Figure 1.6.2.2: Jablonski energy level diagram illustrating Stokes and anti-Stokes Raman scattering in comparison with Rayleigh scattering ir and fluorescence

1 6.2.1 Resonance Raman Spectroscopy

When the excitation frequency falls near or becomes coincident with an absorbance wavelength, v_{abs}, a significant enhancement can be observed   The resonance Raman effect results from the promotion of an electron into an excited electronic-vibrational state, followed by immediate relaxation into a vibrational level of the ground state   The enhancement achieved can be an order of magnitude   The resonance Raman emission process is essentially instantaneous and the resulting spectra consist of narrow bands with good resolution (between 10 and 20 cm^{-1}) Spectra may also be obtained using an excitation frequency just below the absorption band   This is known as preresonance and the resulting enhancement is lower, typically less than tenfold

However, not all normal Raman bands are equally enhanced   Only those vibrations that exhibit a large change in equilibrium geometry upon electronic excitation produce strong enhancement   This leads to two classes of vibrational modes producing intense resonance-enhanced spectra   These are totally symmetrical vibrations and those nontonally symmetrical vibrations that vibronically couple two electronic states   Since an electronic transition is often localised in one part of a complex molecule, the resonance Raman effect provides highly detailed information about the vibrational modes of chromophores that have an absorption band near the wavelength of the incident radiation

Resonance Raman spectroscopy has proved widely applicable in providing information on the structure and dynamics of short lived excited state intermediates of various photochemical and photophysical processes [55] [56] [57] [58] [59] [60] Examples of resonance Raman spectra can be found in work by Balakrishnan et al [61] In this work, time-resolved resonance Raman (TR$_3$) spectroscopy was carried out on the radical anions of menaquinone and naphthoquinone   This resonance technique employs a pump pulse to initiate a photochemical process, followed by a probe pulse, which is used to obtain time resolved resonance enhanced Raman spectra of transient intermediates   In this case, a 266 nm output from a Nd   YAG laser was used as the photoexcitation pump and the probe was obtained from a H_2 Raman shifter of their own design with an output wavelength of 416 nm   The photoexcitation wavelength was chosen according to the absorption spectra of the neutral molecules and the probe

wavelength was chosen according to the absorption spectrum of the radical anion. The probe made it possible to obtain radical anion spectra of naphthoquinone and menaquinone, at time scales of hundreds of nanoseconds. These spectra were compared to ab initio calculations and literature sources on quinones and assignments were carried out. This technique allowed the structural analysis of these short-lived radical anions.

Resonance Raman spectroscopy used in conjunction with electrochemistry was carried out by Zhao et al.[62] In this work, they employed resonance Raman spectroscopy to identify electrochemically generated reduction products and radical anions of isotope-labelled 1,4 Benzoquinone. The reduction products were generated using bulk electrolysis. The employment of this technique allowed them to clearly describe electronic structures, molecular structures and bond properties of various reduction products of the molecule. It also allowed them to distinguish certain marker bands that can characterise the strength of the C=O bond and nature of the six-membered ring, for the first time. From their data, they concluded that the quinoid ring gradually changes to a benzenoid ring upon reduction of the molecule. They also concluded, from the C=O stretching frequency that extra charges on the BQ^{2-} are highly localized at the two oxygen atoms. They proposed that the data collected would prove valuable in the resonant Raman analysis of quinones observed for biological purposes.

1.6.2.2 Coherent Anti-Stokes Raman Spectroscopy (CARS)

This type of enhancement depends on the fact that when an exciting field polarizes a molecule, the polarization contains terms that involve the square, cube and so on of the field strength (non-linear terms) as well as the first power (linear term). The non-linear terms, which are only important when the exciting fields are very strong (e.g. laser excitation), have the effect that the molecule can combine several photons to produce a photon of different but related frequency. In CARS, the sample is irradiated with photons from a laser with frequency v_1, and simultaneously from a tuneable laser with frequency v_2. The frequency from the tuneable laser is varied.

When the difference in frequencies, v_1 v_2, equals a Raman frequency, a new frequency is generated, $v_3 = 2v_1 - v_2$ This new frequency is coherent with the generating frequencies and is quite intense compared with normal Raman lines It is detected in the forward direction and its intensity is plotted against the variable frequency, v_2 The new frequency appears in the anti-Stokes region with respect to the main frequency, v_1 The major experimental advantage of CARS is the magnitude of the signal produced in the anti-Stokes region from similar excitation power compared with spontaneous Raman signals The first experimental demonstration of CARS was carried out by Duncan et al who acquired CARS images of onion cells in D_2O and deuterated liposomes [63] This technique is commonly used in the analysis of highly fluorescent dyes, whose fluorescence in the normal Raman mode would obscure Raman bands Recently, CARS microscopy and correlation spectroscopy have been combined to probe diffusion dynamics in chemical and biological systems [64] [65]

1 6 2.3 Surface Enhanced Raman Spectroscopy

In this technique, Raman scattering is enhanced when the analyte is adsorbed on a metallic surface Colloidal metal surfaces of gold silver and copper have proved most effective in this type of enhancement and as a result have been most commonly used [66] [67] [68]Surface-enhanced Raman scattering (SERS) arises from two mechanisms The first is an enhanced electromagnetic field produced at the surface of the metal When the wavelength of the incident light is close to the plasma wavelength of the metal, conduction electrons in the metal surface are excited into an extended surface electronic excited state called a surface plasmon resonance Molecules adsorbed or in close proximity to the surface experience an exceptionally large electromagnetic field Vibrational modes normal to the surface are most strongly enhanced [69]

The second mode of enhancement is by the formation of a charge-transfer complex between the surface and analyte molecule The electronic transitions of many charge transfer complexes are in the visible, so that resonance enhancement occurs [70] Molecules with lone-pair electrons or pi clouds show the strongest SERS Other aromatic nitrogen or oxygen containing compounds, such as aromatic amines or phenols, are strongly SERS active The effect can also been seen with other electron-rich functionalities such as carboxylic acids

The intensity of the surface plasmon resonance enhancement is dependent on many factors including the wavelength of the incident light and the morphology of the metal surface The absorbance wavelength should match the plasma wavelength of the metal This is about 382 nm for a 5 μm silver particle, but can be as high as 600 nm for larger ellipsoidal silver particles The plasma wavelength is to the red of 650 nm for copper and gold, the other two metals, which show SERS at wavelengths in the 350-1000 nm region The best morphology for surface plasmon resonance excitation is a small (<100 nm) particle or an atomically rough surface

SERS is used to study monolayers of materials adsorbed on metals, including electrodes Many formats other than electrodes can be used The most popular include colloids, metal films on dielectric substrates and, recently, arrays of metal particles bound to metal or dielectric colloids through short linkages   Concentration is proportional to the power of the signal in SERS

SERS has become a powerful tool for the characterisation of a wide range of inorganic and biologically relevant analytes [71] [72] The main advantage is the SERS is an enhancement of between 10^3 and 10^7 of an analyte signal when it is adsorbed at or near to a suitable surface [73] The enhancement mechanism also allows for the detection of single molecules [74] [75]

Initial SERS studies were carried out on small molecules on metal surfaces in order to further understand the enhancement process SERS studies of some α-aminoanthraquinones adsorbed on silver colloidal particles were carried out by Ramakrishnan et al The aminoanthraquinones studied were 1-aminoanthraquinone (AAQ), 1-methylaminoanthraquinone (MAAQ) and 1-propanolaminoanthraquinone (PAAQ) The laser used was a helium-neon laser (He-Ne) operating at a wavelength of 632 8 nm The spectra obtained provided evidence of eight new bands in the AAQ and MAAQ spectra and eleven new bands in the PAAQ spectra compared to previous studies In their examination of the bands associated with the carbonyl group they found that two bands existed that could be attributed to carbonyl stretching vibrations Due to the amino substitution on the molecules the carbonyl group adjacent to the amino group (denoted $C_9=O$) was charged partially negative due to charge transfer between it and the amino group and lone pair electrons of the nitrogen atoms formed good binding sites for the surface adsorption to the silver surface This gave rise to different environments for the two carbonyl groups of the molecules and hence two separate carbonyl bands This also provided evidence that the molecules were not adsorbed flat on the surface but were adsorbed through the amino and $C_9=O$ sites on the molecules This work illustrates how SERS spectra can be used to provide information on the orientation of a molecule on a surface

Sanchez –Cortes et al, provided a further example of the use of SERS as a tool for examining orientation on a metal surface Their study involved a near infrared SERS study of antiretroviral drugs, Hypericin and Emodin, with a less expansive examination of bianthrone Their study consisted of acquiring spectra of the two drugs under conditions of varying drug concentration, DMSO concentration, pH and time They found that both Hypericin and Emodin were present in water in both an aggregated and monomeric form in an equilibrium which leads to the monomeric

molecules approach the silver colloid surface and, as a result, contribute to the SERS signal. The difference in drug concentration SERS profiles revealed that a change in orientation takes place as the concentration increases. A flat orientation predominates in the low concentration while an orientation normal to the surface is observed at high concentrations. They account for this in part according to the selection rules of the electromagnetic model of SERS, stating that a more intense electromagnetic field perpendicular to the surface induces a higher enhancement in those vibrational modes having a high component in this direction. When varying the concentration of hypericin, a change in the relative SERS intensity and in the wavenumber of the bands were observed with the most prominent bands at low concentration being 472, 950 and 1331 cm^{-1} which were claimed to result from the proximity of OH groups near to the metal surface or to a partial out-of-plane character of these modes. At high concentration the most prominent bands were 1250, 1296 and 1376 cm^{-1}. The bands at high concentration are attributed to in-plane ring stretching vibrations which are enhanced as the concentration increases. Similar patterns were noted with varying DMSO concentration, pH and over time. In these cases, the explanation given was a shift between the aggregate and monomeric nature of the molecules. Little was concluded about the nature of bianthrone, only that the patterns observed with hypericin and emodin were not observed with bianthrone. The conclusion drawn from this is that hydroxyl groups on hypericin and emodin are instrumental in the aggregation of these molecules through intermolecular interactions.

Structural differences in self assembled monolayers of anthraquinone derivatives on silver and gold electrodes were studied by Nishiyama et al. using cyclic voltammetry and in situ SERS. The derivatives studied were 1-anthraquinonebutylsulfide (1-AQS) and 2-anthraquinonebutylsulfide (2-AQS). A pH dependence study was carried out for both derivatives on gold electrodes and it was noted that the redox potential changed by ca. –60 mV pH^{-1} for both derivatives, indicating that the reduction process of both anthraquinone derivatives involved a two electron two proton reaction. However, on silver electrodes the redox potential changed by –30 mV pH^{-1}, which suggested that there was a strong interaction between the C=O moiety and the electrode surface, limiting the protonation of the molecule and leading to a two electron one proton reaction. SERS spectra of 2-AQS at low wavenumbers were measured to probe the interaction of the carbonyl group of 2-AQS

with the electrode Spectral bands at 272 and 154 cm^{-1} were observed on these spectra which were assigned to Ag-S stretching A band at 272 cm^{1} was also observed that was assigned to Ag-O stretching of the quinone moiety This band was seen to disappear upon reduction and reappear following reoxidation It was concluded that 2-AQS interacted with the silver surface through the sulphide and the quinone group Similar investigations using gold electrodes at low wavenumbers were hampered by a small S/N ratio of the observed spectra SERS spectra of both anthraquinone monolayers were obtained on gold electrodes Surface concentrations for 2-AQS were calculated to be almost twice that of 1-AQS by cyclic voltammetry However, the intensity of the SERS signal of 2-AQS was far more than twice that for 1-AQS The authors proposed that this could be explained by a difference in orientation When 0 V was applied to the electrode a strong C=O band was observed as was a strong aromatic breathing mode The ratio of ring breathing intensity to the carbonyl intensity ($I_{ring}/I_{C=O}$) of the anthraquinone layer was enhanced compared to that of the powdered sample, suggesting that the orientation was relatively perpendicular to the surface It was noted that the carbonyl stretch disappeared upon reduction and was replaced by an OH bending mode However, the ratio of the ring-breathing mode in the oxidised molecule and the reduced molecule is close to 1, which suggested that the molecule does not change orientation on going from oxidation to reduction Bands assigned to the out-of-plane state of the anthraquinone ring were not clearly observed, meaning that the authors could only propose an approximation of the orientation of the molecule on the gold surface Namely, a perpendicular orientation with interaction between the sulphide group on the molecule with the gold surface Experiments with 1-AQS on silver electrodes at an applied potential of 0 V yielded spectra with characteristic bands for C=O stretching, ring stretching and C-S stretching At –0 4 V, 0 05 V negative of the redox potential, the C=O band disappeared and bands attributed to OH stretching mode were observed As on gold electrodes, the ratio of intensities of in-plane C=C stretching of 1-AQS in the oxidised state to those in the reduced state were close to one, indicating that no significant orientation change took place on the electrode on reduction of the anthraquinone The spectrum of the molecule in the oxidised form was as expected with the characteristic bands for C=O and aromatic ring breathing On reduction of 2-AQS the C=O band disappeared and all bands attributed to the in plane mode were weakened This suggested that a structural change was induced by the reduction

It is important to note that the references cited in this section are not intended to be an exhaustive study   The citations are included as illustrations of the applications of Raman techniques and in their relevance to the work discussed in this document

References

1 Kawai, S H , Gilat, S L , Ponsinet, R , Lehn, J M , *Chemistry-A European Journal, 1, 5, 285, 1995*

2 Andersen, M , Wahl, M C , Stiel, A C , Grater, F , Schafer, L V , Trowitzsch, S , Weber, W , Eggeling , C , Grubmuller, H , Hell, S W , Jakobs, S , *PNAS, 102, 37, 13070, 2005*

3 Nifisi, R , Ferrari, A , Arcangeli, C , Toxxini, V , Pellegrini, V , Beltram, F , *J Phys Chem B, 107, 1679, 2003*

4 Feringa, B L , Jager, W F , de Lange, B , *Tetrahedron, 49, 37, 8267-8310, 1993*

5 Birge, R R , *Biochim, Biophys Acta, 1016, 293, 1990*

6 Ball, P , Garwin, L , *Nature, 355, 761, 1992*

7 Shinkai, S , *Pure Appl Chem , 59, 425, 1987*

8 Tachibana, H , Kawabata, Y , Komizu, H , Manda, E , Matsumoto, M , Nakamura, T , Niino, H , Yabe, A , *J Am Chem Soc, 111, 3080, 1989*

9 Liu, Z F , Fujishima, A , Hashimoto, A , *Nature, 347, 658, 1990*

10 Heller, H G , *Chem and Ind , 193, 1978*

11 Wynberg, H , Feringa, B L , *J Am Chem Soc, 99, 692, 1977*

12 Hush, N S , Bacskay, G B , Reimers, J R , Wong, A T , *J Am Chem Soc , 112, 4192, 1990*

13 Lahann, J Mitragotri, S Tran, T , Kaido, H , Sundaram, J , Choi, S , Hoffer, S , Somorjai, G A , Langer, R , *Science, 299, 371-374, 2003*

14 Korenstein, R , Muszkat, K A , Sharafy-Ozeri S J , *J Am Chem Soc , 95, 6177, 1973*

15 Evans, D H , Xie, N *J Am Chem Soc Vol 105, 315, 1983*

16 Hammerich, O , Parker, V D *Acta Chem Scand B35, 395, 1981*

17 Anders, J , Byrne, H J , Reichenbach, J , Kaiser, M , Schmelzer, M , Wagner, Th , Roth, S *Ber Bunsenges Phys Chem , Vol 97, No 3 1993*

18 Olsen, B A , Evans, D H *J Am Chem Soc , Vol 103,No 4, 1981*

19 Neta, P , Evans, D H *J Am Chem Soc , Vol 103, No 24, 1981*

20 Matsue, T , Evans D H *J Electroanal Chem , Vol 168 287-298, 1984*

21 Matsue T Evans D H *J Electroanal Chem Vol., 163 137-143, 1984*

22 Mattar, S M , Sutherland, D *J Phys Chem Vol 95, 5129-5133*

23 Nicodem, D. E., Fernanda, M., da Cunha, V.; *J. Photochem. Photobio A, Vol 107165-167, 1997*

24 Anders, J., Byrne H. J., Popolawski, J., Roth, S.; *Mol Cryst. Liq. Cryst. Vol 235, 231-236, 1993*

25 Sommer-Larsen, P., Bjornholm, T., Jorgensen, M., Lerstrup; *Mol. Cryst. Liq. Cryst. Vol 234, 89-96, 1993*

26 Jorgensen, M., Lerstrup, K., Frederiksen, P., Bjornholm, T., Sommer-Larsen, P., Schaumberg, K., Brunfeldt, K., Bechgaard, K.; *J. Org. Chem., Vol 58, 2785-2790, 1993*

27 Cuberes, M. T., Schlittler, R. R., Jung, T. A., Schaumburg, K., Gimzewski, J. K.; *Surface Science Vol 383, 37-49, 1997*

28 Forster, R. J., Keyes, T. E., Vos, J. G., Interfacial Supramolecular assemblies, John Wiley and Sons. **2003**

29 Finklea, H. O., Hanshew, D. D., *J. Am. Chem. Soc, 114, 3173, 1992*

30 Bard, A. J., Faulkner,. L. R., Electrochemical Methods, Fundamentals and Applications, Second Edition, John Wiley and Sons, **2001**

31 Bain, C. D., Whitesides, G. M., *J. Am. Chem. Soc., 110, 5987 1988*

32 Laibinis, P. E., Whitesides., G. M., *J. Am. Chem. Soc., 114, 9022, 1992*

33 Prime, K. L., Whitesides, G. M., *Science, 252, 1164, 1991*

34 Finklea, H. O., Encyclopaedia of Analytical Chemistry. Wiley & Sons.

35 Bain, C. D., Troughton, E. B., Tao, Y., Evall, J., Whitesides, G. M., Nuzzo R. G., *J. Am. Chem. Soc., 111, 321-335, 1989*

36 Finklea, H. O., Hanshew, D. D., *J. Am. Chem. Soc, 119, 9, 1992*

37 Bretz, R. L., Abruna, H. D., *J. Electroanal. Chem., 408, 199-211, 1996*

38 Pan, W., Durning, C. J. Turro, N. J., *Langmuir, 12, 4469-4473 1996*

39 Hubbard, J. B., Sillin, V., Plant, A. L., *Biophys. Chem., 75, 163-176, 1998*

40 Muskal, N., Mandler, D., *Electrochim. Acta, 45 537-548, 1999*

41 Simmons, N. J., Aileen Chin, K. O., Harnisch, J. A., Vaidya, B., Trahanovsky. W. S., Porter, M. D., Angelici, R. J. *J. Electroanal. Chem., 482, 178-187, 2000*

42 Forster, R. J., *Anal Chem. 68, 3143-3150, 1996*

43 Ulman, A., Elers, J. E., Tilman, N., *Langmuir, 5, 1147, 1989*

44 He, P., Crooks, R. M., Faulkner, L. R., *J. Phys. Chem. 94, 1135, 1990*

45 Zhang, J., Anson, F. C., *J. Electroanal. Chem., 331, 945, 1992*

46 Hayes, W A , Shannon, C , *Langmuir, 12, 3688, 1996*

47 Gileadi, E , Electrode Kinetics for Chemists, Chemical Engineers and Material Scientists, VCH Publishers Inc , **1993**

48 Schreiber, F , *Progress in Surface Science, 65, 151-256, 2000*

49 Dannenberger, O , Buck, M , Grunze, M , *J Phys Chem B, 103,2202, 1999*

50 Peterlintz, K A , Georgiadis, R , *Langmuir, 12, 4371, 1996*

51 Andrade, J , *Adv Polymer Sci 79, 3, 1986*

52 Norde, W , *Adv Coll Interfac Sci , 25, 276, 1986*

53 Hubbard, J B , Silin, V , Plant, A L , *Biophys Chem , 75, 163-176,1998*

54 Willard, H , Merritt, L, Dean, J , Settle, F , Instrumental Methods of Analysis, Seventh Edition, Wadsworth Inc **1988**

55 Puranik, M , Chandrasekhar, J , Umapathy, S , *Chem Phys Lett 337, 224, 2001*

56 Mohapatra, H , Umapathy, S , *J Phys Chem A, 106, 4513, 2002*

57 Marzocchi, M P , Mantini, A R , Casu, M , Smulevich, G , *J Chem Phys 108, 2, 534, 1998*

58 Biswas, N , Umapathy, S , *J Chem Phys 107, 7849, 1997*

59 Biswas, N , Umapathy, S , *Chem Phys Lett , 234, 24, 1995*

60 Balakrishnan, G , Umapathy, S , *J Chem Soc Faraday Trans , 93, 4125, 1997*

61 Balakrishnan, G , Mohandas, P , Umapathy, S , *J Phys Chem, 100, 16472, 1996*

62 Zhao, X , Imahori, H , Zhan, C-G, Sakata, Y , Iwata, S , Kitigawa, T , *J Phys Chem A, 101, 622, 1997*

63 Duncan, M, D , Reintjes, J , Manuccia, T J , *Opt Lett , 7, 350, 1982*

64 Cheng, J X , Potma, E O , Xie, X S , *J Phys Chem A 106, 8561, 2002*

65 Hellerer, T , Schiller, A , Jung, G , Zumbusch, A , *Chem Phys Chem , 3, 630, 2002*

66 Young, J T , Tsai, W H , Boerio, F J , *Macromolecules, 25, 2, 887, 1992*

67 Sato, Y , Fujita, M , Mizutani, F , Usoaki, K , *J Electroanal Chem 409, 145, 1996*

68 Muniz-Miranda, M , Puggelh, M , Ricceri, R , Gabrielli, G , *Langmuir, 12, 4417, 1996*

69 Dieringer, J A , McFarland, A D , Shah, N C , Stuart, D A , Whitney, A V , Yonzon, C R , Young, M A , Zhang, X, Van Duyne, R P , *Faraday Discussions, 132, 9, 2006*

70 Moskovits, M , *Rev Mod Phys* 57, 783, *1985*

71 McAnally, G D , Everall, N J , Chalmers, J M , Smith, W E , *Appl Spec , 57, 44, 2003*

72 Kneipp, K , Kneipp, I , Itzkan, I , Dassari, R R , Feld, M S , *J Phys Condens Matt , 14, R598, 2002*

73 Baena, J , Lendl, B , *Current Opinion in Chemical Biology, 8, 534, 2004*

74 Habuchi, S , Cotlet, M , Gronheid, R , Dirix, G , Michiels, J , Vanderleyden, J , De Schryver, F C , Hofkens, J , *J Am Chem Soc , 125, 8446, 2003*

75 Bizarri, A R , *Appl Spec 56, 1531, 2002*

2.0 Experimental

"Aaaaah   There's nothing more exciting than science You get all the fun of sitting still, being quiet, writing down numbers, paying attention   Science has it all "

Principal Seymour Skinner, Springfield Elementary

2.1 Characterization of Bianthrone

Bianthrone was obtained, in solid, powdered form from Sigma Aldrich and characterization of was carried out using UV, IR, fluorescent emission spectroscopy, CHN, and HPLC analysis

2.1 1 HPLC analysis

HPLC was carried out using a Hewlett Packard 1100 LC instrument with Chemstation software The injection volume was 20 μl The column stationary phase was polystyrene divinyl benzene with an attached C_{18} group The detection method was uv detection The optimum wavelength used was 254 nm, which, as can be seen by Figure 2 1 3 1 is within a strong absorption band in the spectrum A mobile phase of acetonitrile water was used with a phosphate buffer The chromatogram is presented in Figure 2 1 1 1   The elution time observed for bianthrone was 22 2 minutes The time range for the chromatograms was approximately 30 minutes, and yielded no other peaks, thus indicating that the sample under investigation was pure
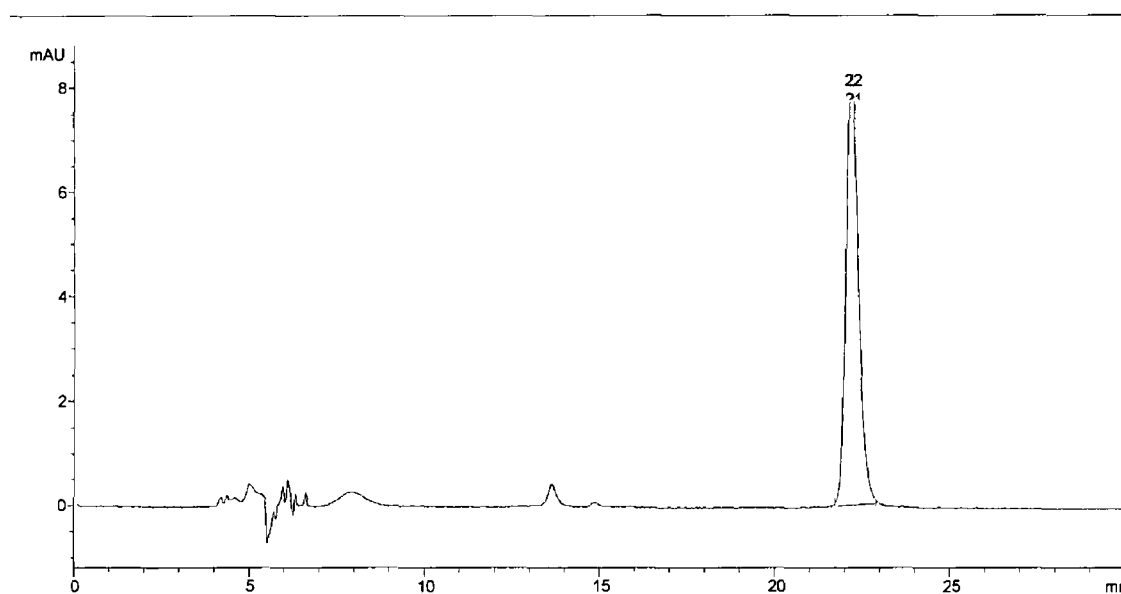
Figure 2 1 1 1   HPLC chromatogram of Bianthrone   Solvent used was acetonitrile The column stationary phase was polystyrene divinylbenzene with an attached C_{18} group   A uv detector was used for detection, which was set at an optimum wavelength of 254 nm

2.1.2 CHN analysis·

Elementary CHN (Carbon Hydrogen Nitrogen) analysis was carried out by the Microanalytical Laboratory in University College Dublin to confirm the presence of bianthrone in the sample The table below details the theoretically expected quantities of Carbon and Hydrogen and the quantities found

	C	H
Theoretical (%)	87 5	4 2
Found (%)	86 7	4 2

2 1 3 UV-Visible spectroscopy·

UV-vis spectra were obtained using a Shimadzu UV-3100 diode array spectrometer interfaced with a PC   Quartz cells of 1 cm path length were used, as these do not absorb in the UV region   The solvent employed, was spectroscopic grade acetonitrile, as it is transparent in the region investigated and dissolves a sufficient quantity of the sample to give well-defined peaks   The spectrum obtained for the sample is comparable to those obtained previously,[1] with a strong band below 300 nm corresponding to π-π* transitions in the molecules   The peak observed at 394 nm is likely to correspond to n-π* transitions that are expected from molecules containing carbonyl groups [2]
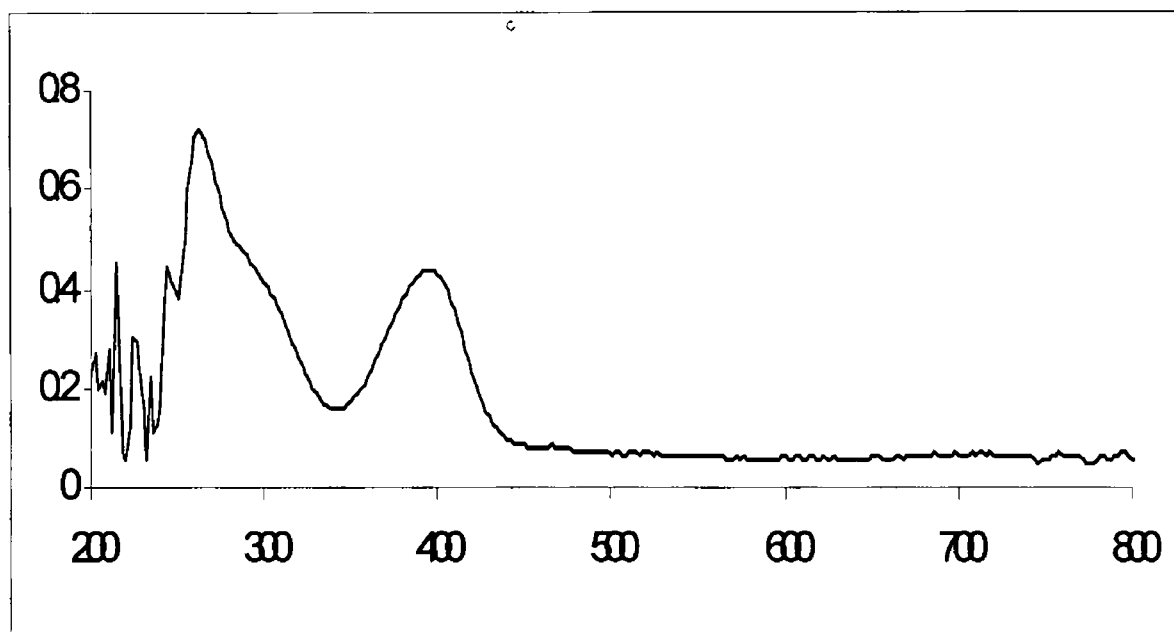
Figure 2 1 3 1   UV spectrum of bianthrone

2.1 4 IR Spectroscopy

In IR spectroscopy the sample is exposed to IR radiation and the bonds within the molecules vibrate at characteristic frequencies The IR spectrum for bianthrone is shown below The spectrum was recorded using a Perkin-Elmer 2000 FT-IR spectrometer The bianthrone sample was in solid form set in a KBr disk The spectrum obtained was comparable to previous spectra obtained from bianthrone [3]

The peaks observed have been assigned The absorption at 1665 cm[1] is due to the stretching vibrations of C=O parallel to the molecular axis The absorption at 1459 cm[1] is due to the parallel skeleton vibration of carbon atoms in a benzene ring with respect to the molecular axis The absorption at 933 cm[1] is due to the inner plane bending vibration of C-H parallel to the molecular plane The absorption at 762 cm[1] is due to the outer-plane bending vibration of C=O perpendicular to the molecular plane These absorptions all correspond to bianthrone in its A conformation
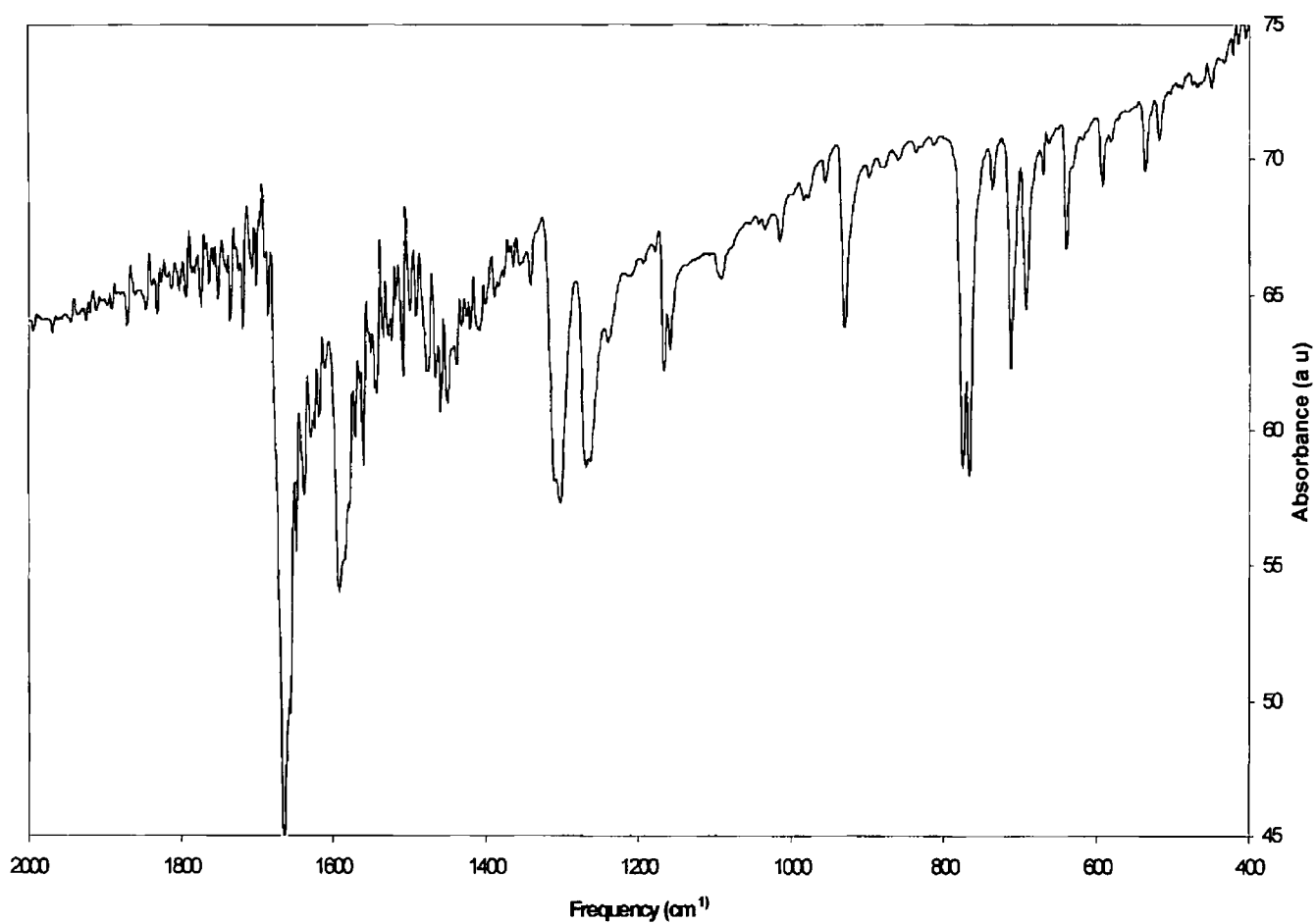
Figure 2 1 4 1 ir spectrum of bianthrone Solid bianthrone was incorporated into a KBr disk

2.1.5 Fluorescent emission

A fluorescent emission spectrum was obtained using a Varian Cary Eclipse spectrophotometer. The excitation wavelength used was 350 nm. The spectrum was obtained by making up a concentrated bianthrone solution dissolved in DMF. A blank DMF solution was used to zero the instrument.
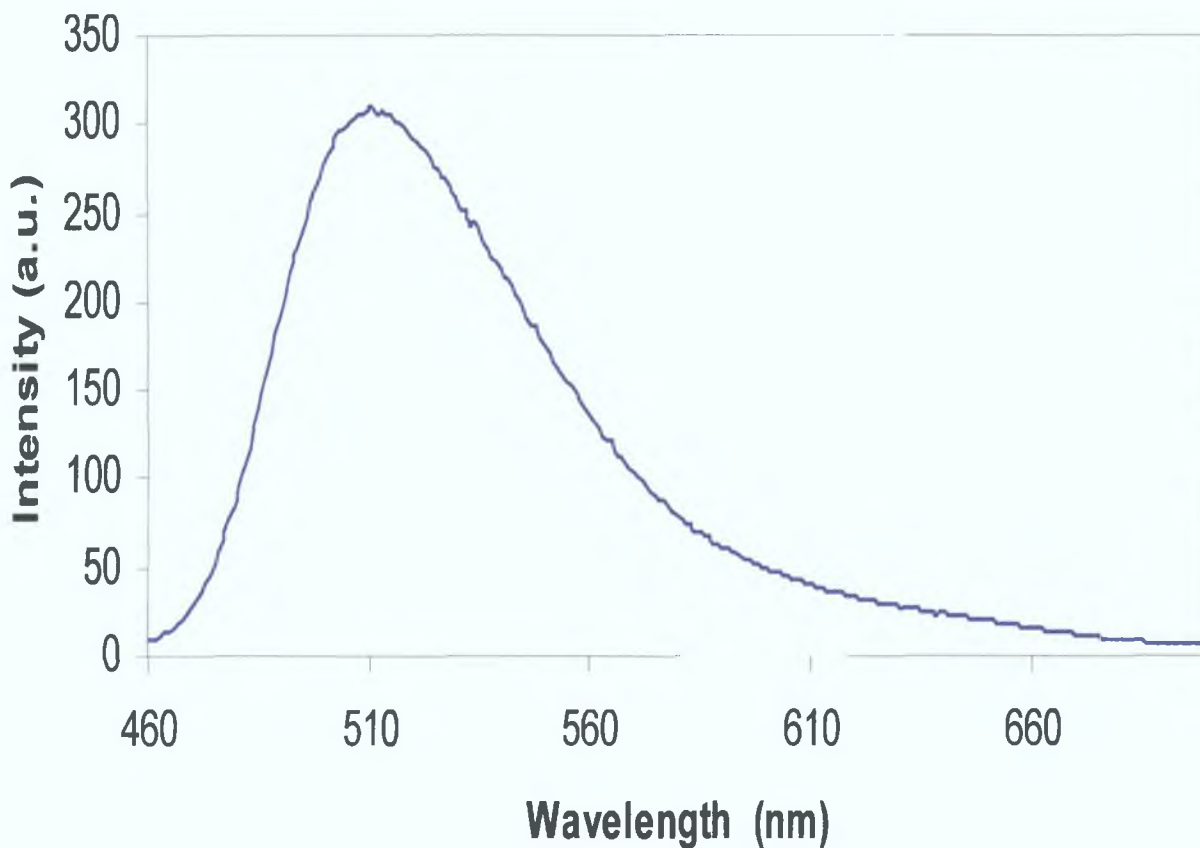

Figure 2.1.4.2 Fluorescent emission spectrum of bianthrone. Excitation was set at 350nm

References

1 Evans, D H , Xie, N *J Am Chem Soc Vol 105, 315, 1983*

2 Gilbert, A , Baggott, J , *Essentials of Molecular Photochemistry, Blackwell Scientific Publications 1991*

3 Mori, T , Mori, K , Mizutani, T , *Thin Solid Films, 393, 143-147, 2001*

3.0 Analysis of Bianthrone Monolayers on Mercury Electrodes

Research is what I'm doing when I don't know what I'm doing
Wernher Von Braun

3 1 Experimental

3 1 1 Instrumentation

Cyclic voltammetry was carried out using a CH Instruments 440 electrochemical workstation, a PAR EG&G model 300 Hanging Mercury Drop electrode and a conventional three-electrode cell Potentials were measured against a potassium chloride saturated silver/silver chloride reference electrode A platinum wire was used as the auxiliary electrode All solutions containing bianthrone were thoroughly deoxygenated by purging with nitrogen for at least twenty minutes The area of the mercury electrode was measured by recording cyclic voltammograms of Anthraquinone-2-carboxylic acid at a sufficiently high concentration to ensure saturation surface coverage of the adsorbate on the electrode

3 1 2 Materials

Bianthrone was obtained from Sigma Aldrich Ltd, as were the solvent, 99% N, N Dimethyl formamide and the electrolyte, 70 % perchloric acid Bianthrone was characterised to ascertain its purity and these results are detailed in the experimental chapter (Chapter 2) of this thesis All solutions were prepared using Milli-Q water In all solutions, the 70% perchloric acid was made up to 1 M and was the supporting electrolyte

3.2 General Electrochemical properties

Figure 3.2.1 shows a cyclic voltammogram for a mercury electrode immersed in a 0.3 μM solution of bianthrone in 1.0 M $HClO_4$. The voltammetry is consistent with an electrochemically reversible redox active species immobilised on an electrode surface in that the peak heights scale linearly with scan rate, v, up to 62.5 Vs^{-1} as opposed to $v^{1/2}$ and the peak shapes are independent of scan rate. A dependence on $v^{1/2}$ would be expected for a freely diffusing species[1, 2, 3]. From this it can be concluded that bianthrone adsorbs onto the surface of the mercury electrode forming an electroactive film.[4]

The surface coverage corresponding to this cyclic voltammogram, which was obtained from the integration of the charge, Q, under the voltammetric waves according to Equation (3.1), is 3.1 x 10^{-11} mol cm^{-2}. The surface coverage was calculated using [5, 6,]

$$\Gamma = \frac{Q}{nFA} \quad (3.1)$$

where Γ is the surface coverage with units of mol/cm^2, Q is the charge calculated from the integrated area under the curves of the cyclic voltammogram in coulombs, C, n equals the number of electrons being transferred (in this case 2), F is Faraday's constant and A is the surface area of the electrode, in this case, A corresponds to a value of 0.0134 cm^2. The full width at half maximum (FWHM), is described by:[7 8 9]

$$FWHM = \frac{90.6}{n} \quad (3.2)$$

n being the number of electrons transferred. This voltammogram exhibited an experimental FWHM of 58.4 mV. A value of 45.3 mV would be expected for an electrochemical response corresponding to a two-electron transfer, however these results indicate a near ideal response for a reversible surface bound redox species.[10] The peak-to-peak separation, ΔE_p for the system was found to be 5 mV. A ΔE_p of 0

mV would also be expected for an adsorbed species on an electrode where no interactions between the molecules are taking place Interactions between adsorbed species is the most likely reason for a ΔE_p greater than zero, however, other possible causes must be considered Briefly, if uncompensated resistance is large enough, the resulting voltage drop can contribute to the ΔE_p This issue is dealt with later in the chapter and it is not considered to contribute to the ΔE_p On the basis of the FWHM data and on previous reports on bianthrone redox in the solution phase that states that bianthrone undergoes a two electron reduction,[11] the redox reaction of bianthrone taking place at low pH is believed to involve the transfer of two electrons and two protons, an illustration of which can be seen in Scheme 3 1
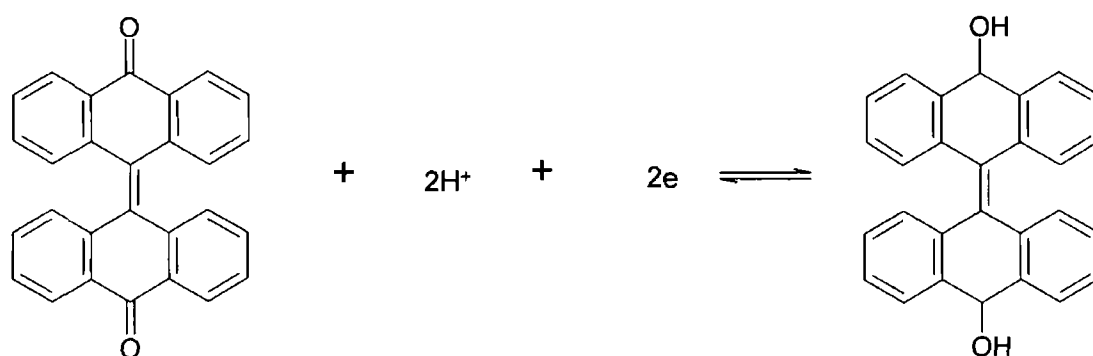
Scheme 3 1   Redox reaction of bianthrone detailing the 2-electron, 2-proton reduction of the molecule
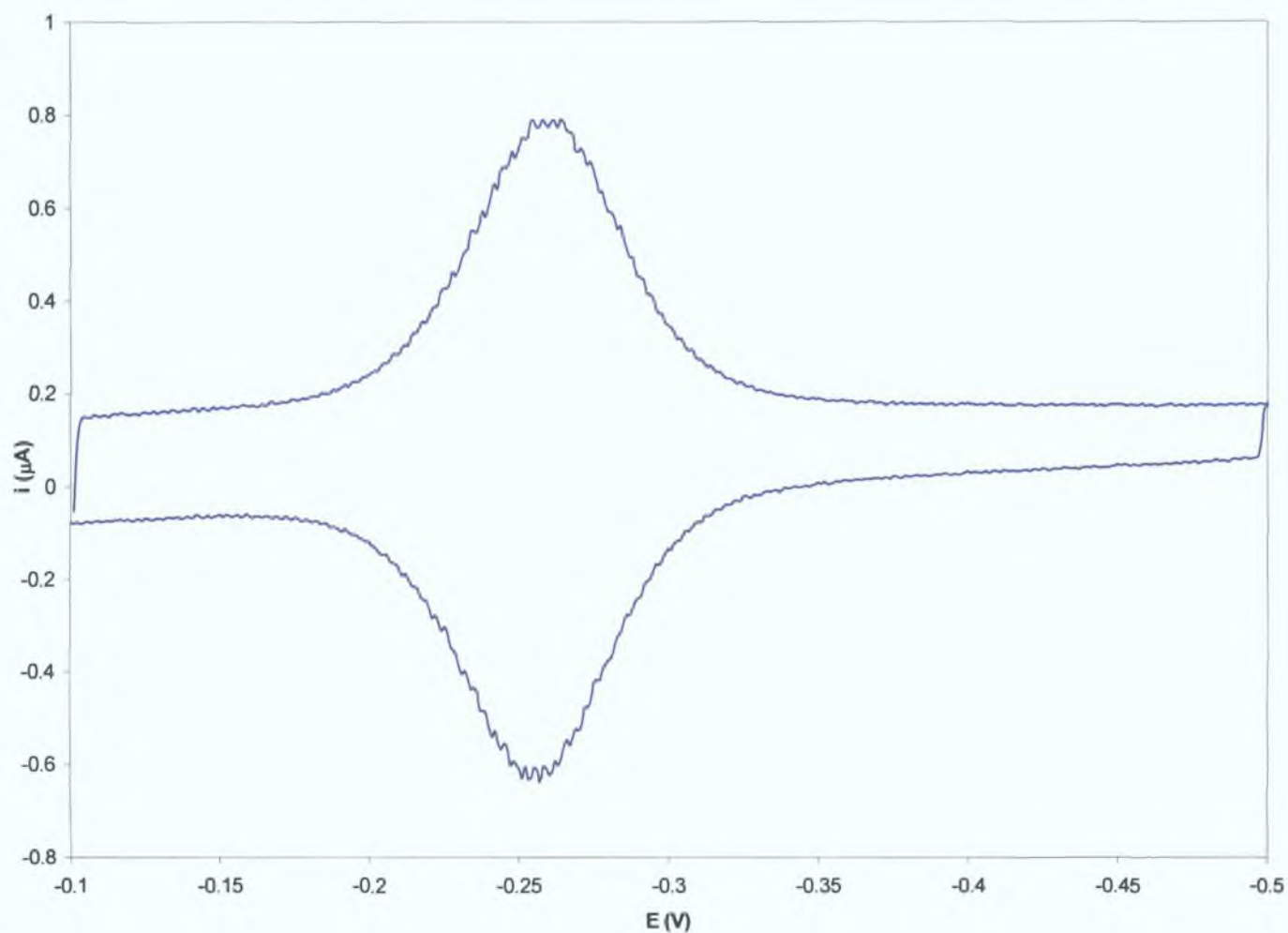
Figure 3.2.1 Cyclic Voltammogram for a hanging mercury drop electrode, with an area of 0.0134 cm² immersed in 0.3μM bianthrone. The supporting electrolyte was 1.0 M HClO₄ and the scan rate was 0.5 Vs⁻¹.

3 2.1 Scan rate dependence

Cyclic voltammograms were run at a number of different scan rates to probe the effect on the voltammetric response   Figure 3 2 1 2 shows the dependence of the peak current on the scan rate   It can be seen that the peak current, i_p, increases with increasing scan rate up to 50 Vs^{-1} As already mentioned, this behaviour contrasts with diffusive tails and $v^{1/2}$ dependence expected for a freely diffusing species and is characteristic of a surface confined species   When the experimental time constant and that of electron transfer are comparable it is expected that the rate of electron transfer across the metal/film interface will influence the voltammetric response   For the range of scan rates from 56 to 100 Vs^{-1} the peak current values deviate from linearity   This would suggest electron transfer effects   As the sweep rate is increased in cyclic voltammetry, the time scale of the experiment becomes shorter so that redox equilibrium is not reached

It can also be seen that peak-to-peak splitting increases with increasing scan rate reaching 129 mV at 100 Vs^{-1} Slow heterogeneous electron transfer can contribute to an increase in ΔE_p at increasing scan rates   However, iR drop can also contribute to this splitting [12]   When charging and discharging faradaic currents flow through a solution, they generate a potential that acts to weaken the applied potential by an amount iR, where i is the total current and R is the cell resistance   A calculation of iR in this system yields a maximum ohmic drop of 0 037 V at a scan rate of 100 Vs^{-1} Therefore, while iR drop may make a small contribution to the peak-to-peak separation at higher scan rates, between 62 5 and 100 Vs^{-1}, it is not large enough to contribute to separation at low scan rates at values from 1 to 50 Vs^{-1}
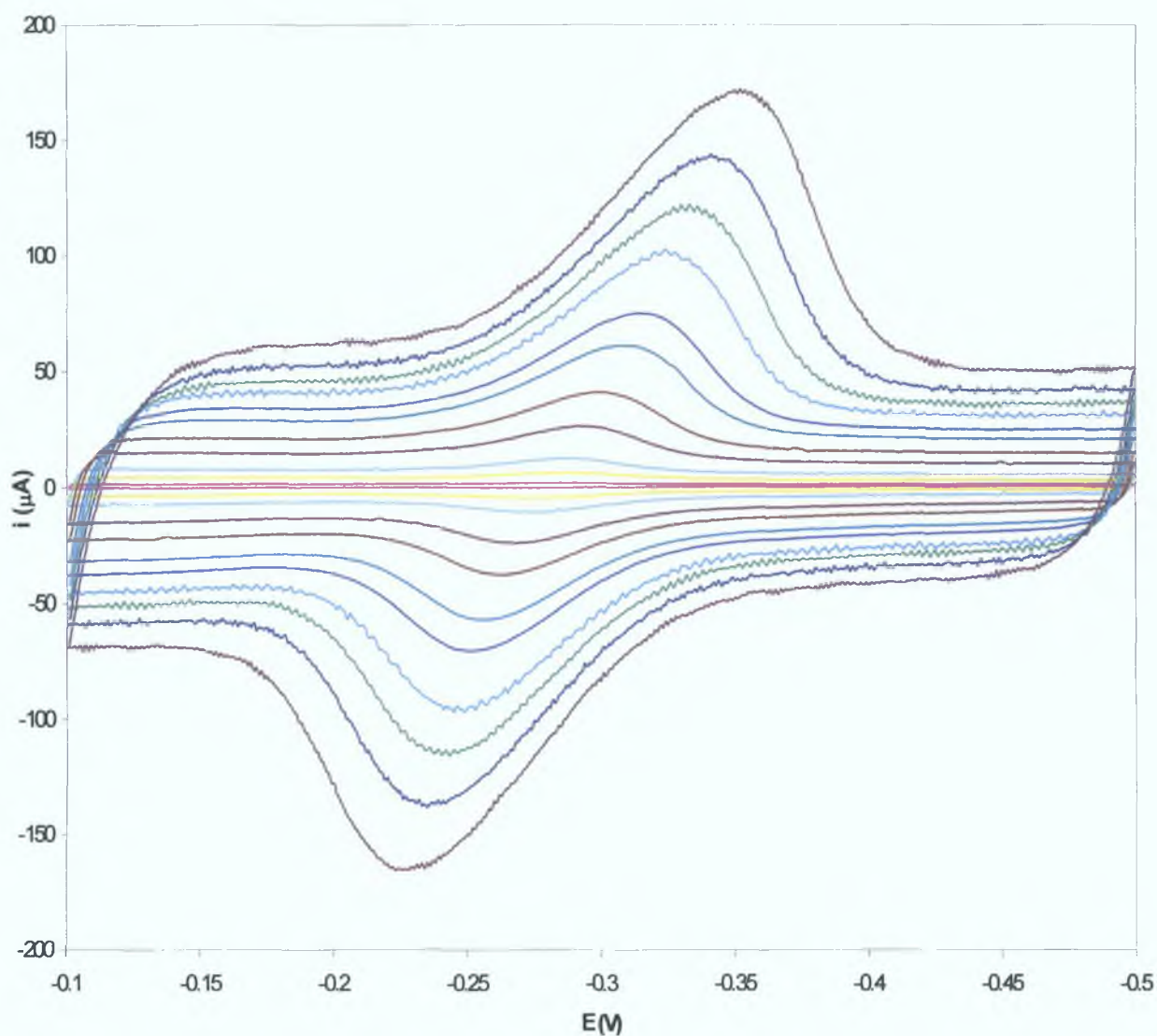
Figure 3.2.1.1 Cyclic Voltammograms for hanging mercury drop electrode with an area of 0.0134 cm² immersed in a 0.15 μM solution of Bianthrone, with 1.0 M HClO₄ as the supporting electrolyte. Scan rates involved are, from inner voltammogram out, 1, 5, 10, 20, 25, 30, 33, 38.5, 42, 50, 56, 62.5, 71, 83, 100 Vs⁻¹
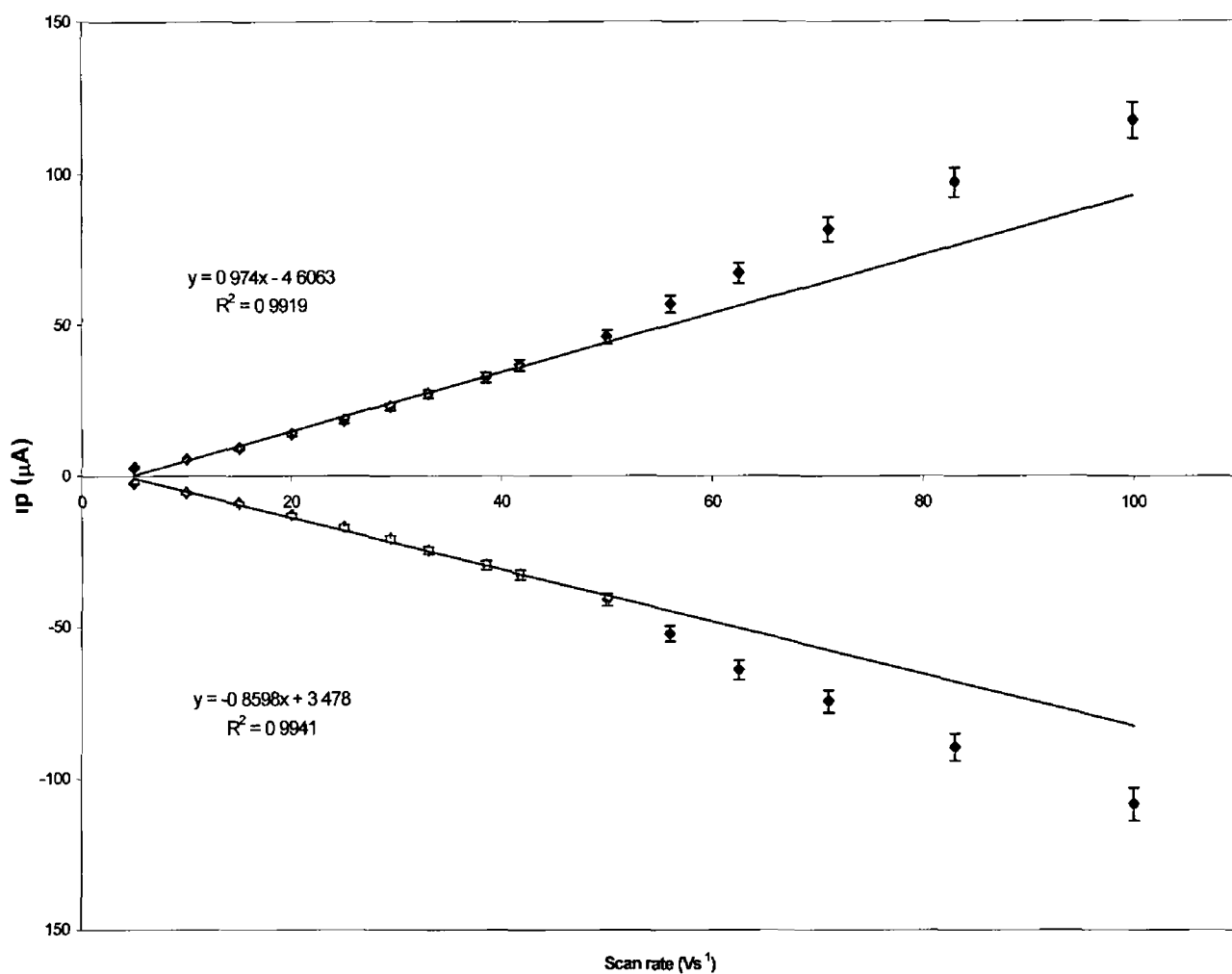
Figure 3 2 1 2 Scan rate dependence of the cyclic voltammetric peak current measured for bianthrone at scan rates of 1-100Vs⁻¹ The concentration of bianthrone in solution is 0 3 µM with 1 M HClO₄ as the supporting electrolyte Cathodic currents are up, anodic down Error bars represent the standard deviation obtained from three measurements

3 3 Surface Coverage Effects Current Spikes

The cyclic voltammogram shown in Figure 3 2 1 displays near ideal behaviour for an immobilised redox couple on an electrode surface However, current spikes were observed in the anodic and cathodic branches of CVs as the surface coverage approaches saturation In the case of the solution with a bulk concentration of 0 3 μM, the anodic spike appears initially followed, at longer time scales by the cathodic spike The first appearance of the anodic spike corresponded to a surface coverage, Γ, of $3\ 9 \times 10^{11}$ mol cm^{2} The cathodic spike, which appears less sharp than the anodic spike, appeared at a corresponding surface coverage of $4\ 2 \times 10^{-11}$ mol cm^{-2} Current spikes in cyclic voltammetric analysis of quinone species have been noted by Zhang and Anson, they noted a current spike in the voltammetry of anthraquinone-2,6-disulphonate, 2,6 AQDS, adsorbed on graphite electrodes, which they ascribed to interactions between molecules at the surface [14] Faulkner et al, in a previous paper, described a similar spike observed when the 2,6 AQDS was adsorbed on a mercury electrode [13] From previous studies on quinone groups and given the similarity of bianthrone to quinones in the carbonyl groups it is likely that the interactions involved are hydrogen-bonding interactions [14,15] [16] In the case of the 0 3 μM bulk solution, the spikes occurred at -0 263 V on the anodic sweep and -0 278 V on the cathodic sweep Given bianthrone's structure it ought to be capable of intermolecular hydrogen bonding between the carbonyl and hydroxy functionalities of the oxidised and reduced species respectively The spikes resulting from these lateral interactions are only observed at high surface coverages, this is due to decreasing distance between individual molecules making the interactions increasingly possible Current spikes can possibly be explained by taking the following example The redox reaction of an adsorbed quinone type species can be represented by

$$H_2Q - 2e\ - 2H^+ \ \leftrightarrow Q$$
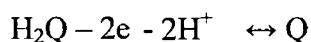
Here, Q is the quinone and H_2Q is the corresponding reduced hydroquinone species This reaction has a formal potential, which is designated E^0_1 As the scanning potential approaches the formal potential the ratio of hydroquinone to quinone on the surface of the electrode is approximately 1 1 When intermolecular hydrogen bonding

interactions occur, a species, H_2Q---Q is formed which has a new formal potential, designated E^0_2 This new formal potential is more negative than E^0_1 and an excess charge is present on the surface This increase in charge is dissipated by means of an increase in current until the redox composition appropriate to E^0_2 is achieved, which is seen in the voltammogram as a current spike

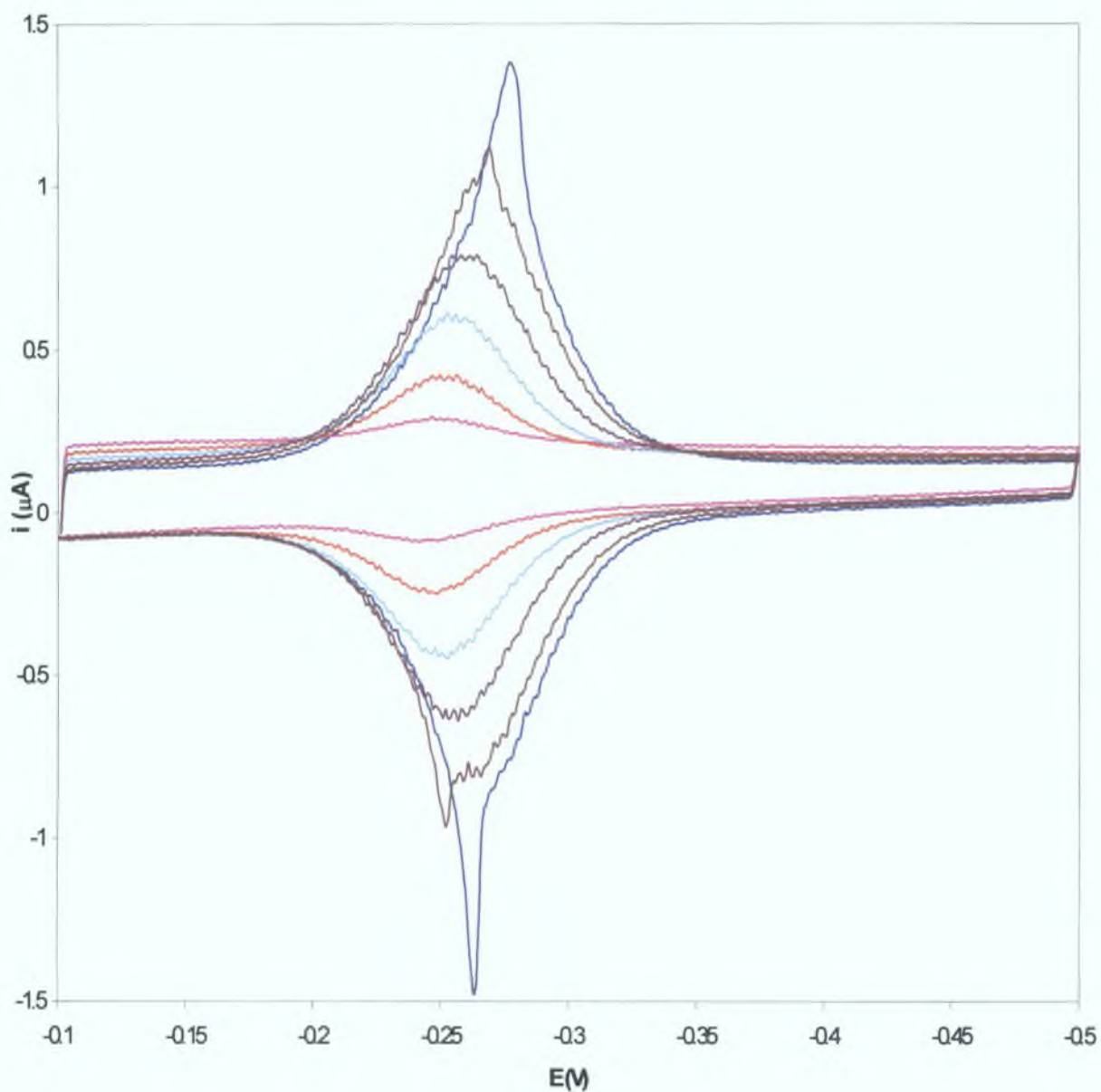*Figure 3.3.1 Cyclic voltammograms of hanging mercury drop electrode immersed in 0.3 μM bianthrone solution with 1.0 M HClO₄ as the supporting electrolyte. The cvs were taken at different times in a continuous run and show the evolution of the current spike. The cvs correspond to, in order of current amplitude 90, 450, 900, 1368, 1809, 2061 s. The scan rate in this experiment was 0.5 Vs⁻¹*

3.4 Capacitance analysis

The behaviour of an electrode solution interface can be described by comparison with a capacitor. A capacitor consists of two metal sheets separated by a dielectric material whose behaviour is described by:

$$C = \frac{q}{E} \quad (3.3)$$

q being the charge on the capacitor, in coulombs (C), E is the potential in volts (units, V) and C is the capacitance, which is measured in farads (F). When potential is applied across a capacitor, charge accumulates on its metal plates until the above Equation (3.3) is satisfied. During the charging process, the charging current flows. A build up of electrons on one plate and a deficiency of electrons on the other constitutes the charge on the capacitor. The electrode solution interface has been shown to exhibit similar behaviour. At a given potential a charge will exist on the electrode and also a charge in the solution, q^M and q^S, respectively. The polarity of the charges depends on the potential across the interface and the composition of the solution, but at all times q^M will be equal to $-q^S$. The charge in the solution is made up of cations or anions close to the electrode surface. This structure of the electrode/electrolyte interface refers to an unmodified surface. Adsorption of electroactive species onto the electrode surface causes specifically adsorbed ions and solvent molecules to be displaced from the interface and causes a change in the double layer capacitance from that observed at a clean unmodified surface. In the case of an electrode coated with a monolayer, the total double layer capacitance, C_{dl} is given by the sum of contributions from the film, C_f, and the diffuse layer, C_{diff}, according to Equation (3.4)[17]

$$\frac{1}{C_{dl}} = \frac{1}{C_f} + \frac{1}{C_{diff}} \quad (3.4)$$

The absolute magnitude of C_{dl} is governed by the magnitude the smaller of the film and diffuse layer capacitances. In high electrolyte concentration the double layer is

compressed and C_{diff} becomes so large that it no longer contributes to C_{dl} The total double layer capacitance is then controlled by the monolayer capacitance

Thus, investigating the extent to which the double layer capacitance decreases upon modification can provide information on the packing density of the monolayer The dependence of double layer capacitance on surface coverage at fixed bulk concentration has been investigated This was done by measuring the double layer capacitance from successive voltammograms that were recorded as a monolayer was formed at the mercury surface from solutions of fixed bianthrone concentration This can give an insight into the formation of the monolayer as it occurs The surface coverage varies from sub monolayer coverage to near saturation surface coverage over time The double layer capacitance was measured at $-0.45V$ and at $-0.13V$, where the monolayer was fully reduced and oxidised, respectively It was found that the double layer capacitance decreased as the surface coverage increased, going from 8.0×10^{-2} μFcm^{-2} at 5.2×10^{-12} $molcm^{-2}$ to 7.3×10^{-2} μFcm^{-2} at a surface coverage of 4.7×10^{-11} $molcm^{-2}$ Figure 3.4.2 shows this behaviour for a 0.3 μM solution The trend is consistent with what is expected for an increasing surface coverage i.e. as bianthrone adsorbs on the electrode surface it displaces adsorbed ions and solvent molecules that contribute to surface charge leading to a decrease in double layer capacitance as bianthrone surface coverage increases

The total interfacial capacitance was determined also This was calculated using Equation (3.5) [18]

$$i_c = \nu C_T A \qquad (3.5)$$

i_c being the charging current taken at $-0.45V$, ν is the scan rate with units of Vs^{-1}, C_T is the total interfacial capacitance, in μFcm^{-2} and A refers to the area of the electrode, which had been previously been calculated as 0.0134 cm^2 A plot of the charging current, i_c versus scan rate gives a value for the interfacial capacitance of 12.5 ± 0.97 μFcm^{-2} on the cathodic sweep and 8.4 ± 0.61 μFcm^{-2} on the anodic sweep This value was observed for five different bulk concentration values That the adsorption of

bianthrone to the mercury surface is seen to be irreversible resulting in comparable maximum surface coverage values regardless of bulk concentration means that it would be expected that there would be no difference between the bulk concentrations
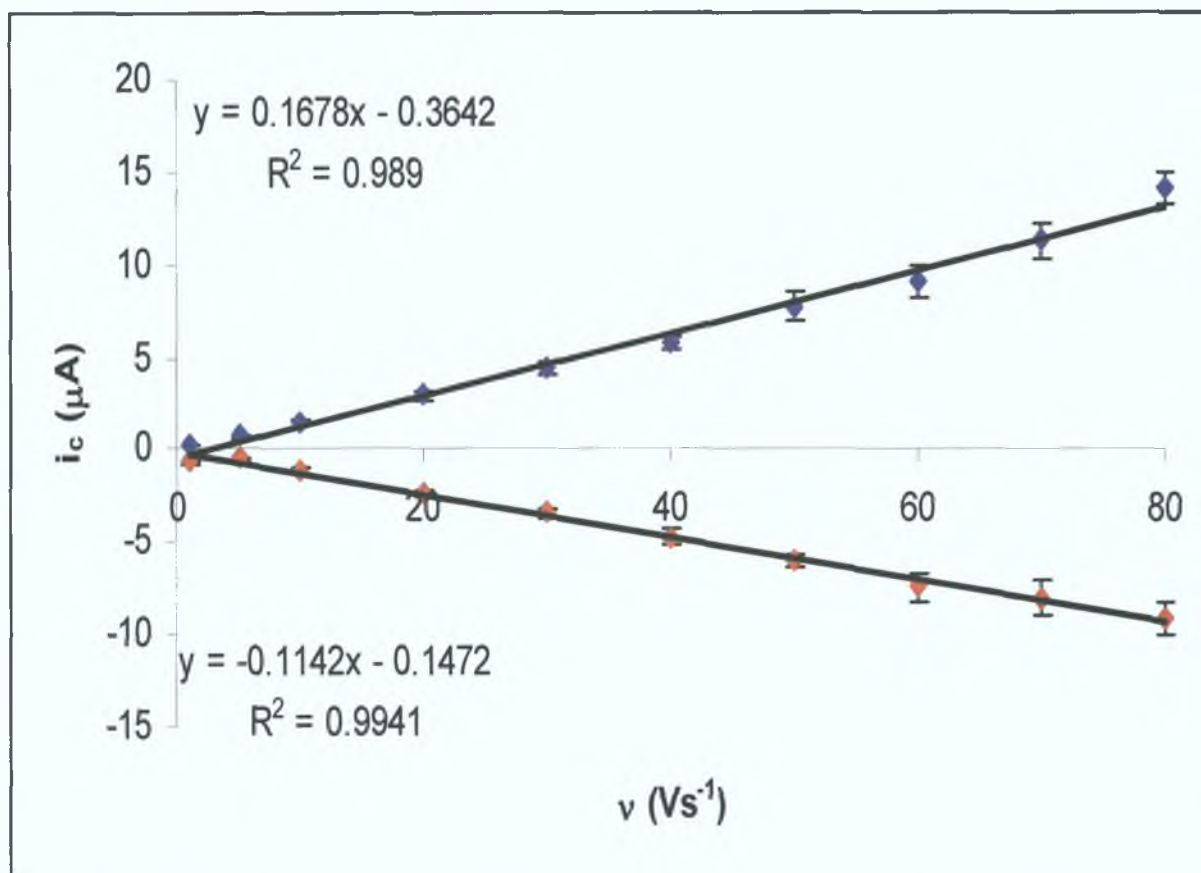
Figure 3.4.1 Plot of charging current, i_c versus scan rate, v, for a monolayer formed by immersion of a hanging mercury drop electrode with an area of 0.0134 cm^2 in a 0.3 µM solution of bianthrone. The supporting electrolyte was 1 M HClO$_4$. The slope of this plot provides a value for the total interfacial capacitance. Error bars are calculated from three values.

$$y = -2E+08x + 0.0797$$
$$R^2 = 0.8788$$
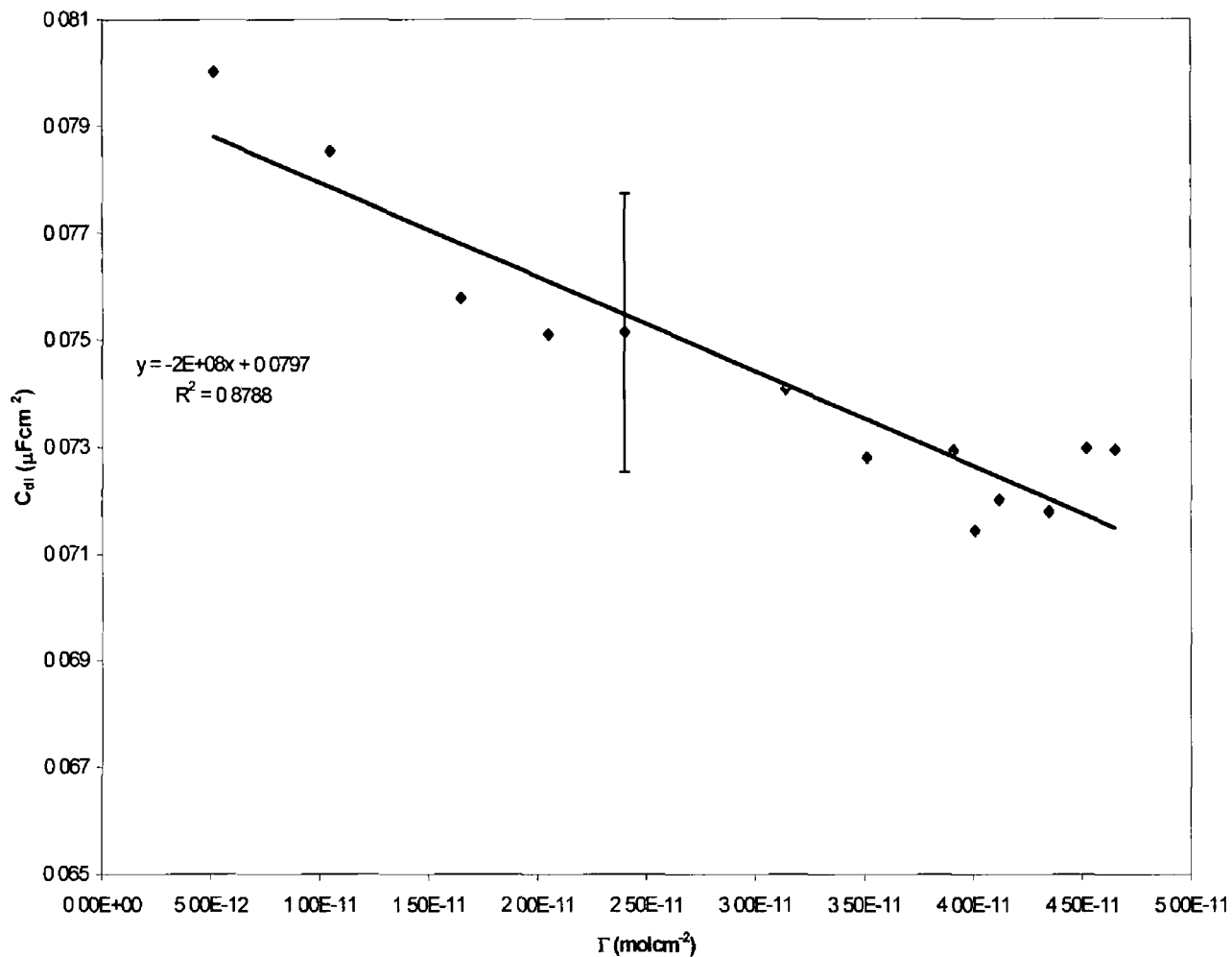
Figure 3 4 2 Plot of double layer capacitance versus surface coverage for a monolayer formed by immersion of a mercury electrode in a 0 3 µM solution of bianthrone The supporting electrolyte was 1 M $HClO_4$ Data was taken at a voltage of −0 45 V where the monolayer is fully reduced The error bar represents the standard deviation from three measurements and serves as a representative error

3.5 Electron Transfer Rate constant

An investigation into the rate constant for electron transfer across the electrode monolayer interface was carried out using the Laviron formulation,[19] described by Equation (3.6)

$$k^0 = \frac{\alpha n F v_c}{RT} = \frac{(1-\alpha)n F v_a}{RT} \quad (3.6)$$

In equation (3.6), k^0 refers to the standard electron transfer rate constant, α is the transfer coefficient, F is Faraday's constant, R is the universal gas constant, T is the temperature and v_a and v_c are the scan rates for anodic and cathodic sweeps respectively. The scan rate range investigated in the data fit to the Laviron method was 1-100 Vs^{-1}. It has been seen that, while there is little peak-to-peak separation in the voltammograms at low scan rates, the peak-to-peak separation increases with increasing scan rate with a final ΔE_p of 129 mV at a scan rate of 100 Vs^{-1}.

A plot of the peak potential of the cathodic and anodic sweeps versus the log of the scan rate provides a value for the electron transfer coefficient, α, which is obtained using Equation (3.7):[20]

$$\alpha = \frac{m_a}{m_a - m_c} \quad (3.7)$$

where m_a and m_c are the slopes of the anodic and cathodic trendlines, respectively, and also a value for the standard rate constant which is calculated using the intersection of the trend lines of the anodic and cathodic data using the above Laviron formulation. The lines through the cathodic and anodic points intersect the x-axis and these scan rates are used to estimate the forward and reverse rate constants.

A concern here would be the contribution to the peak-to-peak separation made by iR drop, which can cause inaccuracies in the calculation of the electron transfer rate constant. The current at which a negligible iR drop of 10 mV is observed is calculated as follows:

106

$$V_{Ohmic} = iR \ (3\ 9)$$

where V_{Ohmic} is the ohmic drop, and R is the resistance of the solution, which has a value of 223 Ω The current value is calculated as 44 8 μA From the plot of scan rate dependence (Figure 3 1 2 2) it can be seen that this current value corresponds to a scan rate value of 60 Vs^{-1} The log of this value is 1 78 Thus, for log(scan rate) values below 1 78, iR contribution to the peak-to-peak separation is negligible

In the results illustrated, in Figure 3 4 1 the trend lines intersect the x-axis at 1 2 and 1 1, for the anodic and cathodic lines, respectively The antilog values of these numbers are 16 and 13 Vs^{1} respectively These values can be entered into Equation (3 6) to yield a rate constant value of $5\ 8 \times 10^{2} \pm 1\ 4\ s^{1}$ This asymmetry in values was examined, to see if the rate of proton transfer to the monolayer had an effect, by first calculating the thickness as follows

$$\delta = \frac{\Gamma}{C_{H_3O^+}} \ (3\ 10)$$

where Γ is the surface coverage of the monolayer, in this case $4\ 56 \times 10^{-11}$ molcm^{-2}, and $C_{H_3O^+}$ is the bulk concentration of protons in solution, in this case 1×10^{-3} molcm^{-3} This produced a δ value of $4\ 56 \times 10^{8}$ cm This film thickness corresponds to the proton transfer timescale as follows[21]

$$\delta = \left(\pi D_{H^+} t\right)^{\frac{1}{2}} \ (3\ 11)$$

where D_{H^+} is the diffusion coefficient of the hydrogen ion,[22] with a value of $9\ 31 \times 10^{-5}$ cm^{2}s^{-1}, and t is time in seconds A t value of $7\ 1 \times 10^{-12}$ s was obtained This timescale is much faster than that of electron transfer and as a result, proton transfer is not a factor that influences electron transfer It is likely that the formation

of the bond between the hydrogen and oxygen in the hydroxyl group contributes to the observed asymmetry
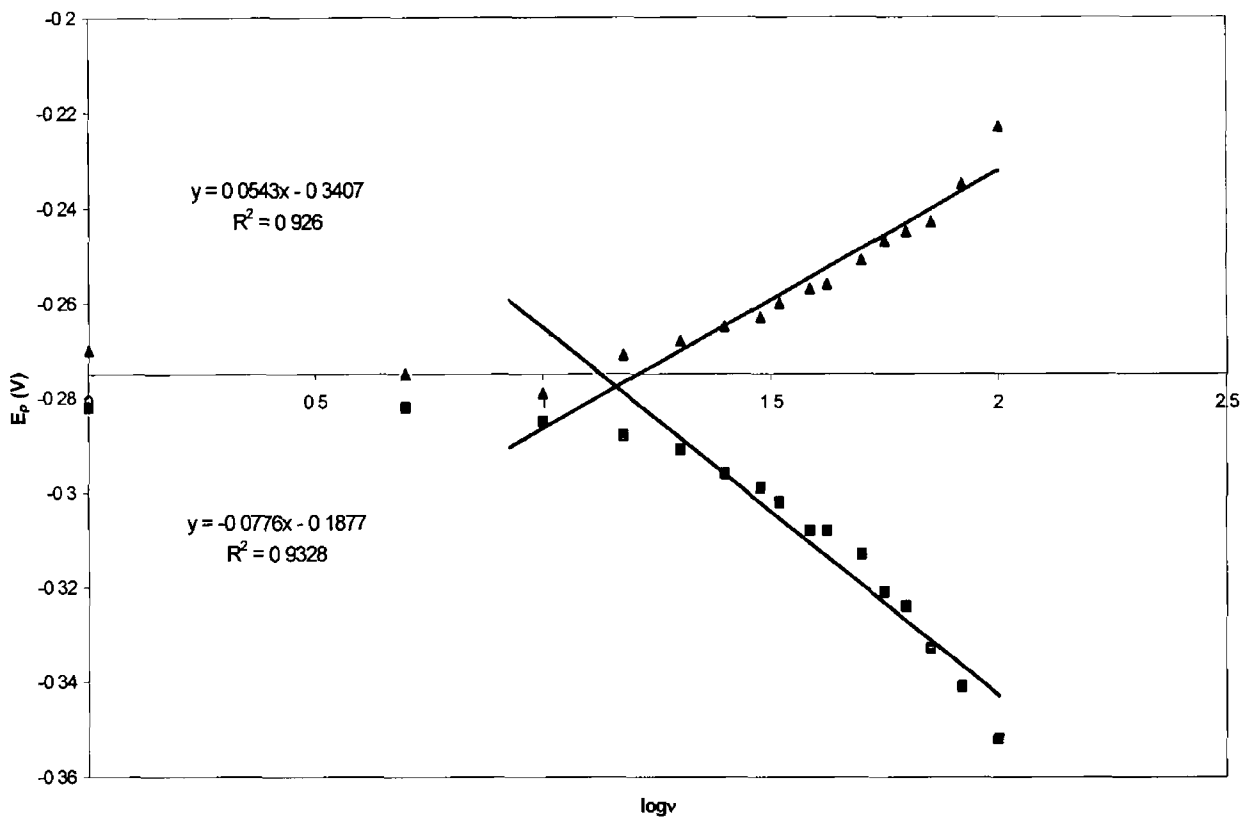
Figure 3 5 1 Corrected plot of ΔE_p vs the log of the scan rate The data was modified by subtracting the peak-to peak separation at low scan rates from the separation at high scan rates The separation at low scan rates is not due to the kinetics of electron transfer

3.6 Dynamics of monolayer formation

3.6 1 Adsorption Kinetics

It was observed that the maximum surface coverage values for bulk concentrations ranging from 0 09 to 0 3 μM were similar, unlike previous studies on other reversible systems which, showed a systematic difference in surface coverage that depended on the bulk concentration of the adsorbent solution [23][24][25] This suggests that the adsorption of bianthrone on the mercury surface is irreversible, the surface coverage increasing until a saturation surface coverage is reached regardless of bulk concentration (Figure 3 6 1 1)

In order to obtain information on the dynamics of bianthrone monolayer formation on mercury, plots of surface coverage versus time were constructed The surface coverage of the bianthrone molecules was calculated by integrating the charge under the voltammetric curves taken from the cyclic voltammograms as a function of time as the monolayer forms These plots were then fitted to a mathematical model that takes into account the influence of diffusional and kinetic parameters as the molecules approach the surface and reorganizational parameters as the monolayer is built up [26] These two parameters are deemed important as the overall rate of monolayer formation can be influenced both by the rate of diffusion of molecules to the surface and, when at the surface by surface reorganization The mathematical form of the model expresses the time dependent surface concentration of an adsorbing species, and a surface reorganization rate constant,

$$\Gamma(t) = \Gamma_m \left\{ 1 - \exp\frac{-KC_o}{\Gamma_m} \left[\frac{D}{K^2} \left(\exp\left[\frac{K^2 t}{D}\right] - erfc\left[\left(\frac{K^2 t}{D}\right)^{1/2}\right] - 1 \right) + \frac{2}{K}\left(\frac{Dt}{\pi}\right)^{1/2} \right] \right\} \quad (3\ 12)$$

In the derivation of this equation it is necessary to assume Fickian diffusion to an imperfectly adsorbing surface whose active sites are blocked by previously adsorbing species

$$\Gamma(t) = \int_0^t d\tau \left(1 - \frac{\Gamma(\tau)}{\Gamma_m}\right) F_D(\tau) \quad (3\ 13)$$

110

where the time dependent surface coverage, $\Gamma(t)$ is expressed in terms of Γ_m, the maximum surface coverage, and the bracketed term in Equation (3 13) is the fraction of the surface that is not covered at time, τ The diffusive flux to the surface, F_D, is given by

$$F_D = KC_0 \exp\left(\frac{K^2 t}{D}\right) erfc\left(\frac{K}{D^{1/2}} t^{1/2}\right) \quad (3\ 14)$$

C_0 is the bulk concentration of the absorbing species, D is the bulk diffusion coefficient, and K is the surface reorganization rate constant K reflects a surface reaction with units of cm s^{1} Hubbard et al speculate that K is the square root of the product of a surface diffusion constant, with units of cm^2 s^{1} and reorganization constant with units s^{-1} At the limit of large K^2/D values, the expression yields a stretched exponential with index ½

$$\Gamma(t) = \Gamma_m\left[1 - \exp\left(-\frac{2C_0}{\Gamma_m}\left(\frac{Dt}{\pi}\right)^{1/2}\right)\right] \quad (3\ 15)$$

At limits of small K^2/D values the approach to saturation is a simple exponential

$$\Gamma(t) = \Gamma_m\left[1 - \exp\left(\frac{KC_0 t}{\Gamma_m}\right)\right] \quad (3\ 16)$$

The stretched exponential is usually designated as diffusion dominated kinetics while the simple exponential is designated a regime dominated by thermodynamic or surface kinetic effects [27] The term, K designates an entire set of complex surface kinetic processes and as a result does not provide explicit information on the surface kinetics of the adsorbate However, it provides a useful guide to the process in that large values of K correspond to instantaneous surface kinetics Small values of K imply that bulk material is partially reflected or repelled by the active surface and that surface kinetic processes are slow relative to diffusion
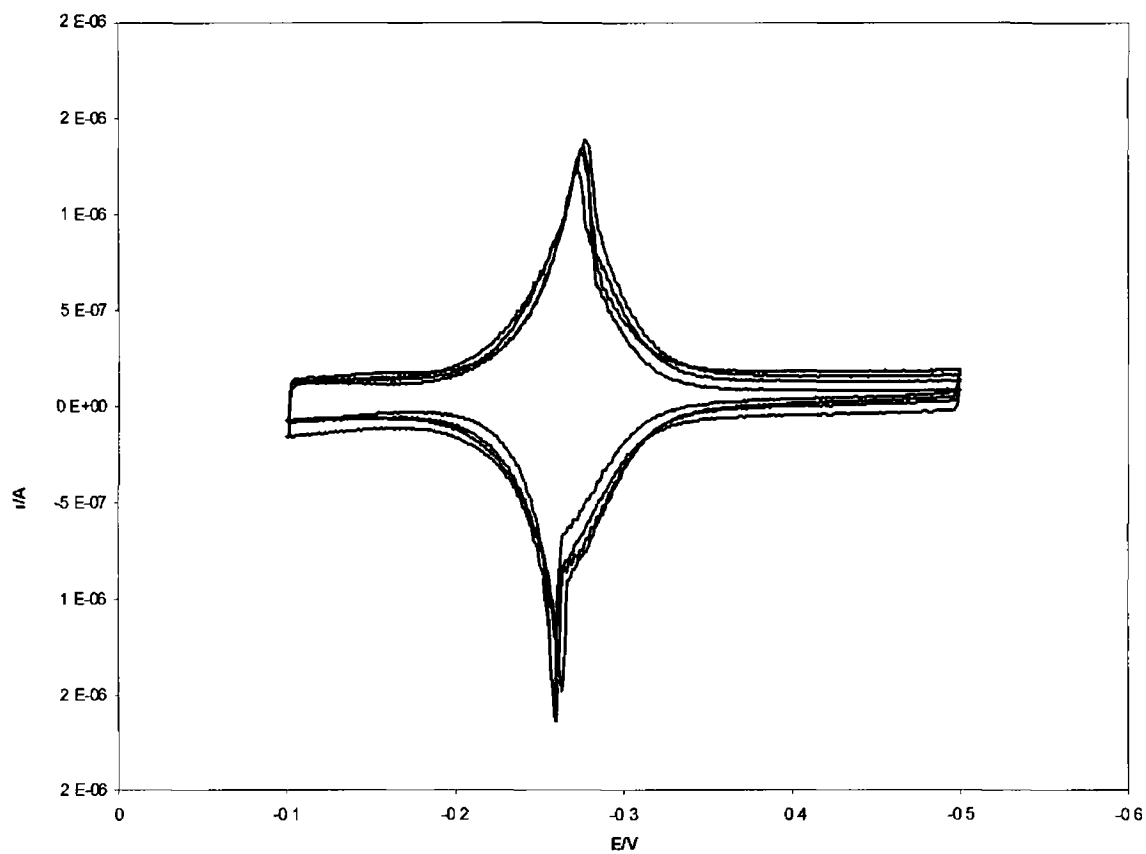
Figure 3 6 1 1 Cyclic voltammograms of bianthrone at different bulk concentrations at saturation surface coverage The supporting electrolyte was 1 M HClO₄ The concentrations are 0 09, 0 12, 0 20, 0 25, 0 30 μM

112

Adsorption data for Bianthrone on mercury was obtained for bulk solutions of concentration 0.09, 0.2 and 0.3 µM. Plots of surface coverage *versus* *time* were drawn and fits were made to the mathematical models described using the Microsoft Excel Solver programme. This programme allows the data to be fit to complex mathematical models based on the sum of squared residuals (SSR) between the experimental data and the data predicted by the model. Parameter values in the model are then varied according to an iterative search algorithm that seeks to minimize the error between the experimental data and the model.[28] The convergence criterion used in the solver program was 1×10^{-200}.

It was found that when applied to the total timescale of the experiment, the theoretical data generated from the diffusion and reorganization models did not provide satisfactory correlation. But it could be seen that at certain time ranges the experimental data did fit to the theoretical prediction. Figure 3.6.1.4 shows the adsorption data between 90 and 540 s compared with the theoretical diffusion model data. Within this timescale the data generated from the diffusion model compares favourably with the experimentally determined surface coverages. Figure 3.6.1.5 shows the experimentally determined surface coverage data with the theoretical data generated by the kinetic model in the range 1000 to 1800 s. Similar to the diffusion model favourable comparison can be made between the experimentally observed surface coverages and that generated by the surface reorganization kinetic model. For this reason, it was considered that adsorption was dominated by diffusion and reorganization parameters, depending on the timescale of the experiment. By separating the data and examining the adsorption process at the portions of the graphs where correlation was established with the respective models, it was possible to confirm the influence of the diffusion and surface reorganization processes at separate ranges of time and of surface coverage. Also, it allowed for the calculation of values for both K and D. It is important to note that the K value is representative of the combination of all unknown kinetic quantities and does not correspond to the specific nature of any surface reorganization process. Below is a table of values for K and for the diffusion coefficient, D, at the different bulk concentrations examined.

| Concentration (μM)	K (cms)	D ($cm^2 s^{-1}$)
0 09	9 31 x 10^{-7}	6 0 x 10^{11}
0 20	2 46 x 10^7	1 5 x 10^{12}
0 30	9 80 x 10^8	1 5 x 10^{-12}

It was found that, initially, adsorption of bianthrone to the mercury surface was dominated by diffusion of the molecule to the clean mercury surface As the surface coverage increases, diffusion becomes less influential to the adsorption of the molecule and the kinetic processes of surface reorganization become more dominant Scheme 3 2 illustrates this The best fits observed for these models were found with a bulk solution of 0 3 μM As adsorption proceeds surface reorganization also loses its influence, this could be seen in the fact that the experimental data begins to deviate from those predicted by the mathematical model It is believed that at this point the surface has become "crowded" and the molecules are now more closely packed Sufficiently packed so that interaction between molecules becomes a factor This can be seen in the decrease of the FWHM value This decreases from a near ideal value of 58 mV to a final value of 35 mV The value expected for a two-electron transfer is 45 3 mV according to Equation (3 2) The deviation from the expected value is an indication of destabilisation brought about by lateral interaction on the surface The surface coverage value at which the experimental data begins to deviate from the surface reorganization model was calculated to be 1 99 ± 0 25 x 10^{-11} molcm^{-2}

A

B

C
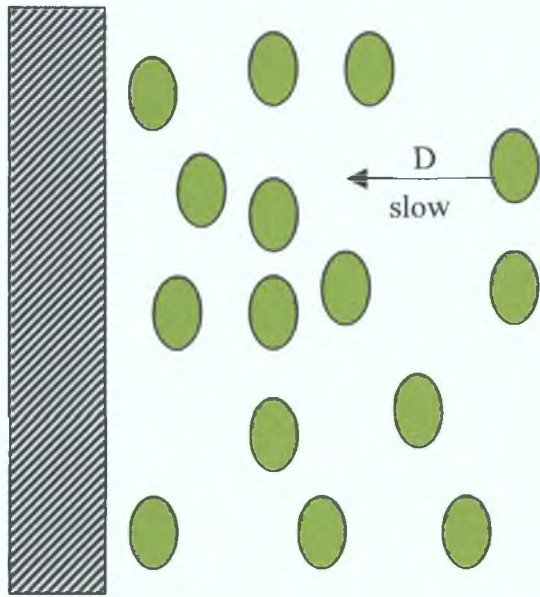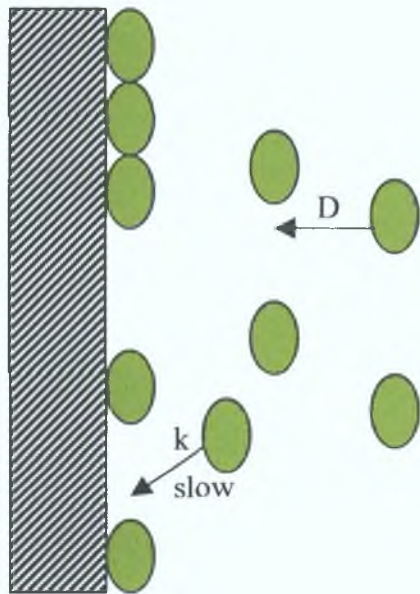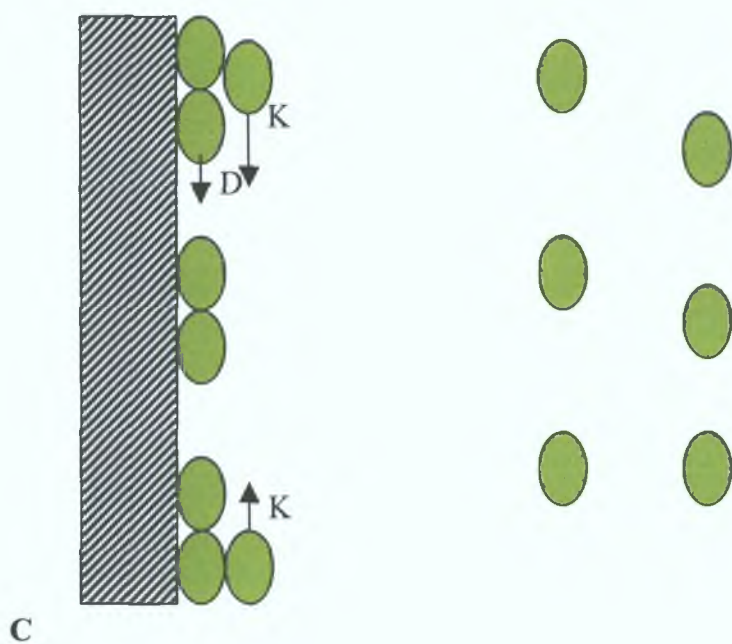
Scheme 3.2: The above scheme illustrates the formation of the bianthrone monolayer as a function of time. **A** *shows the initial stages of adsorption the bianthrone molecules ,* *, approach the surface. At this stage diffusion,* D, *of the molecule towards the surface is slow and the rate of adsorption is dominated by this diffusion.* **B** *shows the molecules begin to arrange themselves on the surface. Diffusion is less of an influence as the layer is depleted of molecules, reorganization at the surface, K, becomes limiting. As more molecules reach the surface and as the monolayer becomes more densely packed,* **C,** *surface reorganization is the limiting factor and is the larger influence on the rate of adsorption.*

From this value, it was possible to calculate the area of each molecule, from Equation (3 17)

$$\frac{1}{\Gamma N_A} = \frac{1}{moleculescm^{-2}} \quad (3\ 17)$$

Here, N_A is Avogadro's number   This provides a value of the molecular area in cm^2 molecule^{-1} It is convenient to convert this answer to $Å^2$molecule^{1} This provides a value of 834 $Å^2$

The molecules adsorbed at the surface are believed to be in the A conformation of bianthrone, i e with the outer rings of each system bent away from each other to relieve steric interaction brought about by the hydrogens in the 1 and 8 positions   With this in mind, it was possible to construct a molecular model for bianthrone using the Hyperchem programme   The Hyperchem programme allows for the construction of molecular models, providing the most energetically viable model of the molecule within parameters of structure and energy   The software produced a model corresponding to the A conformation of bianthrone   With this it was possible to calculate a value for the surface area of the molecule (denoted Van der Waal's area)   The value calculated by the programme was 365 $Å^2$

Figure 3.6.1.2 Plot of surface coverage versus time for a 0.3 μM solution of bianthrone (data points). The supporting electrolyte was 1.0 M HClO₄. The solid black line is the best fit from the kinetics model using the full data set. Error bars represent the standard deviation obtained from three separate measurements
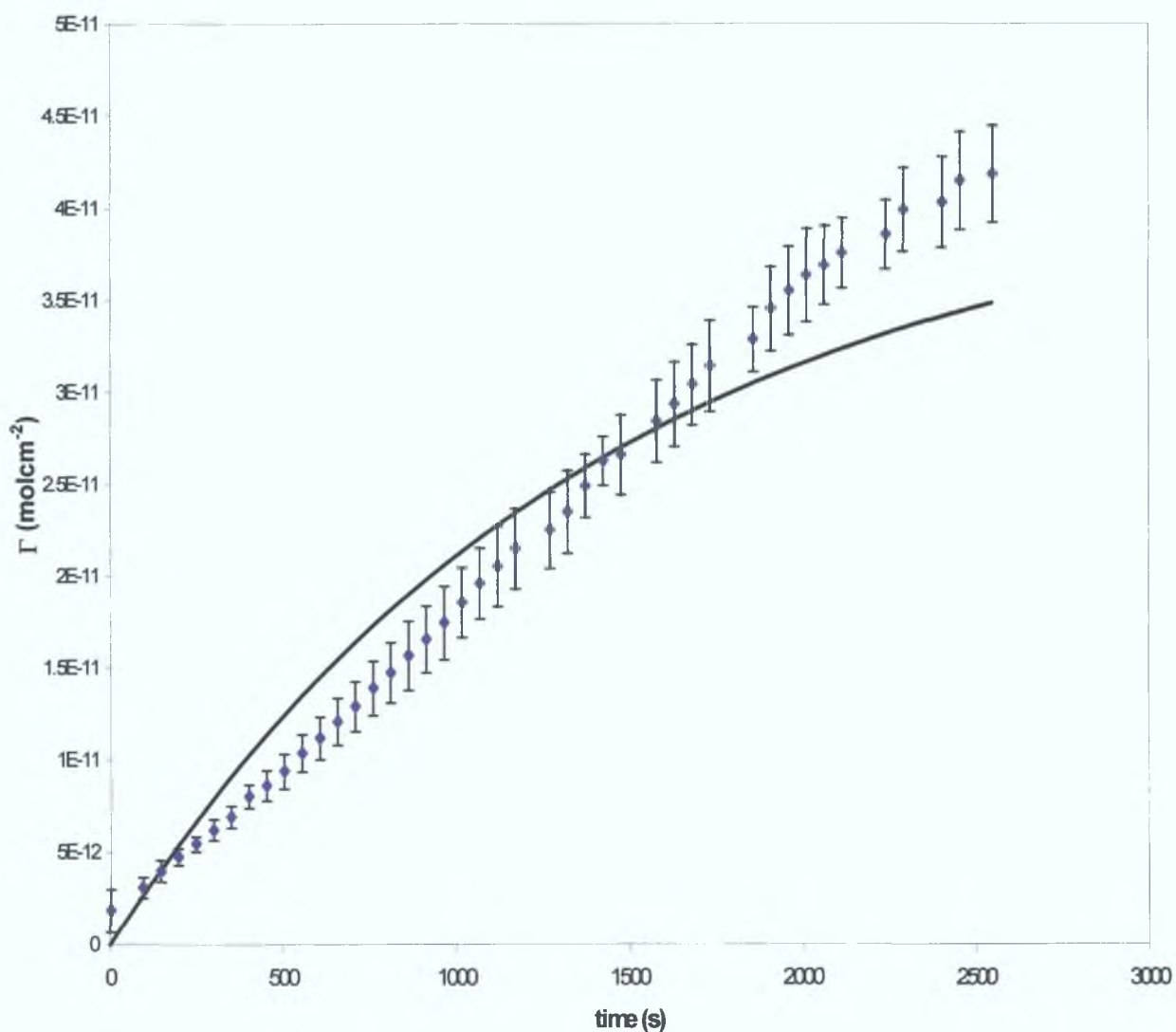
Figure 3.6.1.3 Plot of surface coverage vs. time for 0.3 μM bianthrone solution. The supporting electrolyte was 1.0 M HClO₄. The solid black line is the plot generated from the diffusion model. . Error bars represent the standard deviation obtained from three separate measurements

Figure 3 6 1 4 Plot of surface coverage vs time for 0 3 μM bianthrone solution, from 90 to 540 seconds overlaid with the plot generated from the diffusion model The blue data points represent the bianthrone data, the diffusion model is represented by the black line Error bars represent the standard deviation obtained from three separate measurements

120
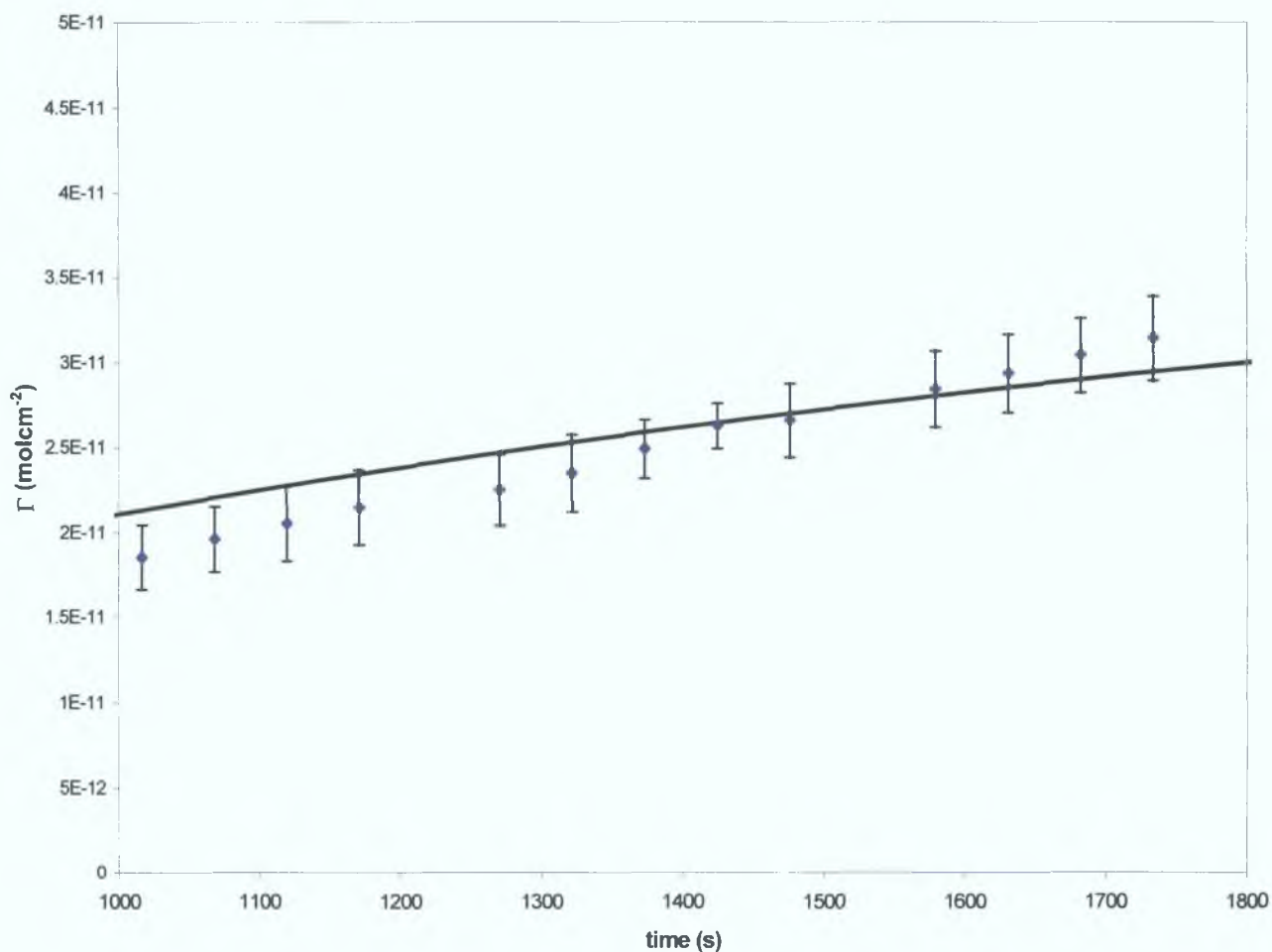
Figure 3.6.1.5 Plot of surface coverage vs. time for 0.3 µM bianthrone solution overlaid with the plot generated by the kinetics model. The blue data points represent the bianthrone data, while the kinetic data is represented by the black line. Error bars represent the standard deviation obtained from three separate measurements
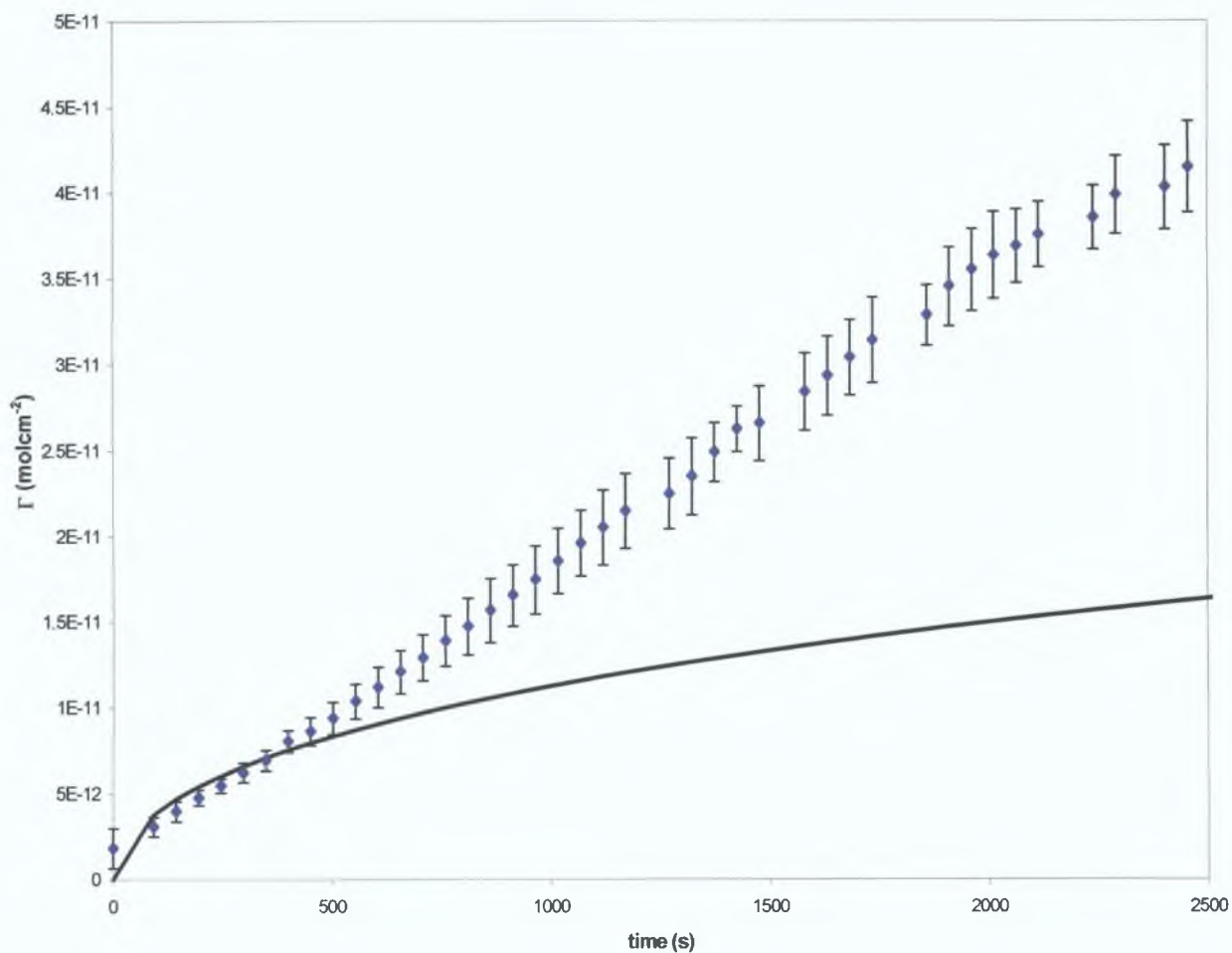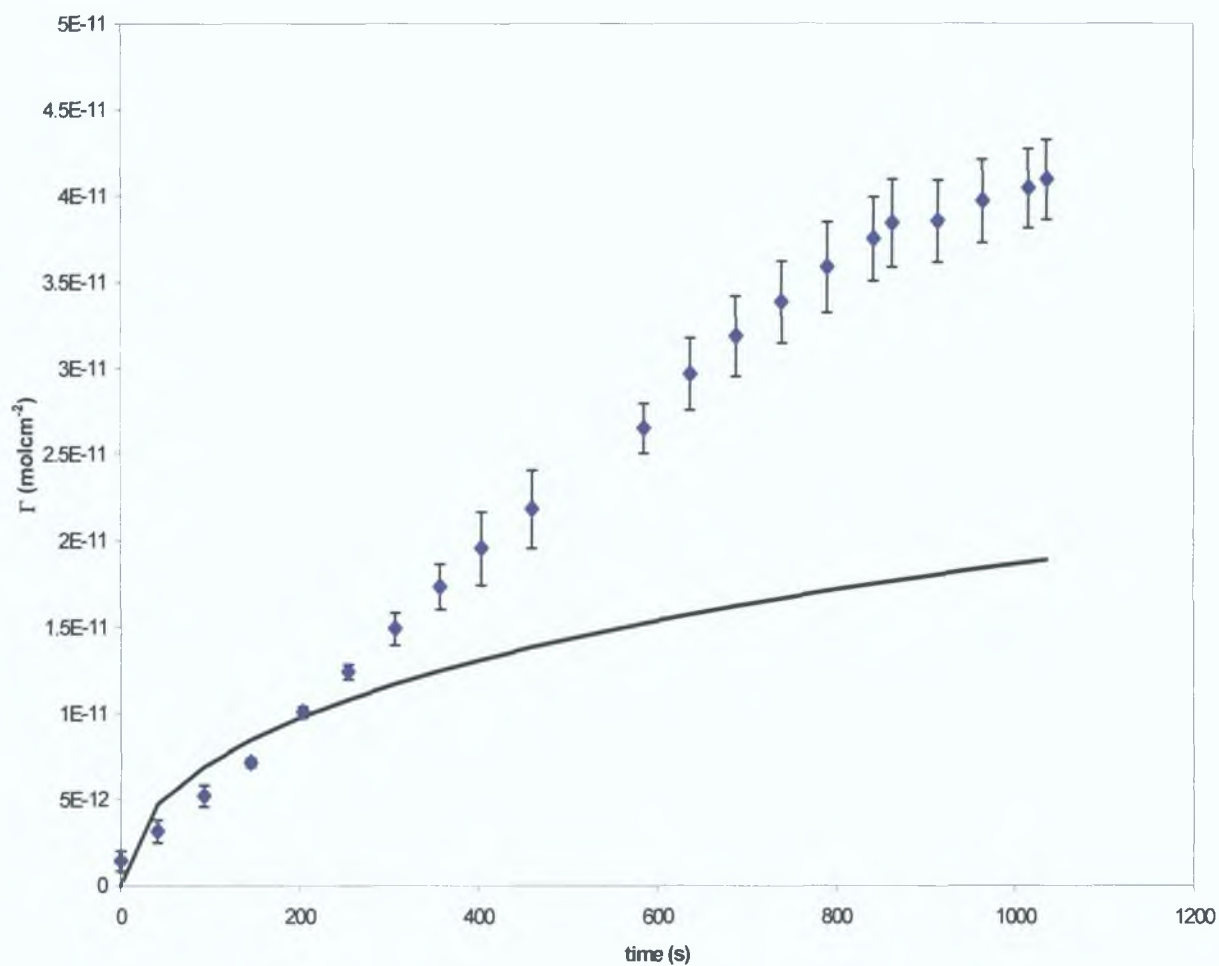
Figure 3.6.1.6 Plot of surface coverage vs. time for 0.09 μM bianthrone solution. The supporting electrolyte was 1.0 M HClO₄. The blue data points are the experimental data, the solid black line is the plot generated from the diffusion model. Error bars represent the standard deviation obtained from three separate measurements.
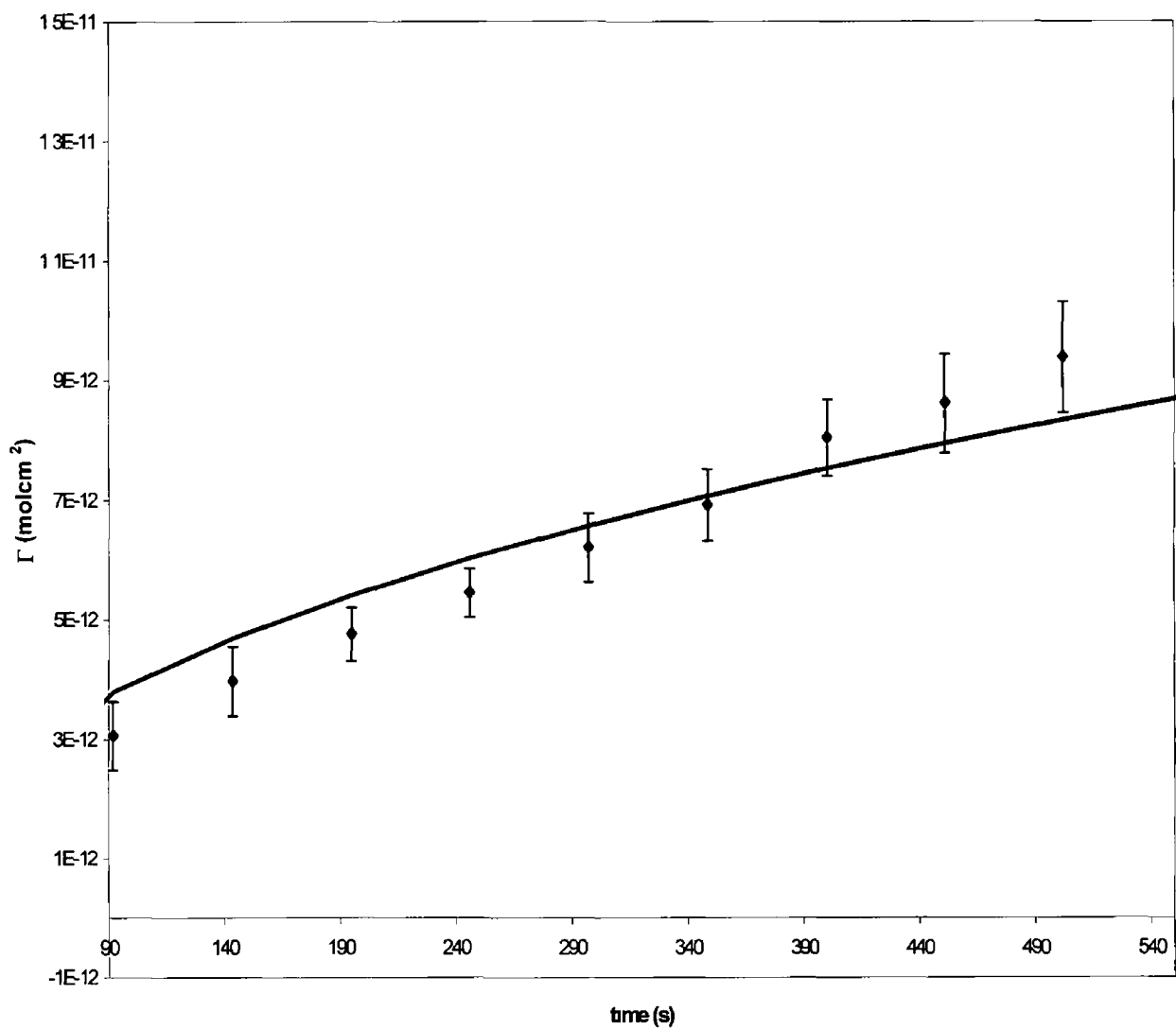
Figure 3 6 1 7 Plot of surface coverage versus time for a 0 09 µM solution of bianthrone (in black) The supporting electrolyte was 1 0 M $HClO_4$ The blue data points represent the experimental data and the solid black line is the best fit from the kinetics model Error bars represent the standard deviation obtained from three separate measurements

3 6 2 Desorption kinetics

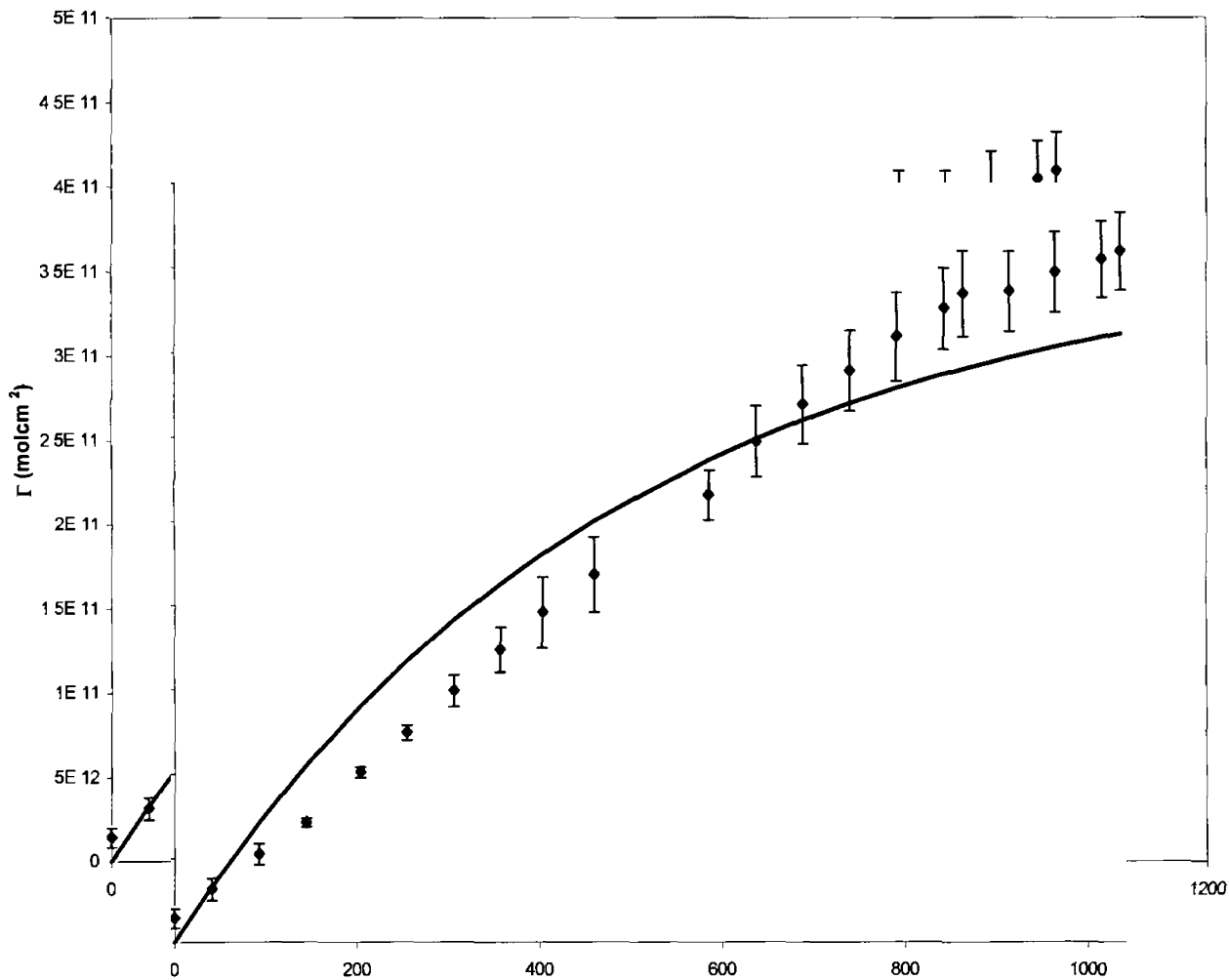Experiments were carried out to examine the desorption of a bianthrone monolayer and to determine a desorption rate constant   These experiments were done by immersing a hanging mercury drop electrode in a 0 15 μM bianthrone solution to allow a monolayer to form, then immersing the modified electrode into a blank solution (containing 90 10 DMF H_2O and 1 M $HClO_4$) and monitoring the desorption of the monolayer with respect to time by cyclic voltammetry   The fractional surface coverage of the monolayer versus time was then graphed and fit to a Diffusion controlled Langmuir model[29]

$$\theta(t) = \exp(-k_m \sqrt{t}) \quad (3\ 18)$$

where $\theta(t)$ is the fractional surface coverage of the monolayer, k_m is the rate constant and t is the time in seconds   From the graph, it can be seen that there is an initial rapid desorption of the monolayer followed by a more gradual desorption which is does not approach completion even after 8000s (approximately 130 minutes)   The model provides a good fit to the experimental desorption data   This can be seen in Figure 3 6 2 1   The experimental data is consistent with the model at short time scales   The model predicts long time scales for desorption to approach completion   However, from ca 440 to 4400 s the deviation from the model is notable   The rate constant of adsorption (or in this case desorption) is related to concentration according to Equation (3 19)

$$k_m = k_a c \quad (3\ 19)$$

where k_a is the rate constant and c is the concentration   It is important to note that θ does not decay to zero but remains constant at ca 45% coverage   In other words, there is no complete desorption of the monolayer   This is in disagreement with the Langmuir model that presumes that the rate of adsorption and the rate of desorption should be close to identical   The k_m value calculated from the Langmuir model was 1 x 10^2 $s^{1/2}$ This corresponds to a k_a value of 6666 7 $M^{-1}s^{-1/2}$ This value, when compared to values obtained by Subramanian et al for the adsorption rate constant of

124

alkanethiols (specifically C_8SH to $C_{18}SH$) on gold electrodes, appears to be significantly slower

Figure 3.6.2.1 Plot of the desorption of the bianthrone monolayer as a function of time. The bulk concentration of the bianthrone solution was 0.15 μM with 1 M HClO₄ as the supporting electrolyte. The black data points represent the experimental data, the red, the model.
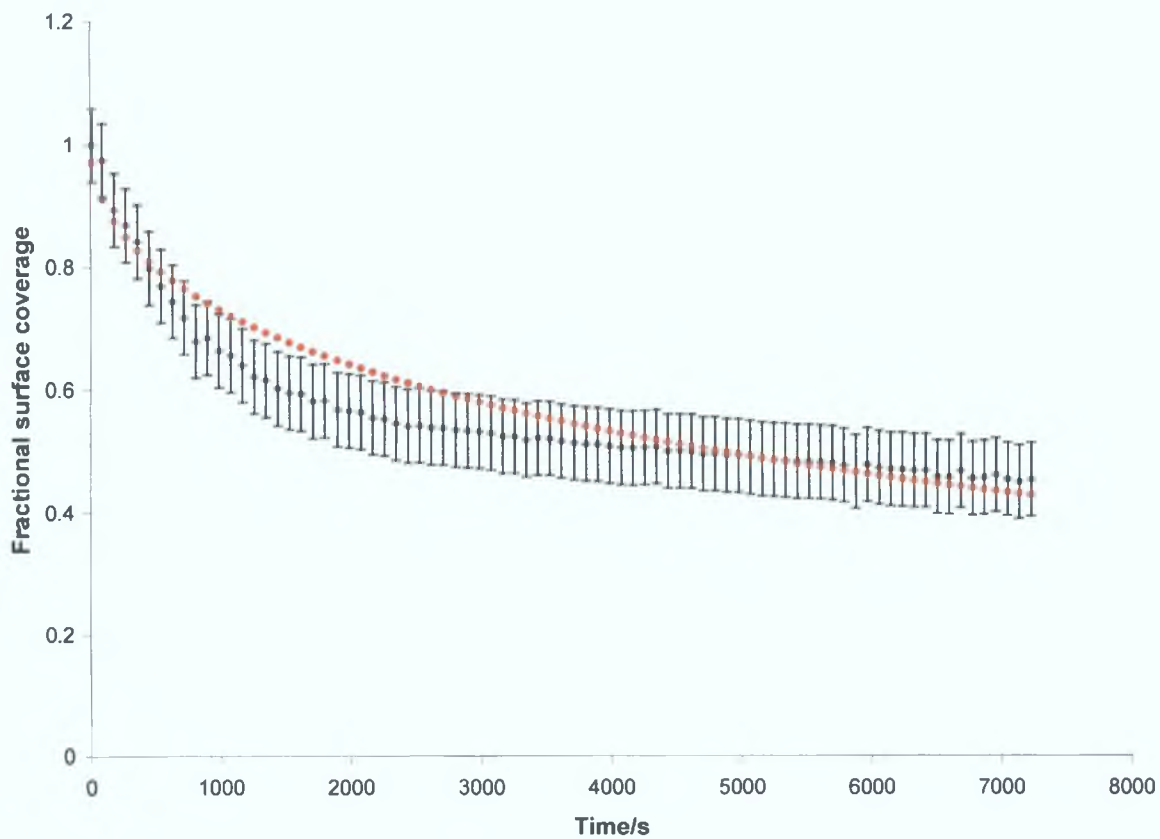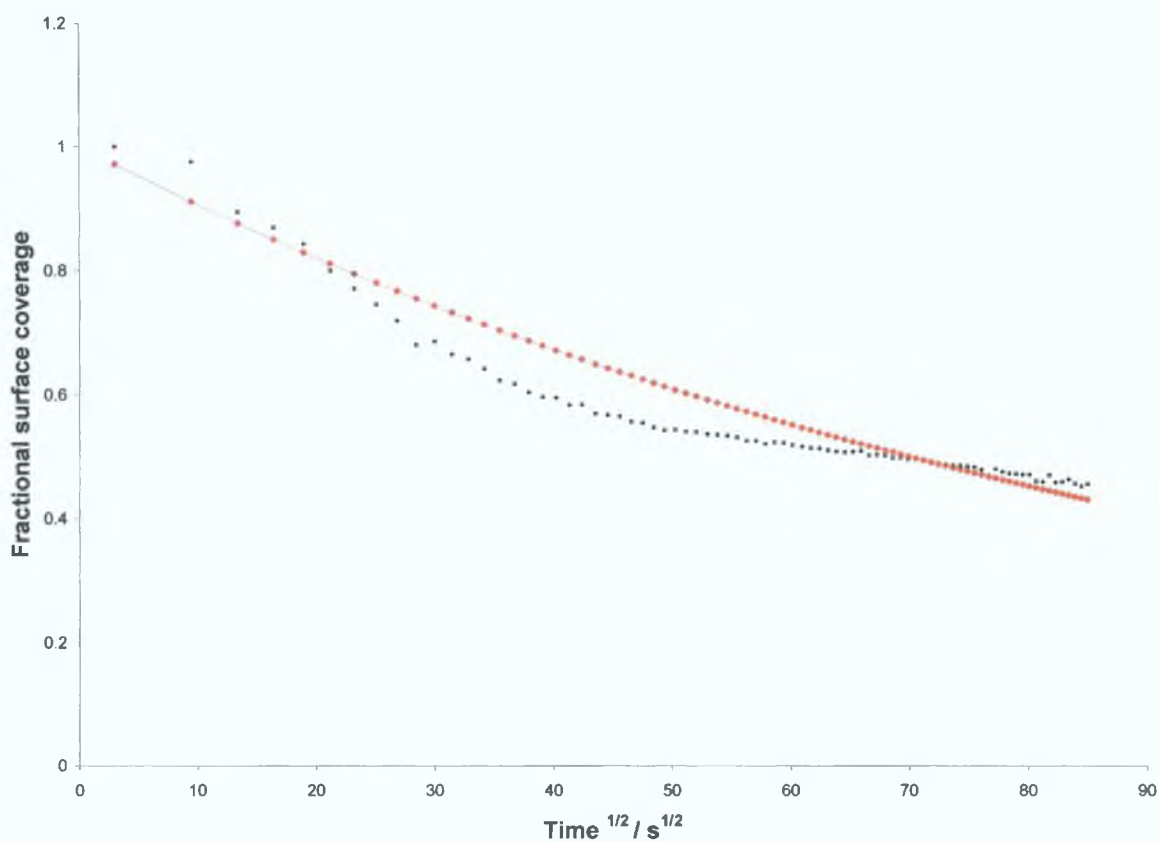
Figure 3.6.2.2 Plot of the desorption of the bianthrone monolayer as a function of the square root of time. The bulk concentration of the bianthrone solution was 0.15 μM and the supporting electrolyte was 1 M HClO₄

3.7 Raman spectra of bianthrone adsorbed on mercury electrodes:

3.7.1 Raman electrochemical cell

A novel electrochemical cell that can be used in conjunction with Raman spectroscopy has been constructed. This cell, constructed from Teflon, consists of a reservoir containing a mercury "pool" working electrode, a coiled platinum counter electrode surrounding the working electrode, and a reservoir linked to the main solution reservoir via a small channel to accommodate an Ag/AgCl –saturated KCl reference electrode. This cell allows for electrochemical measurements to be performed while also allowing a laser to be focussed on the mercury surface. Thus, it is possible to exploit Raman spectroscopy to monitor the surface characteristics of adsorbates. A schematic diagram of the cell can be seen in Figure 3.7.1.1.

Previously, gold, silver and platinum have been used most prominently as SERS substrates, due to their strong surface enhancement effects.[30][31] Mercury has not been exploited to the same extent due to less enhancement effects than the substrates mentioned. Blackwood and Pons relate this to the lack of p or d electrons available for back-bonding interactions.[32] However, there are some examples in the literature where mercury has been employed effectively and where enhancement has been observed. A study by Naaman et al on the adsorption of benzene, pyridine and cyclohexane adsorbed on a mercury drop electrode surface in the absence of voltage reports an enhancement of 10^4 to 10^6 compared to the same molecules in the gas phase or in solution.[33] The mercury drop was suspended in a Pyrex cell that could be filled with solution or gas and the laser was focussed on the drop from the bottom of the cell. However, these reported values were deemed questionable by Ozeki et al with respect to Naaman et al's method in the measurement of spatial size, where light was collected and also in the estimation of the number of contributing molecules. [34] Ford and Weber evaluated the SERS gain from mercury to be a factor of twenty. [35] This value was calculated from theoretical considerations using image enhancement effects and enhanced radiation effect due to near field excitation of surface roughness, which, in the case of liquid mercury corresponds to thermally excited ripplons. However, the development of new-generation Raman instruments that replace optic components with notch filters and incorporate microscopes with greater magnification

and also the application of CCD detectors allow for greater sensitivity with which to detect enhancement effects

Ozeki et al reported on the study of adsorption, condensation, orientation and reduction of quinoline molecules on a mercury electrode using Raman microprobe spectroscopy [34] The spectrochemical cell employed in their contribution was of similar design to that reported here and was fabricated from acryl resin Raman excitation was achieved from a 623 8 nm beam from a He-Ne laser with scattered light collected from the same IC50 objective lens (with 50 times objective magnification) The concentration of quinoline used was 20 mM In the application of combined Raman microprobe spectroscopy and electrochemical measurements the elucidation of surface morphology, molecular orientations, and blocking effects of the electrochemical reactions was achieved It was concluded that quinoline was not directly attached to the mercury surface, as there did not appear to be direct chemical interaction between the adsorbate and the mercury, but was a physisorption dictated by the electric field effects and the hydrophobicity of the quinoline molecule

In the experiments reported here, the intention is to employ the electrochemical cell (Figure 3 7 1 1) to carry out simultaneous electrochemical and Raman spectroscopic analysis of bianthrone monolayers adsorbed on a mercury electrode In doing this it is intended to examine if changes in potential on bianthrone monolayers adsorbed on the mercury electrode induce changes in the conformation of the bianthrone molecules as have been reported by Evans and others for bianthrone molecules in the solution phase [36 37 38 39 40]
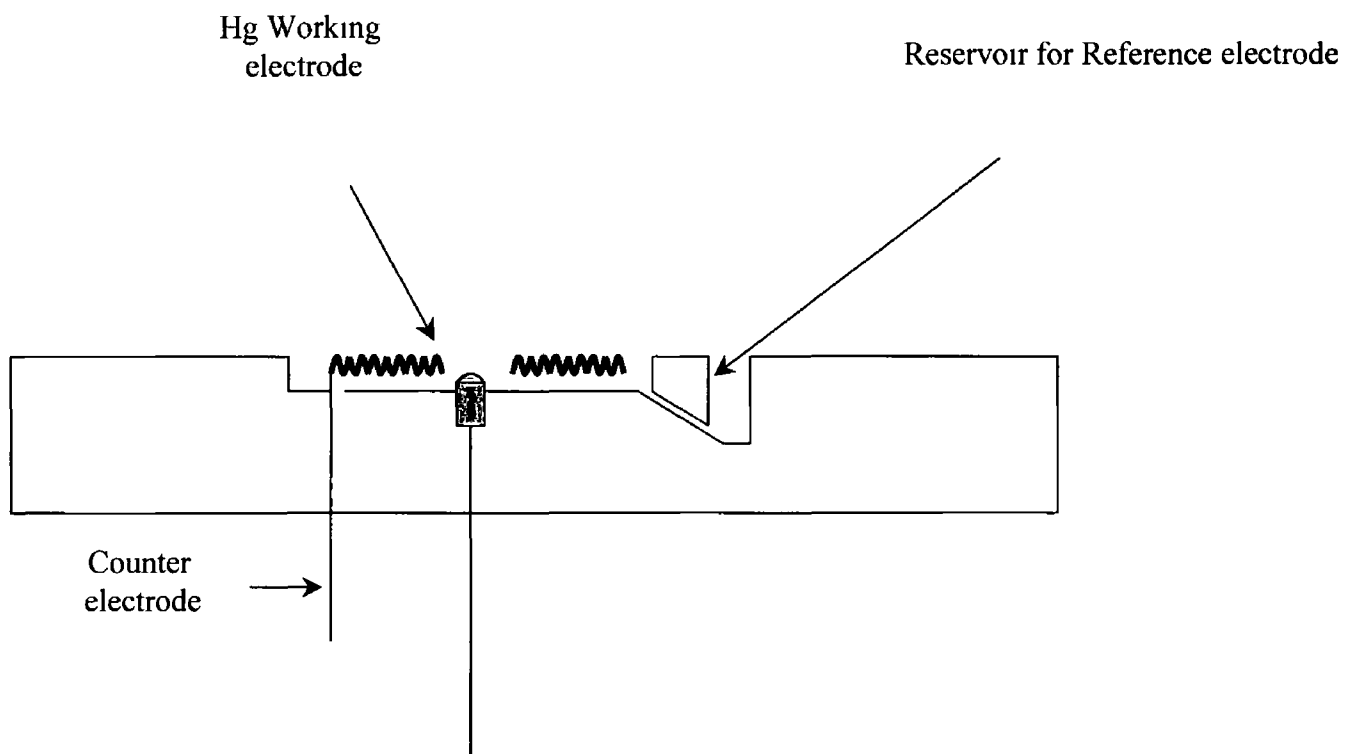
Hg Working
electrode

Reservoir for Reference electrode

Counter
electrode

Figure 3 7 1 1 Side-view schematic diagram of the mercury electrode Raman
cell

3 7 2 Electrochemical analysis

Cyclic voltammetry was employed to investigate the formation of a monolayer of bianthrone from a 100 μM solution in DMF with 1 M $HClO_4$ as the supporting electrolyte The scan rate used was 0 5 Vs^{-1} The cyclic voltammograms obtained were less ideal than those obtained using a conventional three-electrode cell with a HMDE electrode However, given that the aim of these experiments is to structurally characterise the bianthrone monolayers at the mercury surface, the voltammetry proved sufficient to confirm the presence of bianthrone on the mercury surface Namely, the peak potential was close to that previously recorded and current spikes were strongly evident These have previously been observed as the surface coverage of bianthrone approached that of a monolayer These spikes are characteristic of intermolecular interactions and are due to hydrogen bonding at the mercury surface This is sufficient evidence of adsorption of bianthrone on the mercury surface and indicates the redox potential of the adsorbed molecule

Based on the redox potential obtained from the voltammogram it was possible to carry out experiments in which the potential of the electrode was varied incrementally from –0 1 V to –0 4 V between which the redox couple of the molecule occurs This allowed Raman spectra to be obtained at various stages in the reduction of the surface bound molecules Constant potential was achieved by carrying out amperometric i-t curves Figure 3 7 2 2 illustrates an amperometric i-t curve at a potential of –0 1 V
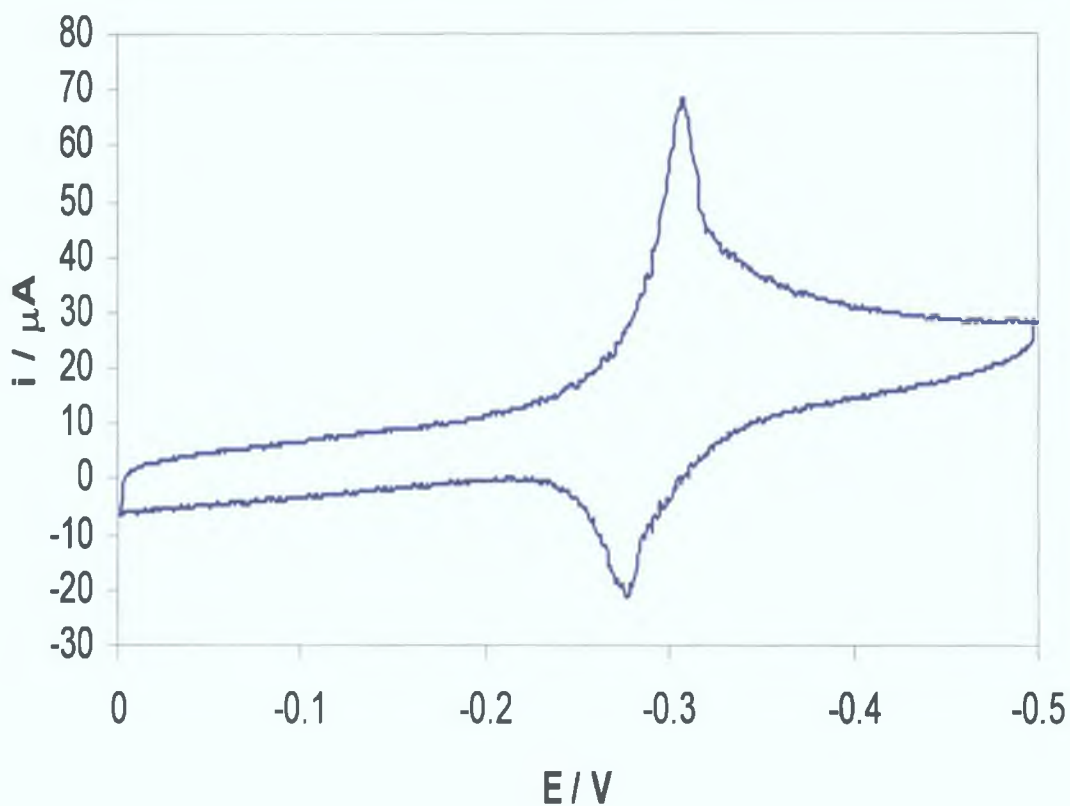
Figure 3.7.2.1 Cyclic voltammogram obtained using the mercury electrode Raman cell shown in Figure 3.7.1.1. The solution was a 100 µM bianthrone dissolved in DMF with 1 M HClO₄ as the supporting electrolyte. The reference electrode was an Ag/AgCl saturated KCl reference electrode.
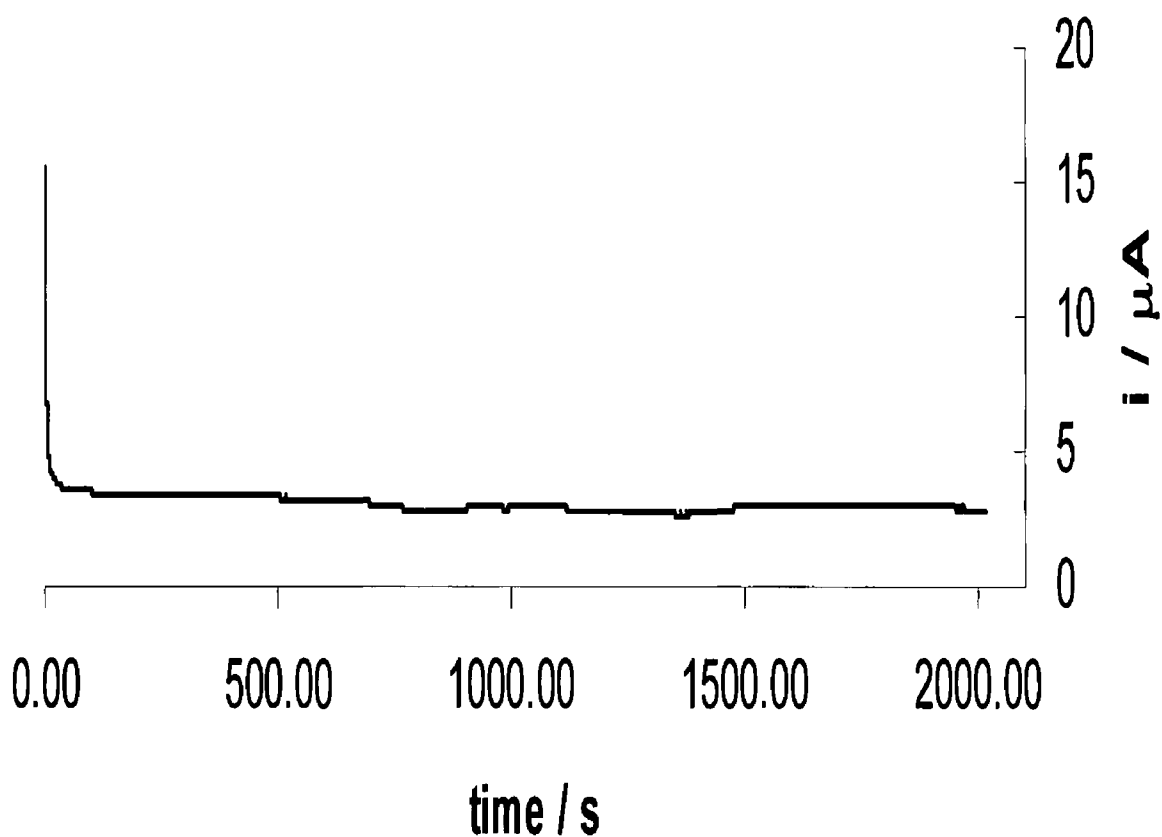
Figure 3 7 2 2 Amperometric i-t curve of a 100 μM bianthrone solution obtained using the mercury electrode cell shown in Figure 3 7 1 1 The potential was set to – 0 1 V

3 7 3 Raman spectroscopy of bianthrone monolayer

Raman spectra were recorded on a Horbia Jobin Yvon LabRAM HR 2000 spectrometer equipped with an integral confocal microscope 457 8 nm excitation line was employed from a water-cooled tuneable argon ion laser The scattered radiation was observed with 180^0 geometry with a cooled (-75 ^{0}C) charge-coupled device (CCD) detector The laser beam was focused through a 300 μm confocal hole onto a spot of 1μm in diameter with a long focal length objective of the order of 10X Data acquisition times were every 6 seconds with 20 accumulations The holographic grating (1800 grooves/mm) allowed resolution of 0 3 cm^{1} The instrument was calibrated using a silicon wafer of surface flatness ca 1μm order (520 cm^{1}) and accuracy was estimated to be less then 0 5 cm^{1} Laser power was about 23mW Further confirmation of the calibration was achieved by recording a spectrum of DMF and comparing it to the spectrum available from Sigma Aldrich

Figure 3 7 4 1 shows the Raman spectrum of a solid bianthrone sample This spectrum was obtained from a solid, powdered sample and the Raman stretches were assigned according to assignments from a paper by Ulicny et al , which was also obtained from bianthrone in the solid phase at room temperature [41] The spectra were obtained using an argon ion laser of wavelength of 457 8 nm to avail of post resonance effects

Prior to the spectroelectrochemical analysis of bianthrone monolayers, a Raman spectrum of solid bianthrone was carried out using an argon ion laser at a wavelength of 457 9 nm   This wavelength was chosen to avail of post resonance Raman effects based on uv-vis spectra taken of a bianthrone sample From this spectrum it was possible to assign features of the spectrum based on previous assignments from reports by Ulicny et al and Sanchez-Cortez et al [42] [43] These assignments are detailed in Table 3 1   It is important to note that, while the assignments of solid bianthrone made by Ulicny et al proved invaluable, there are certain bands in the spectra that were not assigned in their FT Raman analysis of bianthrone However, their work using neutron inelastic scattering, which provided a more detailed bianthrone spectrum, do share some bands with the spectrum of bianthrone adsorbed on the mercury electrode in the absence of potential and with

other spectra obtained. It may be possible that the Raman process involved in the experiments reported here utilises a more sensitive approach. However, given that the instrument model is not detailed in the paper, this cannot be shown conclusively. A spectrum of the adsorbed bianthrone on the electrode surface was recorded in the absence of an applied potential. Given that bianthrone was dissolved in DMF and that perchloric acid was present as the supporting electrolyte, it was necessary to obtain spectra of pure samples of these solutions so that solvent subtraction of the bianthrone spectra could be carried out. For solvent subtraction the vibrational modes 864 cm^{-1} for DMF and 927 cm^{-1} for perchloric acid were used as internal intensity standards.

This spectrum was quite weak, most likely owing to the proportion of bianthrone adsorbed on the mercury surface. However, the spectrum is comparable to the solid bianthrone with minor shifts, most likely due to surface binding. Comparison of the spectrum of the bianthrone monolayer adsorbed on the electrode surface in the absence of potential to the spectrum of solid bianthrone shows a small increase in intensity when the bianthrone is adsorbed on the surface. There is approximately a doubling of the overall intensity in the spectrum of the adsorbed bianthrone compared to the solid. Despite this increase in intensity, it should be noted that the monolayer spectra of bianthrone adsorbed on mercury suffer somewhat from poor signal to noise ratio, which makes identification of some bands, particularly those of intensities below approximately 50 a.u, difficult. The region between 200 and 300 cm^{-1} in the spectrum of bianthrone adsorbed on mercury in the absence of potential illustrates this problem. Where the spectrum of solid bianthrone is reasonably smooth, making bands appear distinct, the spectrum of the monolayer in the absence of potential is noisy making identification difficult. With the benefit of the assignments published by Ulicny et al it is still possible to identify, with some confidence, bands in the spectrum. Also this problem becomes less important in regions of the spectra where the intensities of the bands are above 50 a.u.

The spectrum of bianthrone adsorbed on mercury in the absence of an applied potential is comparable to that of the solid bianthrone sample. The first notable band observed is at 226 cm^{-1}, which is assigned to a CH wagging stretch. This band is of low intensity however, and another more intense peak is observed at 220 cm^{-1}, which corresponds to a stretch reported by Ulicny in spectra obtained by neutron inelastic

scattering The next band reported by Ulicny et al is at 296 cm^{-1} assigned to a CCC and CC stretch Again, in the adsorbed spectrum reported here, the intensity is low, but also, the peak is observed to be part of a "doublet" with the second peak being seen at 299 cm^{-1} The next peak is observed at 322 cm^{-1}, which is of reasonably strong intensity This has been assigned to CCC and CCO stretches by Ulicny et al A relatively intense band is observed at 371 cm^{-1} that has been assigned to CC, CH$_2$ scissoring and CCC stretches This band was observed at 374 cm^{-1} by Ulicny et al Another relatively strong band was observed at 386 cm^{-1}, which is not included in Ulicny's FT-Raman assignment, but is included in the NIS assignment for the same stretches as those at 374 cm^{-1} A broad band of relatively low intensity is observed at 406 cm^{-1} and coincides with Ulicny's assignment at 407 cm^{-1} for a torsional stretch A band at 435 cm^{-1} was observed that corresponds with CC, CCO and CCC stretches This band appears to be one of a group of peaks However, this may be symptomatic of baseline noise The next band of note is observed at 580 cm^{-1}, which corresponds to CCO and CCC stretching and was observed at 578 cm^{-1} by Ulicny et al A band at 678 cm^{-1} is observed, which corresponds to A CH wagging and a torsional stretch occurring in all rings in the molecule A relatively low band at 732 cm^{-1} is observed in the spectrum that is assigned to a CH wagging stretch, a CO wagging stretch and a torsional stretch Another band at 763 cm^{-1}, which appears at 762 cm^{-1} in Ulicny et al's assignment, is assigned to CH wagging and torsional stretches Another band of the same assignment and of similar intensity as that at 762 cm^{-1} appears at 788 cm^{-1} A single peak at 813 cm^{-1} is observed which is close to Ulicny et al's assignment at 816 cm^{-1} and is assigned to CO wagging, CH wagging and torsional stretches A band of high intensity is visible at 903 cm^{-1}, which Ulicny et al assigned, to CCC and torsional stretches However, this band is almost coincident with a band observed in the spectrum of perchloric acid The bianthrone monolayer spectrum was corrected for solvent but it is still difficult to ascertain whether this band is entirely due to bianthrone A relatively strong band is observed at 1042 cm^{-1}, which is close to Ulicny et al's assignment at 1040 cm^{-1} of CC and CCH stretching A band assigned to CC, CCH and CCC stretches is observed at 1089 cm^{-1} Bands assigned to CCH and CC stretches are visible at 1148, 1170, 1213, 1278 cm^{-1} and also at 1458 cm^{-1} A relatively strong band at 1318 cm^{-1} is assigned to CC, CCO, and CH$_2$ A notably strong band is visible at 1352 cm^{-1} Ulicny assigned a band at 1333 cm^{-1} to CC, CCO and CCH stretches However, in all spectra of bianthrone in this thesis a distinct band

is visible at ca 1353 cm^{1} It is proposed that this band is due to the same stretches A broad envelope of bands is visible between approximately 1490 and 1660 cm^{-1}, which is typical of all bianthrone spectra presented in this thesis Included in this envelope of bands is one at 1596 cm^{1} which is assigned to CC stretches and which also may provide information on C=O stretches The other prominent bands in this group are not explicitly assigned by Ulicny et al However, in their NIR Raman study of bianthrone adsorbed on colloidal silver, Sanchez-Cortez et al reported that a band at 1595 cm^{-1} split into two bands at 1578 cm^{-1} and 1607 cm^{-1} This splitting was noted when bianthrone was adsorbed onto colloidal silver In the spectrum of bianthrone adsorbed on the mercury electrode surface bands at 1579 cm^{-1} and

1612 cm^{1} are observed It is proposed that these are the bands reported in both works Finally, a strong band is visible at 1672 cm^{-1} This band corresponds to a C=O stretch, which has been reported at 1668 cm^{1} by Ulicny et al and at 1671 cm^{1} by Sanchez Cortez et al

3 7 4 Effect of Varying Potential on Raman spectra

Using the voltammetry of bianthrone adsorbed on the mercury electrode as a guide, the voltage of the electrode was held at incrementally more negative potentials between –0 1 V and –0 4V as spectra were taken A cyclic voltammogram of the bianthrone monolayer can be seen in Figure 3 7 2 1 The voltage was held using amperometric i-t curves, an example of which can be seen in Figure 3 7 2 2 and the spectra were taken when the current became reasonably constant These spectra can be seen in Figure 3 7 4 2

The spectrum of the bianthrone monolayer at –0 1 V, while being generally of slightly less intensity, displayed many common characteristics with that of the monolayer in the absence of an applied potential This would be expected as bianthrone is in its oxidised form in both cases However, some differences were observed between the two spectra A band is observed at 225 cm^{-1} that corresponds to CCC and CC stretches, albeit at low intensity is observed in the –0 1 V spectrum that is not apparent in the spectrum recorded in the absence of potential A relatively intense band is observed at 381 cm^{-1} observed in the spectrum at –0 1 V, assigned to CC, CCC stretches and CH_2 scissoring, is not readily observed in the absence of potential An intensity increase is observed in the band observed at 818 cm^{-1} in the –0 1 V spectrum compared to the spectrum in the absence of potential This band was assigned to CO wagging CH wagging An increase in intensity is also observed in the –0 1 V spectrum at 1258 cm^{-1} A broad peak is observed in this spectrum, which is present as a narrower, less intense peak in the spectrum in the absence of potential This band is assigned to CCH and CC stretches A slight decrease in intensity is observed in the –0 1 V spectrum compared to that in the absence of potential This band, which appears in all spectra recorded for this thesis, is proposed to correspond to CC CCO and CCH stretches The intensity of the group of bands between 1550 and 1650 cm^{-1} is a slightly decreased at –0 1 V The three main peaks at 1579, 1596, and 1612 cm^{-1} are still visible at the same wavenumbers However, the peak at 1596 cm^{-1} displays a decrease in relative intensity compared to the bands at 1579 and 1612 cm^{-1} The peak assigned to C=O stretches is seen to decrease from a distinct band in the absence of potential to a band of lower intensity at –0 1 V

From the spectra in Figure 3 7 4 2, it can be seen that on going from –0 1 V to –0 2 V, some changes to the spectrum were observed The first example of this is

seen at ca 380 cm^{-1}, which shows a notable increase from the –0 1 V spectrum This band is assigned to CC stretching, CCC stretching and CH$_2$ scissoring A decrease in intensity is observed at 816 cm^{-1}, on going from –0 1 V to –0 2 V This is assigned to CO wagging, CH wagging, and torsional stretching The region between 860 cm^{-1} and 960 cm^{-1} was corrected for solvent as the solvent spectrum contains a group of peaks in this region As a result assignment in this region is somewhat unreliable at very low intensities as there may still be bands associated with the solvent present A notable difference between the two spectra is observed at –0 1 V in the region between ca 1170 and 1300 cm^{-1} with a broad, relatively intense band is present This band is absent at –0 2 V No change is observed at 1353 cm^{-1} between –0 1 and –0 2 V The group of bands between 1550 and 1650 cm^{-1} is seen to decrease in intensity on going from –0 1V and –0 2 V however the band at 1611 cm^{-1} is seen to increase relative to the other two bands in he group The band at 1670 cm^{-1} is seen not to change

Few differences are observed on going from –0 2 V to –0 25 V One of these differences is the presence of a broad band that peaks at ca 1020 cm^{-1} in the spectrum taken at –0 2 V that is not observed in the spectrum taken at –0 25 V The most notable difference, however, that is observed involves the three bands 1578, 1596 and 1611 cm^{-1} This group of bands displays a decrease in intensity at –0 25 V but the band at 1611 cm^{-1} displays an increase in intensity relative to the other two bands The band at 1671 cm^{-1} assigned to C=O is less prominent at –0 25 V than at –0 2 V

The spectrum taken at –0 3 V shows few differences from that at –0 25 V However, as with the changes between –0 2 and –0 25 V, the only prominent difference observed occurs in the group of bands between 1550 and 1650 cm^{-1} Here, the band observed at 1596 cm^{-1} displayed a marked decrease, appearing as a shoulder, while the band at 1611 cm^{-1} increases in relative intensity The band at 1578 cm^{-1} meanwhile, remained relatively unchanged The band observed at ca 1351 cm^{-1} also displayed a small increase

Analysis of the spectra for –0 4 and –0 45 V was difficult due to noise and, subsequently, lack of resolution An example of this lack of resolution can be seen in the spectrum at –0 4 V The characteristic bands at 1578 1596 and 1611 cm^{-1} are indistinct due to noise

Raman band (cm^{-1})	Assignment
225	CH wagg (I, II) τ (I, II, III)
325	CCC (I, II, III), CCO
435	CC (II), CCO, CCC (I, III, III)
589	CCO, CCC (I, II, III)
643	CCC (I, II, III), CCO
761	CH wagg (I, II) τ (I, II, III)
919	CCC (I, II, III), CC (I, II, III)
1023	CC (I, III), CCH (I, III)
1073	
1156	
1215	CCH (I, III), CC (I, II, III)
1278	CCH (I, III), CC (I, III)
1350	CC (I, II III), CCO, CCH (I, III)
1437	CCH (I, III), CC (I, II, III)
1519	
1585	
1596	CC (I, III), C=O str
1612	
1651	
1670	C=O

Table 3 1 Raman assignments based on spectra of a solid sample of bianthrone taken at room temperature   These assignments were obtained from reference 40 by Ulicny et al
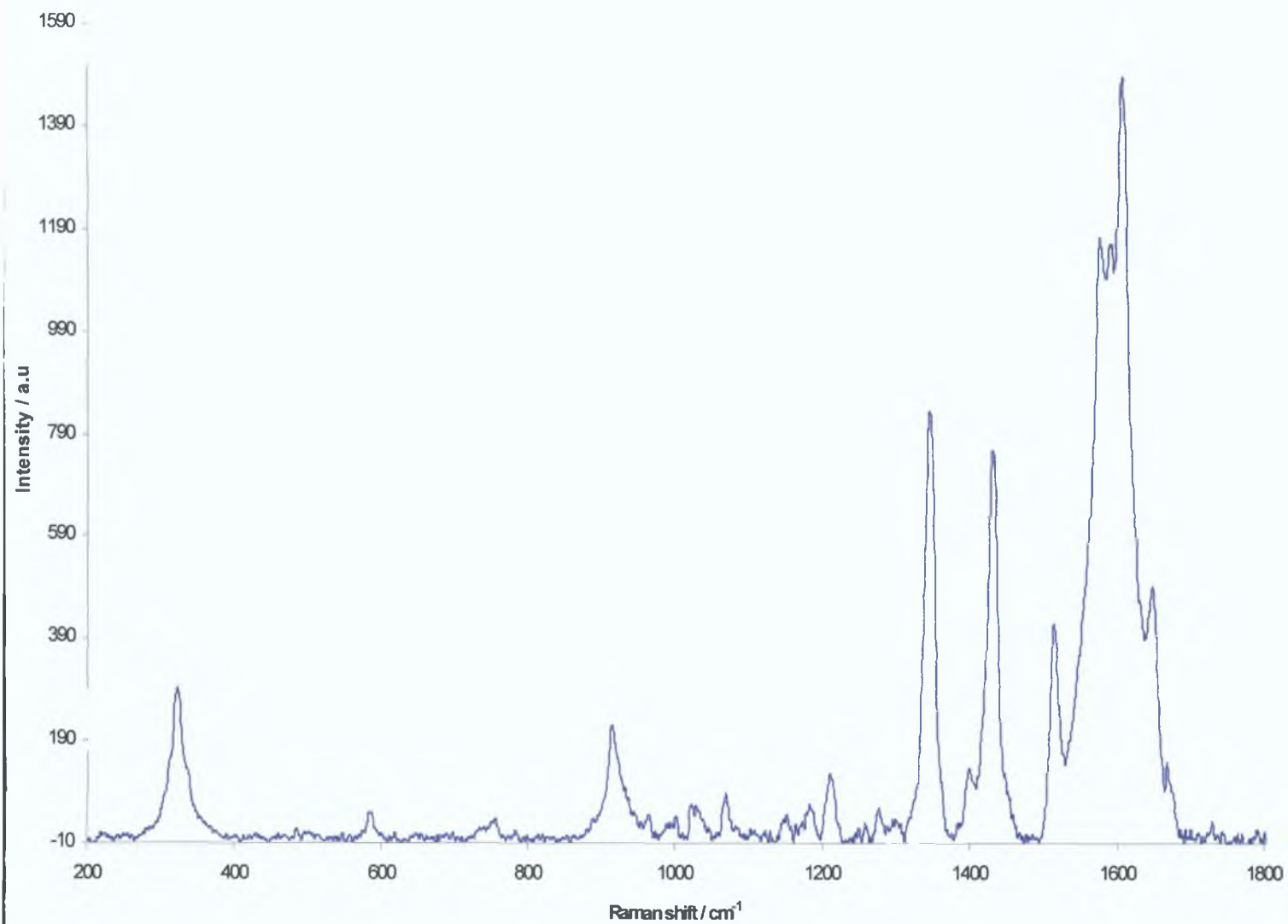
Figure 3.7.4.1 Raman spectrum of solid bianthrone. Excitation was obtained using a 457.8 nm argon ion laser.
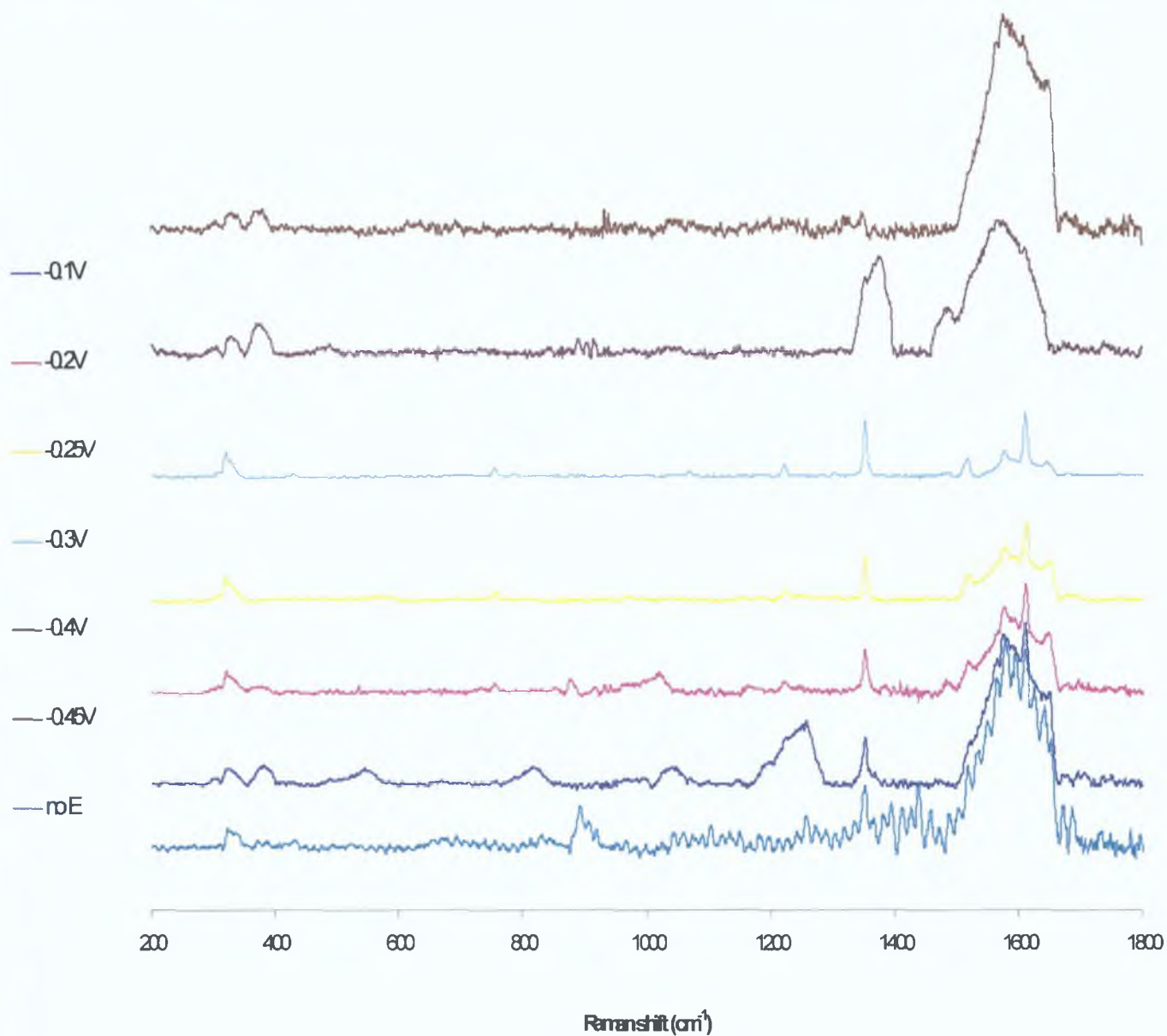
Figure 3.7.4.2 Raman spectra recorded at various potentials from –0.1 V to –0.45 V using the mercury electrode cell shown in Figure 3.7.1.1. An argon ion laser set to 457.8 nm provided Raman excitation. The spectra have been offset for clarity.

Overall, these experiments can be considered successful   Raman spectra of solid bianthrone compared favourably with those quoted in the literature, confirming both the presence of bianthrone as well as the suitability of the instrumental Raman parameters employed   The Raman spectra of the monolayers in turn compared favourably with that of the solid bianthrone spectra confirming the presence of bianthrone adsorbed on the liquid mercury surface   Furthermore, the bulk concentration of the bianthrone solution employed here, 100 μM, is lower than other concentrations that have been quoted in the literature   The cyclic voltammetry obtained using the electrochemical cell compared favourably with that obtained with a conventional electrochemical cell   This was displayed by the similarity in redox potential observed and also in the presence of current spikes, which were extensively observed in bianthrone voltammetry with a conventional cell   These current spikes are due to intermolecular interactions in adsorbed monolayers, a more extensive explanation of the current spikes can be found early on in this chapter   All of these observations confirm the suitability of the electrochemical cell for the purposes for which it was employed in these experiments, and suggest the feasibility of the use of this cell in combined electrochemical and spectroscopic analysis of other compounds

References

1 Laviron, E , *J Electroanal Chem* , *12, 53, 1982*

2 Laviron, E , *J Electroanal Chem,52, 395, 1974*

3 Bard, A J , Faulkner, L R , *Electrochemical Methods Fundamentals and Applications,* John Wiley and Sons Inc **1980**

4 Brown, A P , Anson, F C , *Anal Chem , 49 158, 1977*

5 Faulkner, L R , Forster, R J , *Anal Chem, 67, 1232-1239 1995*

6 Forster, R J , *Langmuir, 11, 2247-2255, 1995*

7 Brett, C M A , Brett, A M O , *Electroanalysis, Oxford Science Publications*

8 Forster, R J , *Anal Chem , 68 3143-3150, 1996*

9 Wopschall, R H , Shain, I , *Anal Chem 39, 1514, 1967*

10 Forster, R J , O Hanlon, D , *Langmuir, 16, 2, 2000*

11 Evans, D H , Xie, N *J Am Chem Soc Vol 105, 315, 1983*

12 Chen, X , Zhuang, J , He, P , *J Electroanal Chem , 271, 257, 1989*

13 He, P , Crooks, M , Faulkner, L R , *J Phys Chem, 94, 1135-1141, 1990*

14 Zhang, J , Anson, F , *J Electroanal Chem 331, 945-957, 1992*

15 Ta, C T , Kanda, V , McDermott, M T , *J Phys Chem B, 103, 1295-1302, 1999*

16 Coverage and Time dependent superstructures in adsorbed monolayers of 1,5-Dimethoxy-Anthraquinone-Farrell, M , Forster, R J , in press

17 Bard, A J , Faulkner, L R , *Electrochemical Methods Fundamentals and Applications* Wiley, New York **1980**

18 Smith, C P , White, H S , *Anal Chem , 64, 2398-2405, 1992*

19 Laviron, E , *J Electroanal Chem , 101, 19-28, 1979*

20 Chen, S , *J Phys Chem B, 104, 4, 2000*

21 Sawyer, D T , Sobkowiak, A , Roberts, J L , *Electrochemistry for Chemists, 2nd Ed,1995, John Wiley & Sons, Inc*

22 Atkins, P W , *Physical Chemistry, Oxford University Press, 1994*

23 Forster, R J , O Kelly, J P , *Analyst, 123, 1987-1993, 1998*

24 Keyes, T , Forster, R J , Farrell, M , O Hanlon, D , *Langmuir, 16, 25, 9871-9877, 2000*

25 Komura, T , Isogai, S , Yamaguchi, K , Takahashi, K , *J Electroanal Chem , 490, 70-78, 2000*

26 Hubbard, J B , Silin, V , Plant, A L , *Biophys Chem , 75, 163-176,1998*

27 Douglas, J F , Frantz, P , Johnson, H E , Schneider, H , Granick, S , *Colloids Surf A , 86, 251-254*

28 Diamond, D , Hanratty, V C A , *Spreadsheet Applications in Chemistry using Microsoft Excel, John Wiley and Sons Inc 1997*

29 Subramanian, R Lakshminarayanan, V , *Electrochimica Acta, 45, 4501-4509, 2000*

30 Nishiyama, K , Tahara, S , Uchida, Y , Tanoue, S , Taniguchi, I , *J Electroanal Chem , 478, 83-91, 1999*

31 Ramakrishnan, V , Krishnamurthy, N , *Spectrochimica Acta, 46A, 11, 1615-1619, 1990*

32

33 Naaman, R , Buelow, S J , Herschbach, D R , *J Phys Chem 84, 2692-2694, 1980*

34 Ozeki, T , Odziemkowski, M , Irish, D E , *J Sol Chem 29, 10, 2000*

35 Evans, D H , Xie, N *J Am Chem Soc Vol 105, 315, 1983*

35 Hammerich, O , Parker, V D *Acta Chem Scand B35, 395, 1981*

36 Anders, J , Byrne, H J , Reichenbach, J , Kaiser, M , Schmelzer, M , Wagner, Th , Roth, S *Ber Bunsenges Phys Chem , Vol 97, No 3 1993*

37 Olsen, B A , Evans, D H *J Am Chem Soc , Vol 103,No 4, 1981*

38 Neta, P , Evans, D H *J Am Chem Soc , Vol 103, No 24, 1981*

39 Matsue, T , Evans D H *J Electroanal Chem , Vol 168 287-298 1984*

40 Matsue, T , Evans D H *J Electroanal Chem Vol , 163137-1431984*

41 J Ulicny, M Ghomi, H Jobic, P Miskovsky, A Aamouche *J Mol Structure, 410-411, 497-501 1997*

42 Sanchez-Cortez, S , Jancura, D , Miskovsky, B , Bertoluzza, A , *Spectrochimica Acta A, 53, 769-779, 1997*

43 Ulicny, J , Ghomi, M , Jobic, H , Miskovsky, P , Aamouche, A , *J Mol Struct , 410-411, 497-501, 1997*

4.0 Analysis of Bianthrone Monolayers on Glassy Carbon Electrodes

A child of five would understand this Send someone to fetch a child of five

Groucho Marx

4.1 Glassy Carbon electrodes

Solid electrodes based on carbon have widespread applicability in electroanalysis. This applicability is due to their broad potential window, in both aqueous and organic media, low background current, rich surface chemistry, chemical inertness and low cost.[1] In addition, their compatibility with a wide variety of electrolytes makes carbon electrodes attractive alternatives to metals in electroanalytical applications. Carbon materials have a basic structure of six-membered aromatic rings with sp^2 bonding, however they differ in the relative density of edge and basal planes at their surfaces, the edge plane being more reactive than the basal plane towards adsorption and electron transfer. The reason for this is that the electrochemistry of edge and basal plane graphite are markedly different. The edge plane exhibits much faster electrode kinetics than the basal plane. This means an electrode consisting entirely of edge plane will show nearly reversible voltammetry while an entirely basal plane electrode surface will exhibit irreversible voltammetry, reversibility being dependent on the amount of edge sites on the surface.[2] Of the carbon electrodes available, glassy carbon (GC) is popular due to its mechanical and electrical properties and reproducible performance. GC structure consists of thin tangled ribbons of cross-linked graphite-like sheets. [3]

Various pre-treatment regimes exist for GC electrodes. These include heat treatment,[4] electrochemical treatment,[5,6,7] laser activation,[8] and mechanical polishing.[9] [10] [11, 12, 13, 14]. It is also not uncommon that more than one pre-treatment regime be carried out prior to electrochemical analysis.[15] Pre-treatment is necessary to ensure a clean active substrate without surface contaminants so as to ensure reproducibility of electrochemical response. The most common technique being mechanical polishing with slurry made up of alumina particles until a mirror-like appearance is achieved followed by sonication in ultra pure water to ensure removal of any residual slurry particles. A particular objective of pre-treatment is to improve electron transfer reactivity. This improvement is attributed to the removal of surface contaminants,

exposure of fresh carbon edges and an increase in the density of surface oxygen groups.

In comparisons with mercury electrodes, some differences exist. Apparent among these differences is the nature of the electrode material. One of the ways that the nature of the electrode material can influence differences in electrode response is in the density of states. It has been seen that the response of an adsorbed species can differ when adsorbed on different electrode materials. For example, the Marcus and Gosavi model predicts a ratio of electron transfer rate constants, k^0_{Pt}/k^0_{Au} of 1.8 on going from platinum to gold.[16] However, in the case of glassy carbon it is important to note that the electrode is made up of ribbon like carbon structures with a wide variety of local densities of acceptor donor states. Electrode history and pretreatment regimes can influence these local densities. Another difference that arises between mercury and glassy carbon electrodes is surface roughness. Mercury, as employed in hanging mercury drop electrodes, is a liquid metal and as such is considered to be perfectly smooth. In contrast, the surface of a glassy carbon electrode, as already discussed is made up of different sites e.g. edge sites, basal plane sites. Therefore, a mercury electrode's active area is considered to be the same as its geometric area. This is not the case with solid electrodes such as glassy carbon and thus electrode pretreatment is necessary to ensure reproducibility of response. Further, other surface groups have been seen to reside on the surface of a glassy carbon electrode. Such surface groups include carbonyl groups and other oxygen functionalities.

To study the correlation of heterogeneous electron-transfer kinetics with surface properties of GC electrodes McCreery et al employed Raman spectra, phenanthraquinone adsorption, capacitance and electron transfer analysis of ferri/ferrocyanide dopamine and ascorbic acid. [1] This analysis was done on GC electrodes following fracturing, polishing and laser activation. They observed that polishing caused minor changes in carbon disorder and microscopic surface area but that the electron-transfer kinetics were poor. The heterogeneous electron transfer rate constant of the ferri/ferrocyanide couple was increased by a factor of 200 following laser activation but only increased phenanthraquinone adsorption by 50 %. From Raman analysis of the electrode surface it was seen that laser activation had little effect on the structure of the GC surface while polishing had a substantial effect on

the edge plane density. It was concluded that the most prominent effect of the laser activation was to remove chemisorbed and/or physisorbed impurities thus exposing active sites for electron transfer.

A wide variety of electrochemical studies have employed GC electrodes. Some of these include the study of anthraquinone monolayers.[17][18][19] In their study of anthraquinonedisulfonate (AQDS) on GC, McDermott et al. studied the adsorption of AQDS on a laser activated GC electrode.[8] Laser activation was used to clear the electrode surface of impurities and polishing debris and was carried out by irradiating the electrode with three 25 MW/cm^2 Nd: YAG laser pulses. Cyclic voltammetric analysis showed that AQDS was well behaved on GC at low bulk concentrations, when the supporting electrolyte was 0.1 M HClO$_4$. Specifically, the peak current of the redox waves was proportional to the scan rate, the full width at half maximum (FWHM) of the redox peaks was 55 mV, and the peak-to-peak separation was 12 mV. Comparison with the theoretical FWHM of 45.3 mV for a two electron process and a ΔE_p of 0 mV suggested that at low concentrations AQDS was a quasi-reversible, surface bound redox centre at GC electrodes. Adsorption of AQDS was seen to follow the Langmuir isotherm.

Xu et al. investigated the electrochemistry of anthraquinone-2,6-disulfonate on various solid carbon based electrode surfaces, including GC, highly ordered pyrolytic graphite (HOPG), hydrogenated glassy carbon (HGC) and boron doped diamond electrodes.[19] This investigation involved the plotting of capacitance-potential profiles for each electrode material in the range –0.5 to 1 V. The capacitance-potential profiles were carried out in 0.1 M HClO$_4$. It was shown that GC exhibited the highest capacitance of the four electrode materials, ranging from 30 to 40 μF over the potential range, which peaked at 0.25 V. This can be explained by the fact that GC is rich in edge plane sites and consequently has a high density of electronic states near the Fermi level. Cyclic voltammetry of a 1mM Fe(CN)$_6^{3-/4-}$, produced well defined peak shaped voltammograms for at each electrode, characteristic of a diffusion controlled response. Cyclic voltammetry of a 10 μM anthraquinone-2,6-disulfonate solution with 0.1 M HClO$_4$ at GC at a scan rate of 0.2 Vs^{-1} yielded close to ideal responses for a surface bound quinone undergoing a two-electron redox reaction. FWHM of 55 mV and ΔE_p of 30 mV were recorded. Chronocoulometric

measurements were also used to evaluate the amount of charge necessary to instantaneously reduce the adsorbed AQDS, Q_{ads}. The method by which this was carried out involved the creating Q vs. $t^{1/2}$ curves for the total charge, Q_{total}, which is the sum of the faradaic charge, the double layer charge and the charge of the adsorbed monolayer, and the double layer charge, Q_{dl}, which is the charge of the bare electrode when immersed in electrolyte. Q_{ads} was obtained by calculating the difference in the y-intercepts of the two plots. This value was calculated as 13.5 μC.

A study of the adsorption behaviour of 1,2-dihydroxyanthraquinones on electrochemically pre-treated GC was carried out by Komura et al.[20] The pre-treatment involved the anodising of the polished electrode at −1.8 V for five minutes followed by successive potential cycling between 1 and −1 V at a scan rate of 0.1 Vs^{-1} thus increasing the amount of surface active graphitic oxides on the surface. The cyclic voltammograms of the anthraquinone showed a pair of well-developed symmetrical waves near −0.2 V, which were stable over five hours. The supporting electrolyte was 0.2 M H_2SO_4. From voltammetric and impedance evidence it was determined that the anthraquinones adsorbed on the surface giving submonolayer or monolayer coverage. The surface coverage was calculated taking the area to be the geometrical area of the electrode. It was found that the adsorption of 1,2-dihydroxyanthraquinones was well described by the Frumkin isotherm, which takes into account lateral interactions between surface bound species.

The references cited here represent a small sample of the research carried out thus far employing GC electrodes. It is clear that GC provides a stable, convenient tool in the electroanalysis of a variety of adsorbates in a wide range of supporting electrolytes and solvents. The work carried out on quinone and quinone type adsorbates indicates GC is a suitable substrate, given that quinones adsorb well to the surface up to monolayer coverage and that this adsorption is stable. Their redox responses are well behaved and in concurrence with other electrodes, namely reversible two-electron transfer. This compares favourably to quinone studies carried out on other electrode materials, for example, mercury. These reasons prompted the use of glassy carbon as a potential means of analysing the electrochemical behaviour of bianthrone and the dynamics of bianthrone monolayer formation that is detailed in this chapter.

4.2 Experimental

4.2.1 Instrumentation

Cyclic voltammetry was carried out using both a CH Instruments model 440 and model 660A electrochemical workstation. Impedance time experiments were carried out using the 660A. The Glassy Carbon (GC) electrodes used in the experiments were obtained from CH instruments and were prepared by polishing on Struers polishing pads with a slurry made up of 0 3 µm α alumina particles from Beuhler and ultra pure Milli-Q water, followed by somcation in Milli-Q and rinsing with acetone and Milli-Q water. The geometric area of these working electrodes was 0 07069 cm^2. The electrochemical cell in the experiments was the typical three-electrode cell, consisting of the GC working electrode, an Ag/AgCl reference electrode and a platinum wire counter electrode. All solutions containing bianthrone were thoroughly deoxygenated by purging with argon. Deoxygenation was maintained during experiments by allowing a flow of argon above the solution creating a blanket of gas to prevent diffusion of oxygen into the solution

4 2 2 Materials

Bianthrone was obtained from Acros chemicals, 99 % reagent grade N,N-Dimethylformamide and 70 % Perchloric acid were obtained from Sigma Aldrich Ltd All were used as received

4.3 General Electrochemical Properties

Figure 4 3 1 shows a typical cyclic voltammogram of a GC electrode immersed in a 1 μM bianthrone solution dissolved in DMF with 1 M $HClO_4$ as the supporting electrolyte The scan rate used was 0 5 Vs^{-1} The FWHM is 82 6 ± 1 8 mV and the ΔE_p is 22 3 ± 2 2 mV Figure 4 3 2 represents the dependence of the peak current on scan rate It can be seen that there is a linear relationship between the peak current and the scan rate within the range 0 1 and 20 Vs^{-1} A dependence on v, rather than $v^{1/2}$, indicates a redox active species immobilised on an electrode surface A dependence on $v^{1/2}$ would be indicative of a freely diffusing species From this it can be concluded that bianthrone adsorbs on the glassy carbon surface forming an electroactive film The full width at half maximum is larger than 45 3 mV, which would be expected for a two-electron transfer process, however, it is less than that expected for a one-electron process This non-ideality may be due to destabilising lateral interactions between the molecules [21] Inhomogeneity of the electrode surface may also contribute to the larger FWHM value As has been shown earlier in this thesis bianthrone undergoes lateral interactions on a mercury electrode surface On mercury, these interactions manifested themselves as current spikes on the reduction and oxidation sweeps of the cyclic voltammograms These interactions involve the transfer of electrons between the carbonyl and hydroxy functionalities of the reduced and oxidized species

Figure 4 3 3 illustrates cyclic voltammograms taken at different scan rates, the peak current versus scan rate corresponding to these voltammograms is illustrated in Figure 4 3 2 It can be seen that there is an increase in ΔE_p at higher scan rates This is consistent with the effects of iR drop

As with mercury drop electrodes, the reduction of surface bound bianthrone at low pH is considered to be via a coupled, two electron two proton transfer
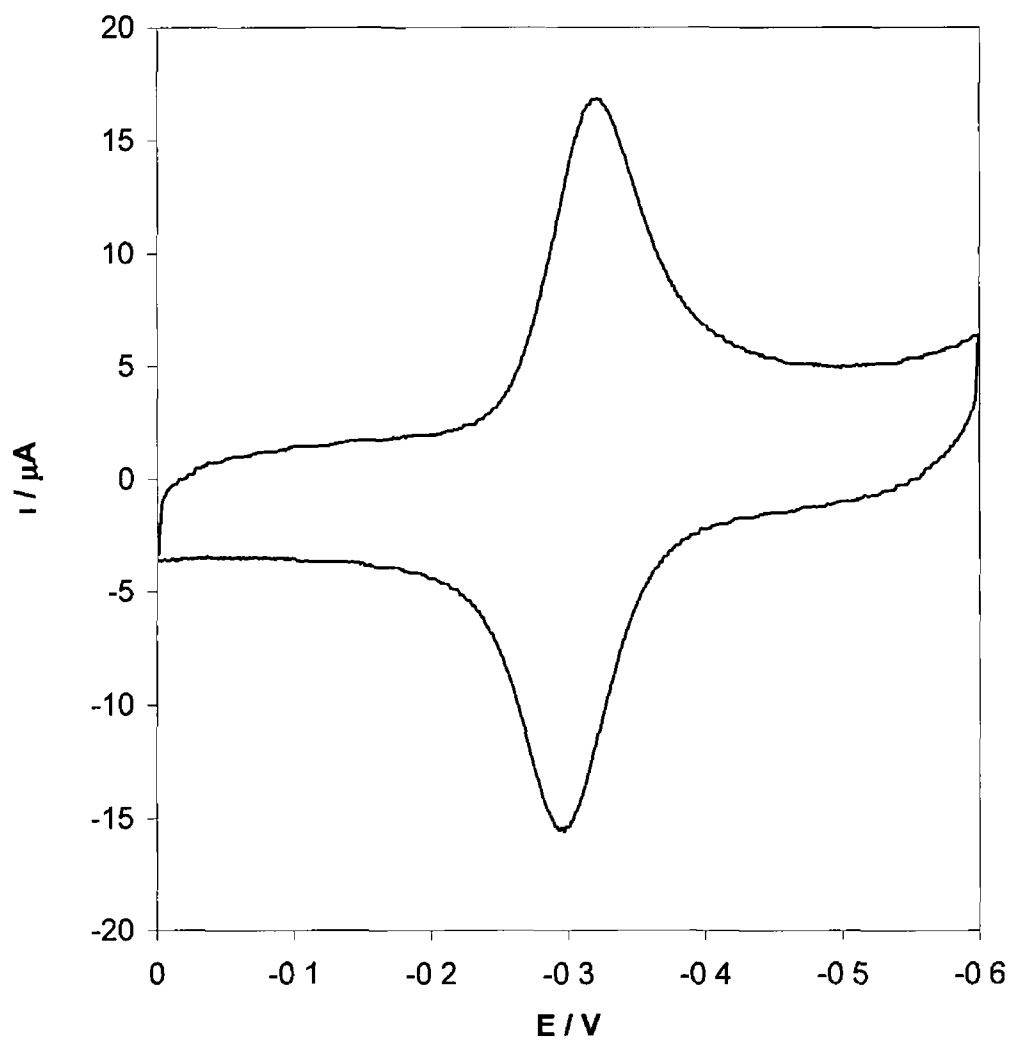
Figure 4 3 1   Cyclic Voltammogram of a GC electrode immersed in 1 μM bianthrone solution dissolved in DMF   Supporting electrolyte was 1 M HClO₄ Scan rate was 0 5 Vs⁻¹   Reference electrode was a Ag/AgCl reference electrode   Counter electrode was a platinum wire
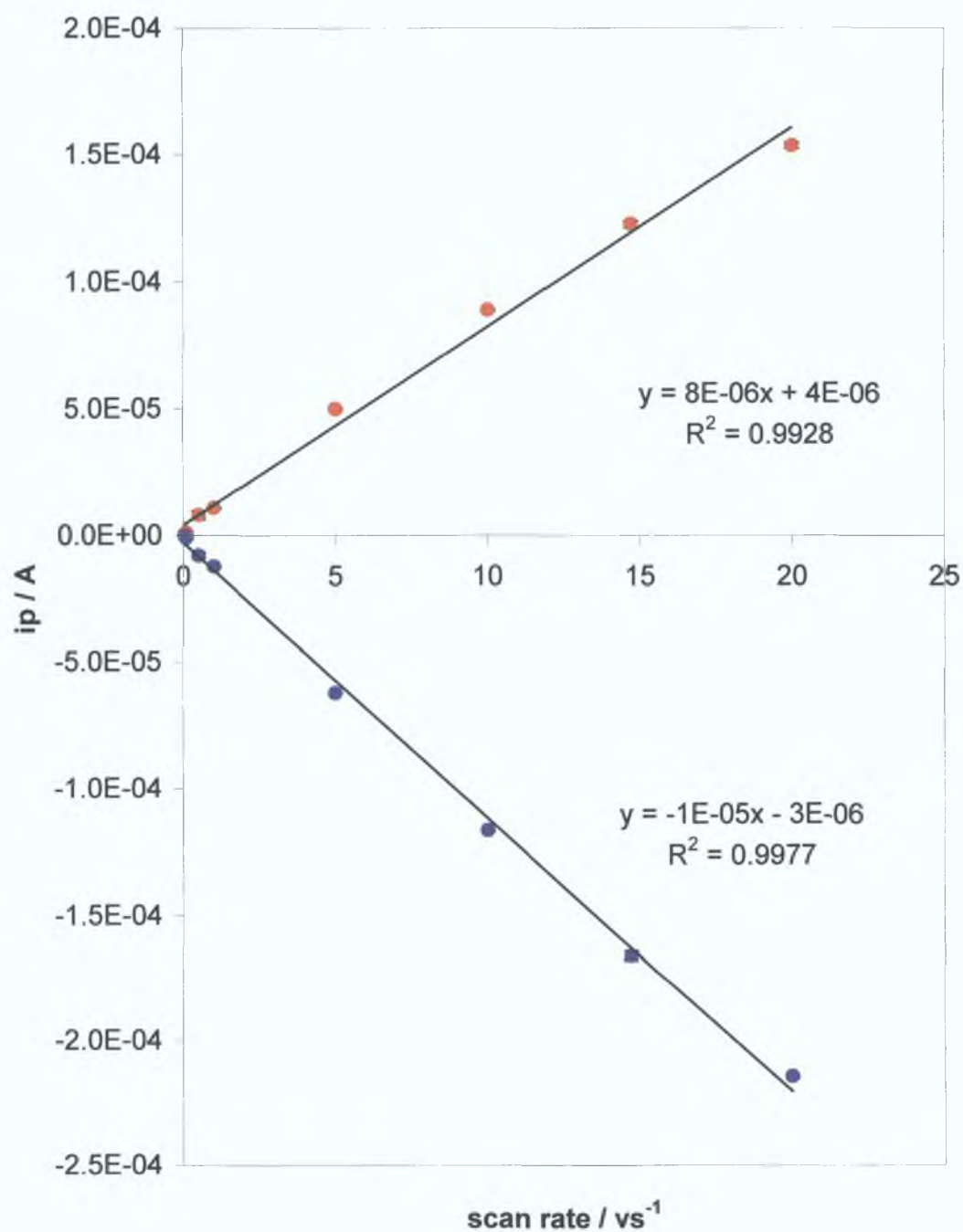
Figure 4.3.2: Scan rate dependence for a GC electrode immersed in a 1 μM bianthrone solution. The supporting electrolyte was 1 M HClO₄. Error bars are present on the graph but are obscured by the data points. They represent the standard deviation obtained from three measurements.
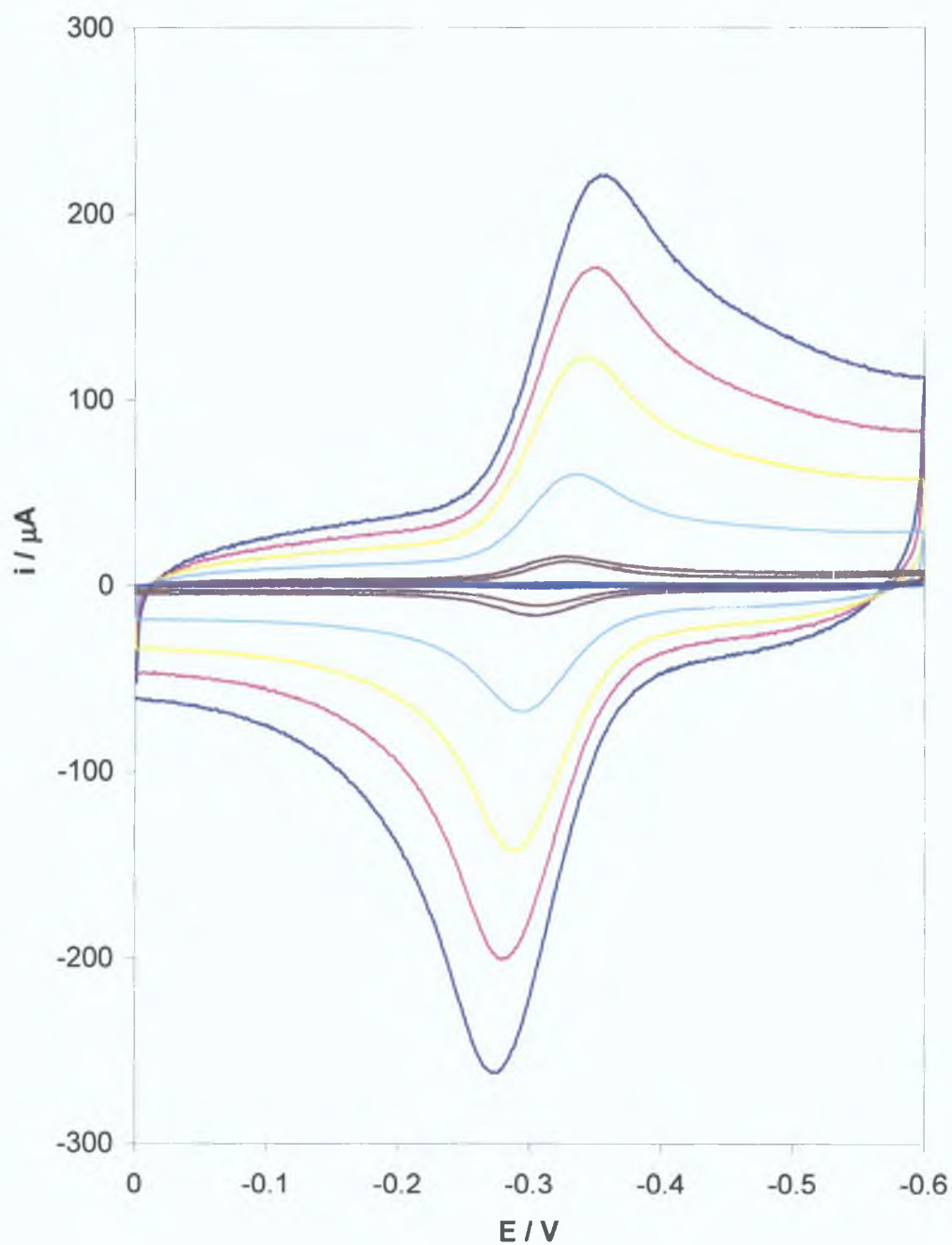
Figure 4.3.3: Overlaid voltammograms of GC electrode immersed in 1 μM bianthrone solution, with 1 M HClO₄ as the supporting electrolyte, at different scan rates. The scan rates are, from smallest cv to largest are 0.05, 0.1, 0.5, 1, 5, 10, 15, and 20 Vs⁻¹

4.4 Dynamics of Monolayer Formation

Investigations into the dynamics of bianthrone monolayer formation were carried out. These investigations involved immersing GC electrodes prepared by polishing with 0.3 μm α alumina followed by sonication in ultra-pure Milli-Q water and rinsing with acetone and Milli-Q water into solutions containing bianthrone dissolved in DMF, with a silver/silver chloride reference electrode and platinum wire counter electrode, with 1 M perchloric acid as the supporting electrolyte. These electrodes were left for different deposition times followed by cyclic voltammetry, at a scan rate of 0.5 Vs^{-1} to investigate the time dependence of monolayer formation. Each deposition time quoted represents the time from immersion of the electrode in the bulk solution to the acquisition of the cyclic voltammogram. Figure 4.4.1 shows overlaid voltammograms taken following these deposition times. The voltammograms included are from two different electrodes, which were prepared as above. Figure 4.4.6 shows a surface coverage versus time plot for 20 μM bianthrone solution dissolved in DMF with 1 M $HClO_4$ as the supporting electrolyte. The surface coverage was calculated from Equation (4.1) [22, 23]

$$\Gamma = \frac{Q}{nFA} \quad (4.1)$$

where Q is the charge obtained by integrating the area under the curve of the cyclic voltammogram, n is the number of electrons transferred, F is Faraday's Constant, and A is the area of the electrode. The area taken was the geometric area of the electrode, a value of 0.0707 cm^2.

It can be seen that 20, 10 and 4 μM bianthrone solutions show similar behaviour, with a saturation surface coverage of similar value being reached. However for 1 μM bianthrone the saturation surface coverage reached is of a lower value. This lower surface coverage could be due to a depletion of the bulk concentration caused by immobilisation of the molecules on the electrode surface. There are two possible explanations for this observation. One explanation is that the

maximum surface coverage is dependent on the bulk concentration This is not considered the case, as the K value calculated for 1 μM is greater than that for 4 μM It was considered possible that solvent polarisation was responsible for the lower value for maximum surface coverage in 1 μM compared to the higher concentrations In other words, the formation of the bianthrone monolayer caused a large enough depletion of the bulk concentration to limit the available molecules for adsorption A simple calculation of the concentration loss incurred by adsorption of the monolayer shows that this is not the case The maximum surface coverage at 3600 s, as seen in Figure 4 4 3, is 1 392 x 10^{-10} mol of bianthrone per cm^2 Given the electrode area is 0 07069 cm^2, this would give a value of 9 84 x 10^{-12} moles of bianthrone on the electrode surface The bulk concentration of the solution was 1 x 10^{-6} moles per litre Given that the volume of bulk solution was approximately 10 cm^3, this would provide approximately 1 x 10^{-8} moles bianthrone in 10 cm^3 Taking into account the number of moles at the surface of the electrode is 9 84 x 10^{-12} moles, this would result in a final concentration following adsorption of the monolayer of 9 99 x 10^{7} M It is clear from this calculation that solution polarisation is not responsible for the low surface coverage value

4.4.1 Adsorption Kinetics

The surface coverage versus time plots generated from the voltammetric data were fit to adsorption models discussed in detail by Hubbard et al.[24] These models have been described previously in Chapter 3. Figures 4.4.3 to 4.4.6 display models fit to adsorption data acquired from the immersion of GC electrodes immersed in bianthrone solutions with bulk concentrations of 1, 4, 10 and 20 µM dissolved in DMF. The supporting electrolyte was 1 M HClO$_4$. The models were fit using the Solver program in Microsoft excel, and the values extracted reflect best fits to the experimental data. The fitting was achieved by systematically varying the kinetic component, K, of the model in order to minimise the sum of squared residuals between the predicted model data and the experimental data. Thus the best fit is that with the lowest sum of squared residuals value. The model used is represented by Equation (4.2)

$$\Gamma(t) = \Gamma_m \left[1 - \exp\left(\frac{KC_0 t}{\Gamma_m} \right) \right] \quad (4.2)$$

This simple exponential models a regime dominated by surface kinetic effects. As before, k could describe a set of complex surface kinetic processes. Consequently, this model may not provide explicit surface kinetic information. Despite this, the model is useful for the purpose at hand in that a large K value translates as instantaneous kinetics. Also, given that bulk concentration is included in Equation (4.2) it is possible to determine whether surface kinetics are influenced by bulk concentration.

As can be seen by the relevant figures, the kinetic models provided satisfactory fits to the experimental data of each bulk concentration. The table below illustrates the K values obtained from the fits obtained. As is clear from this the K values decrease with increasing bulk concentration. Thus, it can be concluded that surface kinetics are dependent on the surface coverage.

Equation (4 3) illustrates the fitting of the diffusion component of the Hubbard model to experimental data obtained from adsorption on GC from 1 µM bianthrone solution The diffusion component is represented by

$$\Gamma(t) = \Gamma_m \left[1 - \exp\left(-\frac{2C_o}{\Gamma_m} \left(\frac{D_t}{\pi} \right)^{\frac{1}{2}} \right) \right] \quad (4\ 3)$$

This plot represents the best fit obtained from all four bulk concentrations examined The fit obtained was poor, suggesting that the adsorption is not diffusion controlled

Concentration / µM	Γ_{exp} / molcm^{-2}	Γ_m / molcm^{-2}	K / cms^{-1}
1	1 39 x 10^{-10}	1 34 x 10^{-10}	1 26 x 10^{7} ± 5 2 x 10^{9}
4	2 17 x 10^{-10}	2 17 x 10^{-10}	9 18 x 10^{8} ± 3 03 x 10^{9}
10	2 24 x 10^{-10}	2 24 x 10^{-10}	9 2 x 10^{8} ± 3 03 x 10^{9}
20	2 54 x 10^{-10}	2 47 x 10^{-10}	4 36 x 10^{8} ± 2 44 x 10^{9}

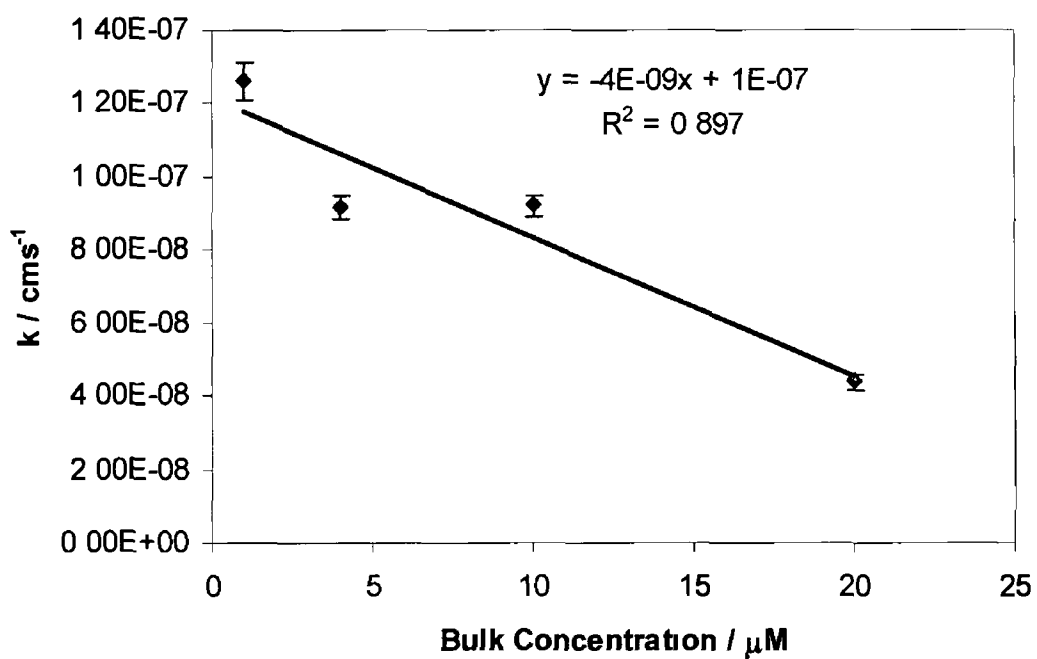*Figure 4 4 1   Plot of surface reorganisation rate constant versus bulk concentration for bianthrone adsorbed on Glassy Carbon   The k values were obtained from the model included above*
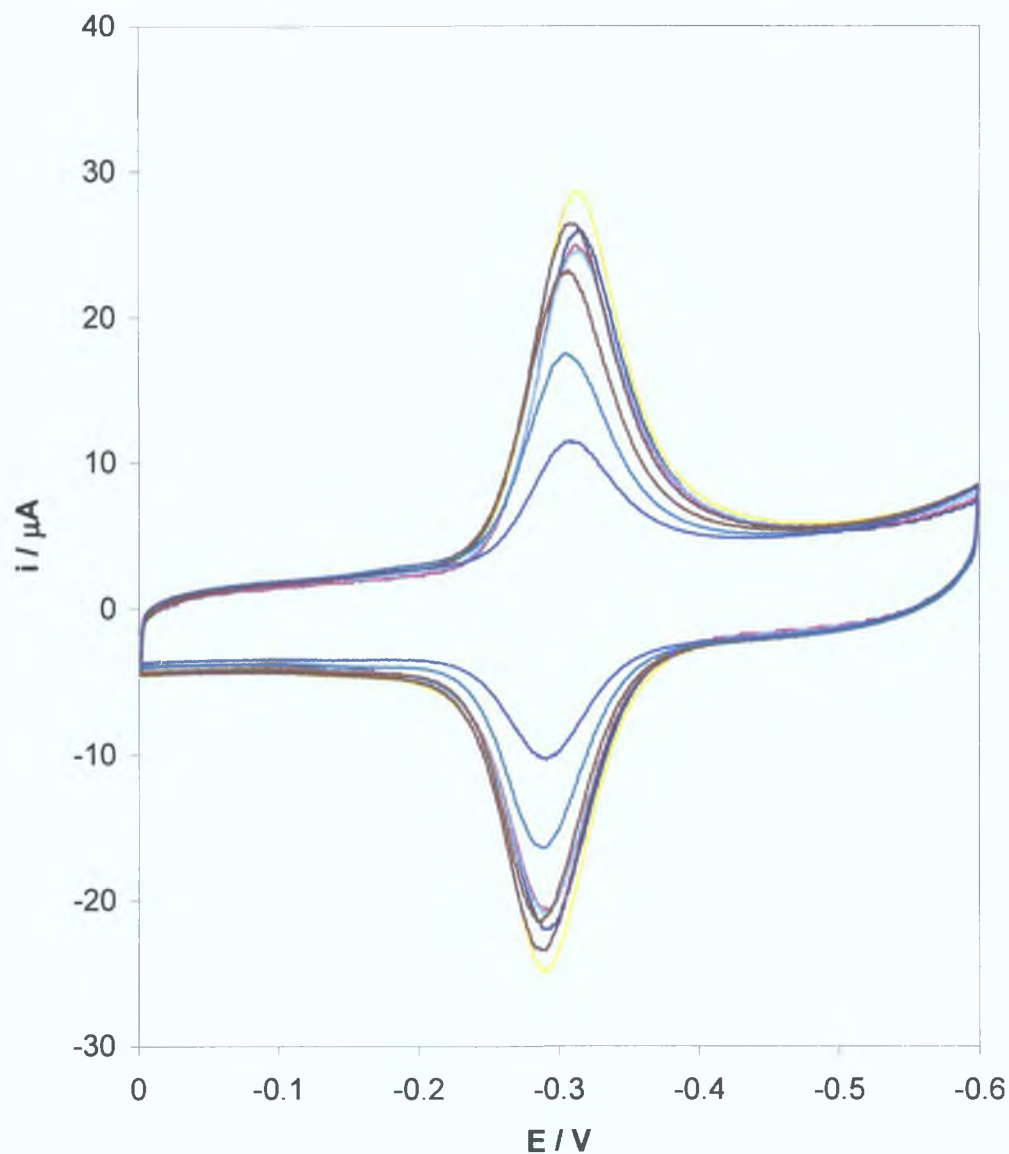
Figure 4.4.2: Overlaid plots of voltammograms recorded over time for a GC electrode immersed in a 20 μM bianthrone solution dissolved in DMF. The supporting electrolyte was 1 M HClO₄. The reference electrode was a Ag/AgCl reference electrode and the counter was a platinum wire. The cvs, from smallest to largest were recorded after 120, 240,360,600, 900, 1200, 1500, 1800 s.
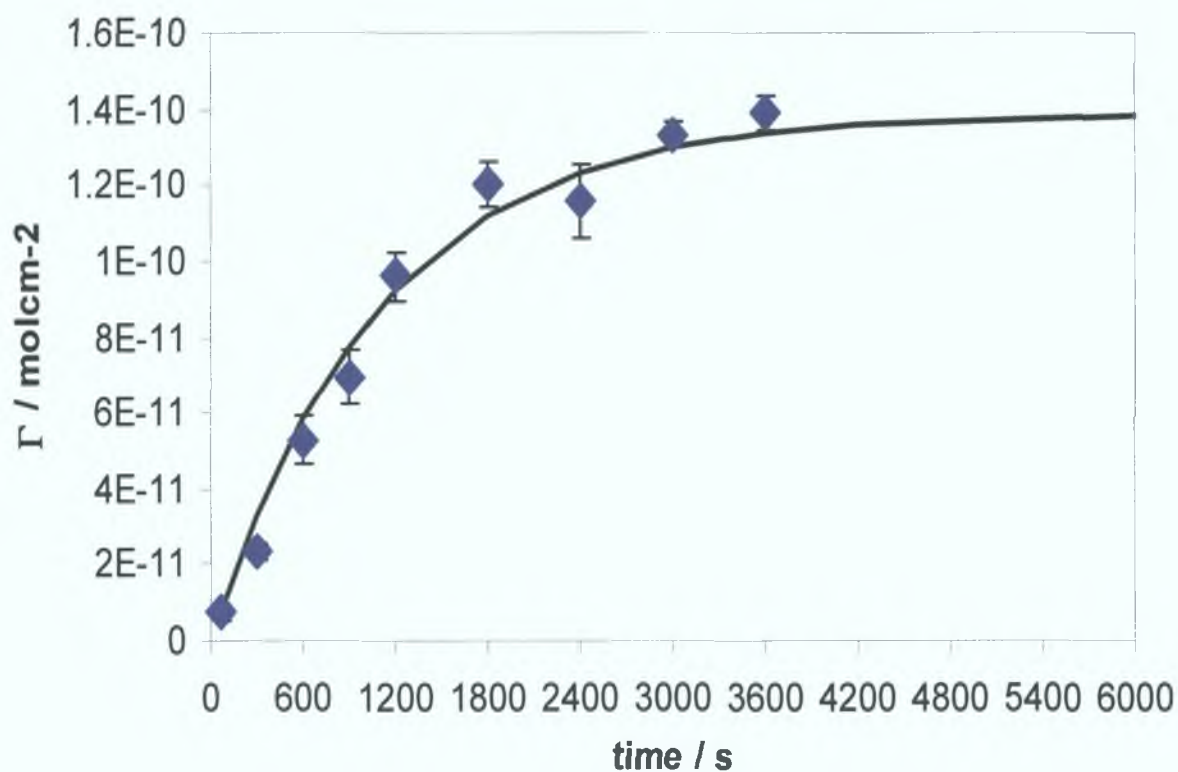
Figure 4.4.3: Surface coverage on a GC electrode versus time for a bulk concentration of 1 μM Bianthrone solution dissolved in DMF with a supporting electrolyte of 1 M $HClO_4$. The data points represent the experimental data while the solid line represents the kinetic model. The geometrical area of the electrode was 0.07069 cm^2. Reference electrode was a Ag/AgCl electrode. Counter electrode was a platinum wire. Error bars represent the standard deviation obtained from three separate measurements

Figure 4.4.4: Surface coverage on a GC electrode versus time for a bulk concentration of 4 μM Bianthrone solution dissolved in DMF with a supporting electrolyte of 1 M HClO₄. The data points represent the experimental data while the solid line represents the kinetic model. The geometrical area of the electrode was 0.07069 cm². Reference electrode was a Ag/AgCl electrode. Counter electrode was a platinum wire. Error bars represent the standard deviation obtained from three separate measurements.
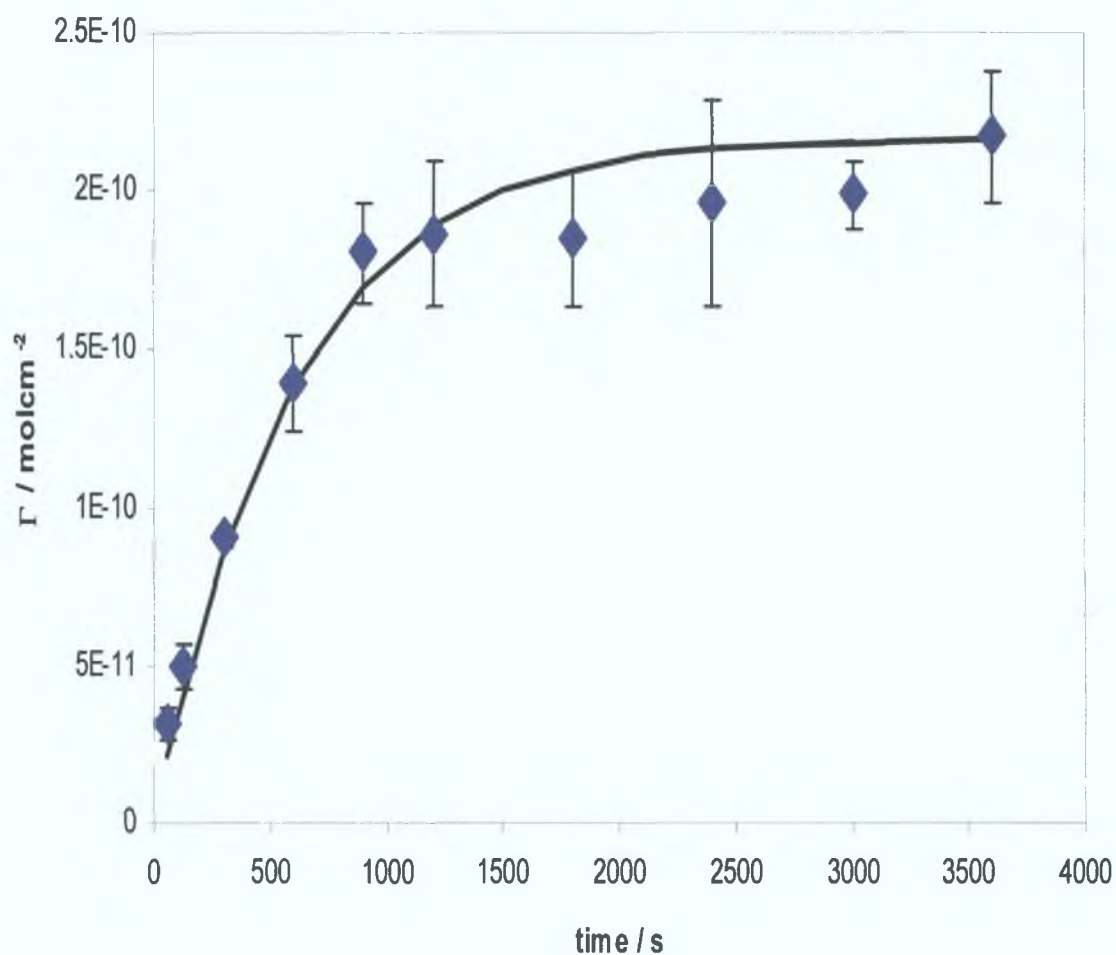
Figure 4.4.5: Surface coverage on a GC electrode versus time for a bulk concentration of 10 μM Bianthrone solution dissolved in DMF with a supporting electrolyte of 1 M HClO₄. The data points represent the experimental data while the solid line represents the kinetic model. The geometrical area of the electrode was 0.07069 cm². Reference electrode was a Ag/AgCl electrode. Counter electrode was a platinum wire. Error bars represent the standard deviation obtained from three separate measurements.
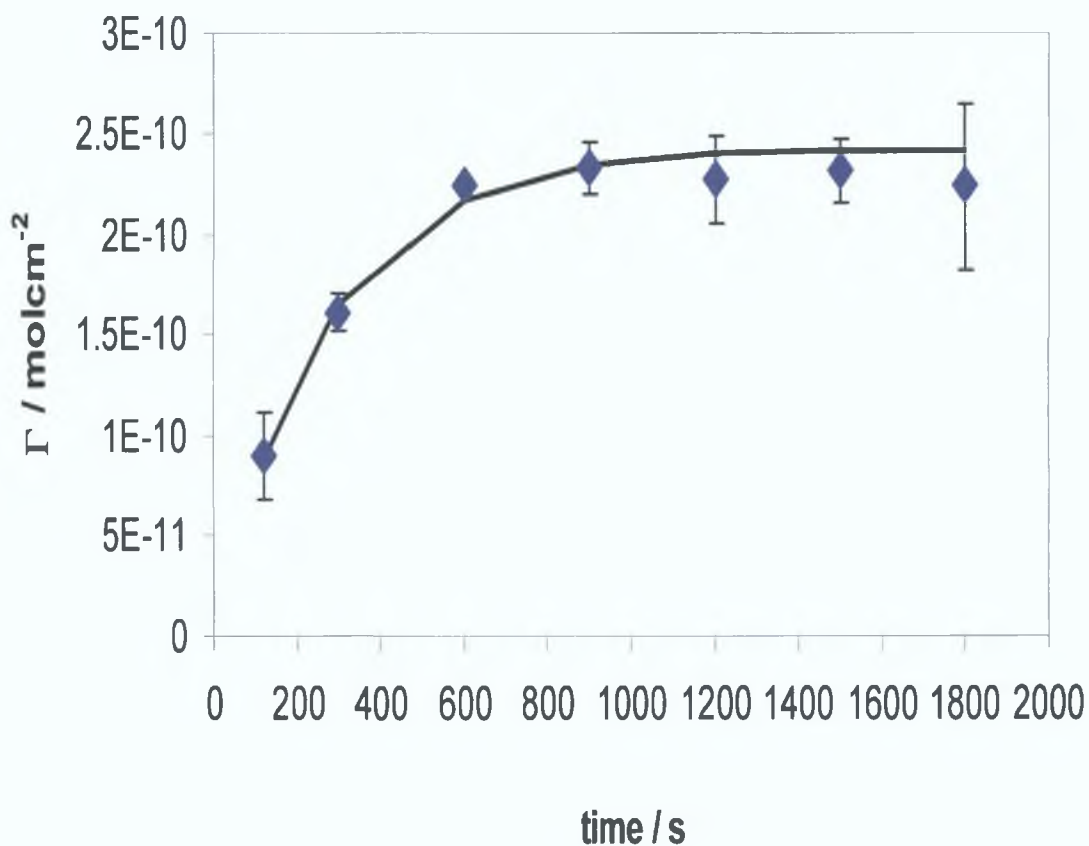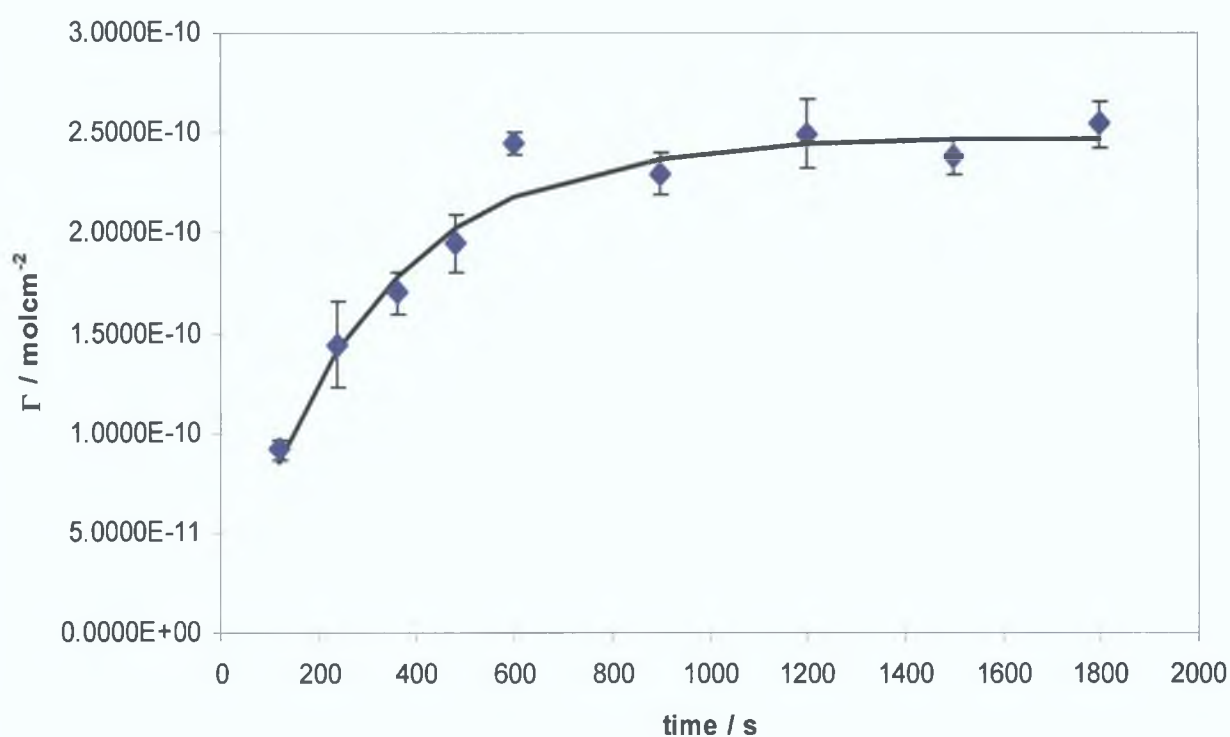
Figure 4.4.6: Surface coverage on a GC electrode versus time for a bulk concentration of 20 μM Bianthrone solution dissolved in DMF with a supporting electrolyte of 1 M HClO₄. The data points represent the experimental data while the solid line represents the kinetic model. The geometrical area of the electrode was 0.07069 cm². Reference electrode was a Ag/AgCl electrode. Counter electrode was a platinum wire. Error bars represent the standard deviation obtained from three separate measurements.

Figure 4.4.7: Surface coverage on a GC electrode versus time for a bulk concentration of 4 μM Bianthrone solution dissolved in DMF with a supporting electrolyte of 1 M HClO$_4$. The data points represent the experimental data while the solid line represents the diffusion model. The geometrical area of the electrode was 0.07069 cm^2. Reference electrode was a Ag/AgCl electrode. Counter electrode was a platinum wire. Error bars represent the standard deviation obtained from three separate measurements.
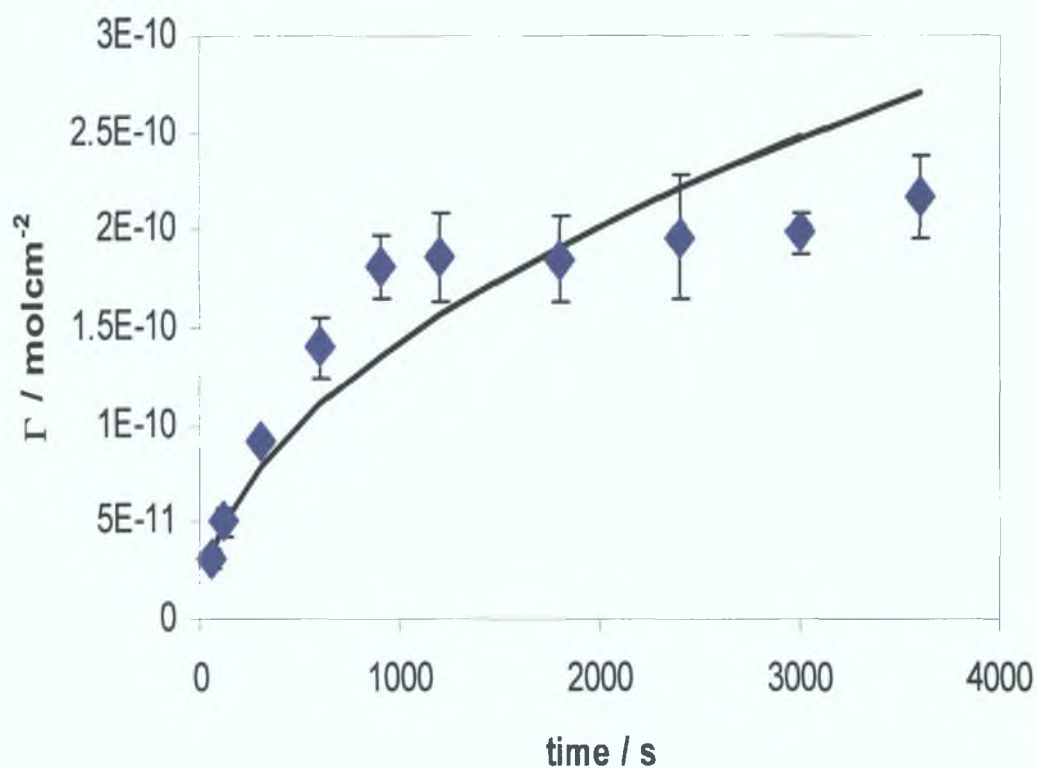
4 5 Impedance analysis

In a preliminary experiment on GC it was found that continuous cycling of the GC electrode modified with bianthrone had an effect on the surface coverage of the bianthrone   Figure 4 11 shows a plot of charge versus time for a GC electrode immersed in a 1 μM solution of bianthrone dissolved in DMF with 1 M $HClO_4$ as the supporting electrolyte   The charge was calculated by integrating the area under the curve of cyclic voltammograms [25]   Initially these voltammograms were taken at five-minute intervals and it can be seen that the surface coverage attains a steady value after approximately 20 minutes   However, after a gap of fifty minutes the charge was seen to increase to a notably higher value   When continuous voltammetric monitoring was resumed it can be seen that the charge decreases to the previous value   This is an indication that cyclic voltammetry affects the surface coverage and that the solubility of bianthrone is lower in the oxidised form   Therefore, it was concluded that an alternative means of monitoring monolayer coverage was needed in order to probe the effect of oxidation state on the adsorption dynamics and energetics of bianthrone on GC   It was this necessity that prompted the use of electrochemical impedance to probe the time dependence of the interfacial capacitance during adsorption

Electrochemical impedance is based on the theory that a modified electrode surface can be represented by a capacitor and resistor in series   The theory incorporates a purely sinusoidal voltage, which is represented by

$$e = E \sin \omega t \quad (4\ 4)$$

where e is the sinusoidal voltage, E is the amplitude of the wave, ω is the angular frequency, which is 2π times the conventional frequency in Hz   It is useful to consider the voltage as a rotating or phasor quantity, as in the diagram below   The length being the amplitude and the frequency of rotation is ω The observed voltage at a given time, e, is the component of the phasor projected on a particular axis (normally 0^0)

Figure 4 5 1   Sinusoidal voltage displayed as phasor quantities

If current, i and voltage, e are considered, each must be represented by a separate phasor, $\dot{I}$ or $\dot{E}$, rotating at the same frequency   Generally, they will not be in phase and one will lag the other by a phase angle ϕ $\dot{E}$ is usually taken as a reference signal and the phase angle is measured with reference to it   The current can be expressed as

$$i = I \sin(\omega t + \phi) \quad (4\ 5)$$

The relationship between the two phasors is constant and thus, so too is the phase angle   Consequently, the references to rotation can be discarded   If a pure resistance, R, is considered across which a sinusoidal voltage is applied, then, according to Ohm's law the current is

$$\left(\frac{E}{R}\right) \sin \omega t \ (4\ 6)$$

or, in phasor notation

$$\dot{I} = \frac{\dot{E}}{R} \quad (4.7)$$

If the resistor is replaced by a pure capacitor, then the fundamental relationship is

$$q = Ce \quad (4.8)$$

or

$$i = C\left(\frac{de}{dt}\right) \quad (4.9)$$

thus

$$i = \omega CE \cos \omega t \quad (4.10)$$

$$i = \frac{E}{X_C} \sin\left(\omega t + \frac{\pi}{2}\right) \quad (4.11)$$

X_c is the capacitive resistance, $1/\omega C$. The phase angle is $\pi/2$ and the current leads the voltage. It is useful to introduce complex notation as the vectors are expanded to a plane. These can be represented by the Argand diagram overleaf. Components along the ordinate are multiplied by $j = \sqrt{-1}$ and are assigned as imaginary. Components along the abscissa are real. The current phasor can be plotted along the abscissa. As a result

$$\dot{E} = -jX_C \dot{I} \quad (4.12)$$

Considering a resistance, R and a capacitance, C, in series, a voltage applied across them must equal the sum of the drops in voltage across the two.

$$\dot{E} = \dot{E}_R + \dot{E}_C \quad (4\ 13)$$

$$\dot{E} = \dot{I}(R - jX_C) \quad (4\ 14)$$

$$\dot{E} = \dot{I}\,Z \quad (4\ 15)$$

Thus the voltage is linked to the current through the impedance, Z The impedance can be represented as

$$Z(\omega) = Z_{Re} - jZ_{Im} \quad (4\ 16)$$

where Z_{Re} and Z_{Im} are the real and imaginary parts of the impedance   This gives

$$Z_{Re} = R \quad (4\ 17)$$

and

$$Z_{Im} = X_C = \frac{1}{\omega C} \quad (4\ 18)$$

The magnitude of Z is given by

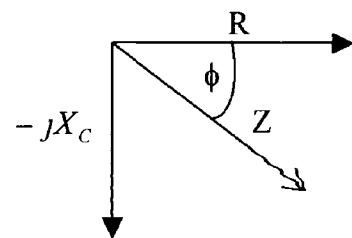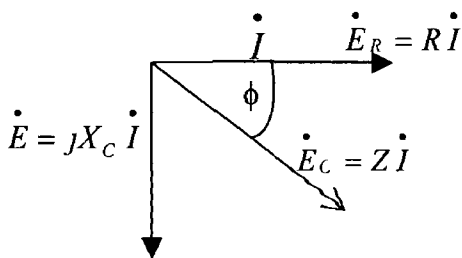$$|Z|^2 = R^2 + X_C^2 = (Z_{Re})^2 + (Z_{Im})^2 \quad (4\ 19)$$

Figure 4 5 2   Argand diagram of impedance

Electrochemical impedance provides the ability to measure the growth of a monolayer at potentials even far from the formal potential This is advantageous if the redox composition is seen to affect the adsorption of the molecule   From the Equation (4 18), it can be seen that the imaginary impedance is proportional to the inverse of the capacitance   Consequently, it is possible to generate a capacitance versus time plot from the imaginary impedance data   Such a plot is shown in Figure 4 5 4   It can be seen that the capacitance, recorded at a potential of –0 1 V, decreases over time before reaching a steady value   The Stern model for the electrochemical double layer predicts that as electrochemically active ions are displaced from the electrode surface by the adsorption of molecules in solution, the capacitance decreases   The data reported here are consistent with this model as the double layer capacitance decreases upon formation of a dense monolayer
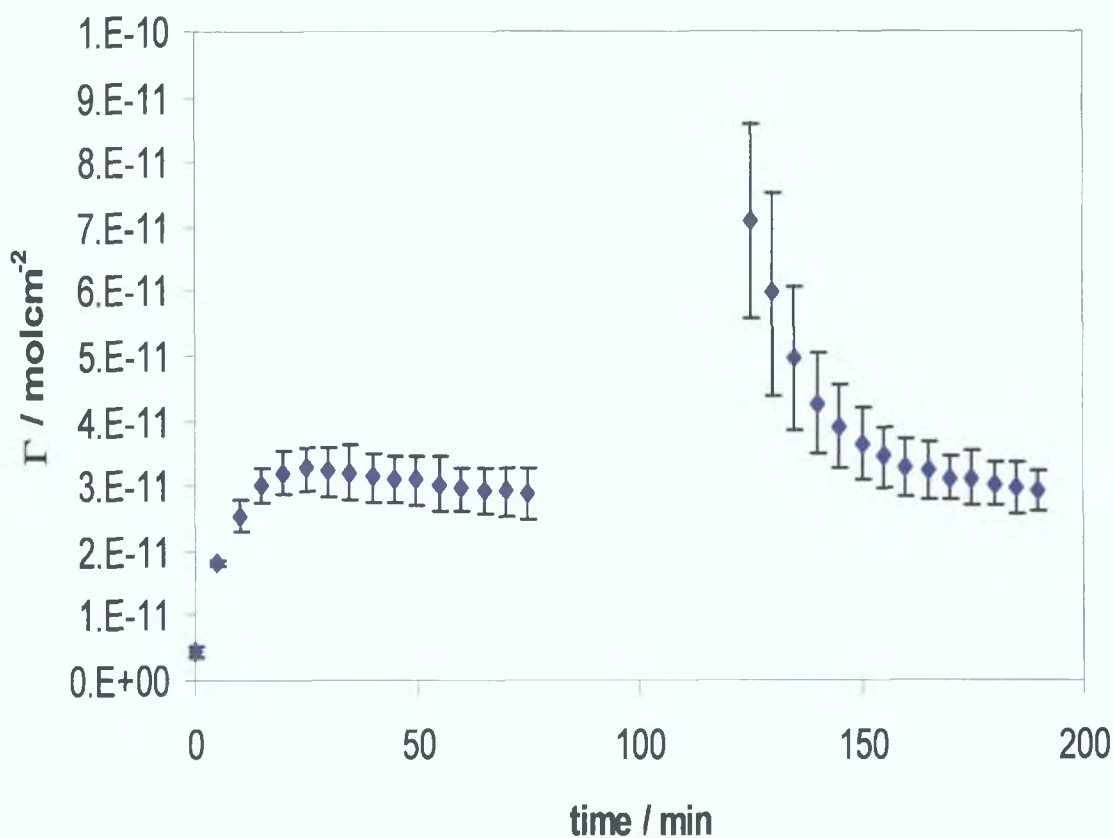
Figure 4.5.3: Surface coverage versus time for a GC electrode immersed in a 1 μM bianthrone solution dissolved in DMF. The supporting electrolyte was 1 M HClO₄. The reference electrode was a Ag/AgCl reference electrode. The counter electrode was a platinum wire. Surface coverage was calculated using Equation 4.1

Figure 4.5.3: Capacitance versus time for the formation of a bianthrone monolayer obtained by the immersion of a polished GC electrode in a 2 μM bianthrone solution dissolved in DMF with 1 M HClO₄ as the supporting electrolyte. The capacitance was obtained by calculation from the equation for imaginary impedance. The potential at which impedance was measured was –0.1 V

4 6 Raman spectra of Bianthrone adsorbed on Glassy Carbon electrodes

4 6 1 Characterisation of the Raman electrochemical cell

A novel electrochemical cell, which was developed for the Raman spectroscopic experiments, is illustrated in Figure 4 6 1 1   It was fabricated from Teflon with a well bored to hold the analyte solution into which the working glassy carbon electrode and platinum counter electrode were located   The working electrode was placed into the cell in an inverted position through the bottom of the cell, as was the counter electrode   A separate well, linked to the main well via a small channel, provided contact for the reference electrode   Prior to any Raman experiments being carried out, some standard electrochemical experiments were completed to evaluate the suitability of the cell for electrochemistry   Figure 4 6 1 2 illustrates a cyclic voltammogram of a bianthrone monolayer adsorbed on a glassy carbon electrode, from a 400 μM bianthrone solution, with a geometric area of 0 07069 cm^2 The counter electrode was a coiled platinum wire and the reference was an Ag/AgCl electrode   The surface coverage of the monolayer calculated using the usual method was 2 14 x 10^{10} mol / cm^2, which represents close to monolayer coverage   It is important to note that while the voltammogram observed is less ideal than those observed using a conventional electrochemical cell, the purpose of these experiments is to structurally characterise bianthrone monolayers with Raman spectroscopy   In this capacity the voltammograms are adequate f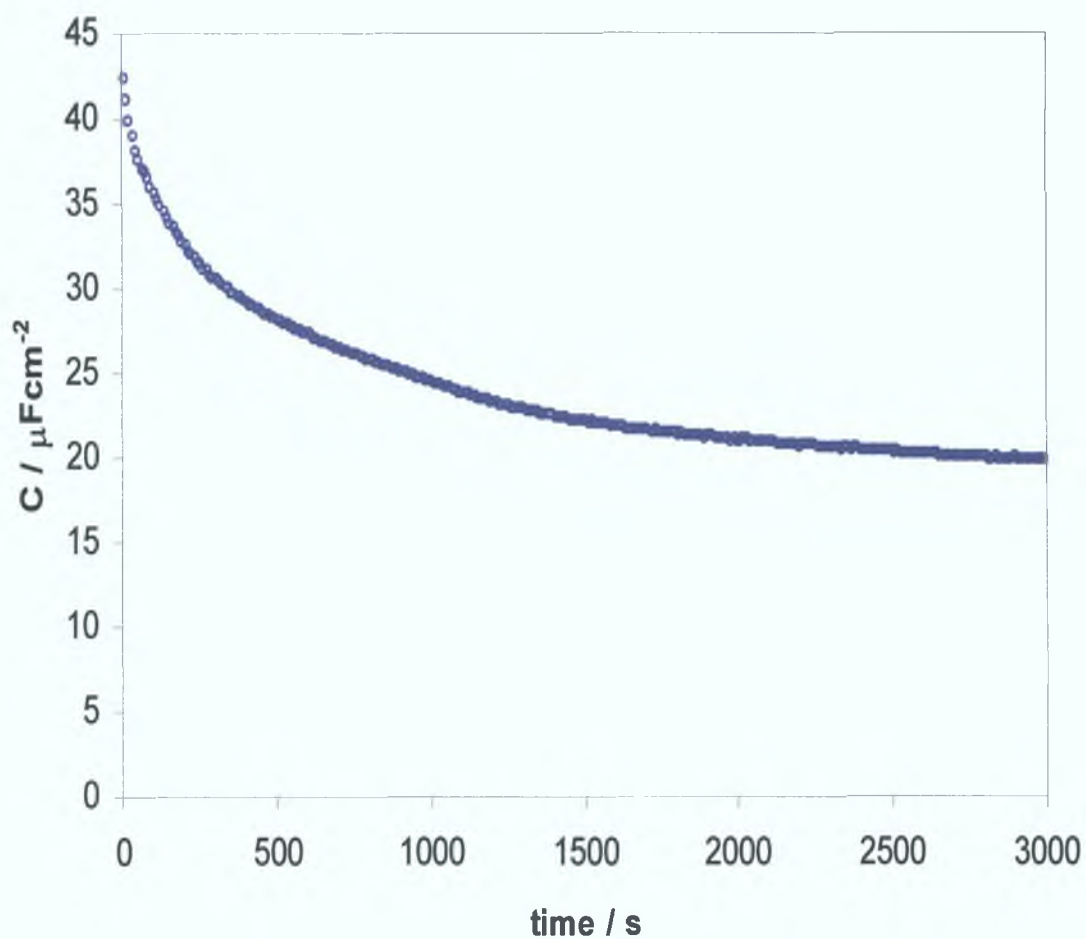or in situ electrochemical characterisation   Scan rate dependence was carried out on a GC electrode immersed in a 203 μM bianthrone solution dissolved in DMF with 1 M HClO$_4$ as the supporting electrolyte   Figure 4 6 1 3 illustrates the dependence of peak current on scan rate   It can be seen that the peak current increases linearly with scan rate up to 20 Vs^1, indicating that the response is due to an adsorbed species on the GC surface   This compares favourably to scan rate dependences obtained from a conventional electrochemical cell   Figure 4 6 1 4 illustrates a Nyquist plot of the cell under the same conditions as that for the scan rate dependence   This plot indicates that the cell resistance, under these conditions, is approximately 50 Ω
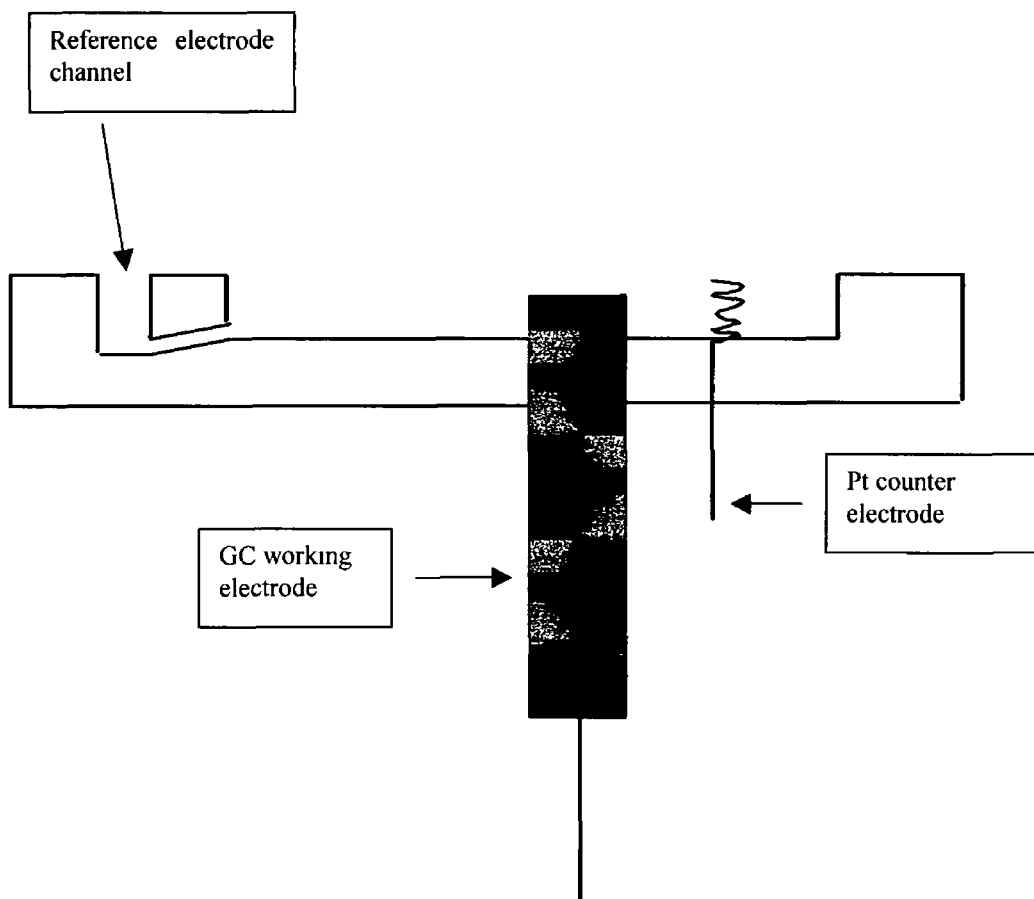
Figure 4 6 1 1   Schematic of the Raman electrochemical cell
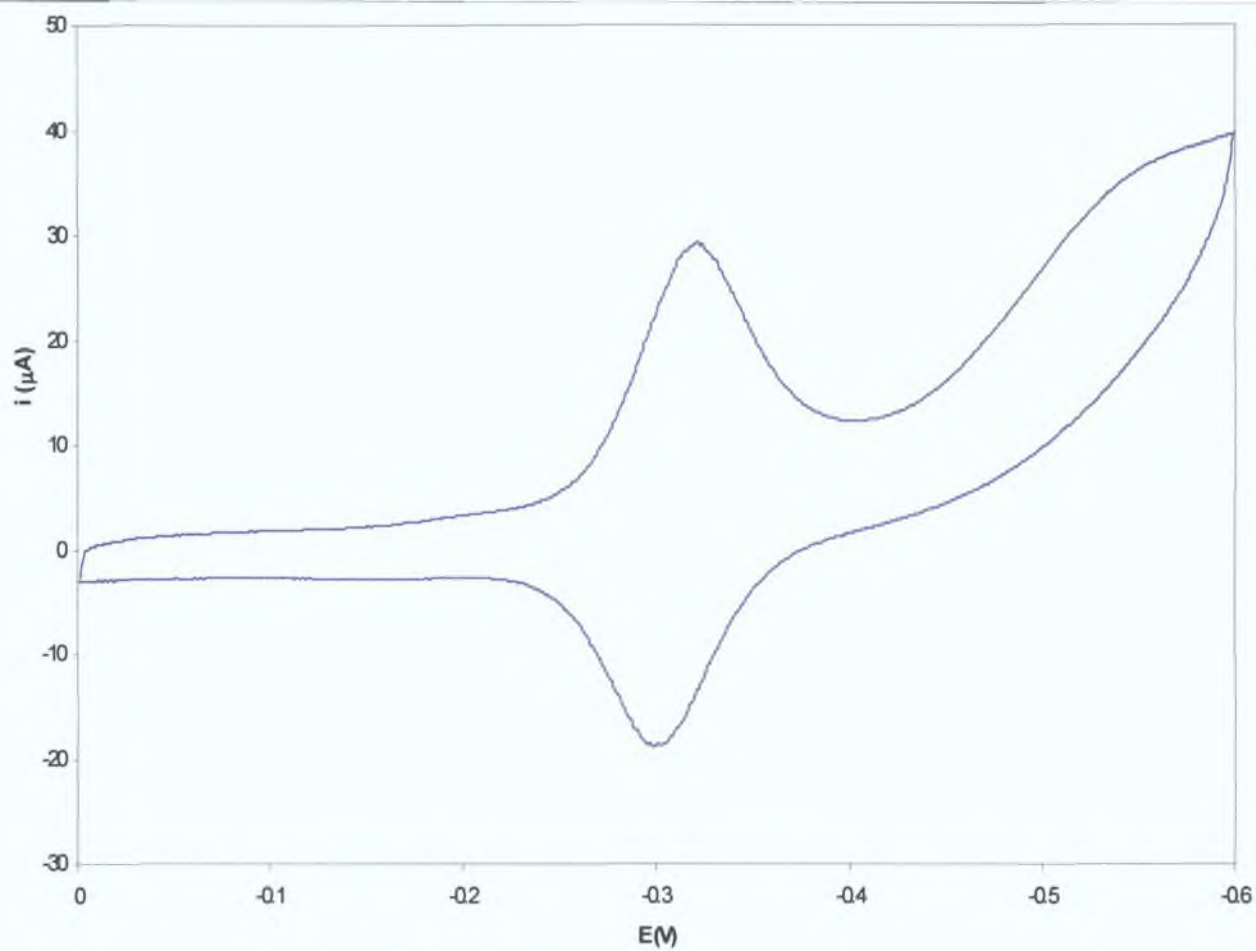
Figure 4.6.1.2 Cyclic voltammogram of a 400 μM bianthrone solution in DMF with HClO₄ as the supporting electrolyte obtained using the Raman cell shown in Figure 4.11. The reference electrode was a Ag/AgCl saturated KCl reference.
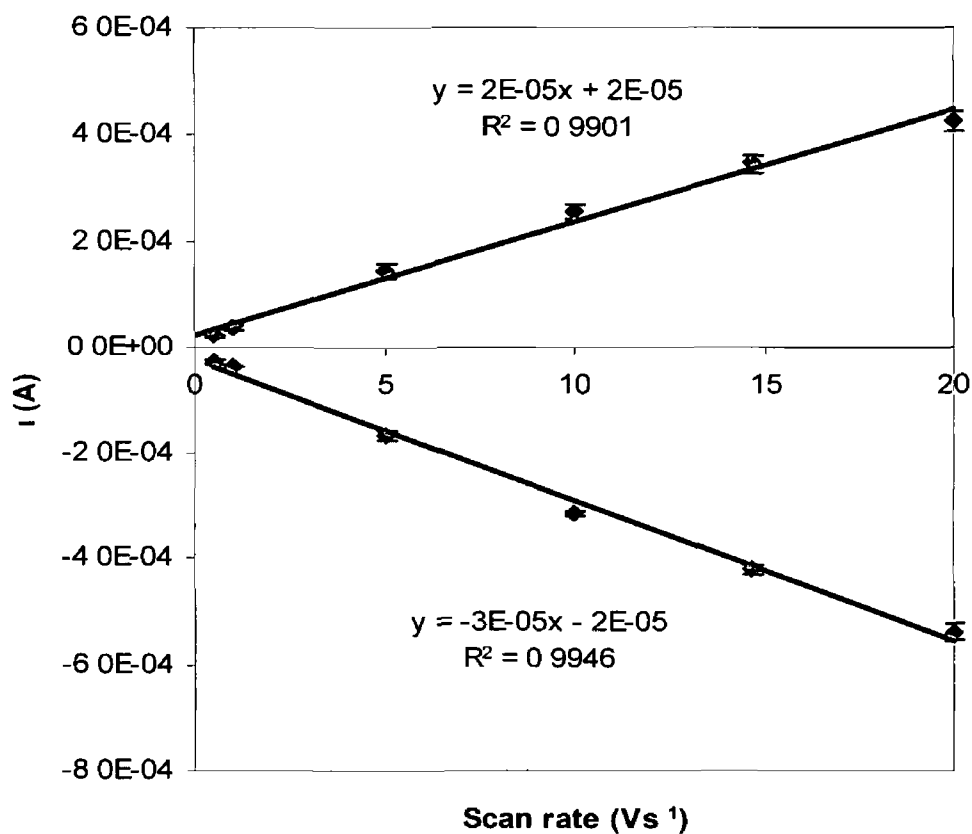
Figure 4 6 1 3 Scan rate dependence of a Glassy Carbon electrode immersed in a 203 μM bianthrone solution Solvent was 99% DMF, electrolyte was 1 M HClO₄ The reference electrode was a Ag/AgCl saturated KCl reference electrode Error bars represent the standard deviation obtained from three separate measurements

Figure 4.6.1.4 Nyquist plot of GC immersed in 203 µM bianthrone solution dissolved in DMF. The supporting electrolyte was 1 M HClO₄.

4 6 2 Solvent subtraction and normalisation of spectra

The bulk bianthrone solution from which these experiments were carried out contained 99% N,N-dimethyl formamide as solvent and 1 M perchloric acid as the electrolyte Consequently, Raman bands attributed to these chemicals had to be removed from the spectra presented here The raman peaks corresponding to DMF were obtained by 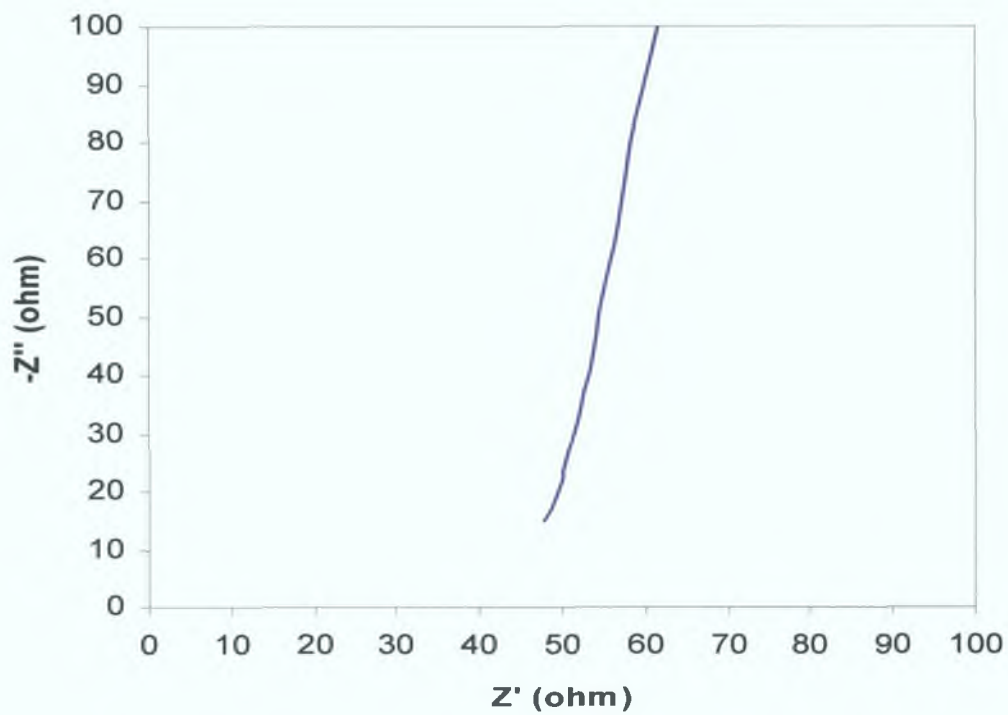acquiring spectra of a neat DMF sample which was compared to a raman spectrum published on the sigma Aldrich website These spectra compared favourably A Raman spectrum of the solvent solution containing 1 M perchloric acid was also obtained This spectrum was then used as a template for the removal of solvent bands from the bianthrone monolayer spectra

As a consequence of this, some features of the raman spectra of bianthrone, illustrated by the spectrum of the solid, that appear in the same spectral regions as the solvent features, were either removed from the final corrected spectra or were distorted This leads to a limiting of the features that could be examined

In terms of normalisation, it was not possible to choose a solvent or electrolyte band as an internal standard as the solvent spectra were removed from the bianthrone spectra Therefore, it was necessary to choose a band from the bianthrone spectrum The band chosen was that at 325 cm^{-1} as this appeared in all spectra with little variance between the spectra at different potentials This made it the most amenable for normalisation

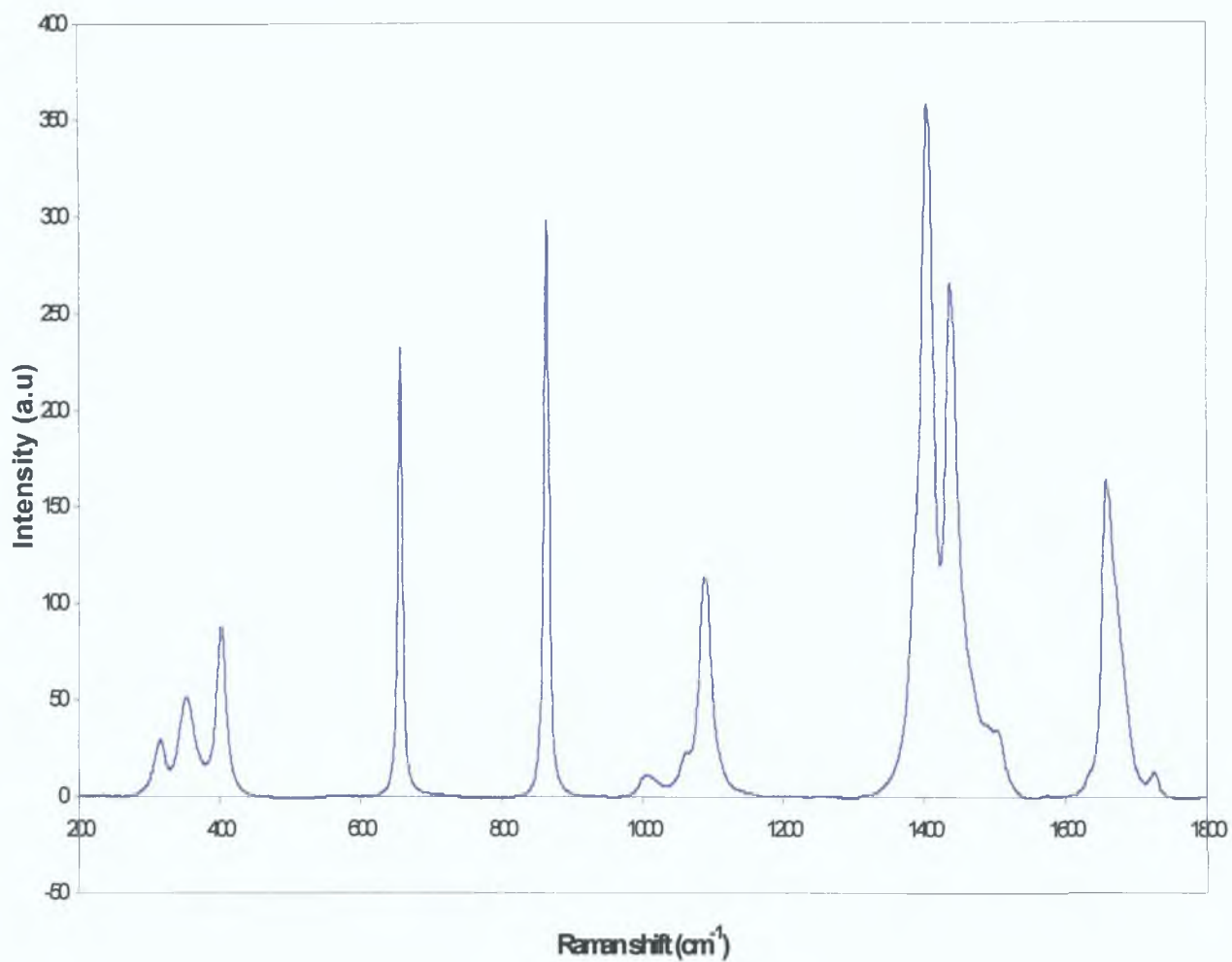*Figure 4.6.2.1 Raman spectrum of DMF. Excitation was provided by an Ar$^+$ laser at a wavelength of 457.8 nm*
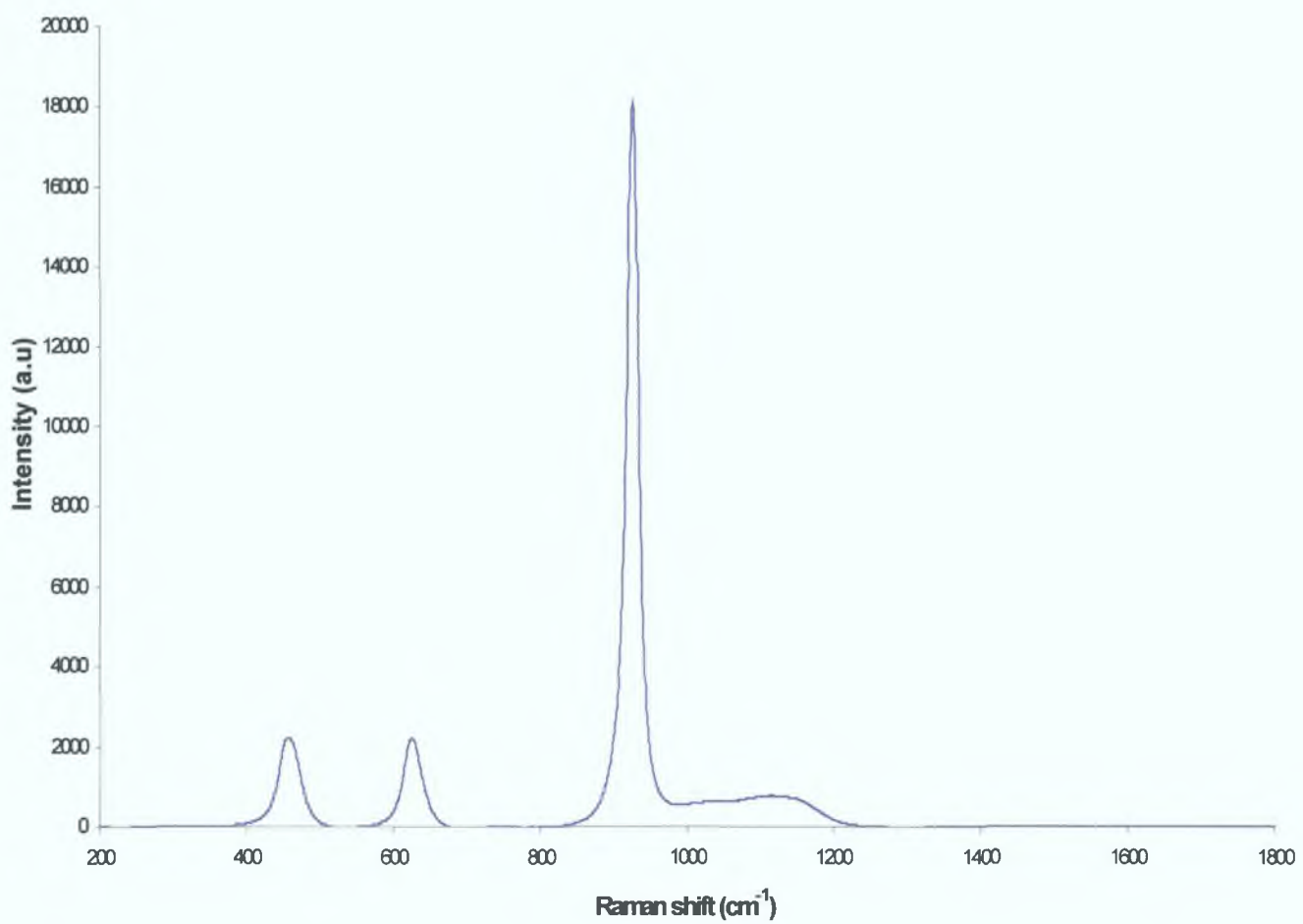
Figure 4.6.2.2: Raman spectrum of perchloric acid. Excitation was provided by an Ar⁺ laser at a wavelength of 457.8 nm

4.6.3 Raman spectra of bianthrone monolayers

Figure 4.6.3.2.1 shows the solvent-corrected Raman spectrum of a bianthrone monolayer adsorbed on a glassy carbon electrode in the absence of an applied potential. It can be seen that this spectrum shares many of the features of the solid bianthrone spectrum observed in chapter 3 (page 136, Figure 3.6.3.2). It can also be seen that some enhancement of the spectrum has been achieved in some bands of the spectrum. An example of this is seen in the group of bands between 1530 and 1640 cm^{-1}, which shows a maximum intensity, which is approximately twice those that appeared in the solid spectrum.

The band visible in the solid spectrum at 225 cm^{-1} and assigned to CH wagging and torsion is not visible in the monolayer spectrum in the absence of potential. The CCC CCO stretch visible at ca. 325 cm^{-1} is clearly visible in the monolayer spectrum with similar intensity. The CCO, CCC stretch visible at 589 cm^{-1} is seen to show an increase in intensity in the monolayer spectrum compared to that in the solid. The band visible at 761 cm^{-1} in the monolayer is a narrower peak than that in the solid spectrum, but is similar in intensity. This band is attributed to CH wagging and torsion. The band at 1215 cm^{-1}, assigned to CCH and CC stretches, appears in both the solid and the monolayer spectrum but has a greater intensity in the monolayer spectrum. A weak band at 1278 cm^{-1} in the solid spectrum, corresponding to CCH and CC stretching is seen to increase in intensity in the monolayer spectrum. However, in the solid spectrum, it is difficult to say with certainty if this band is visible or whether it is actually just baseline noise. A strong band at 1350 is seen in both the solid and the monolayer spectrum. This band appears with slightly greater intensity in the monolayer spectrum, but in both spectra it is quite distinct. This band is assigned a CC, CCO and CCH stretching mode. It may appear that a band at ca. 1435 cm^{-1} in the solid is completely absent in the monolayer spectrum. However, given the fact that this is a region in which there is a strong peak in the DMF spectrum, it is necessary to point out that a band in this region may have been lost due to solvent subtraction. A notable band, visible in the monolayer spectrum as a standalone peak, is observed at ca. 1519 cm^{-1}. The paper by Ulicny et al from which these assignments are obtained does not specify an assignment for this band.[41] However, given the fact that it appears in both the solid and the monolayer spectra it

is possible to rule out that it is from either the solvents or the electrodes used It can be seen that this band is present among a group of bands in the solid spectrum but is present as a standalone peak in the monolayer spectrum The group of bands in the region between ca 1500 and 1690 cm^{-1} can be seen to be quite similar in the monolayer and the solid spectra with distinct peaks at ca 1578, 1598, and 1612 cm^{1}, and also with a similar intensity However, these peaks have a more distinct character in the monolayer spectrum than in the solid

Both the characteristic bands present in the monolayer spectrum, compared to the solid spectrum, and characteristic voltammetry confirm that bianthrone is present on the surface of the electrode The observed differences seen in the spectra may arise because of differences in orientation when the molecule is adsorbed onto the electrode surface Also, it is possible that the interaction of bianthrone molecules with the electrode surface or between individual molecules may contribute to these changes

4 6 3 1 Electrochemical measurements of the monolayer

Raman spectra were taken at incrementally more negative potentials from –0 1 to –0 4 V in order to monitor the monolayer behaviour during its reduction This was achieved by employing amperometric i-t curves, which keep the potential constant Figure 4 6 4 1 1 represents a typical i-t curve
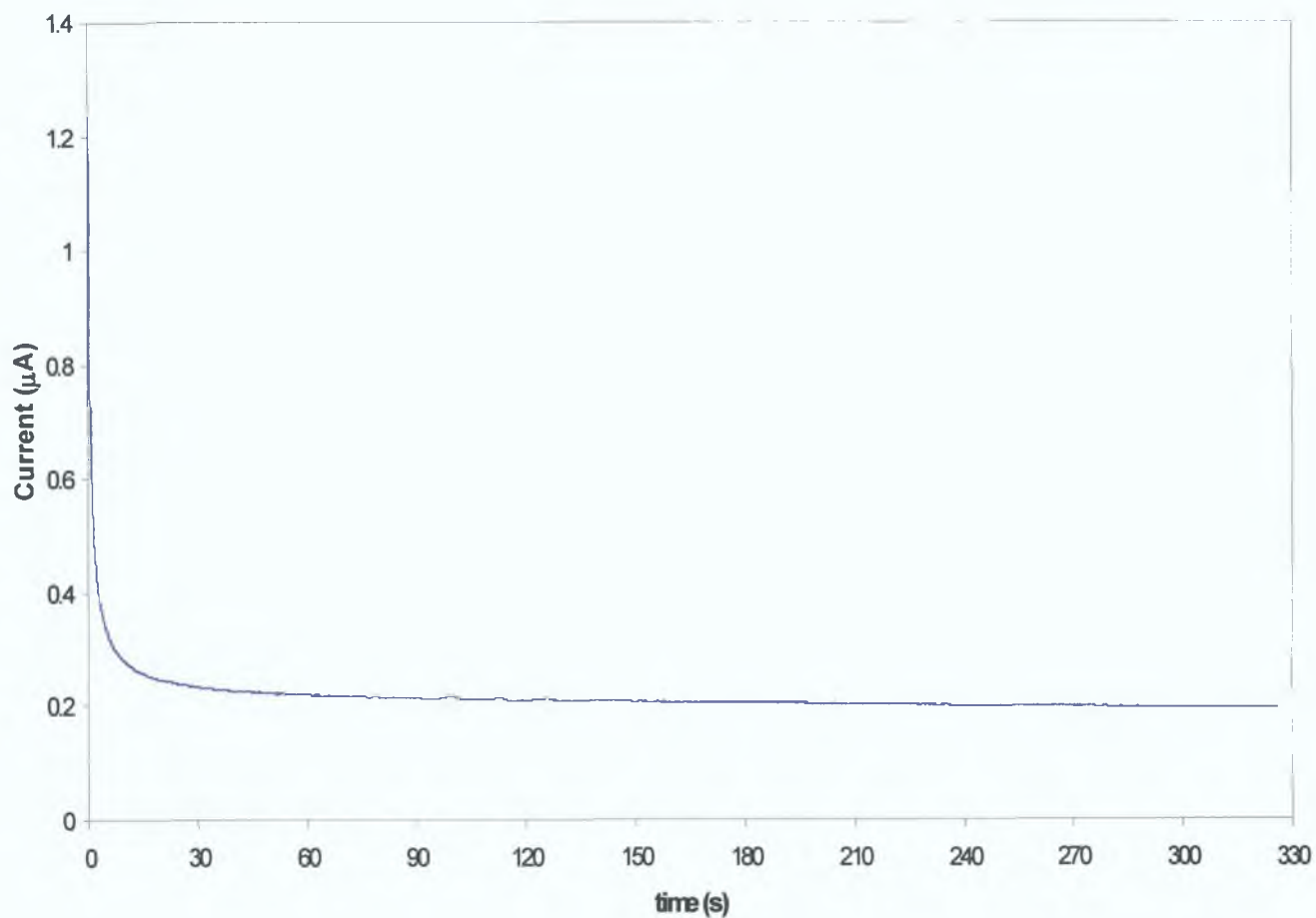
Figure 4.6.3.1.1 Amperometric i-t curve of the bianthrone monolayer at a potential of −0.1V. This technique was used to provide a constant voltage for each potential measurement and the spectra taken with this were done so when the current became constant.

4 6 3.2 Effect of varying potential on Raman spectra

Figure 4 6 3 2 2 displays the solvent-corrected, Raman spectra taken at different potentials As indicated previously, these spectra have been normalised to the band at 325 cm^{-1} of the solid spectrum The potential was varied using amperometric i-t curves, which kept the potential constant as the spectra were acquired The potentials applied were chosen based on the cyclic voltammograms acquired and range from fully oxidised (-0 1 V) through to fully reduced (-0 4 V) Also included is the spectrum of the bianthrone monolayer in the absence of an applied potential

A potential of –0 1 V provides conditions whereby the bianthrone molecules adsorbed on the electrode are fully oxidised The spectrum acquired is similar to that in the absence of an applied potential The first band of note is that at 590 cm^{-1}, assigned to CCO and CCC stretches This mode has similar intensity as that of the spectrum recorded in the absence of an applied potential The intensity of this band increases gradually as the potential is made more negative reaching an intensity similar to that of the band at 325 cm^{-1} at a potential of –0 24 V This band persists until –0 33 V At potentials more negative than this, it is not observed in the spectrum At –0 1 V a band situated at 919 cm^{-1}, is assigned, at 933 cm^{-1} by Ulicny et al to CCC and CC stretches, with an intensity of approximately 200 units This band is observed in spectra under all conditions of potential and increases as the potential is shifted more negative with the exception of –0 33 V where the intensity of the peak is at its lowest It is worth noting that this band is also at a low intensity in the absence of an applied potential The band reported at 1213 cm^{-1} by Ulicny et al is assigned to CCH and CC stretches can be seen in the absence of potential at 1220cm^{-1} It is worthy of note that it does not appear as a distinct band in the spectrum of the solid sample Ulicny reports a band at 1213 cm^{-1}, which is assigned to CC and CCH stretches and in the case of these spectra is observed at 1220 cm^{-1} This mode is seen at each potential applied and also in the absence of applied potential This mode is the spectrum of the solid at 1215 cm^{-1} Ulicny reports a band at 1333 cm^{-1} and assigns it to CC, CCO and CCH stretches While no discernible peak is present at 1333 cm^{-1} in the spectra presented here, there is a broad, intense peak present at approximately 1350 cm^{-1} in all spectra It is proposed that this peak is the band reported by Ulicny but shifted approximately 17 cm^{-1} However, it is unclear as to why this mode is

185

shifted This band appears at a large intensity in the absence of potential, approximately 1300 units The intensity of this band drops slightly to under 1100 units at –0 1 V At –0 2 V the band increases again to approximately 1500 units with a further slight increase observed at –0 24 V A slight decrease in intensity is seen at –0 3 V with a similar band observed at –0 33 V A notable drop in intensity is observed at –0 35 V with a similar observation made at –0 375 V At –0 4 V however, the intensity of the peak increases again to approximately 900 units A band at 1556 cm ^{1}, assigned to CC and C=O stretches, is not so clear in the spectra produced A small shoulder is visible in the absence of potential at ca 1557cm^{-1}, which may be assigned to this band A shoulder appears at 1556 cm ^{1} at –0 1 V and, when compared to the same region in the absence of potential is more distinct, however it is still unclear as to whether this is a genuine band or if it is due to noise A similar mode is observed at –0 2 V At –0 24 V, this shoulder, at 1556, becomes less distinct This continues from –0 3 to –0 4 V, with a barely distinct shoulder It is possible that this band contains structural information about the adsorbed molecule, however, the low intensity of the observed bands precludes reliable interpretation of the band The group of bands in the aromatic region between ca 1560 and 1630 cm ^{1} are clearly the most intense of the spectrum Ulicny assigned a band at 1593 cm ^{1}, which here is seen at ca 1595 cm ^{1} to CC in the ring system stretching, however, the appearance of three main bands in this region is not reported It has been reported in a study by Sanchez-Cortez et al that the band at 1595 cm^{-1} in the Raman spectrum of bianthrone split into two bands at 1607 cm ^{1} and 1578 cm^{-1} when bianthrone was adsorbed onto silver colloids However, no interpretation of this phenomenon was offered It is proposed that the three bands, as reported in both studies, are present in these spectra These bands are visible in the absence of an applied potential and also prior to reduction at –0 2, -0 24, -0 3, and –0 33 V However, their intensities change over this potential range This is best illustrated by comparing the intensity of the 1578 cm^{-1} and 1612 cm ^{1} band to that of the 1595 cm ^{1} band (I_{1578}/I_{1596} and I_{1612}/I_{1596} respectively) This is provided in Table 4 2 The final band listed by Ulicny et al is that at 1670 cm ^{1} which is assigned to C=O stretching In the spectrum of solid bianthrone, a reasonably strong band is observed at 1670 cm ^{1}, attributed to this stretch However, in the monolayer spectrum, this band disappears, to be replaced by a slight shoulder A similar phenomenon was reported by Sanchez-Cortez with bianthrone adsorbed on silver colloidal particles This shoulder could well contain

information on the adsorbed molecule However, given the intensity of the signal compared to that of the surrounding noise, it is difficult to establish, with any certainty, patterns that may be present

In an attempt to explain the spectral changes detailed here, some interpretations are proposed The disappearance of the band at 590 cm^{-1} at potentials more negative than -0 33 V, a potential near the observed redox potential of bianthrone, could be caused by the transfer of protons to the molecule As already stated this band has been assigned to CCO and CCC stretches, and as such the reduction of the carbonyl region of the molecule to C-OH could contribute to the loss of this particular band Similarly, the decrease in intensity of the mode at ca 1350 cm^{-1} in the spectrum taken at -0 4 V compared with that at -0 1 V can be attributed to the reduction of C=O to C-OH as the loss of C=O would be expected to lead to a decrease in intensity of the band

		1581 cm^{-1}	1596 cm^{-1}	1612 cm^{-1}
-0 1v		1154	792	1339
ratio		1 457071	1	1 690657
-0 2v		1581 cm^{-1}	1596 cm^{-1}	1612 cm^{-1}
		1617	1218	1339
ratio		1 327586	1	1 099343
-0 24v		1581 cm^{-1}	1597 cm^{-1}	1612 cm^{-1}
		1998	1471	1846
ratio		1 35826	1	1 254929
-0 3v		1581 cm^{-1}	1597 cm^{-1}	1612 cm^{-1}
		1633	1214	1457
ratio		1 34514	1	1 817787
-0 33v		1582 cm^{-1}	1596 cm^{-1}	1612 cm^{-1}
		1550	1073	1620
ratio		1 444548	1	1 509786
-0 35v		1579 cm^{-1}	1596 cm^{-1}	1613 88 cm^{-1}
		4382	3293	2425
ratio		1 330701	1	0 736411
-0 375v		1578 cm^{-1}	1597 cm^{-1}	1613 88 cm^{-1}
		2700	2137	1652
ratio		1 263453	1	0 773046
-0 4v		1581 cm^{-1}	1594 cm^{-1}	1613 88 cm^{-1}
		2628	2317	1637
ratio		1 134225	1	0 706517

Table 4 2   Ratios of I_{1578}/I_{1597} and I_{1612}/I_{1597} taken from spectra recorded at varying potentials
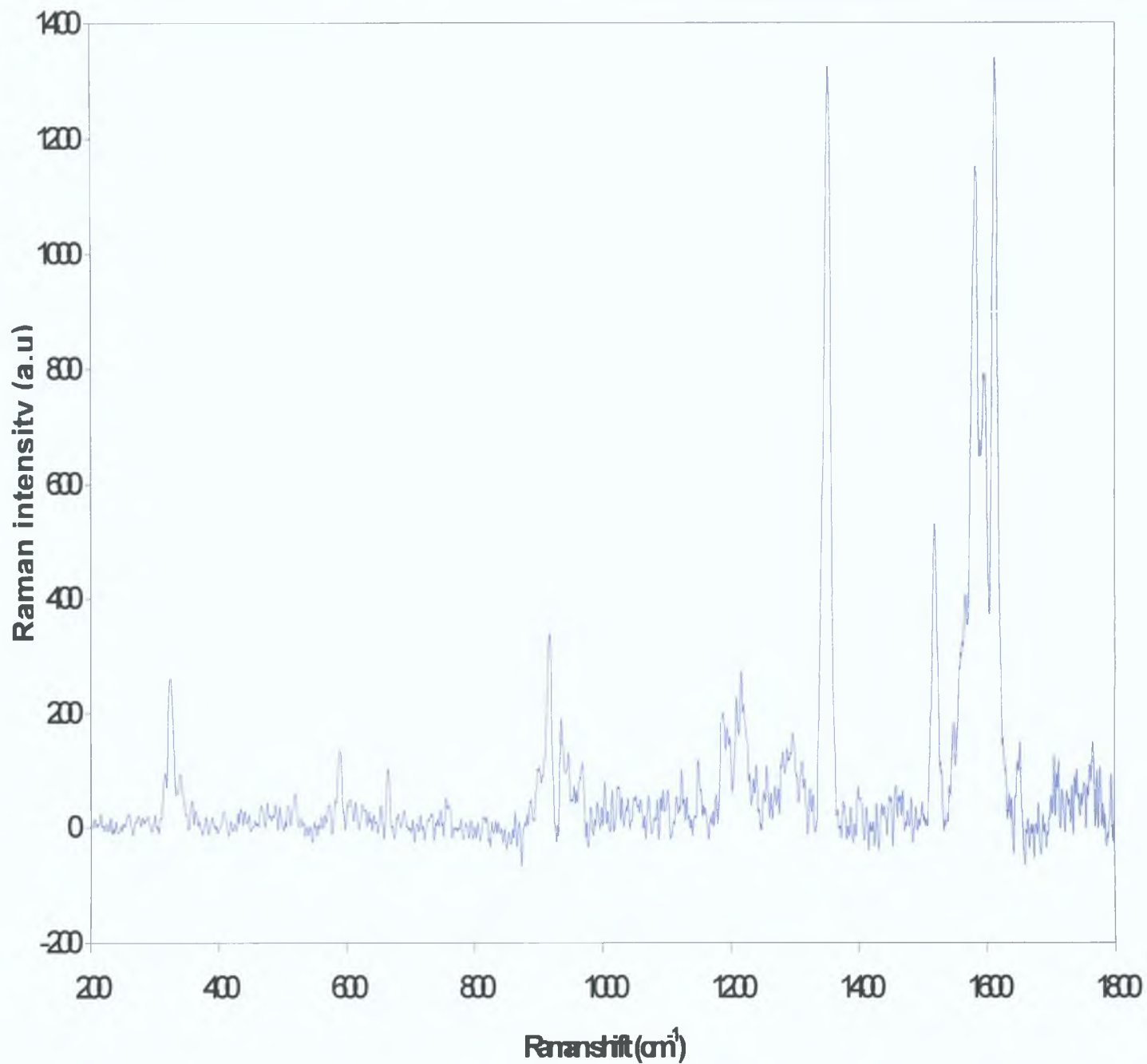
Figure 4.6.3.2.1 Raman spectrum of the bianthrone monolayer adsorbed on a GC electrode using the electrochemical cell shown in Figure 4.6.1.1. Excitation was provided by an Argon ion laser set to 457.8 nm

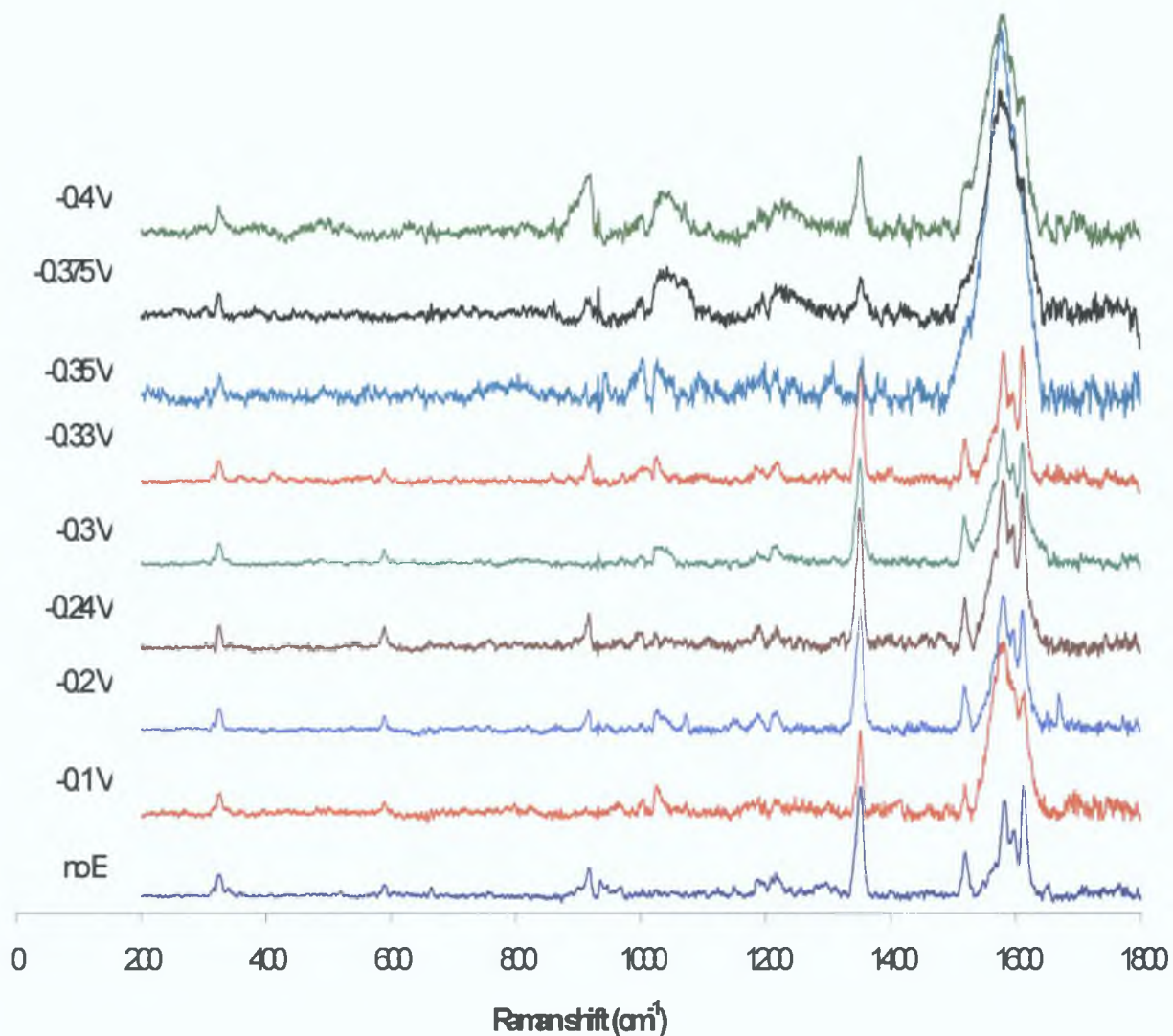*Figure 4.6.3.2.2 Raman spectra of a bianthrone monolayer adsorbed on to a GC electrode surface recorded at various potentials from –0.1 V (fully oxidised) to –0.4 V (fully reduced) using the electrochemical cell shown in Figure 4.11. Excitation was provided by a tuneable Argon ion laser set to 457.8 nm*

References

1 Rice, R J, Pontikos, N M, McCreery, R L, *J Am Chem Soc*, *112, 12,* **1990**

2 Banks, C E, Davies, T J, Wildgoose, G G, Compton, R G, *Chem Commun* *829-841,* **2005**

3 *Analytical Electrochemistry 2nd Ed*, Wang J, *Wiley-VCH,* **2000**

4 Fagan, D T, Hu, I-F, Kuwana, T, *Anal Chem*, *57, 2759-2763,* **1985**

5 Blaedel, W J, Mabbot, G A, *Anal Chem 50, 933, 1978*

6 Engstrom, R C, Strasser, V A, *Anal Chem*, *56, 136-141,* **1984**

7 Blaedel, W J, Jenkins, R A, *Anal Chem*, *47, 1337, 1975*

8 McDermott, M T, Kneten, K, McCreery, R L, *J Phys Chem*, *96, 3124-3130,* **1992**

9 Kamau, G N, Willis, W S, Rusling, J F, *Anal Chem*, *57, 545-551,* **1985**

10 Zhang, J, Anson, F C, *J Electroanal Chem*, *331, 945-957,* **1992**

11 Shi, K, Shiu, K-K, *Anal Chem*, *74, 879-885,* **2002**

12 Tammeveski, K, Kontturi, K, Nichols, R J, Potter, R J, Schiffrin, D J, *J Electroanal Chem*, *515, 101-112,* **2001**

13 Sarapuu, A, Vaik, K, Schiffrin, D J, Tammeveski, K, *J Electroanal Chem*, *541, 23-29,* **2003**

14 Shi, K, Shiu, K-K, *J Electroanal Chem*, *574, 63-70,* **2004**

15 Mogharrab, N, Ghourchian, H, *Electrochem Comm*, *7, 466-471,* **2005**

16 Gosavi, S, Marcus, R A, *J Phys Chem B, 104, 2067,* **2000**

17

18 McDermott, M T, McCreery, R L, *Langmuir, 10, 4307-4314, 1994*

19 Xu, J, Chen, Q, Swain, G M, *Anal Chem, 70, 3146-3154, 1998*

20 Komura, T, Isogai, S, Yamaguchi, T, Takahashi, K, *J Electroanal Chem 490, 70-78,* **2000**

21 *Interfacial Supramolecular Assemblies,* Forster, R J, Keyes, T E, Vos, J G, John *Wiley & Sons,* **2003**

22 Faulkner, L R, Forster, R J, *Anal Chem, 67, 1232-1239 1995*

23 Forster, R J, *Langmuir, 11, 2247-2255, 1995*

24 Hubbard, J B, Silin, V, Plant, A L, *Biophys Chem*, *75, 163-176,* **1998**

25

5.0 Analysis of Bianthrone in the Solid State on Glassy Carbon Electrodes

It is possible to store the mind with a million facts and still be entirely
uneducated
Alec Bourne

5.1 Introduction

Voltammetric studies of redox species are generally carried out, as in the previous chapters of this thesis, in solution or by adsorbing them onto suitable working electrodes. An alternative method of investigation involves immobilising solids onto electrodes such as gold, platinum, graphite or glassy carbon. [1,2,3,4,5] In some cases, this method allows insoluble species to be studied electrochemically. Furthermore, electrodes modified with solid-state redox active species have important applications in optical detection,[6] batteries,[7] redox supercapacitors and sensors. [8,9,10]

Two main methods exist for the transfer of solid materials onto electrodes. One of these, generally known as drop casting, involves the transfer of a paste or suspension of the material in a liquid to the electrode surface followed by drying of the electrode.[11] The other, simpler approach involves mechanical abrasion of the dry powdered material onto the surface of the electrode, resulting in the attachment of a random array of particles. The former method is more often employed when a high surface concentration is necessary. The latter is part of the protocol for the analytical method called abrasive stripping voltammetry.[12] The mechanical abrasion of material to an electrode surface was the method employed here to transfer bianthrone to the glassy carbon surface.

Electrochemistry, particularly voltammetry, is a powerful tool in the study of solid state redox active molecules as it can provide direct information on the identity of the species and redox composition and can also provide information on the mechanism of charge and mass transport through the bulk material.[13] Recently, examples of the use of electrochemistry in the study of solid-state redox activity have become fairly widespread in the literature. An illustrative example can be seen in a study by Keane et al. [2] Here, mechanical abrasion was employed to deposit Osmium Tris Dimethoxy Bipyridyl onto platinum microelectrodes, as a random array of particles, to examine the voltammetric properties of the solid. Comparisons between solid phase voltammetry and solution phase voltammetry revealed similarities between the two phases. The solid phase voltammetry was observed to be close to ideally reversible and the formal potential of the solid phase was observed to be similar to that of the solution phase under the same conditions of electrolyte. These

observations suggested that the local microenvironments in the solid phase were similar to those for the solution phase The measured heterogeneous electron transfer rate constant for both solid and solution phase reactants were also indistinguishable

Examinations into electron self exchange on solid state cocrystals of hydroquinone and bipyridyl triazole were carried out by Keyes et al [14] Mass and charge transport through a solid deposit of the cocrystal were investigated using spectroscopy, electrochemistry and microscopy Electrochemical analysis of the solid deposits revealed what is commonly referred to as "break in phenomena" This phrase describes voltammetric changes that are related to ion movement, solvation of redox centres and redox induced structural changes Such phenomena have been observed elsewhere and are relevant to the results presented here As observed by Keyes et al, the voltammetric changes observed involved the decrease in peak heights by up to 20% over the first fifty cycles This occurred when both sodium perchlorate and perchloric acid were used as supporting electrolyte Shifts in potentials were also observed during break-in In $NaClO_4$, the half wave potential for oxidation shifted more negatively indicating that the film was more easily oxidised after the first few cycles In $HClO_4$, the half wave potential for reduction shifted more negatively, which indicated that the film was more easily reduced in the first cycles Also of relevance to the work presented here was the use of Raman spectroscopy to probe structural changes resulting from the switching of redox state It was seen that Raman spectroscopy only probed the outer layers of the deposit However, this provided useful information on the extent of redox conversion Raman spectra of the solid film deposited on glassy carbon electrodes were recorded at open circuit potential, when the film was fully reduced and at a potential when the film was fully oxidised The supporting electrolyte for these experiments was $LiClO_4$ Comparisons between the spectra recorded when the film was in the two different redox states revealed that bands associated with the hydroquinone, observed at open circuit potential disappeared and were replaced with bands associated with the quinone when fully oxidised A shift in a band characteristic of the carbonyl group to a lower frequency suggested that the carbonyl participated in a H-bonding interaction with the adjacent pyridimum moiety

The main objective of the work presented here is to analyse the voltammetric properties of bianthrone solid deposits on glassy carbon electrodes The intention is

194

to extract information on the solvation of the solid-state deposit and also to examine its redox characteristics compared to the monolayer redox characteristics Detection and examination of any break-in phenomena involved with the effect of the solvent and supporting electrolyte on the solid deposit would be valuable Raman spectroscopy has been used to examine any redox induced structural changes to the bianthrone solid deposit Also Raman spectroscopy has been employed to examine changes to the structure of the solid deposit due to break-in phenomena

Significant insights into the voltammetry of microcrystals attached to electrode surfaces, which are in contact with aqueous electrolytes, have been made However, hydrophobic materials can give poorly defined voltammetric responses under these conditions The addition of a small quantity of organic solvent however can greatly increase the percentage of the species that are electroactive and the dynamics of charge transport through the solid The improvement in voltammetric signal may arise because an organic solvent can solvate the redox active solid, or can trigger structural changes within the solid by either facilitating oxidation state dependent electrocrystallisation or by "swelling" the deposit and thus creating free volume for anion incorporation

Evidence for this phenomenon has been noted in the experiments discussed in this chapter Briefly, no redox activity was observed in voltammetry involving a GC electrode modified with a solid bianthrone layer immersed in water with perchloric acid as the electrolyte Redox activity was achieved following addition of DMF to the solution

5.2 Experimental

5 2 1 Electrode preparation

Solid bianthrone layers were prepared on GC electrodes by mechanical abrasion of solid bianthrone onto the electrode surface Small amounts of solid bianthrone were placed into a clean weighing boat and a freshly polished glassy carbon electrode was pressed and rubbed into the powder This process caused some of the bianthrone solid to adhere to the surface of the electrode as a solid layer This process is similar to previously reported methods of solid deposit formation [15 16 17 18] Prior to the formation of the solid bianthrone deposit on the electrode surface, the electrode was polished with a slurry made of 0 5 μm α alumina and Milli-Q water on a polishing pad until a mirror like finish was achieved The electrode was then sonicated for five minutes and rinsed with acetone and Milli-Q water and dried These modified electrodes were then placed into a solution containing 0 5 M $HClO_4$ with 20 % DMF in Milli-Q water Cyclic voltammetric analysis revealed that no redox activity could be discerned in Milli-Q water with a small $HClO_4$ concentration and as a result DMF was introduced into the solution Redox activity was observed with DMF in the solution It was important to keep the DMF concentration low so as to prevent dissolution and thus to maintain the integrity of the solid layer A 20% DMF concentration was found to be satisfactory to satisfy both issues

5 2 2 Electrochemistry

Electrochemistry was carried out using a CH Instruments 660A potentiostat Reference electrode was a Ag/AgCl sat KCl reference electrode Counter electrode was a platinum wire A diagram of the Raman electrochemical cell can be found in chapter 4 In the Raman experiments, reference was also a Ag/AgCl sat KCl reference electrode and counter electrode was a coiled platinum wire

5 2 3 Raman Spectroscopy

Raman spectroscopy was employed to examine changes in solvation and intermolecular interaction in the solid layer   Also, Raman spectra of the solid layer were recorded at different potentials between $-0\ 22$ V (where the layer is in its oxidised state) to $-0\ 375$ V (where the layer is in its reduced state)   These experiments involved the same electrode cell set-up that was employed to study bianthrone monolayers   Raman spectra were recorded on a Horiba Jobin Yvon LabRAM HR 2000 spectrometer equipped with an integral confocal microscope   A 457 9 nm excitation line was employed from a water-cooled tuneable argon ion laser The scattered radiation was observed with 180^0 geometry with a cooled (-75 ^{0}C) charge-coupled device (CCD) detector   The laser beam was focused through a 300 μm confocal hole onto a spot of 1μm in diameter with a long focal length objective of the order of 10X   Data acquisition times were every 2 seconds with 30 accumulations   The holographic grating (1800 grooves/mm) allowed resolution of 0 3 cm ^{1} The instrument was calibrated using a silicon wafer of surface flatness ca 1μm order (520 cm ^{1}) and accuracy was estimated to be less then 0 5 cm ^{1} Laser power was about 23mW

5 3 General Electrochemical Properties

5 3 1 Cyclic voltammetry

Figure 5 3 1 1 shows a cyclic voltammogram recorded by immersing a polished GC electrode modified with a solid bianthrone layer m to a solution containing 20 % DMF and 0 5 M HClO$_4$ The reference electrode employed was an Ag/AgCl reference electrode and the counter electrode was a coiled platinum wire This voltammogram was taken after three hours immersion in the solution There are obvious differences between this voltammogram and those taken of bianthrone monolayers, an example of which can be seen in Figure 4 3 1 in chapter 4 In particular, the appearance of two redox couples compared to the one observed from monolayer studies The first couple appears at circa –0 2 V The second appears at circa –0 3 V, but is not visible in initial voltammograms taken immediately after the electrode was immersed in the solution This suggests that a change occurs in the solid deposit over time A second observation is that the maximum current, i$_p$ is approximately ten times lower than that for the monolayer This suggests that the molecules in the adsorbed monolayer have greater contact with the surface of the electrode than those in the solid film

5 3 2 Scan Rate dependence and dynamics of charge transport

Investigations into the dependence of the peak current on the scan rate of the solid bianthrone deposit were carried out in order to determine a rate of charge diffusion through the solid deposit It was found that an approximately linear relationship exists between the peak current, i$_p$, and the square root of the scan rate $v^{1/2}$ An illustrative example can be seen in Figure 5 3 2 2 , showing a plot of i$_p$ vs $v^{1/2}$ for i$_p$ taken at –0 224 V This relationship suggests that charge transport through the solid layer is diffusion controlled The relationship between i$_p$ and $v^{1/2}$ is described by the Randles-Sevcik equation [14,22]

$$i_p = \left(2\ 69x10^5\right)n^{3/2} A D_{app}^{1/2} C_a v^{1/2} \quad (5\ 1)$$

In Equation (5 1), I_p is the peak current, n is the number of electrons transferred, A is the area of the electrode, D is the diffusion coefficient C is the concentration of the solid bianthrone deposit and $v^{1/2}$ is the square root of the scan rate When plotted, the slope of the I_p vs $v^{1/2}$ allows for the calculation of D_{app} The fact that bianthrone is in the solid phase in these experiments provided a barrier to the calculation of C_o however it is possible to calculate D for a range of concentration values in the range 1 x 10^{-4} molcm^3 ≤ [Bianthrone] ≤ 1 x 10^3 molcm^3 i e from 0 1 to 1 0 M This provides a diffusion constant for charge transfer of 8 20 ± 0 06 x 10^{12} cm^{2}s^1 for 1 x 10^4 molcm^{-3} and 8 20 ± 0 06 x 10^{-14} for 1 x 10^3 molcm^3

Figure 5.3.1.1 Cyclic Voltammogram obtained from a thick solid film on a polished GC electrode that was immersed in 20 % DMF with 0.5 M HClO₄ as the supporting electrolyte. This voltammogram was recorded following immersion for approximately 3 hours.
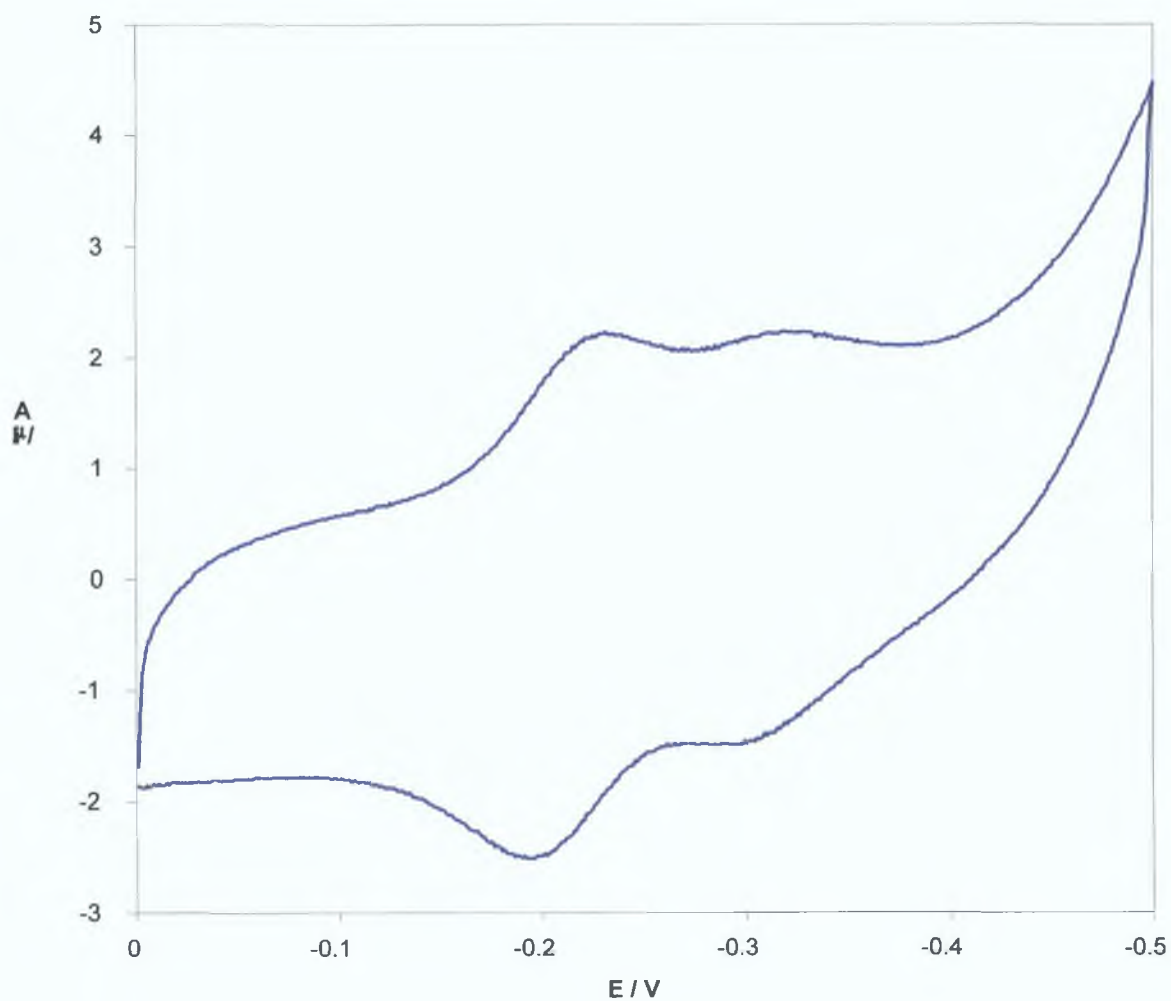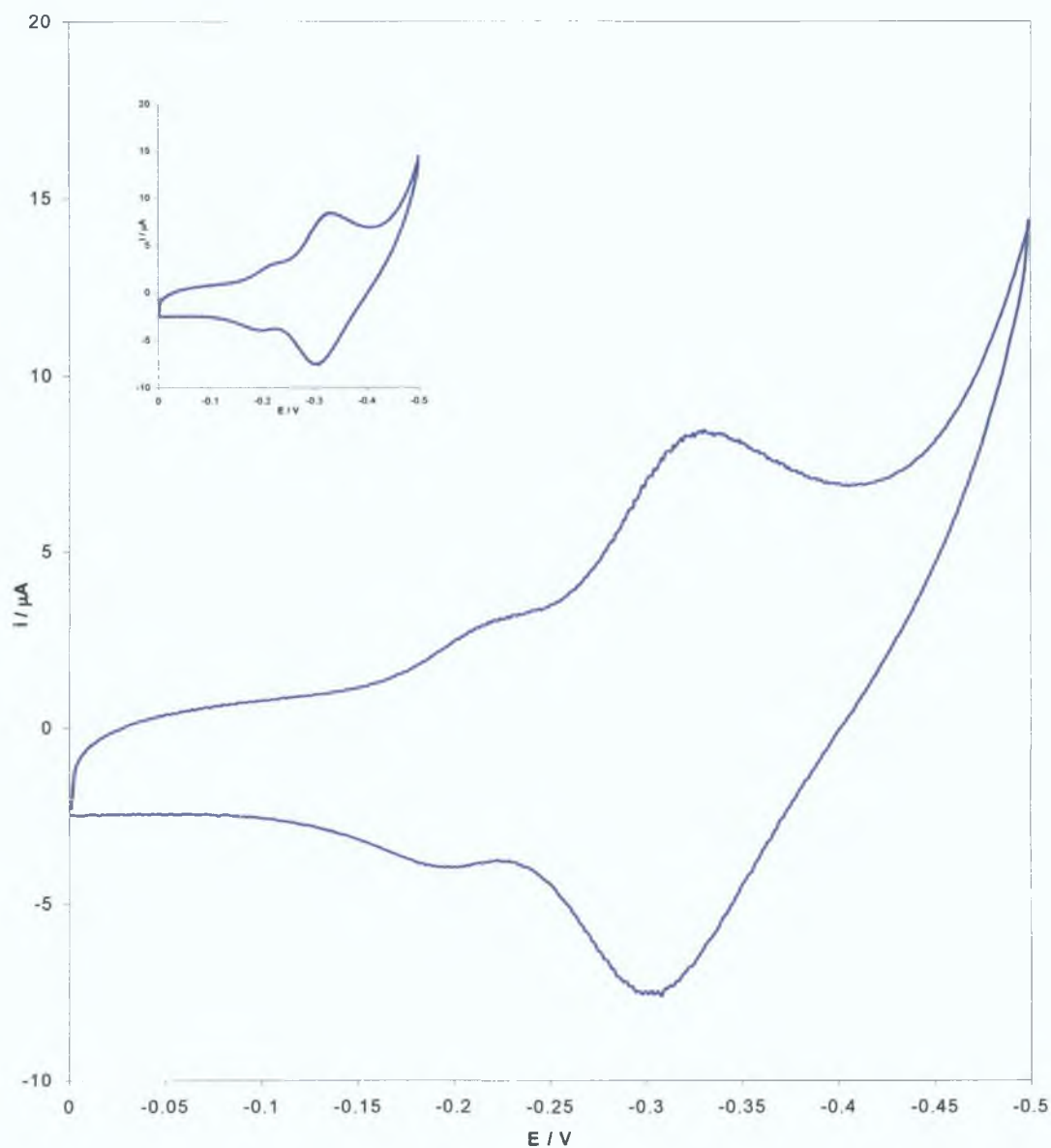
Figure 5.3.1.2: Cyclic Voltammogram obtained from a thick solid film on a polished GC electrode that was immersed in 20 % DMF with 0.5 M HClO₄ as the supporting electrolyte. This voltammogram was recorded following exposure to atmospheric air for approximately 30 minutes. The inset shows a voltammogram of the same thick film taken after approximately 16.5 hours.
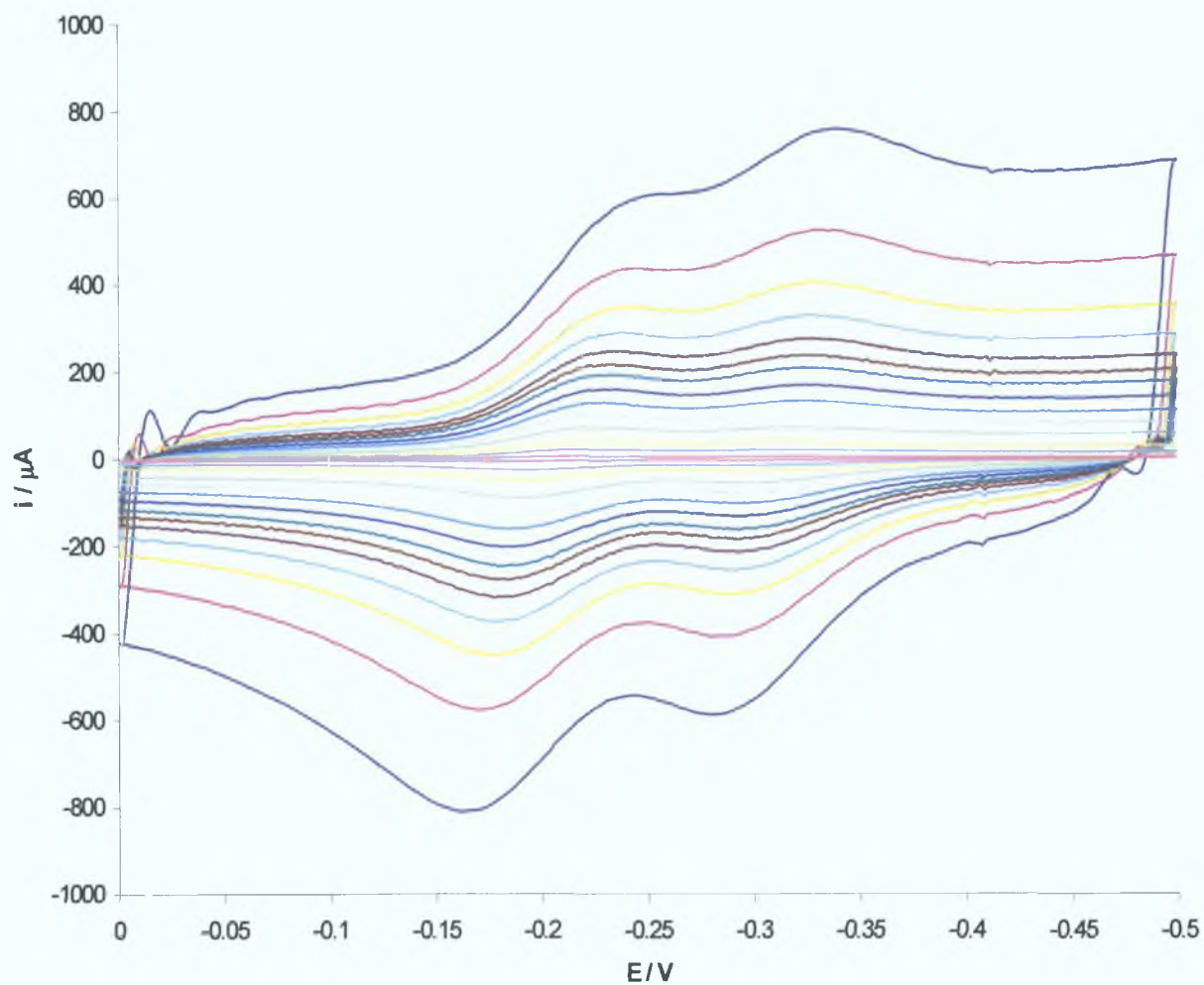
Figure 5.3.2.2:   Overlaid voltammograms at different scan rates for a solid bianthrone deposit modified glassy carbon electrode immersed in 20% DMF 80% H_2O.   Reference was provided by a Ag/AgCl sat KCl reference electrode.   Counter electrode was a platinum wire.   Scan rates are from smallest to largest 1, 5, 10, 20, 29.4, 38.5, 50, 62.5, 71.4, 83.3, 100, 125, 167, 250 vs^{-1}.

y=1 54E-05x - 1 68E-05
$R^2 = 9 83E-01$

y=-1 67E-05x+2 09E-05
$R^2 = 9 71E-01$
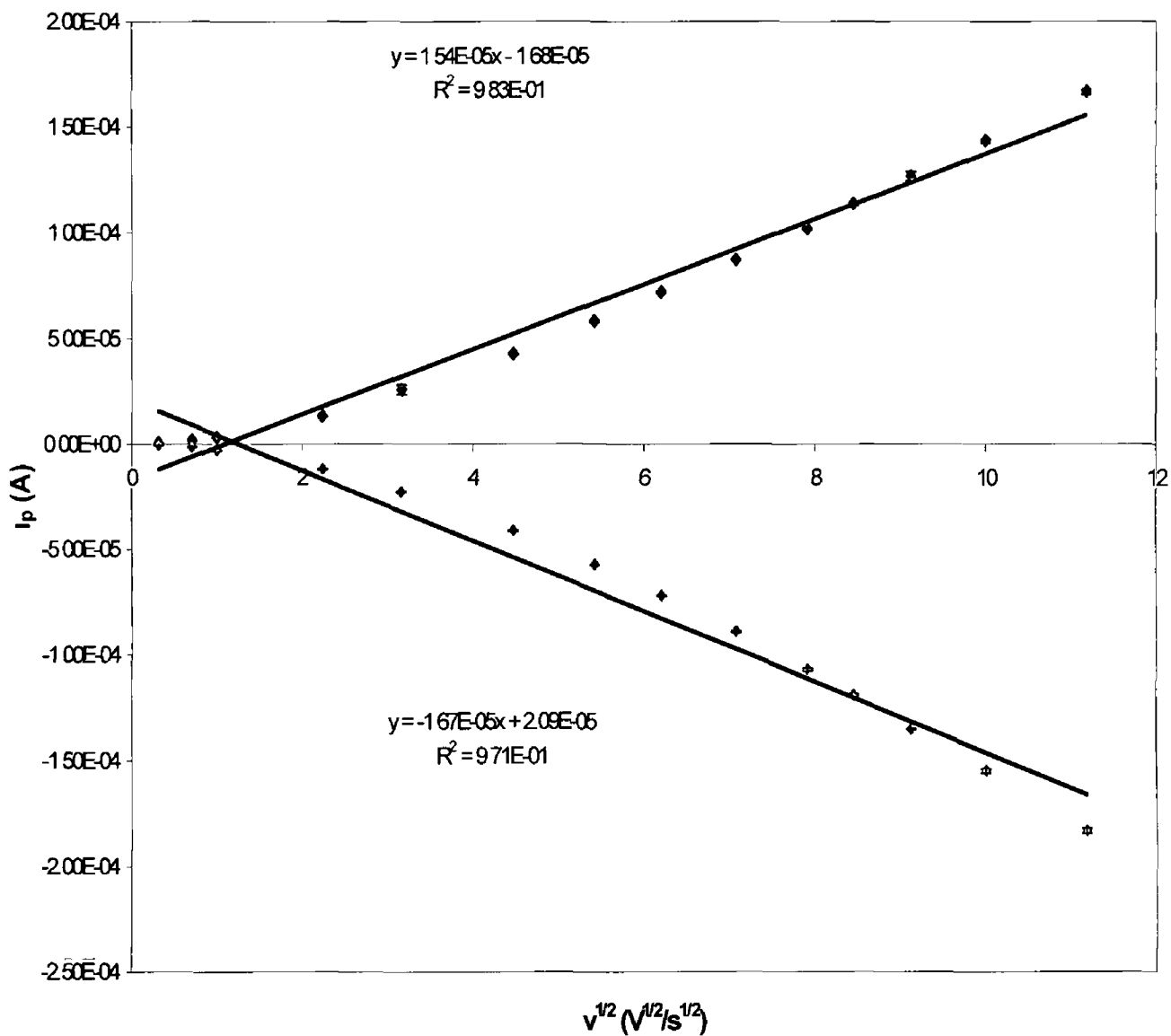
I_p (A)

$v^{1/2}$ $(V^{1/2}/s^{1/2})$

Figure 5 3 2 2   Plot of peak current versus the square root of the scan rate for a solid bianthrone deposit on a glassy carbon electrode immersed in 20 % DMF 80 % H_2O with 0 5 M $HClO_4$ as the supporting electrolyte   Reference was a Ag/AgCl sat KCl reference electrode   Counter electrode was a platinum wire

5.3.3 Analysis of the solid layer over time

Figure 5.3.3.1 shows overlaid voltammograms of the solid film taken over approximately twenty-three hours. It can be seen that initial voltammograms show the emergence of one redox couple at ca –0.29 V, with no appearance of the second redox couple at approximately 3733 s. The area of this curve increases before the emergence of the second couple. However, following its appearance, the second couple, at ca –0.41 V, increases until its area becomes greater than that of the couple at –0.29 V. These observations suggest changes to the solid film are taking place over this time period. Figure 5.3.3.2, a plot of peak current versus time, illustrates this observation. It can be seen that after 5558 s the peak current of the redox couple at –0.29 V reaches its maximum of 3.161 μA and begins to decrease to a final value of 1.36 μA. The peak current of the redox couple at –0.411 V increases from zero at t = 0 s to a maximum, at 18292 s, of 5.616 μA. This result suggests the occurrence of "break in" phenomena in the solid layer. Such phenomena have been reported previously in the solid-state electrochemistry of other compounds immobilised on electrodes and are associated with ionic movement and solvation of the solid layer. [14, 19, 20, 21] It is possible that, over time, the supporting electrolyte solution, perhaps preferentially DMF, permeates the solid layer, facilitating the oxidation of the deposit and giving rise to the peak at –0.41 V. The more negative redox peak is close to the redox potential seen in voltammograms of the adsorbed monolayer suggesting that the local microenvironment of the molecules at this potential is similar to those adsorbed at the electrode surface in monolayers i.e. bianthrone is well solvated. If this hypothesis is correct, the difference in E^0 values arises from differences in the extents to which the immobilised bianthrone molecules are solvated. The difference in free energy between the two redox couples has been calculated by calculating the difference in redox potentials of both couples to get a value for ΔE^0 and inserting this value into Equation (5.2)[22]

$$\Delta G = nF\Delta E^0 \quad (5.2)$$

The difference between the redox potentials is 0.1023 ± 0.008 V. Inserting this into Equation (5.2) gives a value of 19.74 ± 1.54 kJmol⁻¹. While there is limited

experimental data available in the literature, this value compares favourably to the free energy of solvation for large aromatic and quinone type molecules For instance, the free energy of solvation of anthracene in a variety of solvents including supercritical ethane, supercritical CO_2, and supercritical CHF_3 were calculated to be 23 1 ± 0 5, 26 7 ± 1 0 and 30 ± 5 kJmol[1] respectively [23] The free energy of solvation of anthraquinone reported in the same publication in supercritical CO_2 was found to be 17 8 ± 1 0 kJmol[1] Given the difference in free energy between the two redox couples in the voltammograms of the solid bianthrone deposits on GC electrodes and the proximity of the second redox potential to the redox potential of the adsorbed monolayer, it is not unreasonable to speculate that the molecules in the solid deposit are being solvated over time and that the weakly solvated form gets converted, by DMF to a fully solvated form over time
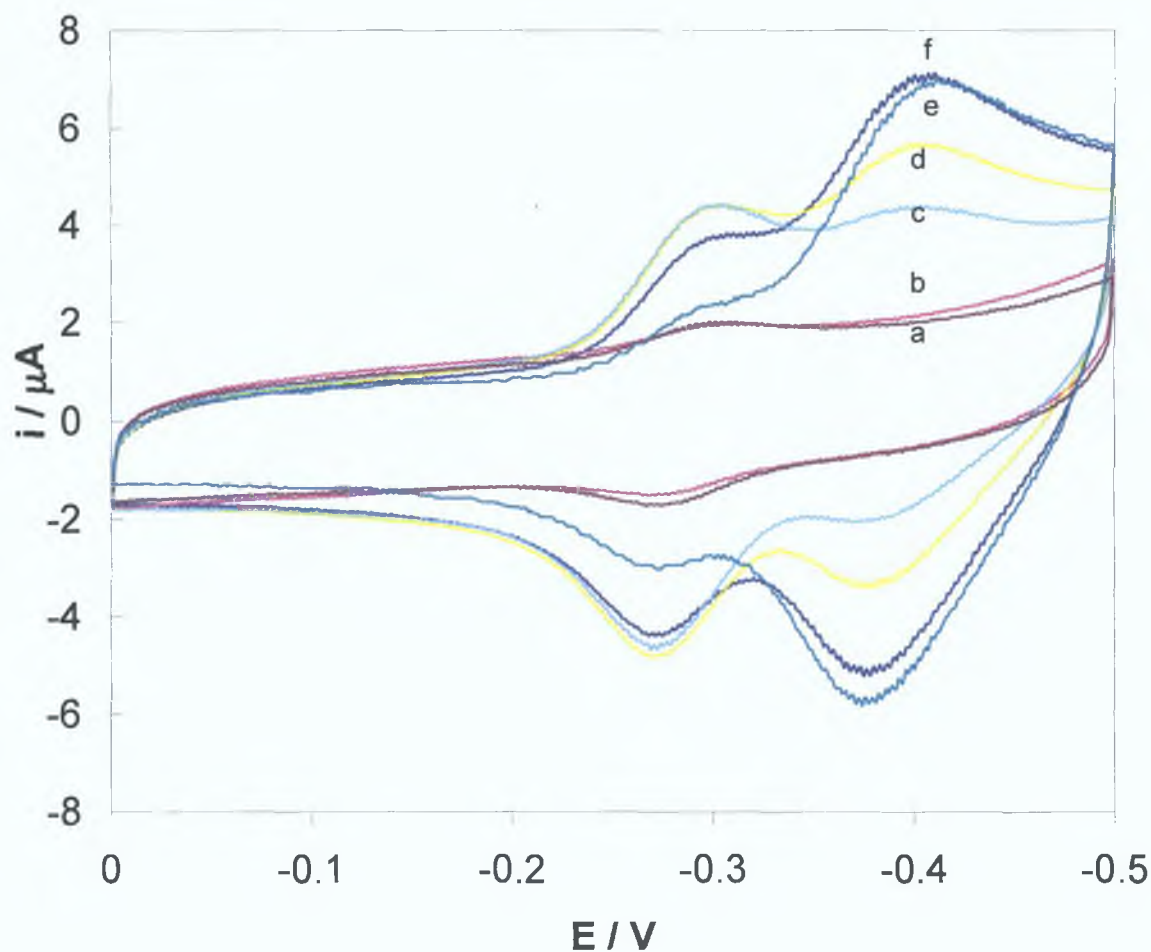
Figure 5.3.3.1: Cyclic voltammograms of a solid bianthrone layer on a GC electrode of area 0.07069 cm^{-1}recorded over time. Supporting electrolyte was 0.5 M HClO$_4$ dissolved in 20 % DMF. Reference electrode was a Ag/AgCl sat. KCl reference electrode. Counter electrode was a platinum wire. The times for the cyclic voltammograms were, from lowest to highest were (a) 0, (b) 104, (c) 3733,(d) 7362,(e) 16435 , (f) 83585 s

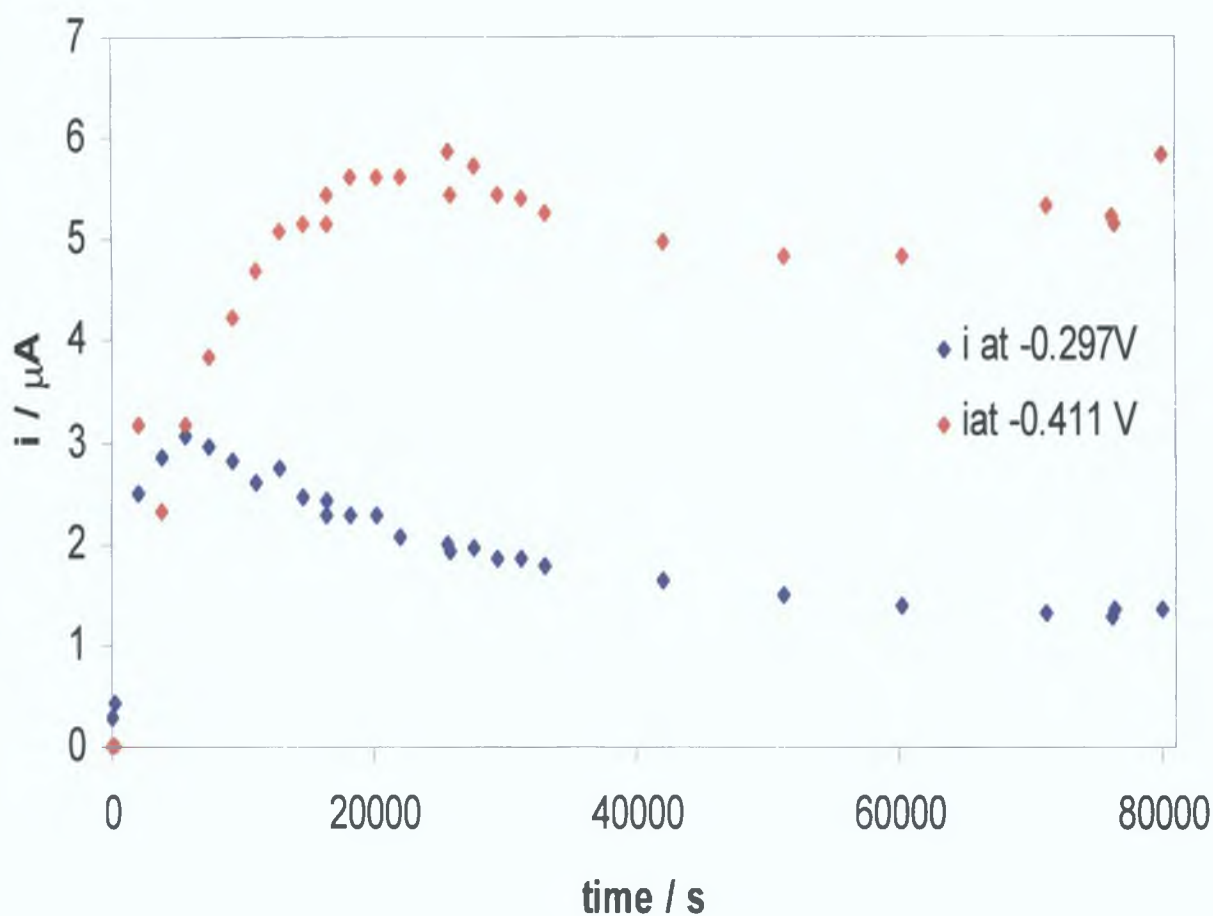*Figure 5.3.3.2: Graph of i_p versus time for the two redox couples visible in the cyclic voltammogram of solid bianthrone on GC of area 0.07069 cm^{-1} recorded over time. Supporting electrolyte was 0.5 M HClO$_4$ dissolved in 20 % DMF. Reference electrode was a Ag/AgCl sat. KCl reference electrode. Counter electrode was a platinum wire.*

5 3.4 Effect of atmospheric air on the Solid Film

Experiments were carried out to examine the effect of atmospheric oxygen on the redox state of the solid film This was done to establish whether atmospheric oxygen would "reoxidise" the thick film when in its reduced state and, if so, the extent to which this phenomenon would occur This was carried out by recording voltammograms prior to air exposure and comparing them with voltammograms recorded immediately after the reimmersion of the modified electrode in to the supporting solution An oxygen free environment around the cell was maintained by placing the electrochemical cell in a glovebag, which was filled with nitrogen gas In the voltammograms recorded following reimmersion the initial potential was set at –0 6 V, where bianthrone is in its reduced state If any reoxidation did occur, it was expected that a larger current would be observed at the initial potential, owing to the reoxidised molecules in the film being reduced If no reoxidation occurs, no increase in current is expected, as all the molecules in the film would still be in their reduced state Figure 5 3 4 1 shows the voltammogram recorded immediately following reimmersion, with, in inset, the voltammogram recorded immediately prior As can be seen, there is an increase in the current observed at ca –0 6 V, where bianthrone should be in its reduced state, which is not apparent in the voltammogram recorded prior to its exposure to air This is due to some reoxidation of the solid layer by atmospheric oxygen
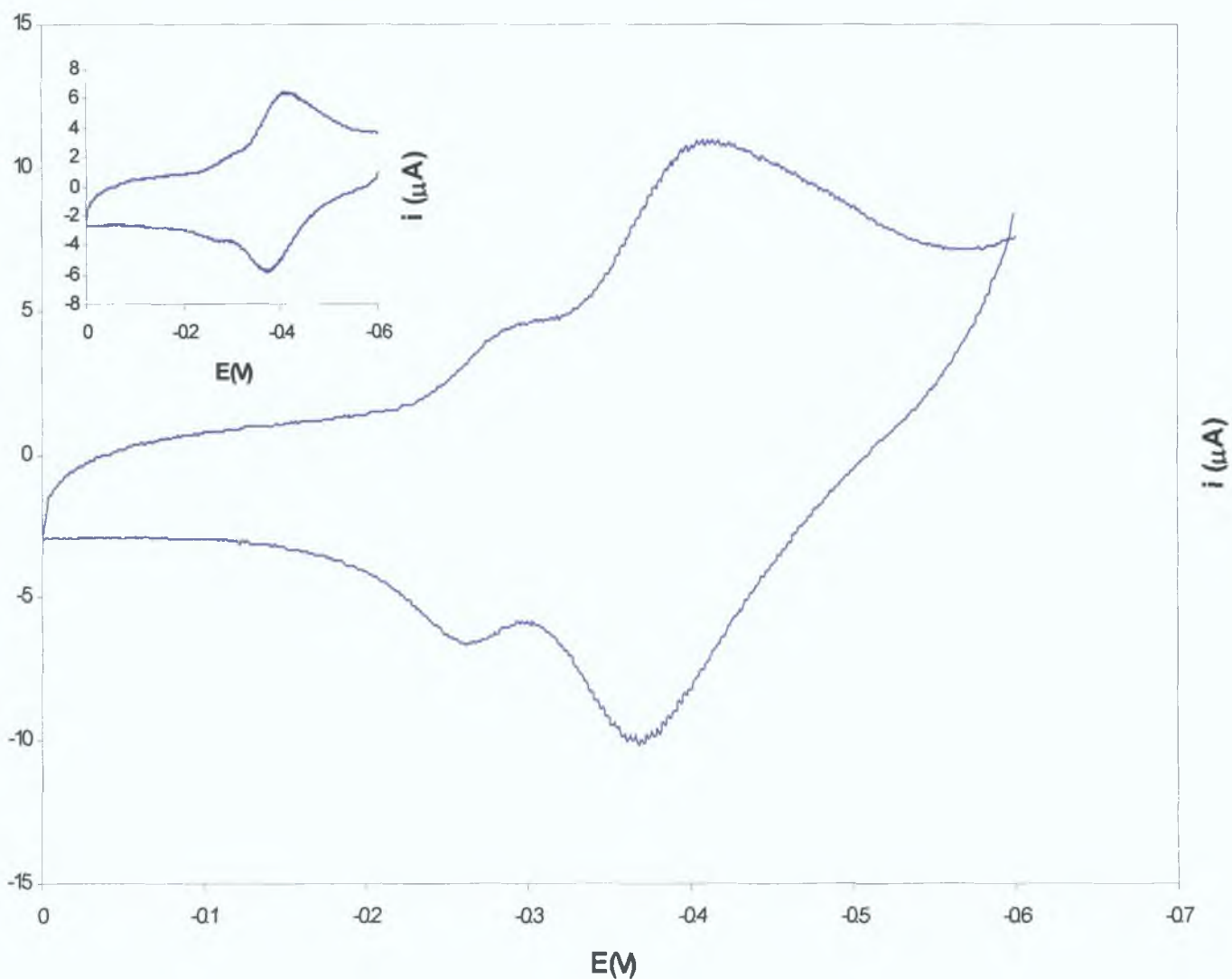
Figure 5.3.4.1: Cyclic voltammogram recorded following exposure of the GC electrode modified with the solid bianthrone layer to atmospheric air for approximately thirty minutes and, in set, cyclic voltammogram recorded prior to exposure. Reference electrode was a Ag/AgCl saturated KCl reference electrode. Counter was a platinum wire. An increase in current can be seen in the voltammogram following air exposure that is absent in the voltammogram prior.

5.4 Raman Analysis of Bianthrone Solid Layer

5 4 1 Solution subtraction and Normalisation

The spectra presented in this chapter have been corrected for the supporting electrolyte solution containing 20 % DMF and 0 5 M $HClO_4$ This was achieved by obtaining a spectrum of the supporting electrolyte solution and subtracting this spectrum from the bianthrone spectra using the software for the Horiba Jobin Yvon LabRAM HR 2000 spectrometer Also, as in previous chapters, the spectra were normalised to the band at 325 cm^{-1} as this band appeared in all spectra and its intensity was relatively constant in all spectra

5.4.2 Raman analysis of the solid bianthrone deposit over time

Prompted by the changes observed in the voltammetry of the bianthrone solid layer over time, Raman spectra were acquired over approximately six hours to see if any changes in spectra, which could indicate changes in solvation or intermolecular interaction, were apparent These spectra were obtained using the same cell as was used to examine bianthrone monolayers on GC electrodes The voltammograms of the solid layer, which were taken at the same time as the spectra are shown in Figure 5 4 2 1 The voltammograms exhibit the same characteristics as have been previously described The second redox couple "grows" over the time period while the first redox couple increases only slightly before reaching a relatively constant area The Raman spectra recorded in conjunction with these voltammograms are shown in Figure 5 4 2 2 and are compared with the solid spectrum

The first spectrum recorded of the layer (denoted 1232 in Figure 5 4 2 2), following subtraction of the supporting electrolyte spectrum, is comparable to that of the solid The corresponding voltammogram shows the appearance of the first redox couple and the complete absence of the second Any differences between the two spectra appear to be differences in band intensities rather than the appearance or disappearance of specific bands This can be seen at lower wavenumbers, with the band at 589 4 cm^{-1} showing a notable increase in the spectrum This band is assigned to CCC and CCO stretches An increase is also observed in the band at 1075 cm^{-1} Ulicny et al reported a band at 1088 cm^{-1} that was assigned to CCH CC and CCC stretches and it is proposed that this band is also due to these stretches [24] The most

notable increase in the spectrum is that of the band at 1353 cm^{-1} This band exhibits a slight shift in wave number from 1350 cm^{-1} in the solid spectrum to 1353 cm^{-1} in the solid layer in the supporting electrolyte solution There is also an almost doubling of this bands intensity The bands in the region 1450 to 1710 cm^{-1} exhibit a decrease in intensity between the solid powder and the solid layer in the supporting electrolyte solution However, the three bands at ca 1584 cm^{-1}, 1601 cm^{-1} and 1620 cm^{-1} become much more distinct than those in the powdered solid spectrum The increase observed at 1350 cm^{-1} in the 1232 spectrum remains over the whole time scale of the experiment As in previous chapters, the band at 1435 cm^{-1} in the powdered solid spectrum coincides with a band in the supporting electrolyte spectrum and as a result was not considered further Its disappearance from the spectra in the supporting electrolyte solution is not, therefore, a result of any physical or chemical change in the solid layer

Aside from the change to the band at 1353 cm^{-1}, no obvious changes were apparent from the spectra recorded over time The bands in each spectra remained and none were seen to change in intensity This may be due to the fact that there is no change occurring at the "top" of the layer, and that the changes evidenced by the voltammetry were occurring at the electrode surface, inaccessible to the excitation laser of the Raman spectrometer
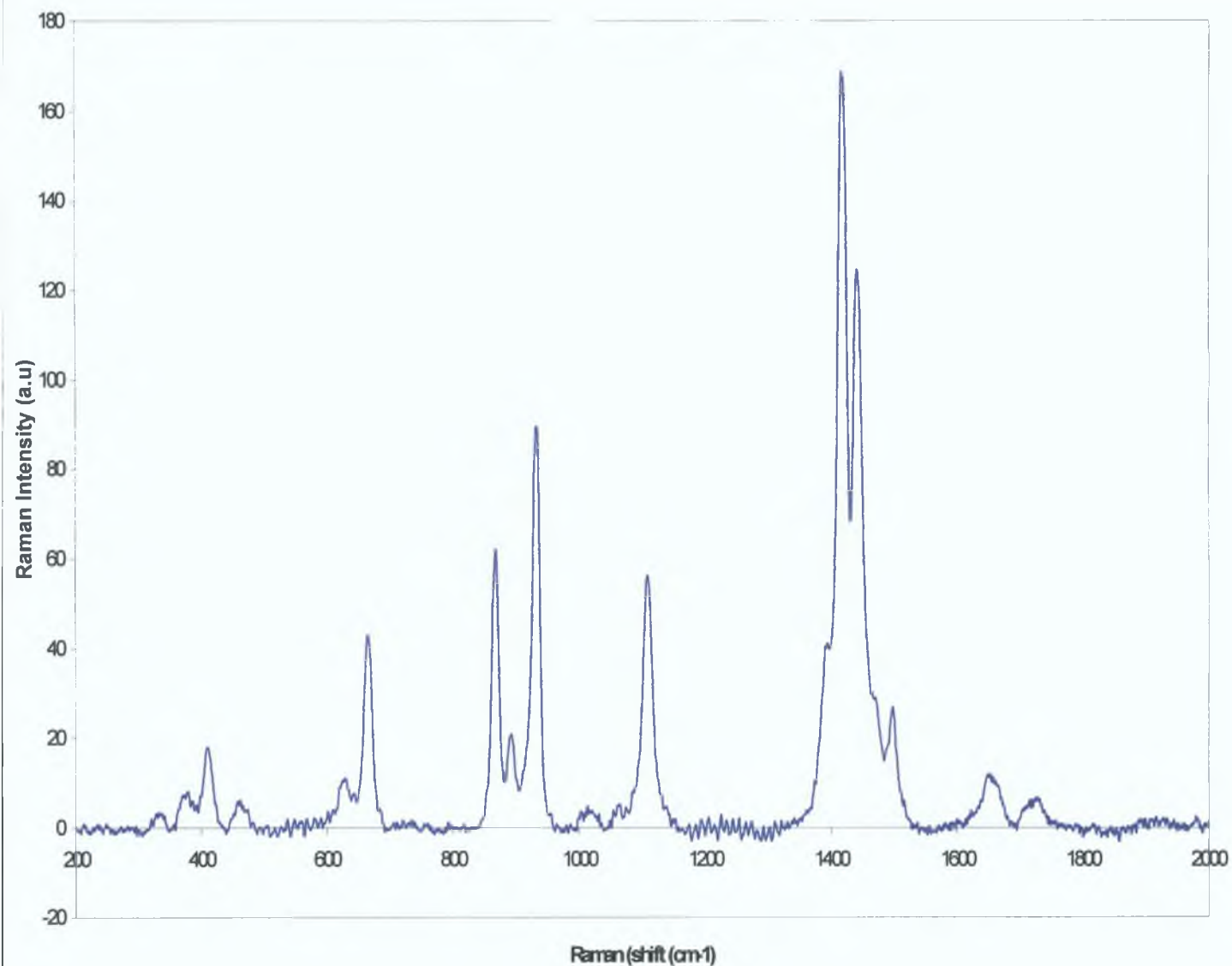
Figure 5.4.1.1: Raman spectrum of supporting electrolyte solution. Solution contained 20 % DMF in Milli-Q water with 0.5 M HClO₄. Raman excitation wavelength was 457.8 nm from a tuneable argon ion laser. This spectrum was used for solvent subtraction from spectra of bianthrone solid layers on GC electrodes.
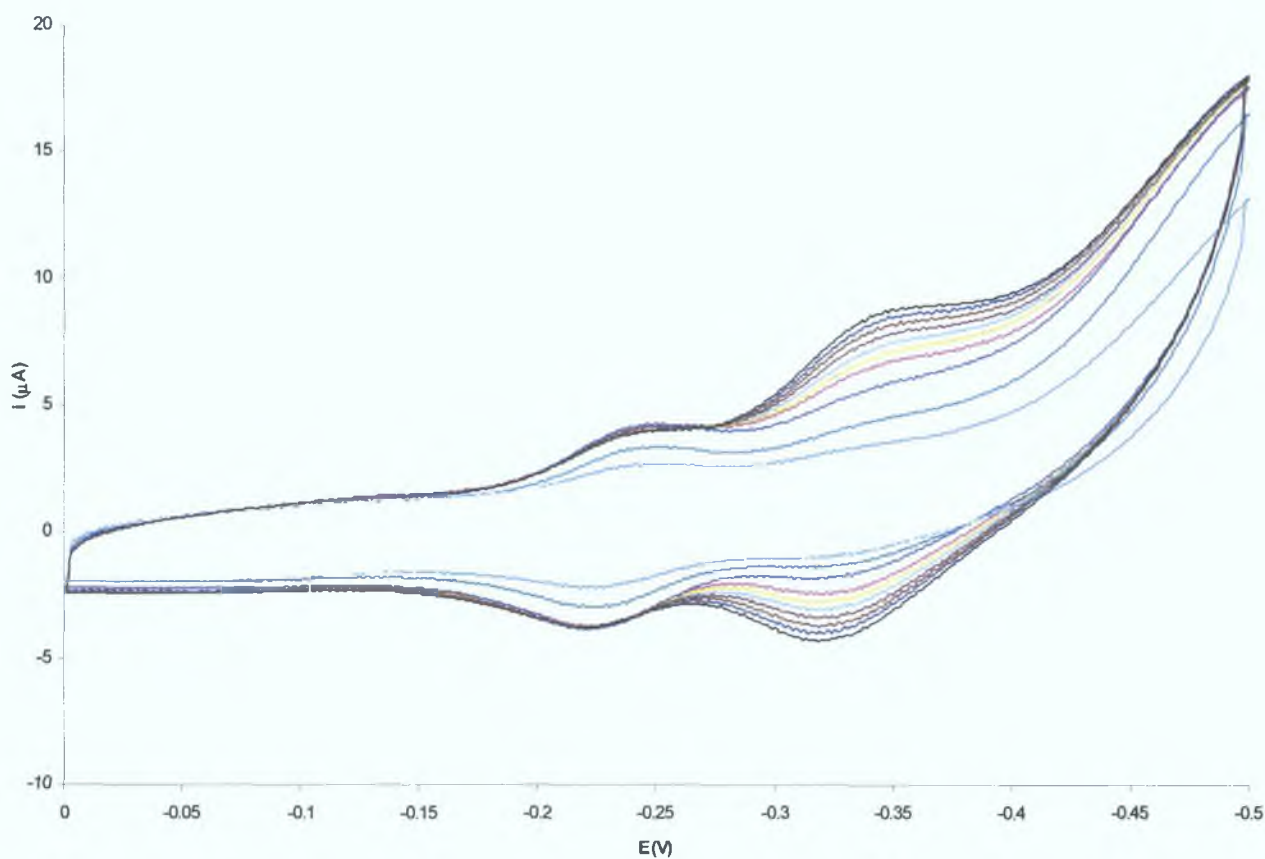
Figure 5.4.2.1: Overlaid cyclic voltammograms of a solid bianthrone layer on a GC electrode of area 0.07069 cm⁻¹. Voltammograms were obtained using an electrode cell modified for use in conjunction with a Raman microscope. The reference electrode was a Ag/AgCl sat KCl reference. Counter electrode was a coiled platinum wire (see cell diagram in Chapter 4). Voltammograms are taken at different times.
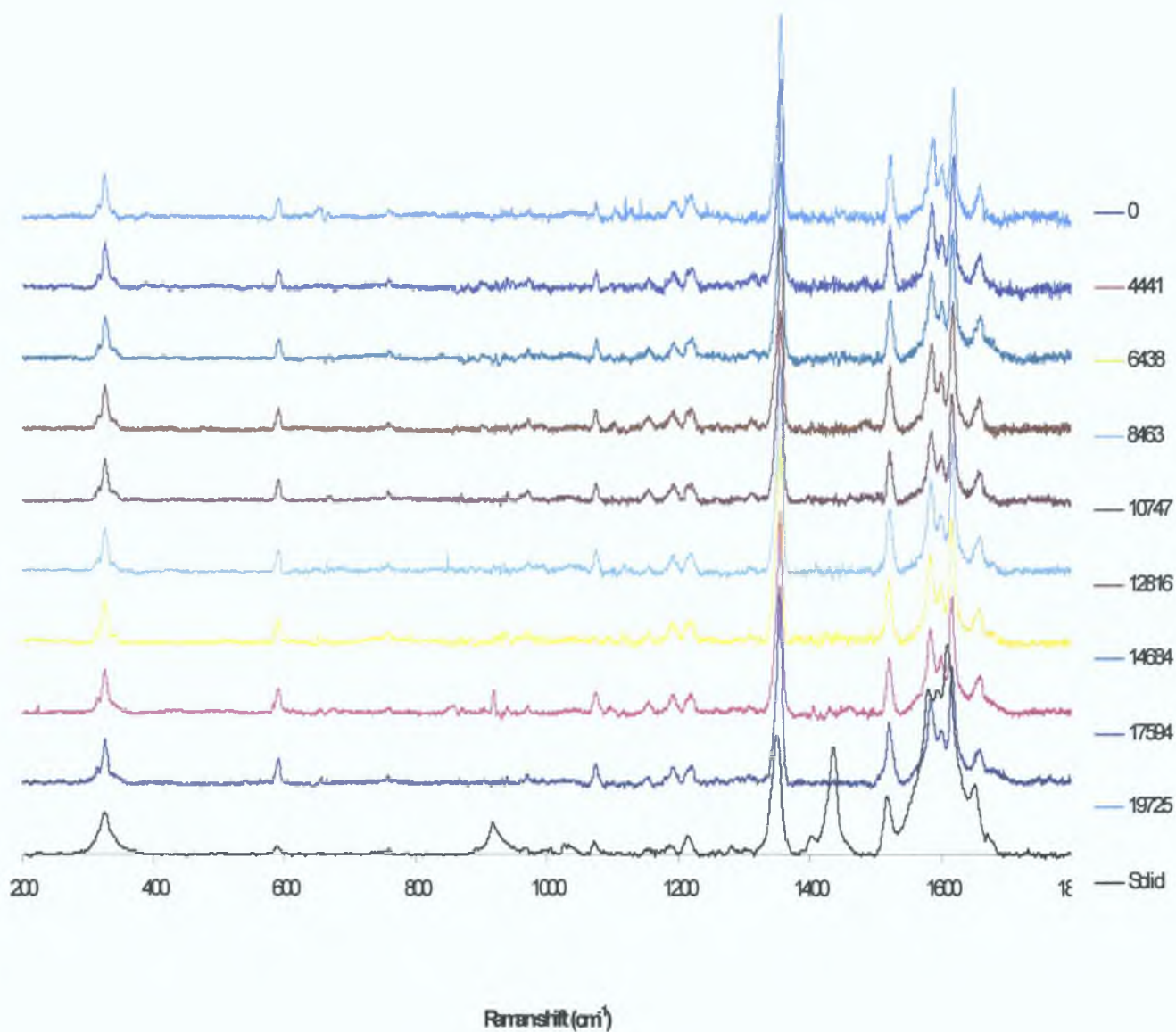
Figure 5.4.2.2: Raman spectra of solid bianthrone layer on a GC electrode, of area 0.07069 cm^{-1}, at different timescales. The legend shows the time in seconds at which the spectra were taken. The excitation wavelength was 457.8 nm

5 4 3 Effect of Potential on Raman spectra

Raman spectra of the solid bianthrone layer were recorded at different potentials based on the data provided by cyclic voltammetry The potentials chosen ranged from $-0\ 22$ V, when the layer is in its oxidised state to $-0\ 375$ V, when it is reduced The potentials were maintained by employing amperometric i-t curves, as in previous chapters, with the Raman spectra recorded when the measured current became constant Figure 5 4 3 1 shows an amperometric i-t curve for the solid layer at a potential of $-0\ 25$ V

A comparison between the spectrum of the solid powdered bianthrone and that of the solid layer at a potential of $-0\ 22$ V, reveal few differences One of the main differences of note is the increase in Raman intensity of the band situated at ca 592 cm^{-1} This band corresponds to CCO and CCC stretching The $-0\ 22$ V spectrum shows an approximately four-fold increase compared to the powdered solid spectrum Another increase is observed at 1074 cm^{1} This band in the $-0\ 22$ V spectrum is almost three times larger than the same band in the powdered bianthrone spectrum Another notable difference occurs at 1350 cm^{1} Here there is a slight shift in wavenumber to 1353 cm^{1} along with an increase in intensity of the band The band more than doubles in the solid layer spectrum at $-0\ 22$ V compared to the spectrum of the powdered solid

Comparisons between the spectra at increasingly negative potentials yield few differences in the presence or absence of specific bands or in the intensity of the bands present The most notable difference between the spectra is found in the band at 1353 cm^{-1} This band, which almost doubles when compared to the powdered sample, can be seen to slightly decrease, as the potential of the electrochemical cell is made more negative This is the only clearly observable change that occurs in these spectra
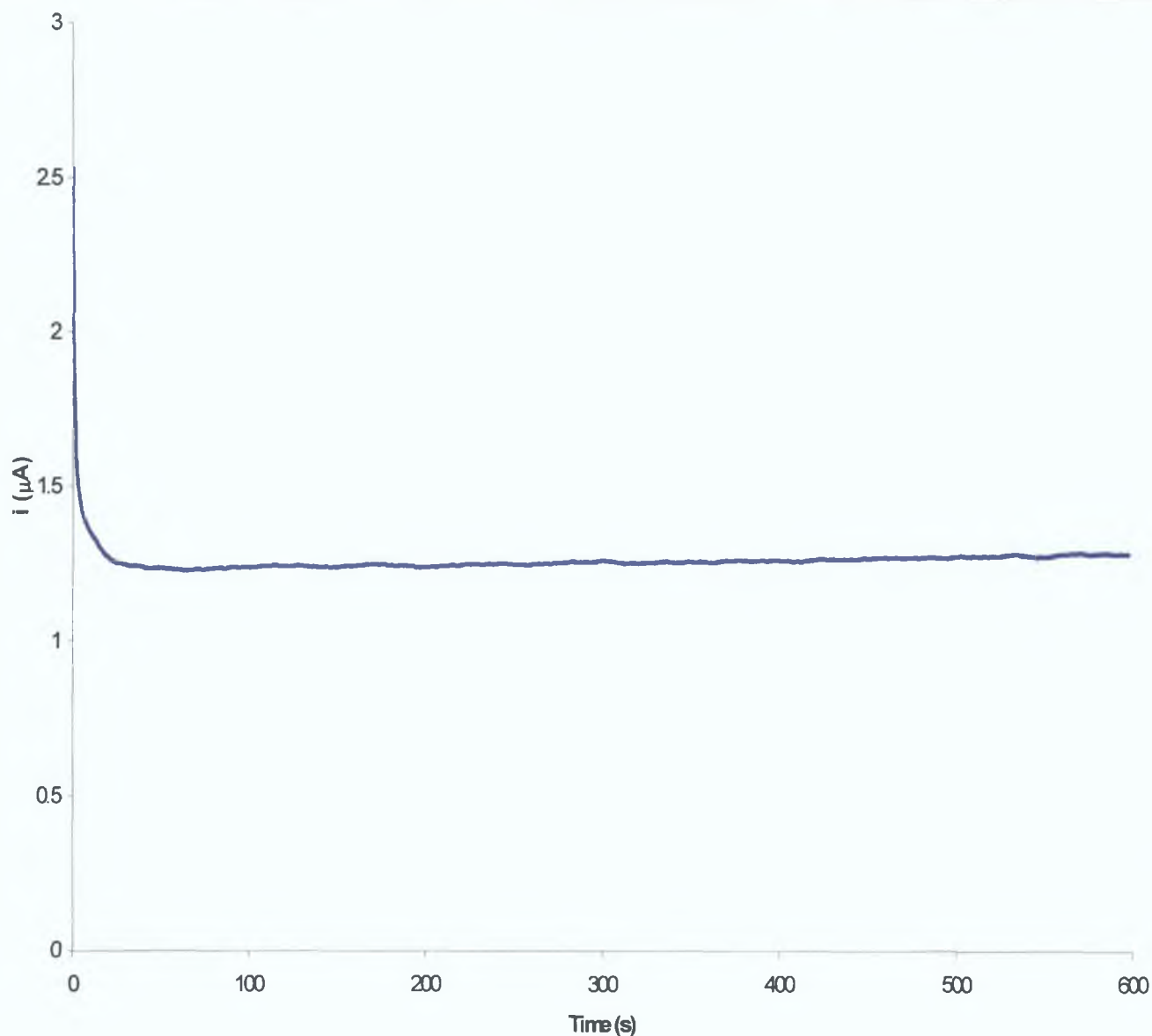
Figure5.4.3.1: Amperometric I-t curve of solid layer on a GC electrode of area 0.07069 cm⁻¹ that was obtained using an electrochemical cell modified for use in conjunction with a Raman microscope (a diagram of which can be found in chapter 4). The potential was held at −0.1 V. The reference electrode was a Ag/AgCl saturated KCl reference and the counter electrode was a coiled platinum wire.

Figure 5.4.3.2: Raman spectra of a solid bianthrone layer on a GC electrode of area 0.07069 cm^{-1} taken at different potentials. The potentials were maintained by constructing amperometric I-t curves. Excitation wavelength was provided by a tuneable argon ion laser set to 457.8 nm

References

1 Forster, R J , Iqbal, J , Hjelm, J , Keyes, T E , *Analyst, 129, 1186, 2004*

2 Keane, L , Hogan, C , Forster, R J , *Langmuir, 18 4826-4833, 2002*
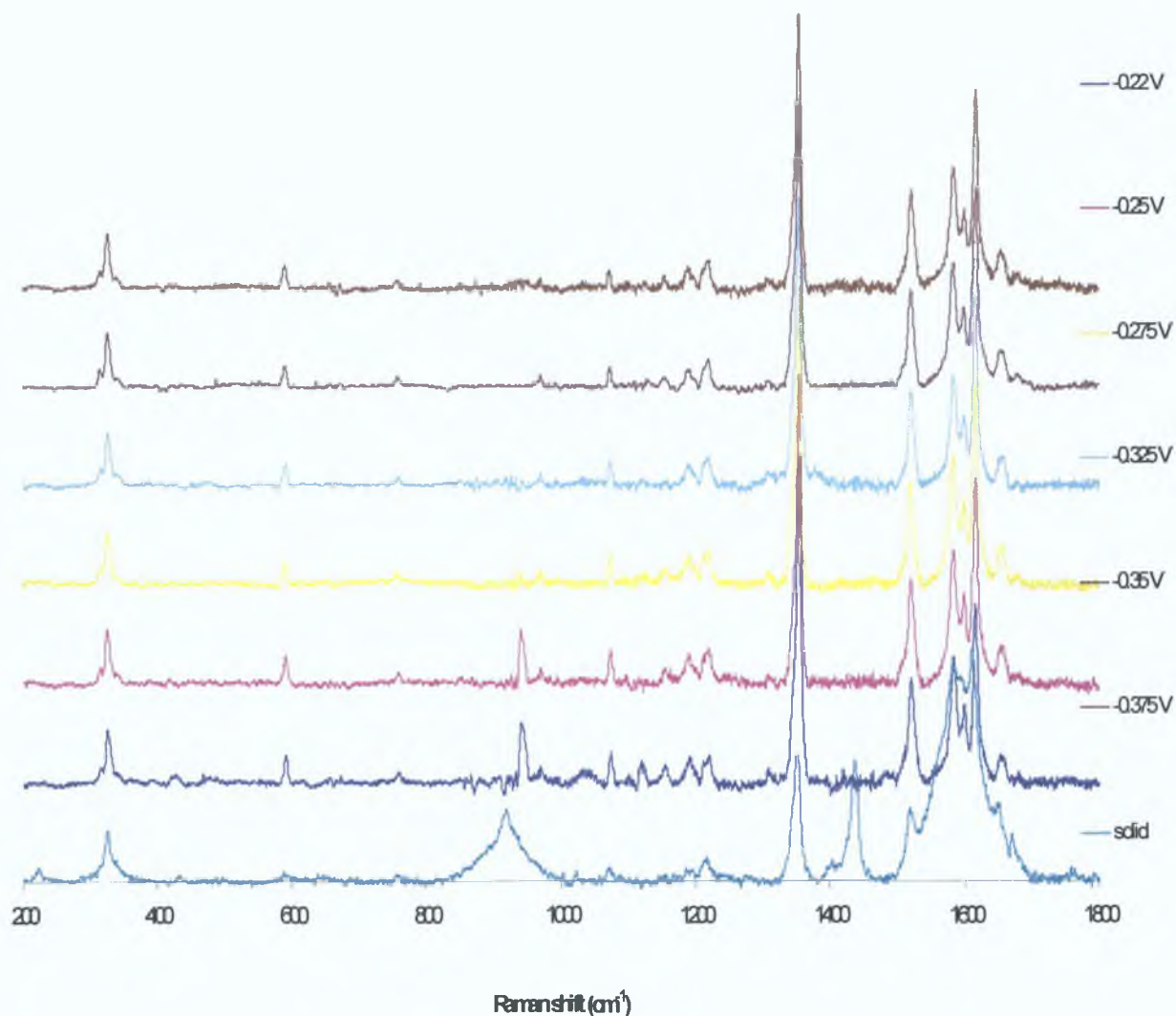
3 Bond, A M , Cooper, J B , Marken, F, Way, D M , *J Electroanal Chem, 396, 407, 1995*

4 Wu, P , Chenxin, C , *J Electroanal Chem , 576, 49, 2005*

5 Hogan, C F , Bond, A M , Neufeld, A K , Connelly, N G , Llamas-Rey, E , *J Phys Chem A, 107, 1274, 2003*

6 Yang, C , He, G , Wang, R , Li, Y , *J Electroanal Chem , 471, 32, 1999*

7 Nazar, L F , Goward, G , Leroux, M , Duncan, H , Kerr, T , Gaubicher, J , *Int J Inorg Mater , 3, 191, 2001*

8 Wrighton, M S , *Science, 231, 32, 1986*

9 Chidsey, C E D , Murray, R W , *Science, 231, 25, 1986*

10 Tredicucci, A , Gmachi, C , Capasso, F , Sivco, D L , Hutchinson, A L , Cho, A Y , *Nature, 396, 350, 1998*

11 Bond, A M , Marken, F , *J Electroanal Chem , 372, 125, 1994*

12 Scholz, F , Lange, B , *Trends Anal Chem , 11, 359, 1992*

13 Bond, A M , Lamprecht, V , Tedesco, V , Marken, F , *Inorg Chim Acta , 291, 21, 1999*

14 Keyes, T E , Forster, R F , Bond, A M , Miao, W , *J Am Chem Soc , 123, 2877, 2001*

15 Bond, A M , Colton, R , Marken, F , Walter, J N , *Organometallics, 13, 5122, 1994*

16 Snook, G A , Bond, A M , Fletcher, S , *J Electroanal Chem , 554-555, 157-165, 2003*

17 Schroeder, U , Scholz, F , *Inorg Chem 39, 1006, 2000*

18 Forster, R J , Keyes, T E , *Phys Chem Chem Phys , 3, 1336, 2001*

19 Bond, A M , Fletcher, S , Symons, P G , *Analyst, 123, 1891, 1998*

20 Bond, A M , Scholz, F , *J Phys Chem , 95, 7640, 1991*

21 Bond, A M , Scholz, F , *Langmuir, 7, 7640, 1991*

22 Bard, A J , Faulkner, L R , *Electrochemical Methods Fundamentals and Applications, John Wiley & Sons,Inc , 2001*

218

23 Su, Z , Maroncelli, M , *J Chem Phys 124, 164506,* **2006**

24 J Ulicny, M Ghomi, H Jobic, P Miskovsky, A Aamouche *J Mol Structure,*
410-411, 497-501 **1997**

6.0 Conclusions

Time flies like an arrow Fruit flies like a banana
Groucho Marx

6 1 Introduction

The redox chemistry of quinones and their analogues can be seen in virtually all living organisms and without them, important biological functions would not be possible They are an essential component in bioenergetics and occur naturally as components in many biochemical molecules Examples of this can be seen in such compounds as ubiquinone, which acts as an electron carrier in the mitochondrial membrane and as a redox component for the coupling of electron and proton transfer in the generation of pH gradients across the mitochondrial membrane[1] Also naphthoquinone is known to be the parent compound to vitamin K[2] This is not to mention the antiviral, anti-inflammatory and antitumour nature of many quinone analogues[3][9] Therefore, the study of such molecules is of vital importance in the field of healthcare The redox properties of quinone and its analogues, particularly species that display an observable change between their oxidised and reduced species, has also shown potential in the field of molecular electronics and sensors and also provide accessible models for the study of electron transfer Much work has been done to develop an understanding of such molecules and further study is vital to expand this understanding and encourage the exploitation of these molecules

In work prior to this thesis, focus has been placed on the electrochemical and photochemical analysis of bianthrone in solution   Examples of electrochemically and photochemically induced conformational changes of bianthrone in solution are detailed in chapter 1 [4][5][6] In brief, bianthrone undergoes a conformational change from a puckered form to a twisted form when undergoing a two-electron transfer in solution This was described as an ECE mechanism[7] Few studies were carried out into the behaviour of the molecule when immobilised on a substrate One such study was carried out by Cuberes et al in which 4,4'-dimethylbianthrone monolayers were deposited by sublimation onto a copper substrate and was studied by STM[8] This work showed that when adsorbed onto the copper surface 4,4'-dimethylbianthrone was primarily in its puckered form Aside from this however, no electrochemical studies had been carried out on bianthrone self- assembled monolayers immobilised on electrode surfaces and no evidence existed to suggest that the conformational behaviour of bianthrone in monolayer form would be comparable to its behaviour in solution

221

6.2 Electrochemical and Spectroelectrochemical analysis of bianthrone monolayers on mercury electrodes

In chapter 3, studies into the formation of self-assembled monolayers of bianthrone on mercury electrodes was carried out. General electrochemical properties suggests that bianthrone undergoes a two-electron, two-proton transfer. This can be seen in the FWHM data obtained. It was found that bianthrone adsorption was irreversible. Bianthrone voltammetry showed evidence of current spikes that appeared in the voltammetry as the surface coverage approached full surface coverage. These spikes were indicative of intermolecular interactions between molecules on the surface. Studies into the dynamics of bianthrone monolayer formation were carried out by comparing a theoretical model, obtained from a paper by Hubbard et al. that described the influence of diffusion of molecules to the surface and the reorganization of molecules on the electrode surface, with surface coverage/time data obtained by cyclic voltammetry. It was found that, initially, at low values of surface coverage, adsorption was more strongly influenced by diffusion while at longer timescales, as the surface coverage of the monolayer increased diffusion became less dominant and surface reorganization became a more influential factor. By manipulation of the parameters of the theoretical models and by taking measures to minimise the sum of squared residuals between the theoretical predictions and the experimentally observed surface coverages, values for the diffusion rate constant and the surface reorganization rate constant were obtained. The diffusion rate constants ranged from 6.0×10^{-11} for 0.09 μM to 1.5×10^{-12} for 0.3 μM. The surface reorganization rate constants, K, ranged from 9.31×10^{-7} for 0.09 μM to 9.8×10^{-8} for 0.3 μM. A desorption rate constant was also obtained for bianthrone desorbing into a blank electrolyte solution following adsorption from a 0.15 μM solution using a diffusion controlled Langmuir model. A pertinent observation was that bianthrone surface coverage did not decay to zero but remained at ca 45 % of the total coverage. A value for the desorption rate constant, k_m, of 1×10^{-2} $s^{-1/2}$ was observed.

A spectroelectrochemical cell in which electrochemistry could be carried out while being incorporated into a Raman microscope was fabricated to examine bianthrone monolayers adsorbed on mercury electrodes. A schematic of the cell can be found in chapter 3. The objective was to investigate whether conformational changes could be observed from molecules immobilised on the electrode surface.

Raman spectra of the adsorbed monolayer in the absence of an applied potential compared favourably with spectra of the solid bianthrone obtained at room temperature and with spectra obtained by others [9][10] An assignment published by Ulicny et al proved quite useful [7] Voltammetry obtained using the spectroelectrochemical cell compared favourably to voltammetry obtained conventionally The potential of the cell was held at different points between where the monolayer was fully oxidised and fully reduced according to the cyclic voltammetry obtained and Raman spectra were recorded at these points The spectra taken at these potentials were compared and contrasted to elucidate any structural differences that occurred in the reduction of the monolayer This analysis revealed some subtle changes in intensity in the lower wavenumber region of the spectra However, there were no changes indicative of a large structural change to the monolayer As a result of this analysis, it is not believed that bianthrone undergoes conformational changes that would induce major structural changes to the monolayer upon reduction

6 3 Electrochemical and Spectroelectrochemical analysis of bianthrone monolayers on glassy carbon electrodes

In chapter 4, studies into the formation of bianthrone monolayers on glassy carbon electrodes were carried out The voltammetry is consistent with a surface adsorbed molecule undergoing a two-electron, two-proton transfer The adsorption is also irreversible Unlike adsorption on mercury, current spikes are not observed Studies into the dynamics of monolayer formation on GC were also carried out using the same theoretical model as published by Hubbard et al In comparisons between the predicted theoretical surface coverages and the observed experimental data it was found that the increase in surface coverage over time was most satisfactorily described by the surface reorganization model with poor fits observed for the diffusion model By manipulation of the parameters of the theoretical model and by taking measures to minimise the sum of squared residuals between the theoretical predictions and the experimentally observed data for surface coverage, values for the surface reorganization rate constant were obtained This value ranged from $1\ 26 \times 10^{7}$ $\pm 0\ 05$ cms^{1} for 1 μM to $4\ 36 \pm 0\ 02 \times 10^{8}$ cms^{1} for 20 μM.

It was seen in a preliminary experiment that continuous voltammetric cycling had a notable effect on the surface coverage of the monolayer This can be seen in chapter 4 Consequently, continuous voltammetric monitoring of the monolayer was considered unfeasible Electrochemical impedance was considered to be a useful alternative This involved indirectly monitoring the capacitance of a monolayer at a constant potential outside of the range of the redox potential

A spectroelectrochemical cell in which electrochemistry could be carried out but that could still be incorporated into a Raman microscope was fabricated This cell is similar in design to that described in chapter 3 except in the fact that this cell could accommodate a GC electrode, or, in fact, any electrode with similar dimensions to those used in this work A schematic of this cell can be seen in chapter 4 The cyclic voltammetry compared very favourably with that achieved conventionally and preliminary characterisation of the cell confirmed that it was fit for use as an electrochemical cell As in chapter 3, the objective was to investigate whether conformational changes could be observed from bianthrone molecules adsorbed on the GC surface Raman spectra of bianthrone monolayers recorded in the absence of an applied potential compared favourably with the spectra of solid bianthrone and spectra obtained in the literature[67] The potential of the cell was held constant at different points between where the monolayer was oxidised and reduced according to the voltammetry obtained The spectra recorded at each potential were compared and contrasted to elucidate any structural differences that may have occurred at these potentials as the monolayer is reduced Some changes in intensity at certain bands were observed, however, there were no large changes in the spectra associated with large structural changes arising from conformational changes in the molecule From this, it was concluded that conformational change in the molecule did not occur when it was immobilised on the glassy carbon surface

6 4 Solid-state Electrochemical and Spectroelectrochemical analysis of bianthrone on glassy carbon electrodes

Electrochemistry was carried out on bianthrone in the solid state, on a glassy carbon electrode The glassy carbon electrode was modified by attaching a small amount of powdered bianthrone solid by mechanical abrasion, giving a random array of particles, a method that has been reported previously Electrochemistry revealed that, unlike the adsorbed monolayer voltammetry of bianthrone, two redox couples were observed at ca -0 2 V and at ca -0 3 V The charge under these curves was also seen to be approximately ten times lower than that for the adsorbed monolayers The charge of the redox couple at ca -0 3 V, which was non-existent in initial, scans was seen to increase over time, becoming larger than that at ca -0 2 V The charge of the redox couple at ca -0 2 V increased from initial scans before decreasing over a short timescale The redox couple at ca -0 3 V coincides with that of the redox couple of bianthrone in the adsorbed monolayer A possible explanation for this electrochemical behaviour is that the initial redox behaviour at -0 2 V is due to the mechanically attached particles, which over time are dissolved by the supporting electrolyte "breaking in" to the layer The redox couple observed at -0 3 V is due to bianthrone molecules becoming dissolved by the supporting electrolyte and adsorbing onto the surface

Raman spectroscopy of bianthrone in the solid state on GC electrodes was carried out using the spectroelectrochemical cell described in chapter 4 The objective here was to examine whether the observed changes in the voltammetry were accompanied by large structural changes in the solid layer over time Raman was also employed to probe the effect of changing potential on the layer The Raman spectra observed of bianthrone in the solid state over time revealed little change with the only observable change being the initial increase in intensity of the band at 1353 cm^{-1} almost doubling However, no discernible change was subsequently observed It was concluded that the changes observed in the voltammetry were due to activity at the electrode surface and that there is no activity observed at the surface of the solid layer Raman was not sufficient to penetrate the solid layer to observe any changes Raman spectra were also recorded under different conditions of potential as described previously The spectra were recorded between potentials ranging from -0 22 V at which the solid is in the oxidised state to -0 375 V where the solid should be reduced

There are few discernible differences between these spectra save for a notable increase in intensity, from the spectrum of the solid to the spectrum taken at –0.22 V, of the band at 1353 cm^{-1}. This band then decreases slightly as the potential is shifted more negative with the lowest intensity observed for the band seen at –0.375 V.

As discussed in Chapter 1, the demand for high data storage densities high switching rates, switching devices and miniaturization has stimulated the search for organic materials suited for applications in switching devices. A prime requirement of a molecular switch is that it should be stable in two distinctly detectable states that can be reversibly switched. Many studies carried out showed that, in solution, bianthrone displayed such characteristics, where it was possible to distinguish, spectroscopically, between the A conformation and the B conformation.[15, 16, 17, 18, 19] If similar conformational change and bistability were evident when the molecule was immobilised on an electrode, a significant step towards a viable molecular switch that was mechanically stable enough for incorporation into a device could have been achieved. However, as shown in the experiments here, while reduction of the molecule was observed, conformational change was not observed when adsorbed on either a mercury or glassy carbon surface. This is likely due to the interaction of the π-electrons in bianthrones ring system with the electrode surface and also the presence of intermolecular hydrogen bonding. The work here reveals that the solution phase electrochemical behaviour of bianthrone cannot be directly transferred to an electrode surface. To develop a bianthrone monolayer system in which conformational switching is possible will probably require the introduction of a short linker , e.g., ethylene thiol, that prevents the aromatic moieties from interacting so strongly with the surface. Despite this result, bianthrone monolayers have the attractive feature that electron transfer is highly reversible and its rate can be modulated by the pH of the contacting electrolyte. However, despite the extremely short electron transfer distance involved, less than 4A, the rate is remarkably slow, i.e, of the order of 10^3 s^{-1}. From the perspective of developing molecule based electronics, this finding poses significant challenges since conventional silicon circuits can be switched at the nanosecond timescale. While the origin of this relatively slow electon transfer is not entirely certain it most likely involves a significant contribution from inner sphere reorganisation and is influenced by the electric field of the electrode. In common with the strategy of including binding groups that move the adsorbate a short distance off

the surface to allow conformational switching, it is possible that *increasing* the electron transfer distance may *increase* the electron transfer rate by decreasing the strength of the electric field While this approach requires further exploration, it is likely that systems can be developed where the electric field can be used to *enhance* conformation switching rates without causing a slow electron transfer rate to be observed

References

1 Johnsson Wass, J R T , Ahlberg, E , Panas, I , Schiffrin, D J , *J Phys Chem A, 110, 2005,* **2006**

2 Matthews, C K , van Holde, K E , Ahern, K G , *Biochemistry, 3rd ed , Benjamin Cummings, San Francisco, CA,* **2000**

3 Papageorgiu, V P , Assimopoulu A N , Couladouras, E A , Hepworth, D , Nicolaou, K C , *Agnew Chem Int Ed Engl 38, 270,* **1999**

4 Evans, D H , Xie, N *J Am Chem Soc Vol 105, 315,* **1983**

5 Olsen, B A , Evans, D H *J Am Chem Soc , Vol 103,No 4,* **1981**

6 Neta, P , Evans, D H *J Am Chem Soc , Vol 103, No 24,* **1981**

7 Hubbard, J B , Silin, V , Plant, A L , *Biophys Chem , 75, 163-176,* **1998**

8 Cuberes, M T , Schlittler, R R , Jung, T A , Schaumburg, K , Gimzewski, J K , *Surface Science Vol 383, 37-49,* **1997**

9 Sanchez-Cortez, S , Jancura, D , Miskovsky, P , Bertoluzza, A , *Spectrochim Acta A, 53, 769,* **1997**

10 J Ulicny, M Ghomi, H Jobic, P Miskovsky, A Aamouche *J Mol Structure, 410-411, 497-501* **1997**

u

ỉ

'

: